A Study of Globular Cluster Systems in the Shapley Supercluster Region with the Hubble Space Telescope

by

REGINA G. BARBER DEGRAAFF

A dissertation submitted in partial fulfillment of
the requirements for the degree of
Doctor of Philosophy

WASHINGTON STATE UNIVERSITY
Department of Physics and Astronomy
August 2011

To the Faculty of Washington State University:

The members of the Committee appointed to examine the dissertation of Regina G. Barber DeGraaff find it satisfactory and recommend that it be accepted.

John P. Blakeslee, Ph.D., Chair

Michael Allen, Ph.D.

Philip Marston, Ph.D.

Guy Worthy, Ph.D.

Abstract

A Study of Globular Clusters Systems in the Shapley Supercluster Region with the Hubble Space Telescope

by Regina G. Barber DeGraaff, Ph.D.

Washington State University

August 2011

After a brief introduction to astronomy and topics related to this thesis, we present three projects directed towards expanding our understanding of globular cluster (GC) systems, or populations, in galaxies within clusters.

We first present two-band *Hubble Space Telescope* imaging of the "transitional" S0 galaxy NGC 1533 in the Doradus group of galaxies. We study the globular cluster system of this galaxy in detail and estimate its distance using three different methods, two of which are based on mean properties of the galaxy's GCs.

We next present an investigation of ultra-compact dwarfs (UCDs), which are dense stellar systems closely associated with GCs, in the giant elliptical galaxy ESO325-G004. We find a significant sample of UCD candidates in the field of this galaxy; we discuss the implications of these results and possible follow-up strategies.

The main part of the thesis is a survey of the globular cluster systems of 11 giant elliptical galaxies in clusters associated with the Shapley Supercluster, the largest mass concentration in the local universe and possibly a major source of the Local Group's $\sim$630 km s^{-1} motion with respect to the cosmic microwave background

radiation. The sample galaxies were imaged with the Advanced Camera for Surveys Wide Field Channel in the F814W bandpass and are in the redshift range $z = 0.035$–0.048. The radial density distributions and constraints on the total GC populations of these 11 galaxies are presented. We find substantial globular cluster systems in all the galaxies, with the specific frequencies being larger for more central galaxies. The most massive galaxies in our sample, ESO444-G046 at the center of the extremely rich cluster Abell 3558 and ESO383-G076 at the center of Abell 3571, may contain the largest globular cluster populations studied to date.

For one galaxy in our sample, ES0325-G004, additional multi-band imaging was obtained. We analyze the color data and find that ESO325-G004 has a bimodal globular cluster color distribution with characteristics typical of most giant ellipticals, and we discuss new ideas about the underlying causes of such distributions.

The final chapter provides a summary of the thesis and possible future work.

Acknowledgements

I would like to thank my advisor, John Blakeslee for his infinite patience and help. He may be the nicest astrophysicist alive. The members of the University of Washington Astronomy Department deserve thanks for offering me words of encouragement and office space during part of this thesis. Instruction at McMaster University by William Harris on DAOphot was essential for Chapter 4 and I thank him immensely.

Special thanks to family and friends for being understanding through these stressful years. Thank you to my parents for taking care of me by cleaning, cooking, babysitting, taking me on undeserved trips, and believing in me. Lastly, I would like to thank my husband for putting up with me while I went crazy because of this thesis and my daughter for being so cute that it made me forget about the pressure.

Contents

List of Figures

List of Tables

DEDICATION

This thesis is dedicated to my daughter Dorian Reina DeGraaff. The time of her birth might cause some to think motherhood may have been the cause for a delay in finishing my degree. However, I would like Dori to know that she is the reason I had the strength to finish at all.

Chapter 1

Introduction

I first heard of globular clusters when I was 17 working on restoring the Western Washington University Planetarium. The projector was a relic from before the makers discovered that a sphere is a good shape to house a light source to recreate the sky. This projector consisted mainly of a huge 3D polygon with vacuum tubes. In a smelly, cramped, domed room, I memorized a standard planetarium presentation. The show contained information and slides to dazzle the guests such as supernovae and eclipses, but also to educate, like globular clusters. I had never heard of these dense star clusters, that were not galaxies, and instantly felt like I was "in-the-know" but at the same time perplexed about their existence. Apparently, many in the past were in awe of these mysterious globular clusters, as I was, but sadly a lot is still not known about these stellar systems. To further understand the origins of globular clusters and their host galaxies more studies, such as those that are described in this thesis, are needed.

1.1 Globular Clusters

A globular cluster (GC) is a collection of a hundred thousand to a few million stars tightly bound by gravity, all created at approximately the same time from the same cloud of dust and gas. Even with amateur telescopes you can resolve the individual stars in GCs that halo our own galaxy, the Milky Way. These dense star clusters are devoid of gas and dust, which had been used up in the formation of the cluster. These stellar systems can be found in the tens to tens of thousands haloed around most galaxies. However, the ages of these GCs are older than their host galaxies and are some of the oldest objects in the sky at 9-14 billion years. The ubiquity of globular clusters and their approximate uniform ages give a possible window into the evolution of their host galaxy, host cluster and subsequently the universe. Figure 1.1 shows an image taken by the Hubble Space Telescope (HST) of the globular cluster NGC2808. HST will also be discussed in more detail in a later section of this chapter.

1.1.1 History

Before I discuss the recent development of globular cluster research, it is interesting to look into how these object contributed to the recent and revolutionary notion that the Milky Way does not constitute the entire universe.

The Messier Catalog, William Herschel and the New Galactic Catalog

Many ancient cultures charted the skies and had catalogs of the stars and planets and their positions during the year. However, many people felt annoyance or curiosity at the occurrence of unpredictable objects in the sky, such as sudden bright objects that could be seen in the daytime which faded over time, supernovae, or the retrograde motion of planets. These inconsistent objects led to the whole heliocentric universe transforming from the geocentric universe, as well as elliptical orbits of planets, but that is a whole other topic that the reader can find elsewhere. After the religious (western) and scientific revolutions that created proper models to ex-

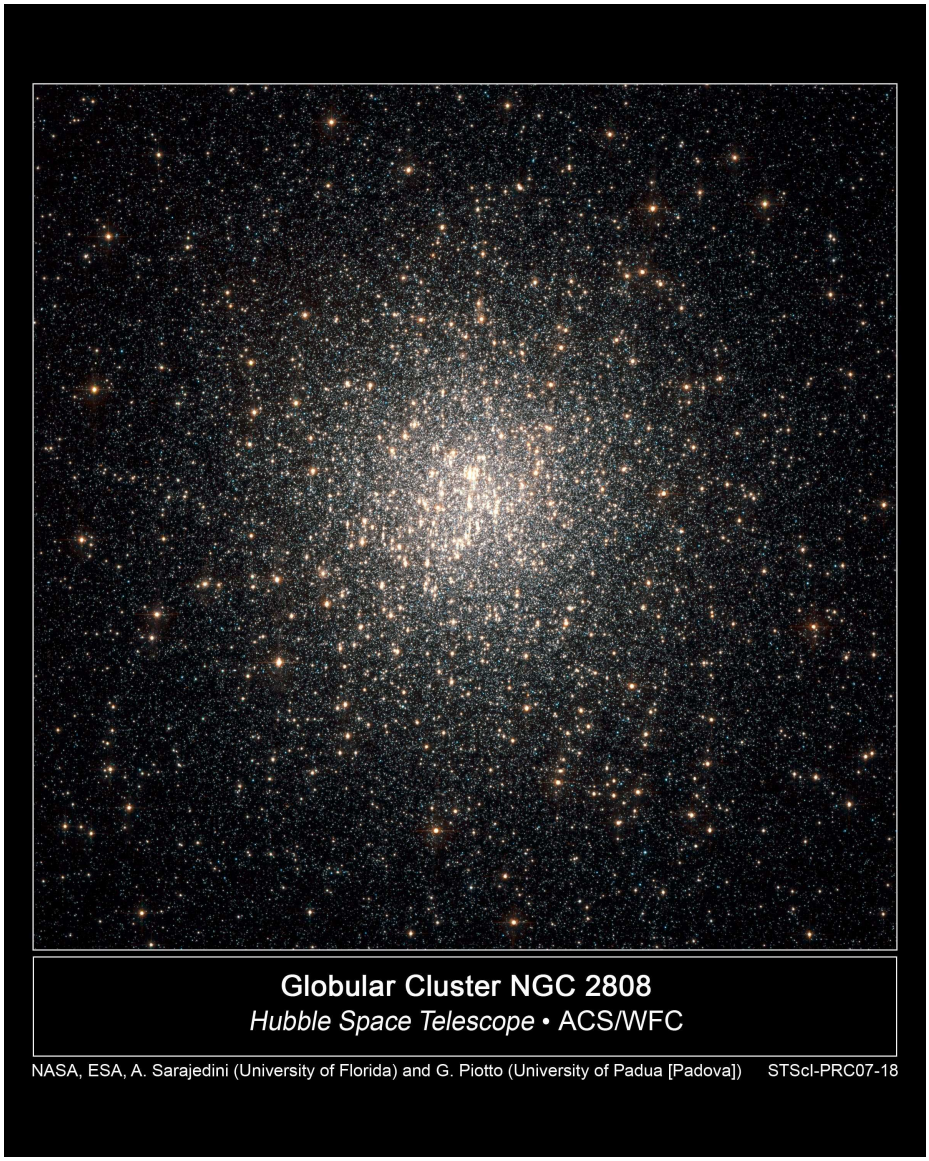

Figure 1.1 Hubble Space Telescope image of globular cluster NGC2808.

plain the motions of the heavens, observers still wanted catalogs of stars and things they believed were definitely not stars. Galileo was the first to turn a telescope toward the milky ribbon in the sky, the Milky Way, to discover that it was made up of many stars, not a celestial liquid. Other fuzzy objects in the sky turned out to be collections of stars whose combined brightness created concentrated hazes. The concept that some stellar objects were composed of many stars themselves and could possibly be other 'universes' (actually galaxies) like our own, was proposed by Kant in his Universal National History and Theory of the Heavens (1755). He called them "island universes." Most scientists were not ready to believe that these objects were not within our own galaxy. However, let us get back to catalogs of stellar objects and stars.

One comet enthusiast named Charles Messier created a famous catalog that contained not only comets but also objects that were small fuzzy blobs. These fuzzy objects were soon called nebula and were a mystery for some time. The catalog was the Messier Catalog and totaled a number of 109 objects that could be seen from the Northern Hemisphere (Messier 1781).

In the 1700s, telescopes became advanced enough to resolve some nebula in the Messier catalog to show that they, like the Milky Way, were made up of stars. One example is the famous Andromeda Galaxy, a "nebula" that can be seen in the Andromeda constellation with your naked eye, recorded in the Messier catalog as M31. The first nebula viewed to be a dense cluster of stars was M22, by William Herschel. Herschel first started using the term GC as a visual description of these objects.

Since these objects halo our own Milky Way galaxy, a few globular clusters can be seen with the naked eye. With an amateur telescope M22 can been seen clearly and Figure 1.2 shows a highly resolved image using HST. Now that the Messier catalog was known to contain different kinds of nebula, astronomer William Herschel, his sister, Caroline, and son, John, spent years making a more comprehensive list of nebula. Later, John Dryer, an astronomer in the late 19th century, expanded this list to create the New Galactic Catalog. These objects have the designation NGC before an ID number, such as Figure 1.1. One object NGC1533 is the subject of chapter two of this thesis. Herschel began increasingly to believe Kant's theory of island universes

with every "nebula" he studied. Figure 1.3 is Herschel's model of the Milky Way published in 1785. The inclusion of the Sun's location is a modified version used in a University of Washington astronomy course. This idea that our galaxy is just another galaxy in the universe was a point of major contention, which came to head at the National Academy, an American institution, in 1920, an event astronomers call the Great Debate (Binney 1998).

Harlow Shapley and the Great Debate

In the 20th century the astronomer Harlow Shapley, the namesake of the supercluster studied in this thesis, did a study on known GCs and as a result changed the perception of our location in the universe.

At the time of Shapley, very early 20th century, the location of the Sun in the Milky Way galaxy was thought to be close to the center. This model was analogous to the geocentric belief for our solar system in early astronomy. We had come to a heliocentric theory for our galaxy. Using the distribution of globular clusters, Shapley began to notice that these objects were not distributed uniformly in our sky. Figure 1.4 shows the locations of Milky Way globular clusters using Herschel's model. Shapley proposed that if these objects are an essential structural component of the galaxy, which he believed them to be after his study, they should be distributed uniformly around the center of the galaxy. The non-uniformity of the known globular clusters led him to believe that the Sun is not at the center of the galaxy (Shapley 1918).

The location of our Sun was just one of the issues discussed in the "Great Debate" which involved Heber Curtis and Harlow Shapley. The main point debated was the ideas of nebula outside or inside of our galaxy. Was our galaxy the universe or was the universe much larger than our galaxy? The latter would validate the idea of "island universes" or other galaxies like our own. The debate was actually a lot more complicated than this statement and more of a presentation then a debate. Curtis studied spiral nebulae and presented an argument that some nebulae were galaxies of their own. However, he did not believe Shapley's distance measurements that

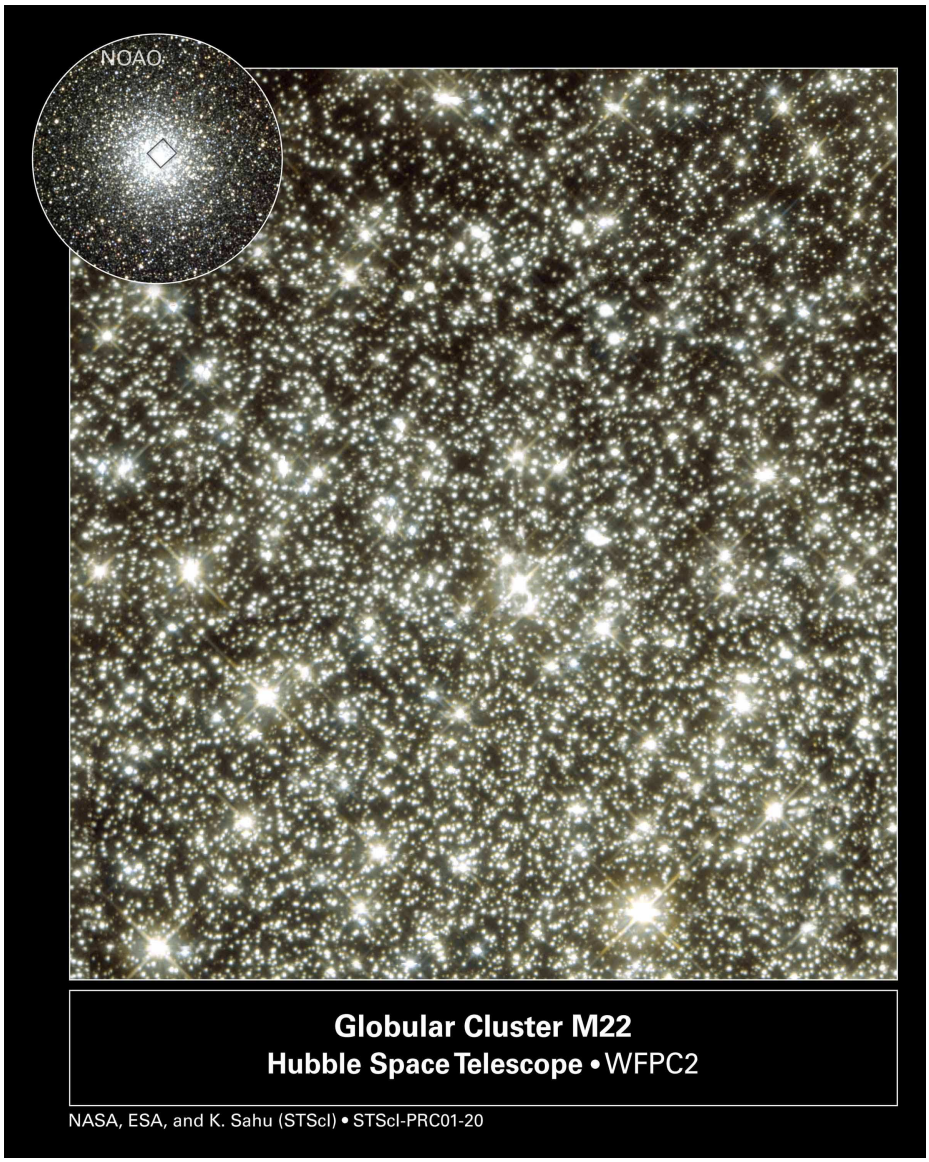

Figure 1.2 Hubble Space Telescope Image of the Messier 22 with an insert of M22 from ground-based NOAO image (Burrell Schmidt telescope, Kitt Peak, AZ).

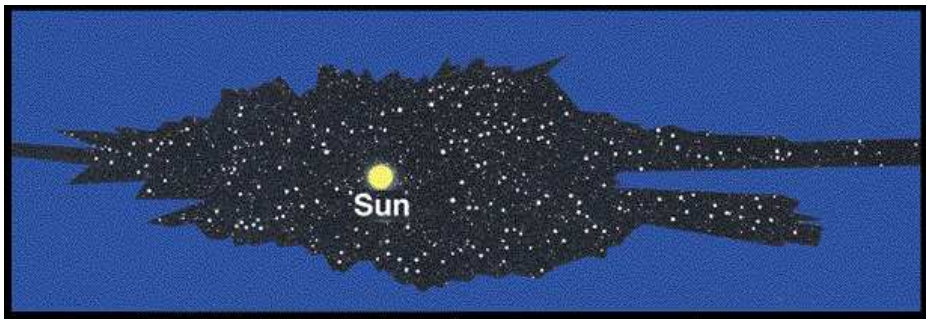

Figure 1.3 Herschel's model for the Milky Way (1785). This is a modified version used by University of Washington's Astronomy department for the purposes of an astronomy course.

suggested a huge size for the Milky Way galaxy. It was Shapley's own measurements that placed him on the other side of the "debate". Since some nebula had such small angular sizes, they would have to be at distances Shapley was not willing to accept. Decades after the two "debaters" published their stances, it turns out both were wrong and right; our galaxy is not the entire universe and the universe was huge since Shapley's location for our solar system and distance measurements were more accurate (Shapley 1921; Curtis 1921).

1.2 Distance Indicators

Before we understand how Shapley got these distances, we need to first explore the distance terms and methods used in astronomy. In this thesis, we use a few of the following methods to obtain an accurate distance to NGC1533, chapter 2.

1.2.1 Geometic Parallax

Parallax is a way to directly measure distance. Viewing an object from two different locations can give the distance from the viewing location to the object using

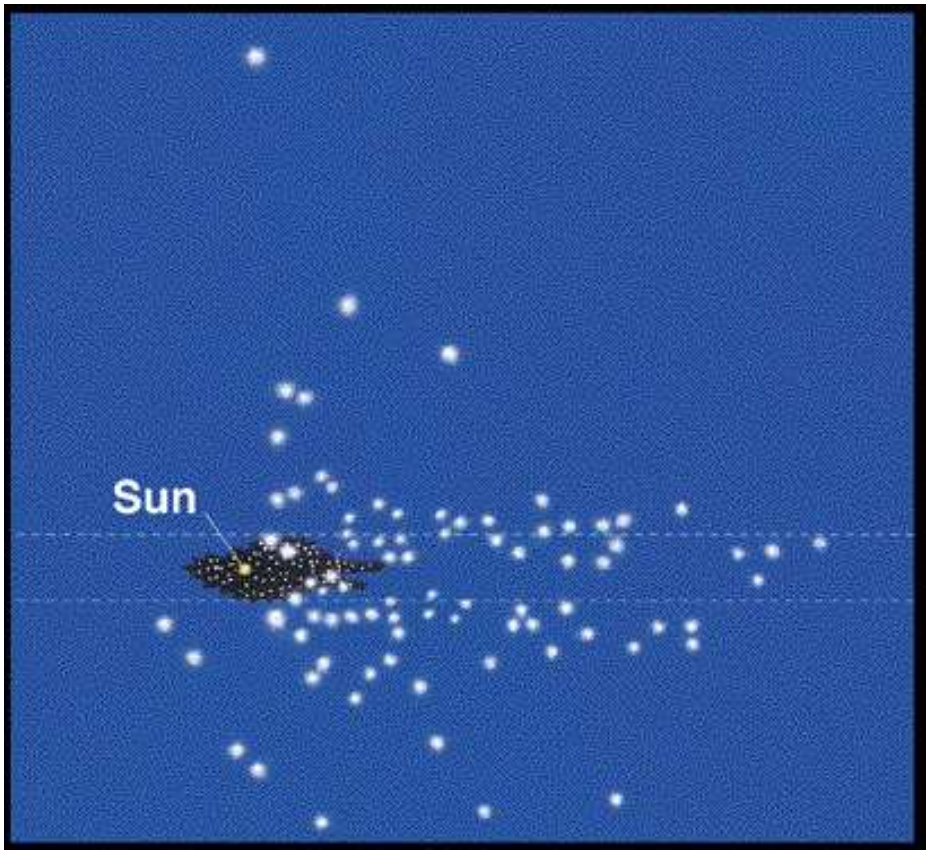

Figure 1.4 Herschel's model with the Milky Way globular cluster distribution, used by University of Washington's Astronomy department for the purposes of an astronomy course.

simple geometry. This can be done because the apparent location of a foreground object with respect to more distant objects changes when viewed from different locations. The simplest example in everyday life is with your own eyes. If you close one eye and view the lamp across the room and then shut the other eye while opening the previously closed eye, the lamp will appear to have moved location. Now if one knows the distance between your eyes, and the apparent displacement of the lamp, the distance from you to the lamp could be calculated. In astronomy we can measure the distance to nearby stellar objects and planets using parallax. When the Earth is at the two extreme points in its orbit around the Sun, winter and summer for instance, the location of a close object in the sky appears to move. Figure 1.5 shows this phenomenon with a nearby star in front of a constellation of background stars that are too far away to move in the night sky. We see that the foreground star appears in different locations compared to the stationary distance stars (Binney 1998).

Distance in astronomy is usually measured in parsecs, which is an abbreviation of 'parallax of one second'. In Figure 1.5 one can see that the angles that the lines make around the nearby star are symmetric. That angle is measured in arcseconds, 1/3600th of one degree. Separation in the night sky is described by astronomers in arcseconds. One parsec (pc) is the distance from the Sun to an object with a parallax angle of one arcsecond. The following is the conversion of one parsec to other distance units.

$$1 \text{ pc} = 3.26 \text{ light years} = 3.09 \times 10^{13} \text{ km} = 1.92 \times 10^{13} \text{ mi} \tag{1.1}$$

The galaxies studied in this thesis are at distances of 19.4×10^6 pc or 19.4 Mpc for NGC1533 and about 150 - 190 Mpc for the Shapley Supercluster.

Parallax can be used only for stellar objects and systems that have apparent displacement, in the sky, between the seasons. Once an object of interest does not exhibit this movement, such as the background stars in Figure 1.5, assumptions must be made to calculate distance. Parallax does not depend on anything other than geometry and is therefore a direct measurement in astronomy. However, distance can

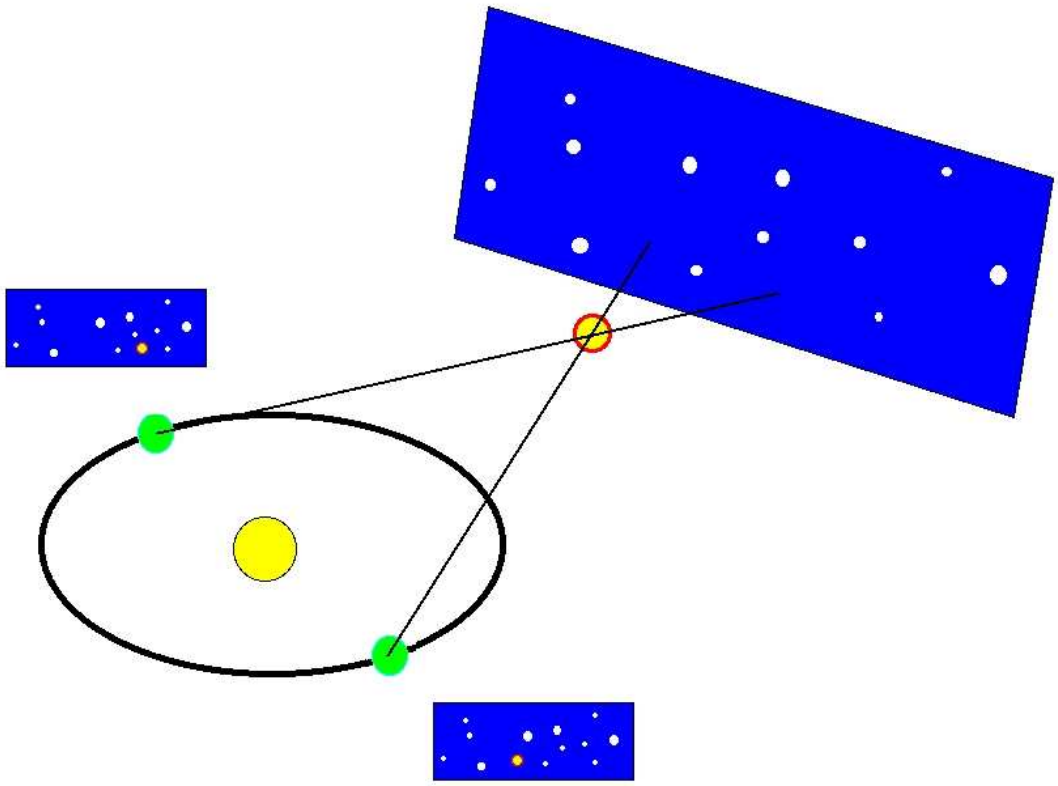

Figure 1.5 Parallax of a nearby star when Earth is positioned 6 months apart in its orbit about the Sun. The star appears in different locations in the night sky, compared to the background distant stars.

dim a bright object, like a lighthouse flame far from the shore. If the exact brightness of a far away object is known, a distance could be estimated from the brightness observed.

1.2.2 Hipparcus, Magnitude Scale and Distance Modulus

The only data we receive from stellar objects is light and on Earth we receive only a small portion of the electromagnetic spectrum. The ancient Greek astronomer Hipparcus first divided the brightness of stars into six classes; the brightest ones being Class-1 and the faintest being Class-6. This is the basis of the magnitude scale astronomers currently use

$$m = -2.5log\frac{f}{f_0} = -2.5log\frac{L}{4\pi d^2} + C \tag{1.2}$$

where m is an apparent magnitude or brightness seen from Earth, d is the distance from Earth, f is the observed flux, and f_0 is reference flux (such as for the star Vega). This definition of magnitude continues Hipparcus' system of stellar objects being assigned larger magnitude values while having a dimmer brightness.

The absolute magnitude, M, is a measure of the true brightness of the star. Currently, the scale of apparent magnitude goes into the negatives with the Sun at -26.74 and the extremely dim 26 magnitudes, which are discussed in this study of GCs surrounding NGC1533 and the 11 Shapley Supercluster galaxies. Galaxy magnitudes and globular cluster magnitudes use the same stellar magnitude scale. Our study uses the powerful Hubble Space Telescope to obtain images that can be analyzed to get magnitudes for globular clusters well beyond our own galaxy and will be discussed in the following sections. A distance can be calculated if the apparent magnitude is measured and if the absolute magnitude is known. The absolute magnitude is defined as the apparent magnitude that the object would have if it were at a distance of 10 pc. This relation can be written in the following equation,

$$M = -2.5\ \log\frac{L}{4\pi 10^2} + C \tag{1.3}$$

where this is the apparent magnitude equation with $d = 10$ pc.

For galaxies, which have diameters much greater than 10 pc, the absolute magnitude is that of a star of same luminosity as the whole galaxy. The difference between the apparent magnitude, m, and the absolute magnitude, M, is called the distance modulus.

$$\text{distance modulus} = m - M \tag{1.4}$$

The distance modulus or DM can be used to find the distance to the object by combining equations 1.2 and 1.3 the following way,

$$DM = m - M = 2.5log\frac{d^2}{10^2} = 5 * log\frac{d}{10pc} \tag{1.5}$$

where d is the distance measured in pc.

1.2.3 Filters and Color

Keep in mind that the value for magnitude will differ with the filter or bandpass used to image the light from a star or galaxy. The filter allows only certain wavelengths to pass and be collected. Common filters, that limit these ranges, in astronomy are the UBVRI bands, which is the Johnson system which designates U for ultraviolet and I for infrared, with BVR covering blue, visible, and red, respectively. There are many more filters used by astronomical instruments which cover other wavelengths in the electromagnetic spectrum. The magnitude taken in the B band is called m_B or just B. Taking the difference between magnitudes taken in two different filters is called a color; B - V is the color from the difference in m_B - m_V = M_B - M_V, since the absolute magnitude is just a shift of the apparent magnitude.

1.2.4 Standard Candles

If the absolute magnitude is known (or is estimated from assumptions), that class of object is called a standard candle. An example of a standard candle is a variable star, which is a star whose brightness changes in a periodic fashion. Variable

stars close enough to get a distance measurement using parallax were discovered by Henrietta Swan Leavitt to have a correlation between the period of variation and the luminosity. There are several classifications of variable stars that follow different period-luminosity relations, such as type I and II Cepheid variables and RR Lyrae stars. The assumption that all variable stars follow the same period-luminosity relation was the reason Shapley's distance measurements were not as accurate as they could have been. However, Cepheid variables played a major role in finding accurate distances to globular clusters and in turn the location of our solar system within the Milky Way.

1.2.5 Globular Cluster Luminosity Function

Globular clusters later proved to be useful in measuring distance. It was first noticed by Shapley (1953) that the average luminosity of the globular clusters in our own galaxy the Milky Way, the Andromeda Galaxy (M31), and the Large Magellanic Cloud were all very close. Once magnitudes to GCs associated with the Milky Way and M31 were obtained, the number of GC are binned by magnitude and plotted. This histogram seemed to follow a Gaussian curve, expressed in the following equation,

$$\frac{dN}{dm} = A * e^{\frac{-(m-m_0)^2}{2\sigma_m^2}} \tag{1.6}$$

where m_0 is the peak of the Gaussian curve and σ is the deviation which is a parameter of the Gaussian shape. Equation 1.6 is called the Globular Cluster Luminosity Function (GCLF) and is used as a distance estimator. The peak magnitude can be used in the distance modulus formula, equation 1.5, substituting m = m_0 and M = M_0, when one assumes M_0 to be a standard constant for globular clusters, making the GCLF a standard candle. This value of M_0 depends on the photometric bandpass since stars and galaxies look different through different filters (Binney 1998). Values for two different M_0s are given in Chapter 2 and a distance is found using this method.

1.2.6 Surface Brightness Fluctuation

Another indirect distance method used in Chapter 2 to obtain a distance to NGC1533 uses surface brightness fluctuations of the stellar object and is called the SBF method. This method takes advantage of the CCD camera, described in the next section, and the graininess of the image and was first described in Tonry and Schneider (1988). Since a galaxy is made up of individual stars, the graininess or surface brightness fluctuation is directly proportional to its distance. Using models of a galaxy made up of N number of stars and a Poisson distribution, $\sqrt{N}$ for any portion of the galaxy, we can relate variations in brightness to distance. If a galaxy is at double the distance, the variance will fall by 1/4. The CCD camera helps get a more accurate measure of the galaxy's brightness variation by being able to measure number and luminosity of each star that falls into individual pixels within the image.

1.2.7 GC Size

This method is based on the assumption that the median half-light radius, a size measurement that corresponds to the radius from the core that contains half the total mass, of globular clusters surrounding a galaxy is constant. This method is used in Chapter 2 and assumes this mean size is about 3 pc, which was derived from a Virgo cluster survey discussed in Jordan et al. (2005). Once the GC sizes are measured from an image, the median size can be used in the following equation,

$$d = \frac{0.552 \pm 0.058}{\langle \hat{r}_h \rangle} \text{ Mpc}, \tag{1.7}$$

where $\langle \hat{r}_h \rangle$ is the corrected median half-light radius in arcseconds. This method is a good estimate but is not as accurate as SBF or GCLF measurements.

1.2.8 Redshift and Hubble's Law

The subject of cosmology is too large of a subject to be explained in a small section. However, I will briefly try to discuss the motions of galaxies in our universe and how those motions relate to distance from Earth.

In 1914, Vesto Slipher first published the observation that almost all galaxies had spectral lines that were systematically shifted to the red. This observation suggests that the galaxies with "redshifted" spectral lines are all traveling away from the Milky Way. Edwin Hubble investigated this phenomena and found a relation between the shift and the galaxy's distance from Earth. The redshift, z, can be used to find distance the following way,

$$d = \frac{cz}{H_0} \text{ Mpc}, \tag{1.8}$$

where d is distance, c is the speed of light (3×10^5 km/s), z $\ll$ 1 and H_0 is the Hubble constant. The Hubble constant currently ranges from 70-75 km/s^{-1} Mpc^{-1}, depending on what study is used and error (73.8 $\pm$ 2.4, Riess et al. 2011 and 72.6 $\pm$ 3.1 Suyu et al. 2010). The value cz (speed of light $\times$ redshift) represents the recession velocity of the galaxy.

This discovery gave way to the notion that the Universe is expanding, which is described by Hubble's Law. The source of these velocities is what astronomers call the Big Bang event. The Big Bang theory describes the universe initially concentrated in extremely small size scale which began to expand rapidly. This expansion is also called the Hubble Flow.

1.3 Galaxy Types

In this globular cluster study, the host galaxies NGC1533 and the 11 Shapley Supercluster galaxies are various kinds of Elliptical galaxies (E) and an S0 galaxy. To better understand what those galaxy classifications mean and how they further relate to formation scenarios, a list and description of various classification types is discussed below. However, we must keep in mind that the appearance of a galaxy or cluster can vary greatly depending on which wavelength or filter in which it is being viewed.

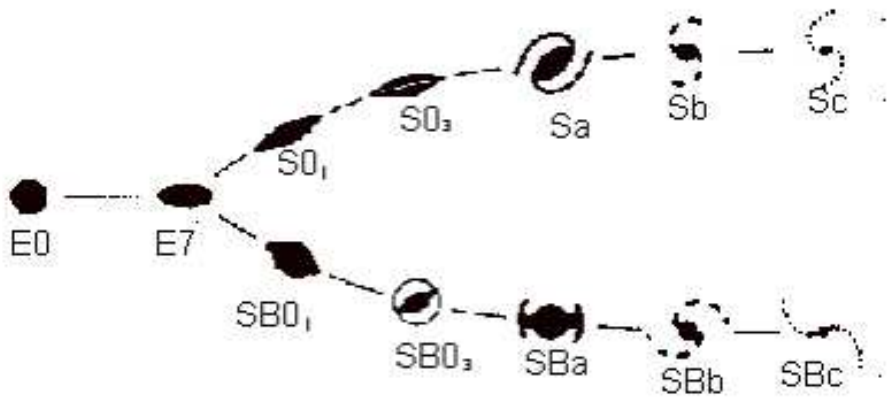

Figure 1.6 Hubble tuning fork of galaxy types

1.3.1 Hubble

When discussing galaxy morphology, the convention in most common use is the Hubble tuning fork diagram, Figure 1.6.

This Figure illustrates the progression of what astronomers at the time thought of as a formation diagram of galaxies. This is why galaxies at the left hand side of this tuning fork, elliptical galaxies, are still called Early-Type galaxies and spirals are still called Late-Type galaxies. It will be discussed in the formation section that this name convention should probably be switched but was never corrected. The tuning fork shows regular galaxies which are symmetric and then there were classifications for Irregular galaxies that did not fit this nice diagram.

Regular

The galaxies at the handle of the tuning fork were spherical in shape and designated as Elliptical (E). Progressing to the end of the tuning fork galaxies become more and more spiral. The top prong of the fork, Figure 1.6, contain Spirals (S) and the bottom prong containing barred Spirals (SB), which describes galaxies that have cores that resemble bars like our own Milky Way Galaxy. These prongs break at S0 then extend from Sa to Sc. The galaxy in this study, NGC1533, is a Lenticular Galaxy (the formal name for an S0 galaxy). Lenticular galaxies are in-between E and

S. The galaxies in the Shapley Supercluster study are all elliptical.

Irregular

When a galaxy is asymmetrical it is called Irregular, (Irr). There were two types of Irregular galaxy in the Hubble classification scheme (not displayed on the fork). The Irr I galaxies are asymmetrical, without well defined spiral arms and contain knots of young, hot stars. The Irr II galaxies are smooth, asymmetrical galaxies.

de Vaucouleurs

In the 1950s astronomer Gerard de Vaucouleurs felt that the Hubble sequence did not take into account the wide variations of galaxies and extended the prongs in the Hubble tuning fork with another Sd galaxy and renamed the Irregular classifications. He also restricted the definition of Lenticular Galaxy, S0, as a galaxy that could not be confirmed to have a bar. The de Vaucouleurs classification is seen as a modified Hubble classification.

1.3.2 Dwarfs and cD galaxies

Elliptical galaxies with low luminosity are called dwarf elliptical galaxies (dE). The other end of the size spectrum contains the central dominated galaxy or cD galaxy. This classification is from the Yerkes classification scheme but seems to pop up whenever a giant elliptical at the center of a cluster is being described. The definition of a cD galaxy is a galaxy whose light profile falls by $R_{1/4}$, where R is the radius from the galaxy center. Most of the galaxies that dominate a cluster are cD galaxies.

1.4 Cluster Types

Just like galaxies, the clusters in which the galaxies reside are also grouped into types. The most basic classification is describing clusters as rich or poor clusters. This description directly relates to the number and density of galaxies within a cluster, cluster members. Also, the classification of regular and irregular referring to symmetry of the object applies to clusters just as it applied to galaxies.

1.4.1 Bautz-Morgan type

This cluster type was developed by astronomers Laura Bautz and William Wilson Morgan in 1970 to describe the kind of members a cluster possesses. If a cluster is dominated by a cD galaxy larger than the other cluster members, it is designated with a Bautz-Morgan(BM) type I. A cluster with many members having similar sizes and luminosities, with no dominating galaxy, was given a BM type III. BM types of I-II, II, and II-III were given to clusters that exhibited a morphology between these two extremes.

1.4.2 Rood-Sastry type

This cluster classification scheme is much like the Hubble galaxy classification since it utilizes the tuning fork. Rood-Sastry tuning fork was first published in 1971, Figure 1.7. It is basically the Bautz-Morgan system in fork form and more consideration is given to the locations of the cluster members. A cD cluster has one dominating bright cD galaxy where the B cluster has two dominant galaxies, binary galaxies. The fork then splits into two prongs with L clusters and C clusters. The L (linear) clusters have some of the brightest galaxies arranged in a line and the C cluster with brightest members concentrated toward the center. The fork ends with the F cluster and I cluster. The F cluster has galaxies distributed in a uniform flat manner as opposed to the I cluster that has an irregular distribution of galaxy members. The problem with this classification scheme is its high degree of subjectivity.

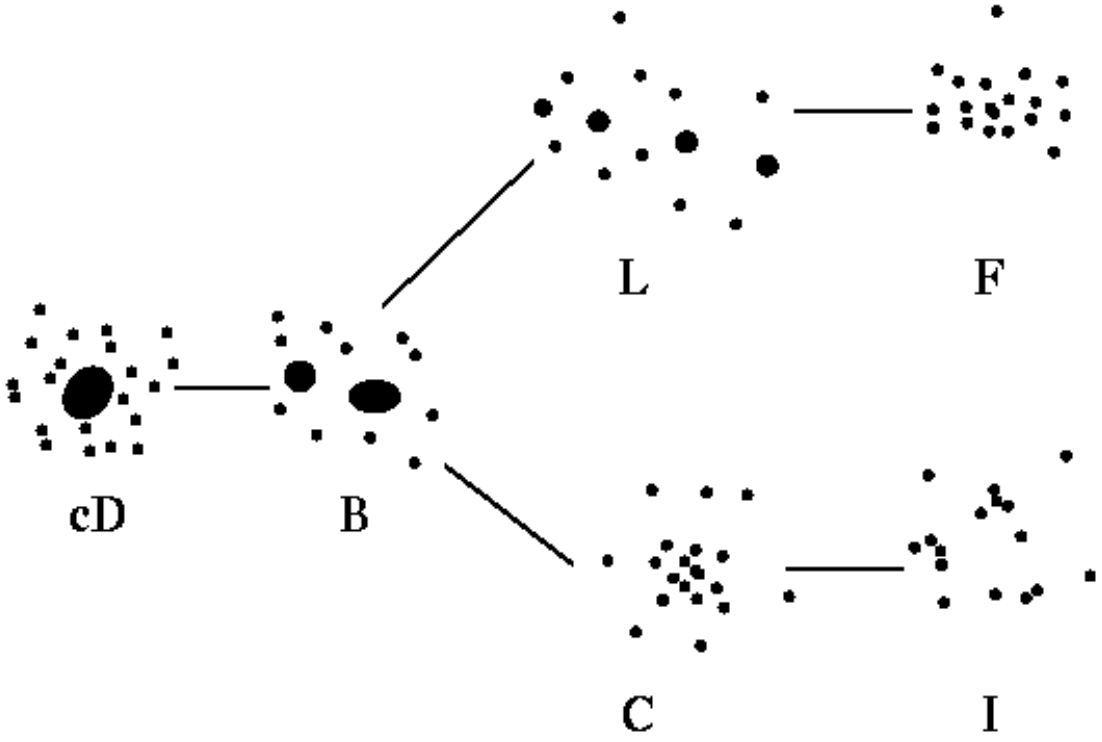

Figure 1.7 Rood-Sastry tuning fork first published as Figure 1 in Rood and Sastry 1971.

1.5 Formation Scenarios

A galaxy formation model that describes characteristics, such as globular clusters, currently does not exist. Although, I will try to summarize astronomy's best attempt (Mo, van den Bosch, and White 2010).

1.5.1 Old Thought

The first idea that tried to describe galaxy formation can be summed up in one word: Gravity. First let us start with spiral disk galaxies like the Milky Way. Collapse of a gas cloud, due to gravity caused by a large amount of mass, with some initial angular momentum may eventually flatten the cloud and star formation is ignited with the collapse. This explanation is entirely too simple since we are really dealing with a many body problem due to the number of stars that build a galaxy and we know that many body problems are extremely difficult. However, let us go with it for now and consider elliptical galaxies. To describe the formation of elliptical galaxies, such as the bulk of the type of galaxy in this study, we can consider two possibilities: mergers and monolithic collapse.

Merger

A scenario where the formation of an elliptical galaxy is a result of two or more merging spirals is one attempt to explain elliptical galaxy formation. This process would mean that the notion that the Hubble tuning fork, Figure 1.6, shows galaxy evolution as false unless you start at the prong end of the fork. In this scenario the star formation occurs before the merger, within the spiral galaxies, and the stars are just reassembled in the interaction of the merging spirals to create the elliptical galaxy.

Monolithic Collapse

This scenario requires a quick collapse of the gas cloud to create an elliptical galaxy. If the star formation occurs relatively quickly compared to the free-fall time scale, then the collapse will dissipate little or no energy. A single burst of star formation can be used to explain the homogeneous class that elliptical galaxies seem to be. However, this scenario does not explain what initial conditions are needed to create such an event.

1.5.2 New Thought and Dark Matter

It turns out the neither the merger scenario nor the monolithic collapse scenario can fully explain our observations of galaxy morphology. Computer simulations fail at reproducing galaxies as we see them today by just using a luminosity-mass relation. Assuming that most of the mass in galaxies is from stars, we can estimate the mass of each galaxy observed. However, when mass is increased well past the value that is derived from the galaxy brightness, the end result from simulations start to resemble the galaxies that can are seen in the sky. So where is this extra mass coming from? Well, we do not know but we can name it. Scientists have used their collective imagination and dubbed this mystery non-visible mass source, dark matter. The model where galaxies are surrounded by a dark matter halo is successfully used in computer simulations trying to produce an elliptical galaxy by merging two spirals (Cox et al. 2006) and even can be matched up with images taken by HST, displayed in a public press release, and shown in Figure 1.8.

It turns out that the differences between the Merger and Monolithic Collapse scenarios may not make them mutually exclusive. As seen in Figure 1.8, mergers and interaction happen in the universe. Also, the majority of the stellar populations of ellipticals have been found to be old which supports the notion of major star forming events. The attempt to create models with younger stellar ages has failed to reproduce results that resemble the ellipticals we observe (Renzini 2006). The more likely hierarchical merger of galaxies, to produce an elliptical galaxy along with star

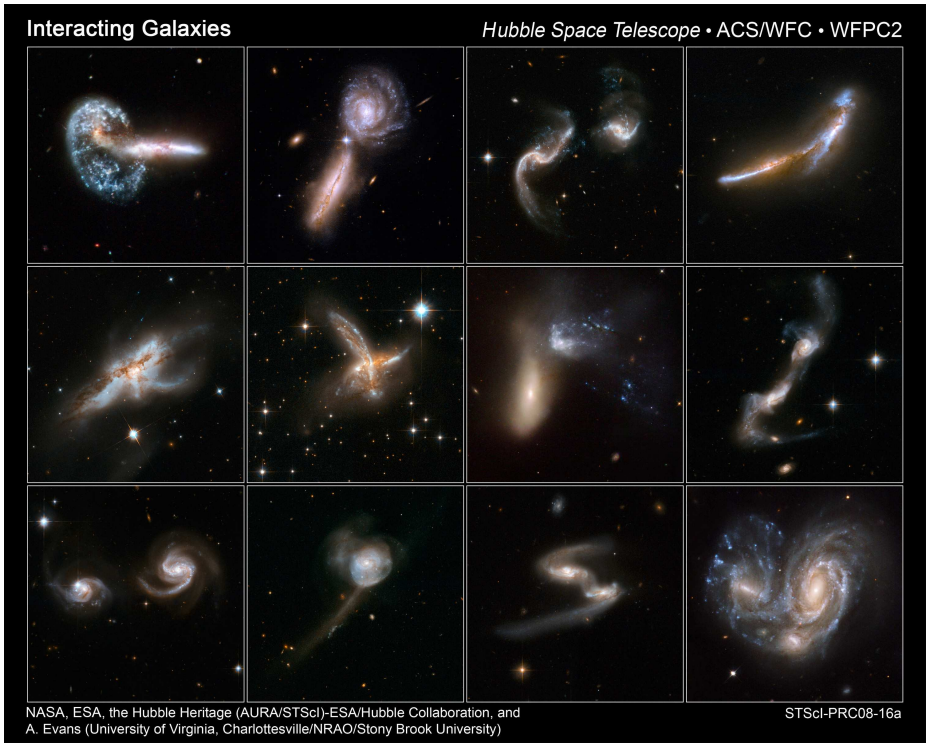

Figure 1.8 HST mosaic of galaxy mergers

formation during the interaction, is the accepted theory to date.

1.6 The CCD and the Hubble Space Telescope

The CCD camera and Hubble Space Telescope (HST) have contributed to recent breakthroughs in the study of globular clusters. However, before I describe these breakthroughs I will first describe the instrument that has changed the landscape of astronomy. The CCD or Charged Coupled Device is used to electronically record light signals. CCDs have a much greater efficiency than photographic plates. CCDs are cooled with liquid nitrogen or electrically to reduce thermal noise, and the data are digitally transferred. Efficiency in photon detection reduces the number of exposures needed to match the quality of images taken with a photographic plate. The CCD consists of an array of capacitors on a semiconductor substrate. The capacitors store the charge or data that is transferred and the semiconductor is the photo-active region that detects the photons.

Since the 1920s, astronomers hoped it would be possible to orbit giant telescopes around the Earth. A space telescope takes advantage of the absence of atmosphere. It was discovered very early in astronomy that the atmosphere blocked certain wavelengths, and created the twinkling effect of stars. The Hubble Space Telescope was launched into orbit in 1990. HST has a 2.4 meter mirror and is equipped with cameras and spectrometers, which detect data in the visual, near IR and near UV spectrum, as the instruments in Figure 1.9. Initially it was discovered that the HST mirror had a defect. Once it was corrected in 1993, HST has been supplying the scientific community with the most detailed images, in this spectral regime, ever produced of galaxy cores, supernovae, globular clusters and many more stellar objects. This wealth of data has contributed to the advancement in the areas of stellar and galactic evolution and cosmology, directly and indirectly.

The instruments aboard HST have changed over the years so that the most advanced cameras could be utilized as well as replacing instruments that have run their life expectancy in space. One current instrument, nearing its own end of operation,

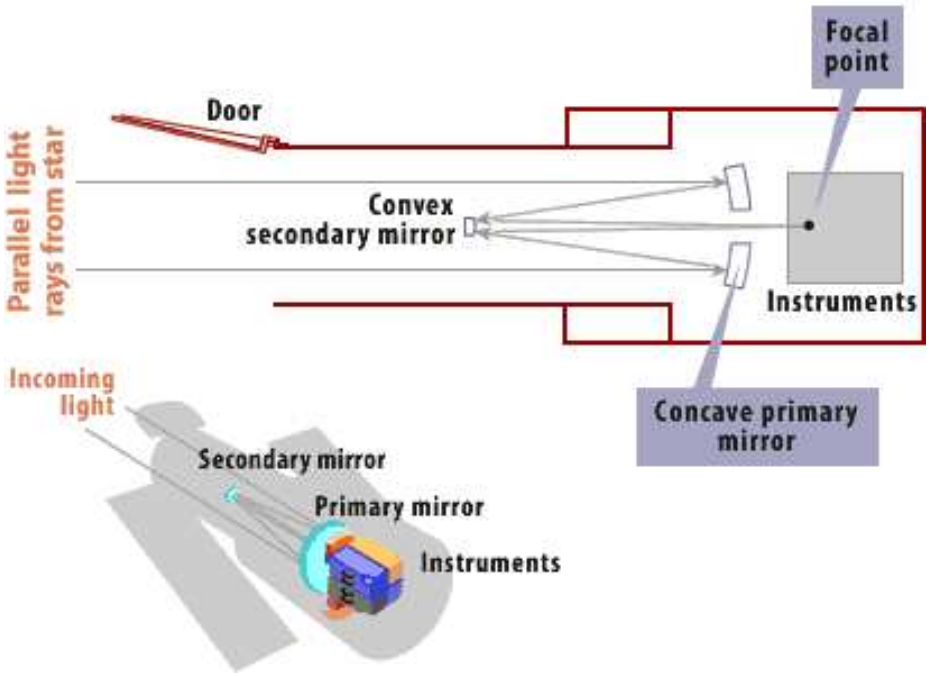

Figure 1.9 A simple diagram of the Hubble Space Telescope initially equipped with two cameras and two spectrometers in the instrument region, courtesy of NASA/STSCI.

is the Advanced Camera for Surveys. This is the camera that was used in each of the projects discussed in this thesis. It images objects in optical wavelengths and will be revisited in following chapters, along with its specific filters (Binney 1998).

1.7 Globular Cluster Characteristics

Now that we have covered a brief history of globular clusters, classification, evolution and astronomical instruments, we can finally dive into the topics that affect current GC studies. Here we detail a few of these topics which astronomers feel may be clues to the mystery of GC evolution: color bimodality of GC populations and specific frequency of host galaxies.

1.7.1 Color Bimodality

Images can be taken in a variety of wavelengths and as stated above, the difference in magnitude is called color. When the bandpasses are significantly separated in wavelength, it has been seen that globular cluster populations around galaxies have been found to be bimodal. It seems that when a histogram is created with number of galaxies verses color magnitude bins, two peaks become present. However, since globular clusters are thought to be objects that differ little from host galaxy to host galaxy as well as lacking in complexity due to the stellar population of a globular cluster being homogeneous, color bimodality was concluded to be directly related to metallicity. Metallicity is the relative chemical abundance of iron with respect to hydrogen, [Fe/H]. The assumption that color and metallicity are directly related is further investigated in Chapter 6. The Milky Way GC population has been known to be bimodal for some time and spectroscopy of these globular clusters has shown that the two subpopulations do indeed differ in metallicity. A current review on globular clusters by Brodie & Strader (2006) makes the bold claim that this phenomena is prominent with ellipticals as host galaxies, so much so that "no massive elliptical (E) galaxy has been convincingly shown to lack GC subpopulations". This statement is

supported by this thesis.

The seemingly universal occurrence of bimodality of GC populations in ellipticals seems to hint at galaxy evolution. The two current theories that try to explain color bimodality are different generations of globular clusters or/and mergers. If galaxy formation occurs in short bursts of stellar formation (monolithic collapse), then the early one would produce the halo GCs since ages derived for globular clusters are found to be older then the host galaxies and possible later ones would produce another subpopulation with higher metal content. In the case of "closed-box" self-enrichment, the younger a stellar object is the more metal rich it is due to supernovae as the main mechanism that creates these heavier metals. The second theory of dry merger (merger scenario in galaxy formation) claims that GC populations that halo two or more different galaxies with different metallicities merge to create one galaxy with two color subpopulations of globular clusters. The most likely scenario being one giant galaxy with a red population of GCs merging with many smaller galaxies with blue GC populations.

These two theories have problems matching the observations. One problem with the different generation theory comes from recent studies finding that most GC subpopulations that show color bimodality do not have the age difference required to explain the metallicity bimodality (Chies-Santos et al. 2011). One problem with the dry merger scenario is that it relies too heavily on low mass objects to make the large galaxies that are observed (West et al. 2004). Also, why do these massive ellipticals more than often have only two subpopulations? If there are more than one interaction in creating a galaxy then there would also be more occurrences of more than two subpopulations.

The statement that all massive ellipticals show subpopulations is further investigated in this study by supplying more data. We also consider the assumption of the direct link between color and metallicity.

1.7.2 Specific Frequency

The notion that globular cluster evolution is intertwined with the evolution of its host galaxy is extended in the concept of Specific Frequency, S_N. If the stellar components of a galaxy contribute to its luminosity, then the number of GC should directly relate to the magnitude of the host galaxy in the visible band, M_V. The mathematical definition of S_N is,

$$S_N = N_{tot} 10^{-0.4(M_V+15)} \tag{1.9}$$

where N_{tot} is the total number of GCs associated with the host galaxy. This equation is normalized to the specific frequency of the Milky Way. If ellipticals are born from a merger of two spirals, then the specific frequency of that elliptical would equal that of the S_N of the spirals since the birth was created through dry mergers. S_N values for most spirals are found to be 1-2 and the values of ellipticals have a large range from 2-20. The range seems to sometimes result from distance a host galaxy is to its cluster's center. This is found in this study as well as in Blakeslee and Tonry (1995). Therefore, an investigation into S_N values can give insight into galactic evolution.

In this study specific frequency is calculated for all galaxies. We consider the notion that globular clusters might be taken or added to host galaxies in mergers and may be associated with the cluster of galaxies as opposed to the host galaxy, as previously thought.

1.8 Thesis Outline

Chapter 2, details a study done on the GC system of NGC1533, a S0 galaxy with star formation in its outer regions. In the following chapter, chapter 3, we will investigate new stellar objects currently named Ultra Compact Dwarfs, which are another subpopulation with sizes larger than GCs and smaller than dwarf galaxies. This study is on the UCD population of Shapley Supercluster galaxy in AS0740, ESO325-G004. Chapters 2 and 3 both describe published work and the chapters are

basically the corresponding published papers. Chapter 4 describes the data analysis on the one-band imaging GC study done on the 11 Shapley Supercluster galaxies. This chapter also includes a brief introduction to the Shapley Supercluser and the motivations for obtaining the data. The results from this F814W band study and conclusions reside in Chapter 5. Chapter 6 is a revisit to the special galaxy in our Shapley survey, ESO325-G004 and its GC population. Using the two additional filters we were able to use results from Chapter 5 and further investigate the GC population with color data. We conclude with a summary of these three projects and future related work in Chapter 7.

Bibliography

[1] Bautz, L. P., & Morgan, W. W. 1970, ApJ, 162, L149

[7] Binney, J., & Merrifield, M. 1998, Galactic astronomy / James Binney and Michael Merrifield. Princeton, NJ : Princeton University Press, 1998. (Princeton series in astrophysics) QB857 .B522 1998

[3] Blakeslee, J. P., et al. 2010, ApJ, 724, 657

[2] Blakeslee, J. P., & Tonry, J. L. 1995, ApJ, 442, 579

[6] Brodie, J. P., & Strader, J. 2006, ARA&A, 44, 193

[10] Chies-Santos, A. L., Larsen, S. S., Kuntschner, H., Anders, P., Wehner, E. M., Strader, J., Brodie, J. P., & Santos, J. F. C. 2011, A&A, 525, A20

[7] Cox, T. J., Di Matteo, T., Hernquist, L., Hopkins, P. F., Robertson, B., & Springel, V. 2006, ApJ, 643, 692

[23] Curtis, H., 1921, The Scale of the Universe, Bull. Nat. Res. Counc., 2, part 3, 194-217

[10] Harris, W. E., & van den Bergh, S. 1981, AJ, 86, 1627

[10] Herschel, W. 1785, Royal Society of London Philosophical Transactions Series I, 75, 213

[11] Hubble, E. 1929, Proceedings of the National Academy of Science, 15, 168

[29] Jordán, A., et al. 2005, ApJ, 634, 1002

[13] Kant, I. 1755, Zeitz, Bei W. Webel, 1798. Neue aufl.,

[23] Messsier, Charles, Catalogue des Nbuleuses & des amas d'toiles. Connoissance des Temps for 1784 (published 1781) pp. 227-267 [Bibcode: 1781CdT..1784..227M]

[19] Mo, H., van den Bosch, F. C., & White, S. 2010, Galaxy Formation and Evolution by Houjun Mo, Frank van den Bosch and Simon White. Cambridge University Press, 2010. ISBN: 9780521857932,

[16] Piotto, G., et al. 2007, ApJ, 661, L53

[17] Renzini, A. 2006, ARA&A, 44, 141

[18] Riess, A. G., et al. 2011, ApJ, 730, 119

[19] Rood, H. J., & Sastry, G. N. 1971, PASP, 83, 313

[20] Seeds, M. A. 1998, Horizons : exploring the universe / Michael A. Seeds. Belmont, CA : Wadsworth Pub. Co., c1998. QB45 .S44 1998

[21] Shapley, H. 1918, PASP, 30, 42

[23] Shapley, H., 1921, The Scale of the Universe, Bull. Nat. Res. Counc., 2, part 3, 171-193

[23] Shapley, H.,1953, Proc. Nat. Acad. Sci. (Wash), 39, 349.

[24] Slipher, V. M. 1914, Lowell Observatory Bulletin, 2, 66

[25] Suyu, S. H., Marshall, P. J., Auger, M. W., Hilbert, S., Blandford, R. D., Koopmans, L. V. E., Fassnacht, C. D., & Treu, T. 2010, ApJ, 711, 201

[26] Tonry, J., & Schneider, D. P. 1988, AJ, 96, 807

[27] West, M. J., Côté, P., Marzke, R. O., & Jordán, A. 2004, Nature, 427, 31

Chapter 2

Structure, Globular Clusters, and Distance of the Star-Forming S0 Galaxy NGC 1533 in Dorado

This chapter was published under the same title in *The Astrophysical Journal*, Vol. 371, Issue 2, pp 1624-1639 (2007). The work presented in Chapter 2 was undertaken in collaboration with Dr. John Blakeslee, who completed the data analysis in sections 3 and 4.

Synopsis

We use two-band imaging data from the Advanced Camera for Surveys on board the Hubble Space Telescope for a detailed study of NGC 1533, an SB0 galaxy in the Dorado group surrounded by a partial ring of H I. NGC 1533 appears to be completing a transition from late to early type: it is red, but not quite dead. Faint spiral structure

becomes visible following galaxy subtraction, and luminous blue stars can be seen in isolated areas of the disk. Dust is visible in the color map in the region around the bar, and there is a linear color gradient throughout the disk. We determine an accurate distance from the surface brightness fluctuations (SBF) method, finding $(m-M) = 31.44 \pm 0.12$ mag, or $d = 19.4 \pm 1.1$ Mpc. We then study the globular cluster (GC) colors, sizes, and luminosity function (GCLF). Estimates of the distance from the median of the GC half-light radii and from the peak of the GCLF both agree well with the SBF distance. The GC specific frequency is $S_N = 1.3 \pm 0.2$, typical for an early-type disk galaxy. The color distribution is bimodal, as commonly observed for bright galaxies. There is a suggestion of the redder GCs having smaller sizes, but the trend is not significant. The sizes do increase significantly with galactocentric radius, in a manner more similar to the Milky Way GC system than to those in Virgo. This difference may be an effect of the steeper density gradients in loose groups. Additional studies of early-type galaxies in low density regions can help determine if this is indeed a general environmental trend.

2.1 Introduction

The Hubble Space Telescope (*HST*) has opened the door to our understanding of extragalactic star cluster systems, revealing numerous globular clusters (GCs) in early-type galaxies (e.g. Gebhardt & Kisler-Patig, 1999; Peng et al. 2006) as well as "super-star clusters" (SSCs) in late-type galaxies (Larsen & Richtler 2000), especially starbursts (e.g. Meurer et al. 1995, Maoz et al. 1996). In early-type systems the color distribution of the GCs is often bimodal, consisting of a blue metal-poor component and a red metal-rich component (e.g. West et al. 2004; Peng et al. 2006). This observation gives a hint to the connection between the early- and late-type systems. Mergers often have particularly strong starbursts and rich populations of SSCs, as seen for example in NGC4038/39 - "the Antennae" system (Whitmore & Schweizer 1995; Whitmore et al. 1999), and this is one possible origin for the redder population of GCs in early-type galaxies (e.g., Ashman & Zepf 1998).

Much of the research on GC systems has concentrated on galaxy clusters which are rich in early-type galaxies (e.g., the ACS Virgo Cluster Survey, Côté et al. 2004; the ACS Fornax Cluster Survey, Jordán et al. 2007). Early-type galaxies in groups and the field are somewhat less studied, particularly with *HST* and the Wide Field Channel (WFC) of its Advanced Camera for Surveys (ACS). The relatively wide (3.′4) field of view of the ACS WFC combined with its fine pixel sampling make it an exceptional tool for imaging GCs out to a few tens of Mpc where they have measurable angular sizes (Jordán et al. 2005).

Here we report *HST* ACS/WFC imaging of the SB0 (barred lenticular) galaxy NGC 1533 in the Dorado group. This group is in the "Fornax wall" (Kilborn et al. 2005) and hence at a similar distance to the Fornax cluster (e.g., Tonry et al. 2001). Dorado is interesting in that it is richer than the Local Group but still dominated by disk galaxies (its brightest members being the spiral NGC 1566 and the S0 NGC 1553), and its members have H I masses similar to non-interacting galaxies with the same morphology (Kilborn et al. 2005). While the apparent crossing time of the group is only $\sim 13\%$ of the age of the universe (Firth et al. 2006; see also Ferguson & Sandage 1990), the most recent analyses conclude the group is unvirialized (Kilborn et al. 2005; Firth et al. 2006), which may explain the richness in spirals and H I.

NGC 1533 is the seventh brightest member of the Dorado group. It lies within the virial radius, but is a ~ 2-σ velocity outlier (Kilborn et al., 2005; Firth et al. 2006) so that it is moving at high speed through the intra-group medium. A vast H I arc is seen in the outskirts of NGC 1533 and is connected to its Sdm companion IC 2038 (Ryan-Weber et al. 2004), suggesting that NGC 1533 is "stealing" ISM from its companion. As is typically seen in S0 galaxies, star formation is weak in NGC 1533. Observations of this galaxy in spectroscopic surveys note the presence of emission lines (Jorgensen et al. 1997; Bernardi et al. 2002); the nuclear spectrum available from the 6dF survey (Jones et al. 2005) shows [N II]6584 and weak Hα. Hα imaging from the Survey of Ionization in Neutral Gas Galaxies (SINGG, an Hα imaging survey of H I selected galaxies; Meurer et al. 2006) shows a few weak H II regions beyond the end of its bar (the nucleus is too bright to allow faint nuclear H II regions to be detected in the SINGG images), as well as a scattering of very faint "intergalactic H II regions".

These are discussed in more detail by Ryan-Weber et al. (2004) who show that they are so faint that it would only take one to a few O stars to ionize each one. The weak star formation in NGC 1533 illustrates a possible new channel for building up cluster systems in early-type galaxies: slow re-ignited star formation in ISM stripped from companions.

The ACS WFC images of NGC 1533 used in the present study were obtained with *HST* as "internal parallel images" while the ACS High Resolution Channel (HRC) was pointed at the intergalactic H II regions (*HST* GO Program 10438; M. Putman, PI). The HRC observations will be discussed elsewhere (J. Werk 2007, in preparation). Here we use the WFC observations to measure the structural properties of the galaxy, characterize its GC population, and use the GC luminosity function (GCLF), GC half-light radii, and surface brightness fluctuations (SBF) measurements to provide an accurate distance estimate. The contrast between NGC 1533, a (weakly) star-forming gas-rich barred S0 in a loose group environment, and galaxies in the richer environments of the ACS Virgo and Fornax cluster surveys, provides a useful test of the ubiquity of the various relations found in the denser environments.

The following section describes the observations and data reductions in more detail. Sec. 3.4 discusses the galaxy morphology, structure, color profile, and isophotal parameters. Sec. 2.4 presents the SBF analysis and galaxy distance, while Sec. 2.5–2.7 discuss the GC colors, effective radii, luminosity function, and specific frequency. The final section summarizes our conclusions.

2.2 Observations and Data Reduction

As noted above, during the primary ACS HRC observations of H II regions in the halo of NGC 1533, the WFC was used for parallel imaging of the main galaxy. These observations were carried out on 2005 September 25 with *HST* V3-axis position angle PA_V3 = 110.°15 and on 2005 November 18 with PA_V3 = 170.°75; we refer to these throughout as "roll 1" and "roll 2," respectively. Figure 2.1 shows the positions and orientations of the primary ACS/HRC fields, and the overlapping parallel ACS/WFC

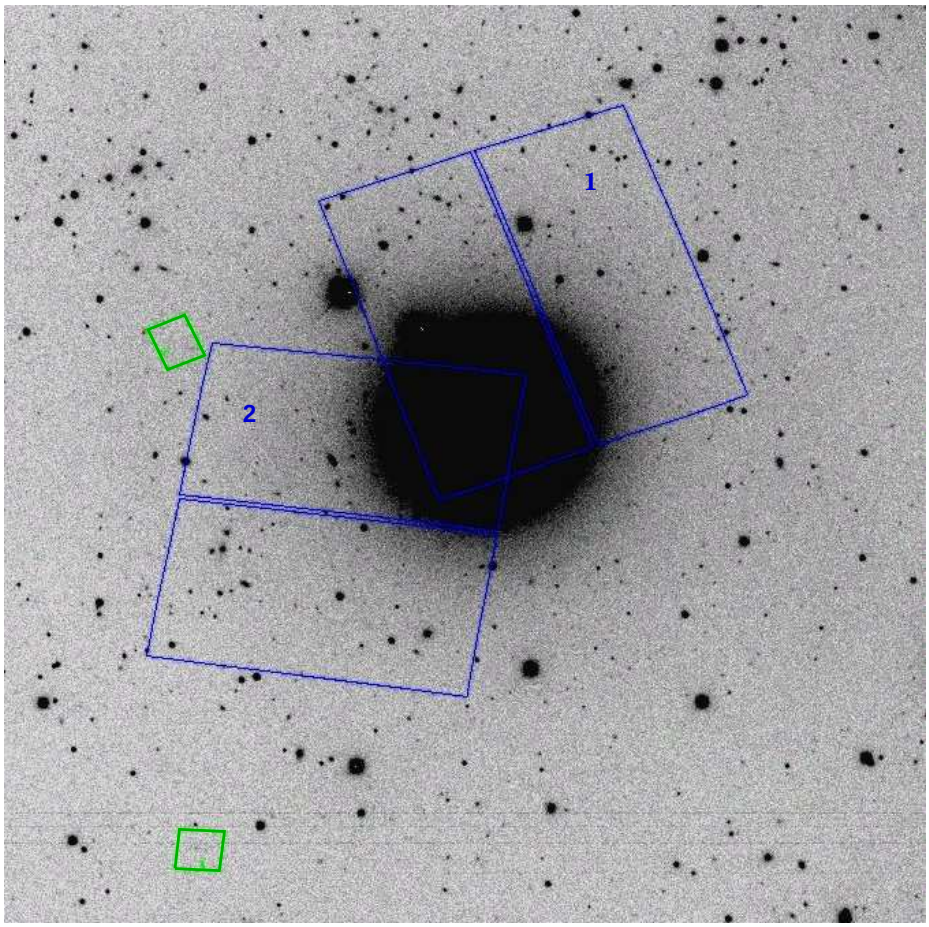

Figure 2.1 ACS HRC (green) and WFC (blue) fields of view for the two HST roll angles described in the text (labeled 1 and 2). The outlines of the camera fields are overlaid on a ground-based *R*-band image from the SINGG survey. North is up and East is to the left.

fields, at the two roll angles.

2.2.1 Image Processing

NGC 1533 was imaged in the F814W and F606W bandpasses of the ACS/WFC. Eight exposures totaling 4950 s in F814W, and four exposures totalling 1144 s in F606W, were taken at each of the two roll angles. Following standard calibration by the STScI archive, the data were processed with the ACS IDT "Apsis" pipeline (Blakeslee et al. 2003) to produce final, geometrically corrected, cleaned images with units of accumulated electrons per pixel. Apsis also ensures the different bandpass images are aligned to better than 0.1 pix and performs automatic astrometric recalibration of the processed images.

We calibrated the photometry using the Vega-based m_1 zero points from Sirianni et al. (2005): $m_{1,\,F606} = 26.398$ and $m_{1,\,F814} = 25.501$. Galactic extinction was taken into account using the dust maps of Schlegel et al. (1998) and the extinction ratios from Sirianni et al. (2005). We determined corrections of $A_{606} = 0.045$ mag and $A_{814} = 0.029$ mag for the F606W and F814W bandpasses, respectively. For comparison to other studies, we also converted the measured (F606W − F814W) colors to Johnson–Cousins $(V-I)$ using the empirically-based prescription given by Sirianni et al.

We processed the data at the two roll angles with Apsis both separately and combined together. The upper left panel of Figure 2.2 shows the result from the combined processing, which is useful for analyzing the galaxy 2-D surface brightness distribution and isophotal parameters using the largest angular range. However, for the SBF and globular cluster analyses, we considered each pointing separately and then merged the results at the end. This was done to avoid PSF and orientation mismatch effects (e.g., diffraction spikes and effects due to the gate structure of the CCDs do not match up when combining images with differing orientations). For each filter image at each pointing, we modeled the galaxy light using the "elliprof" software written by J. Tonry for the SBF Survey of Galaxy Distances (Tonry et al. 1997) and described in more detail by Jordán et al. (2004). Saturated areas, bright

sources, diffraction spikes, and dusty regions were masked out for a better model fit. The galaxy model was then subtracted from the image, revealing faint sources and residual features, including faint spiral structure as discussed in Sec. 3.4.

2.2.2 Object Photometry

Object detection was performed with Sextractor (Bertin & Arnout 1996) using the galaxy-subtracted image for detection and an RMS image for the weighting. The RMS image gives the uncertainty per pixel including the effects of instrumental and photon shot noise, as well as the additional "noise" from the galaxy surface brightness fluctuations. It is constructed as described in detail by Jordán et al. (2004):

$$\mathrm{RMS} \;=\; \sqrt{(\mathrm{RMS}_{Ap})^2 + (K_F * \mathit{model})}\,, \tag{2.1}$$

where RMS_{Ap} is the Apsis RMS image based on the instrumental and shot noise alone (Blakeslee et al. 2003), *model* is the galaxy surface brightness model, and K_F gives the ratio of the variance per pixel from SBF, σ_L^2, to that from photon shot noise from the galaxy, σ_p^2. The K_F factor depends on the bandpass, exposure time, galaxy distance (which determines the apparent amplitude of the SBF), and the image resolution; it can be estimated as

$$K_F \;=\; \frac{\sigma_L^2}{\sigma_p^2} \;=\; \frac{1}{p}\, 10^{-0.4(\bar{m}_F - m^*_{1,F})}\,, \tag{2.2}$$

where $m^*_{1,F} = m_{1,F} + 2.5\,\log(T)$, T is the total exposure time, $\bar{m}_F$ is the SBF magnitude in the given bandpass, and p is a factor that reduces the SBF variance because of the smoothing effect of the PSF. We adopt $\bar{m}_{F814} \approx 30$ for NGC 1533 based on the measurement from Tonry et al. (2001) in the very similar I_C bandpass (and confirmed by our SBF result in Sec 2.4) and assume $\bar{M}_{F606} - \bar{M}_{F814} \approx 2$ based on expectations from stellar population models (Liu et al. 2000; Blakeslee et al. 2001, Cantiello et al. 2003) to determine $\bar{m}_{F606}$. Following Jordán et al. (2004), we convolved simulated noise images with the ACS PSFs to determine the p factor in Eq. 2.2; thus, we reduced the variance ratio by 12 for F606W and by 13 for F814W and finally determined the values $K_{F606} = 1.1$ and $K_{F814} = 6.0$.

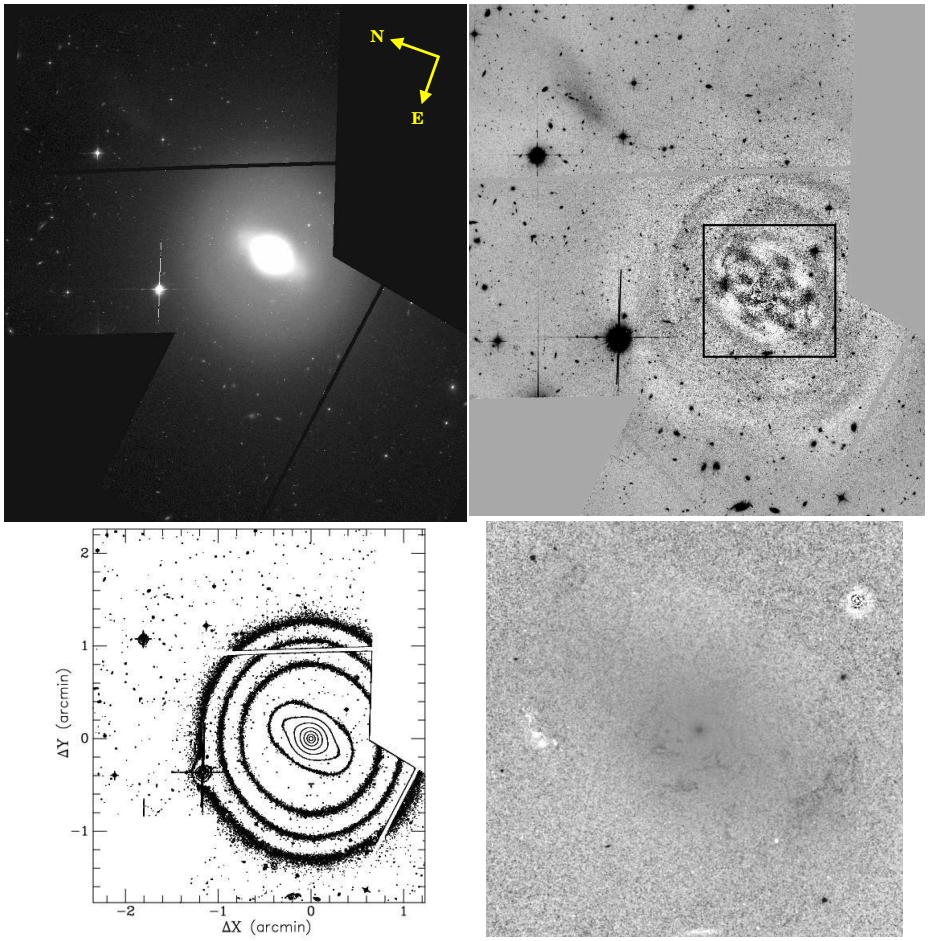

Figure 2.2 *Upper left:* Combined F814W ACS/WFC image of NGC 1533. *Lower left:* Contour map of a 3.6′.3×4′.0 portion of the image. Contours are plotted in steps of a factor of two in intensity, with the faintest being at $\mu_I = 20.7$ mag arcsec^{-2}. *Upper right:* The image following galaxy model subtraction, showing the faint spiral structure (the "plume" 2′ north of the galaxy is a ghost image). The same 3.6′.3×4′.0 field is shown; the box marks the central 1′. *lower right:* Colormap of the central 1′ region of NGC1533, with dark indicating red areas and white indicating blue. The dark spot at center marks the center of the galaxy. Dust can be seen as faint, dark, wispy features. A compact blue star-forming region is visible to the left of the galaxy center, near the center-left of the map.

After some experimentation, we decided to run SExtractor in "dual image mode," such that object detection, centroiding, and aperture determination was performed only in the deeper F814W image, while the object photometry was performed in both the F606W and F814W images. This ensures that the same pixels are used for the photometry in both images (see Benítez et al. 2004 for a detailed discussion). The catalogs produced by SExtractor include magnitudes measured within various fixed and automatic apertures. By comparing color measurements of the same objects at the two different roll angles, we chose to use the colors measured within an aperture of radius 4 pixels. Since we are mainly interested here in compact, only marginally resolved, globular cluster candidates, we applied a uniform correction of 0.016 mag to the colors measured in this aperture, based on the difference in the F606W and F814W aperture corrections (Sirianni et al. 2005). These colors were transformed to $(V-I)$ following Sirianni et al., as described above. For the total I-band magnitude, we use the extinction-corrected, aperture-corrected Vega-based F814W magnitude I_{814}. According to Sirianni et al., for objects with $(V-I) \approx 1$, this should differ from Cousins I_C by $\lesssim 0.006$ mag, or less than the expected zero-point error of ~ 0.01 mag.

2.3 Galaxy Properties

Tonry et al. (2001) reported SBF distances to six members of the Dorado group. However, one of these (NGC 1596) was found to be about 20% closer than the others; omitting it gives a mean distance modulus for Dorado of $\langle m-M \rangle = 31.40 \pm 0.09$ mag, or $\langle d \rangle = 19.1 \pm 0.8$ Mpc. (We have revised the published numbers downward by 3%, as noted in Sec. 2.4 below, before taking the average.) NGC 1533 itself had a poorly determined ground-based SBF distance of $d = 20.8 \pm 4.0$, the largest among the Dorado galaxies, but in agreement with the mean distance given the large uncertainty. Based on 24 Dorado group members, Kilborn et al. (2005) report a mean velocity of 1250 ± 57 km s^{-1}, with $\sigma = 282$ km s^{-1}. NGC 1533's velocity is 790 km s^{-1}, indicating a peculiar motion of ~ 460 km s^{-1}.

2.3.1 Morphology

The morphological type of NGC 1533 in the RC3 is $T = -3$ (de Vaucouleurs et al. 1991), indicating an early-type S0. Buta et al. (2006) classify it as (RL)SB0^0, meaning that it is a barred, intermediate-type S0 containing both an inner lens structure and a ring-like feature within the disk. In a morphological study of 15 early-type disk galaxies, Laurikainen et al. (2006) gives an inner radius of 44″ for this ring. Some of these features are evident in the left panels of Figure 2.2. The convex-lens shape of the outer bulge, the bar, and the disk are clearly seen in the contour map. In addition, the model-subtracted image in the upper right panel reveals spiral features that are difficult to see in the original image. The faint spiral arms appear to emanate from the ends of the bar and wrap around by 360°. Sandage & Brucato (1979) also noted a "suggestion of weak spiral pattern in outer lens (or disk)" in NGC 1533. It seems likely that this is the "ring" seen by Buta et al. (2006) and Laurikainen et al. (2006). Thus, NGC 1533 appears to be in the late stages of transition from an early-type barred spiral to a barred S0 galaxy.

The subtracted image also shows luminous material about 2.′0 to the north/northwest of the NGC 1533 galaxy center, beyond the galaxy disk. This feature is only visible in the F814W image, not in the F606W or ground-based images. It is apparently an internal camera reflection from a bright star outside the field of view.

The color map in the lower right panel of Fig. 2.2 reveals the presence of wispy dust (darker areas in the color map) to the east and south of the nucleus within the central 20″ along the bar. Moreover, a compact region of bluer light is visible at the center left edge of the color map, about 23″ to the northeast of the galaxy nucleus. This position coincides with an H II region found by Meurer et al. (2006). Thus, luminous blue stars are powering the ionization. The areas of dust and star formation support the view of NGC 1533 as a galaxy recently converted from spiral to S0. However, it should be noted that dust features are found in roughly half of bright early-type galaxies when studied at high resolution (Ferrarese et al. 2006), and isolated star formation is not too uncommon.

At larger radius within the disk (outside the color map in the figure), we find

several other small groups, or isolated examples, of unresolved blue objects with colors $(V-I) \approx 0$ and magnitudes $I_{814} \gtrsim 23.5$. Some of these are visible in Figure 2.3, and the ones associated with H II regions are marked in the color-magnitude diagram presented in Sec. 2.5. They may be a mix of post-asymptotic giant branch (PAGB) stars, indicating an intermediate age population, and small isolated regions of star formation. A string of about five such blue objects highlighted in Figure 2.3 are spread out along one of the spiral arms. The likely connection with the spiral arm in this case points towards these being a small, dispersed group of fairly young stars.

2.3.2 Galaxy Surface Photometry and Structure

Although NGC 1533 has a complex isophotal structure, it can also be enlightening to study the simple one-dimensional light profile. Figure 2.4 (left panel) shows the galaxy surface brightness profiles in F606W and F814W. Within a radius of about $16''$, the profile is reasonably well fit by a de Vaucouleurs $r^{1/4}$-law profile (a straight line in the figure). Between $16''$ and $\sim 45''$, the profile becomes much flatter; this includes the inner disk and area around the bar. In the outer disk, beyond $\sim 50''$, the profile steepens again.

The right panel of Figure 2.4 shows the galaxy color profile. In addition to our measured (F606W − F814W) profile, we show the ground-based $(V-I)$ photometry for this galaxy from the Tonry et al. (1997) study (which provides median and average surface photometry measured in $3''$ radial bins, without removal of external sources). The ground-based data come from multiple long exposures with the Cerro Tololo 4 m Blanco telescope at a pixel scale of $0\farcs47$ pix^{-1}. They suffer from poor seeing ($1\farcs5$ in I, $1\farcs8$ in V) and severe central saturation; however, the systematic error on the color is only 0.018 mag (Tonry et al. 2001). Similar gradients are observed in both sets of photometry. By binning the data at the same scales and comparing colors over a radial range of $10'' - 50''$, we determined:

$$(V-I)_0 \;=\; (1.196 \pm 0.003) \;+\; (1.2 \pm 0.2)\,[(\mathrm{F606W} - \mathrm{F814W})_0 - 0.95]\,, \qquad (2.3)$$

with an RMS scatter of 0.010 mag in the fit. This relation yields $(V-I)$ colors be-

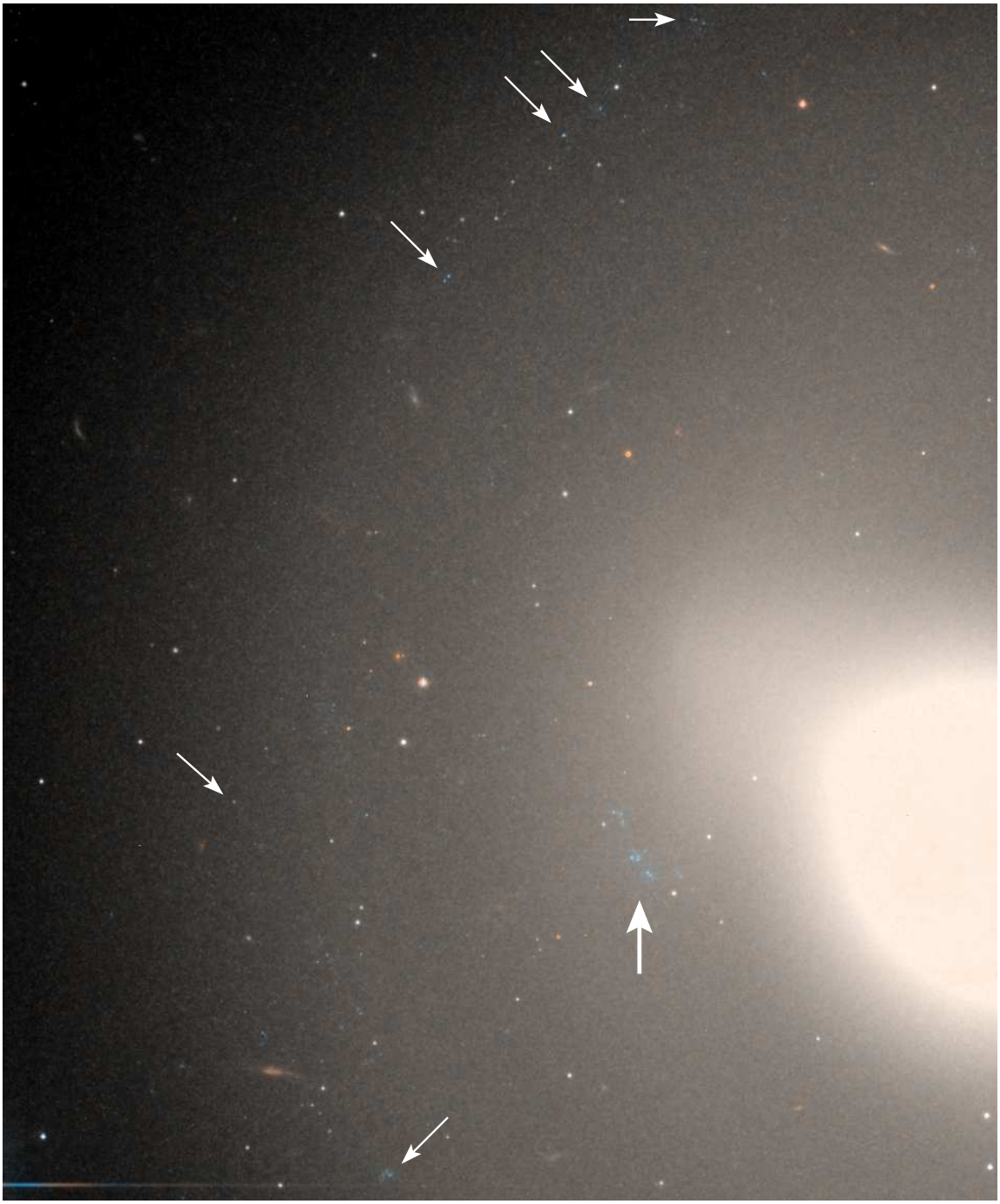

Figure 2.3 Blue objects in a $0'.8 \times 1'$ region in NGC 1533. The galaxy center is at the lower right edge of the field. The large vertical arrow marks the known H II region, and the smaller arrows point out fainter, unresolved blue objects which appear to spread out along one of the possible faint spiral arms.

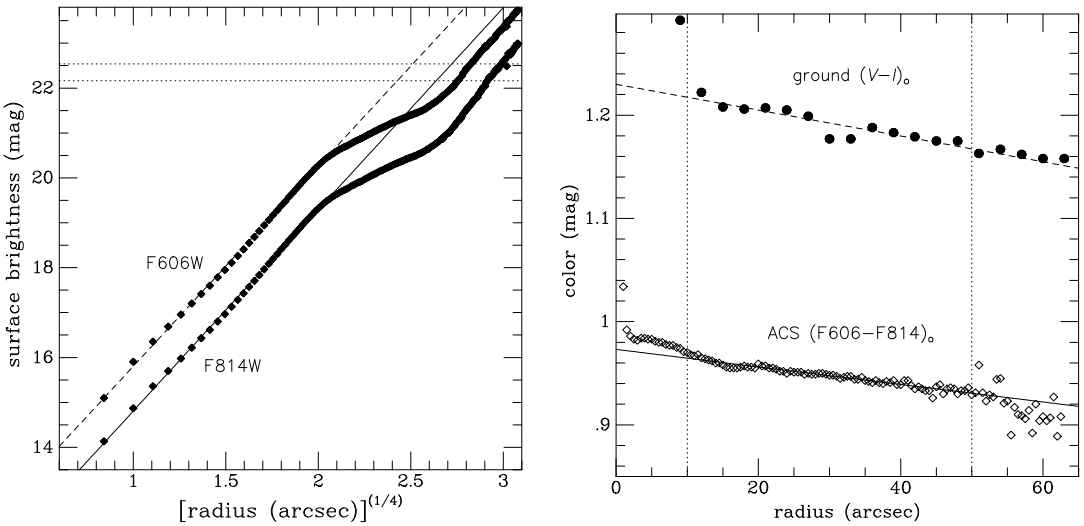

Figure 2.4 Surface brightnesses in 0.5" circular rings for the Vega-calibrated F606W and F814W bandpasses are plotted as a function of $r^{1/4}$ (*left*). The dashed and solid lines show linear fits to the data inside a radius of 16″ where the bulge dominates. The upper and lower dotted lines show the sky levels in F606W and F814W, respectively. NGC 1533 colors from the ground-based $(V-I)$ data (solid circles) of Tonry et al. (1997) and our ACS (F606W − F814W) imaging (open diamonds) is shown as a function of radius (*right*). The lines show linear fits to the data points in the radial range $10 < r < 50$.

tween the empirical (based on stellar photometry) and theoretical (based on synthetic spectra and the bandpass transmission curves) transformations provided by Sirianni et al. (2005), which differ between themselves by ~ 0.07 mag in this color range. It is in better agreement with the empirical transformation, differing by about 0.02 mag, as compared to ~ 0.05 mag with the synthetic transformation, which is probably more uncertain because the F606W bandpass differs substantially from standard V. Likewise, Brown et al. (2005) reported that when transformations were calculated based on the bandpass definitions, empirical corrections of order ~ 0.05 mag were required to match globular cluster data from $(V-I)$ to (F606W − F814W). In any case, Eq. 2.3 allows for a precise matching of our measured (F606W − F814W) colors to Johnson–Cousins $(V-I)$ over the small range of the galaxy color gradient. This is important for calibrating our SBF measurements in Sec. 2.4 below.

We also performed parametric 2-D surface photometry fits with Galfit (Peng et al. 2002). For the simplest case, we used a double Sérsic model to represent the bulge

and disk. This analysis yielded a bulge-to-total ratio $B/T = 0.42$, with half-light radii of $7''$ and $46''$ for the bulge and disk, respectively. The Sérsic index for the bulge was $n = 2.0$, intermediate between an exponential and a de Vaucouleurs profile (Sérsic 1968). However, the fit gave $n = 0.4$ for the disk, or a profile that goes as $\sim \exp(-\alpha r^{2.5})$, which is even more spatially truncated than a Gaussian. This agrees with what was seen in the 1-D plot, where the profile remains fairly constant over a large radial range then drops off more steeply beyond about $50''$. We also made fits with 3 and 4 components. These gave better model residuals, but the different components did not neatly break down into clearly distinct physical components such as bulge, bar, disk, halo (or lens, etc.), so the interpretation was unclear.

2.3.3 Isophotal Parameters

Figure 2.5 presents the radial profiles of the isophotal ellipticity, position angle, and A_3 and A_4 harmonic parameters. The upper left panel of the figure shows that the galaxy is quite round within $10''$ (bulge) and beyond $40''$ (disk). However, it reaches a maximum ellipticity $\epsilon = 0.41$ at a semi-major axis distance of $24''$, corresponding to the semi-major axis of the bar. As seen in the lower left panel, there is also a gradual isophotal twist from $PA \approx 125^\circ$ near a radius of $1''$, to $PA \approx 170^\circ$ where the ellipticity reaches its maximum. Laurikainen et al. (2006) found similar ellipticity and orientation trends for NGC 1533 from their analysis of ground-based K-band data, although they do not appear to have resolved the structure inside a few arcseconds.

The right panels of Figure 2.5 show the amplitudes of the third-order and fourth-order harmonic terms, which measure the deviations of the isophotes from pure ellipses (Jedrzejewski 1987). The values reported by elliprof are the relative amplitudes of these higher order harmonics with respect to the mean isophotal intensity, i.e., $A_3 = I_3/I_0$ and $A_4 = I_4/I_0$. The upper right panel of the figure shows that the galaxy remains quite symmetric at all radii, since the A_3 component remains near zero. However, the A_4 component, an indicator of "diskiness," reaches a maximum of 13% at a major axis of $21''$, then drops suddenly. Thus, A_4 reaches its maximum at a smaller radius than does the ellipticity, since the major axis of the lens-like isophotes

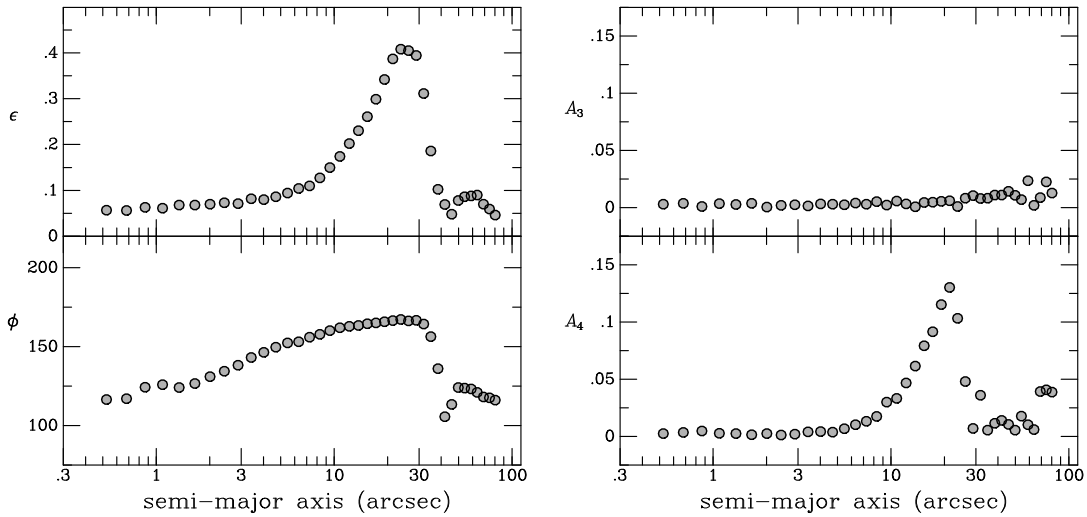

Figure 2.5 Isophotal parameters for NGC 1533. Ellipticity ϵ and position angle ϕ from the galaxy isophote modeling are shown versus the semi-major axis of the isophote (*left*). The higher-order A_3 and A_4 harmonic terms, measuring deviations of the isophotes from pure ellipses, are shown versus the isophotal semi-major axis (*left*). The peak in the A_4 profile occurs at $21''$, whereas the peak in ϵ occurs at $24''$.

is smaller than that of the bar. This agrees with the contour map in Figure 2.2, where the "convex lens" shape appears embedded within the oblong bar.

2.4 Surface Brightness Fluctuations Distance

We measured the SBF amplitude in four radial annuli for each of the two F814W observations at the different roll angles. We used the software and followed the standard analysis described by Tonry et al. (1997), Ajhar et al. (1997), Jensen et al. (1998), Blakeslee et al. (1999, 2001), and references therein. More details on the SBF analysis for ACS/WFC data are given by Mei et al. (2005) and Cantiello et al. (2005, 2007). Briefly, after subtracting the galaxy model as described above, we fitted the large-scale spatial residuals to a two-dimensional grid (we used the SExtractor sky map for this) and subtracted them to produce a very flat "residual image." All objects above a signal-to-noise threshold of 10 were removed (masked) from the image. We used this high threshold to avoid removing the fluctuations themselves, or the brightest giants in the galaxy. As described in the following sections, with the

resolution of *HST*/ACS we are able to detect and remove globular clusters (the main source of contamination) to more than a magnitude beyond the peak of the GCLF, and the residual contamination is negligible. We also used the F606W image and the color map to identify and mask the dusty regions and small areas of star formation.

We then modeled the image power spectra in the usual way, using a the template WFC F814W PSF provided by the ACS IDT (Sirianni et al. 2005) and a white noise component. We performed the analysis in four radial annuli: $64 < R_p \leq 128$, $128 < R_p \leq 256$, $256 < R_p \leq 512$, and $512 < R_p \leq 840$, where R_p is the projected radius in pixels. The annuli grow by factors of two in order to preserve the same approximate signal level in each; the outermost limit is set by the proximity of the galaxy to the edge of the ACS image.

The SBF amplitude is the ratio of the galaxy image variance (normalization of the PSF component of the power spectrum) to the surface brightness; it has units of flux, and is usually converted to a magnitude called $\overline{m}$. The absolute I-band SBF magnitude has been carefully calibrated according to the galaxy $(V-I)$ color (Tonry et al. 1997, 2000). With a 0.06 mag adjustment to the zero point (Blakeslee et al. 2002) as a consequence of the final revisions in they Key Project Cepheids distances (Freedman et al. 2001), the calibration is

$$\overline{M}_I \;=\; -1.68\pm0.08 \;+\; (4.5 \pm 0.25)[(V-I)_0 - 1.15]\,. \tag{2.4}$$

For objects with colors similar to the GCs or the mean galaxy surface brightness, we have assumed $I_{814} = I_C$, since both the empirical and synthetic transformations from Sirianni et al. (2005) agree in predicting that the difference should be < 0.01 mag. However, the SBF is much redder, with a typical color $\overline{M}_V - \overline{M}_I \approx 2.4$ mag (Blakeslee et al. 2001). This is outside the color range of the empirical transformation, but the synthetic one gives $\overline{M}_I = \overline{M}_{814} + 0.04$, with an estimated uncertainty of ~ 0.02 mag. We apply this correction and tabulate our SBF results in Table 2.1 for the four annuli at the two different roll angles. The table also gives the galaxy color converted to $(V-I)$ using Eq. 2.3 in the same annuli and with the same masking as used for the SBF analysis, and the resulting distance moduli determined from Eq. 2.4.

Figure 2.6 provides a graphical representation the SBF results. The measurements

Table 2.1. SBF Measurements for Various Annuli in NGC 1533

$\langle r \rangle^{(a)}$ (arcsec)	$(V-I)_0{}^{(b)}$ (mag)	$\overline{m}_{I,1}{}^{(c)}$ (mag)	$\overline{m}_{I,2}{}^{(d)}$ (mag)	$(m-M)_1{}^{(e)}$ (mag)	$(m-M)_2{}^{(f)}$ (mag)
3.8	1.2329 ± 0.0007	30.145 ± 0.009	30.094 ± 0.013	31.452 ± 0.009	31.401 ± 0.014
9.2	1.2194 ± 0.0024	30.099 ± 0.011	30.059 ± 0.007	31.467 ± 0.016	31.427 ± 0.012
17.9	1.2029 ± 0.0075	30.018 ± 0.012	29.972 ± 0.006	31.460 ± 0.036	31.414 ± 0.034
32.9	1.1899 ± 0.0142	29.963 ± 0.014	29.920 ± 0.010	31.464 ± 0.065	31.421 ± 0.065

Note. — Quoted uncertainties reflect internal measurement error only. See text for discussion of systematic errors and final averaged distance.

[a] Mean radius of annulus.

[b] Mean galaxy $(V-I)_0$ color in annulus.

[c] SBF $\overline{m}_I$ measurement from roll angle 1 observation.

[d] SBF $\overline{m}_I$ measurement from roll angle 2 observation.

[e] Distance modulus from galaxy color and roll 1 SBF measurment.

[f] Distance modulus from galaxy color and roll 2 SBF measurment.

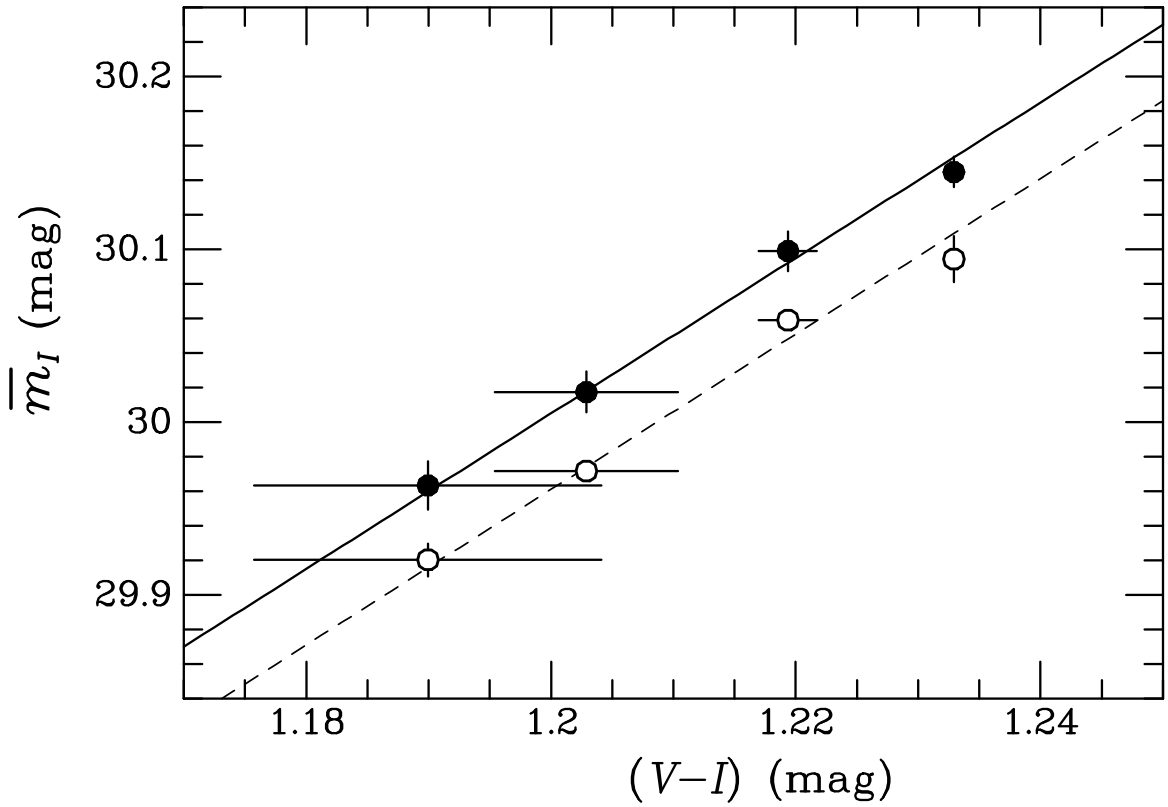

Figure 2.6 SBF measurements for the four radial annuli in NGC 1533 from the roll 1 (filled circles) and roll 2 (open circles) observations. The solid and dashed lines both have slopes of 4.5 as given by the published $\overline{m}_I$–$(V-I)$ calibration, and are fitted only in the zero point. Although internally quite consistent, the two different observations give distance moduli that differ by 0.04 mag.

at the two different roll angles are remarkably consistent, except for a systematic offset of 0.04 mag. Weighted averages of the annuli give mean distance moduli and formal errors of 31.456 ± 0.008 and 31.416 ± 0.009 mag for rolls 1 and 2, respectively. The galaxy appears at very different locations in the field of view for the two observations, in fact on different CCD chips. We verified that the difference in the photometry itself was negligible (about ten times smaller than the $(m-M)$ offset). However, the ACS/WFC does have some spatial variation in the PSF (Krist 2003), and temporal variations can be caused by jitter, sun angle, etc. Any mismatch in the PSF template used for the power spectrum analysis directly affects the SBF measurement, and this is the most likely cause of the small difference.

We therefore average the results from the two roll angles and use the 0.04 mag

difference as a more realistic estimate of the measurement uncertainty. To this, we add uncertainties of 0.01 mag in the absolute calibration of F814W, 0.02 mag for the transformation of $\overline{m}$ to the standard I band, $4.5 * 0.018 = 0.08$ mag from the systematic uncertainty in the $(V-I)$ color used for the calibration (Sec. 2.3.2), and 0.08 mag from the $\overline{M}_I$ calibration zero point. Finally, we obtain $(m-M) = 31.44 \pm 0.12$ mag, or $d = 19.4 \pm 1.1$ Mpc. This is an improvement by a factor of 3.5 compared to the ground-based distance from Tonry et al. (2001), and agrees well with the mean SBF result for the Dorado group (see Sec. 3.4 above). Thus, although NGC 1533 is something of a velocity outlier, its distance is the same as the group mean. Our measurement translates to a spatial scale of 94.0 pc per arcsec, or 4.70 pc per ACS/WFC pixel, which we adopt for the globular cluster analysis in the following sections.

2.5 Globular Cluster Colors

To obtain a sample of globular cluster candidates from the object photometry described in Sec. 2.2.2 above, we selected objects with $19 < I_{814} < 24$ mag, $0.5 \leq (V-I) \leq 1.5$, FWHM ≤ 4 pix ($0\farcs2$) in each bandpass, and galactocentric radius R_g in the range $10'' < R_g \leq 108''$ (~ 0.9 to ~ 10.2 kpc). Figure 2.7 shows a color–magnitude diagram of sources that have already been selected according to these radial and FWHM constraints. The shaded region marks the color and magnitude constraints on the GC candidates. The figure also shows a dozen objects, marked with blue stars, that are brighter than $I_{814} = 25$ and lie within the borders of the H II regions found my Meurer et al. (2006). These objects mainly have colors $(V-I) \approx -0.2 \pm 0.2$; their magnitudes and colors are similar to those found for stars in the halo H II regions in the HRC data studied by Werk et al. (2007).

However, the two brightest compact sources found to lie within the H II regions are actually GC candidates, as shown in the figure. One of these objects has the color of a typical "blue GC" with $(V-I) \approx 0.9$, while the other is a typical "red GC" with $(V-I) \approx 1.2$. Both are marginally resolved (i.e., nonstellar). We suspect that this is a simple case of projection and that these GC candidates are not physically

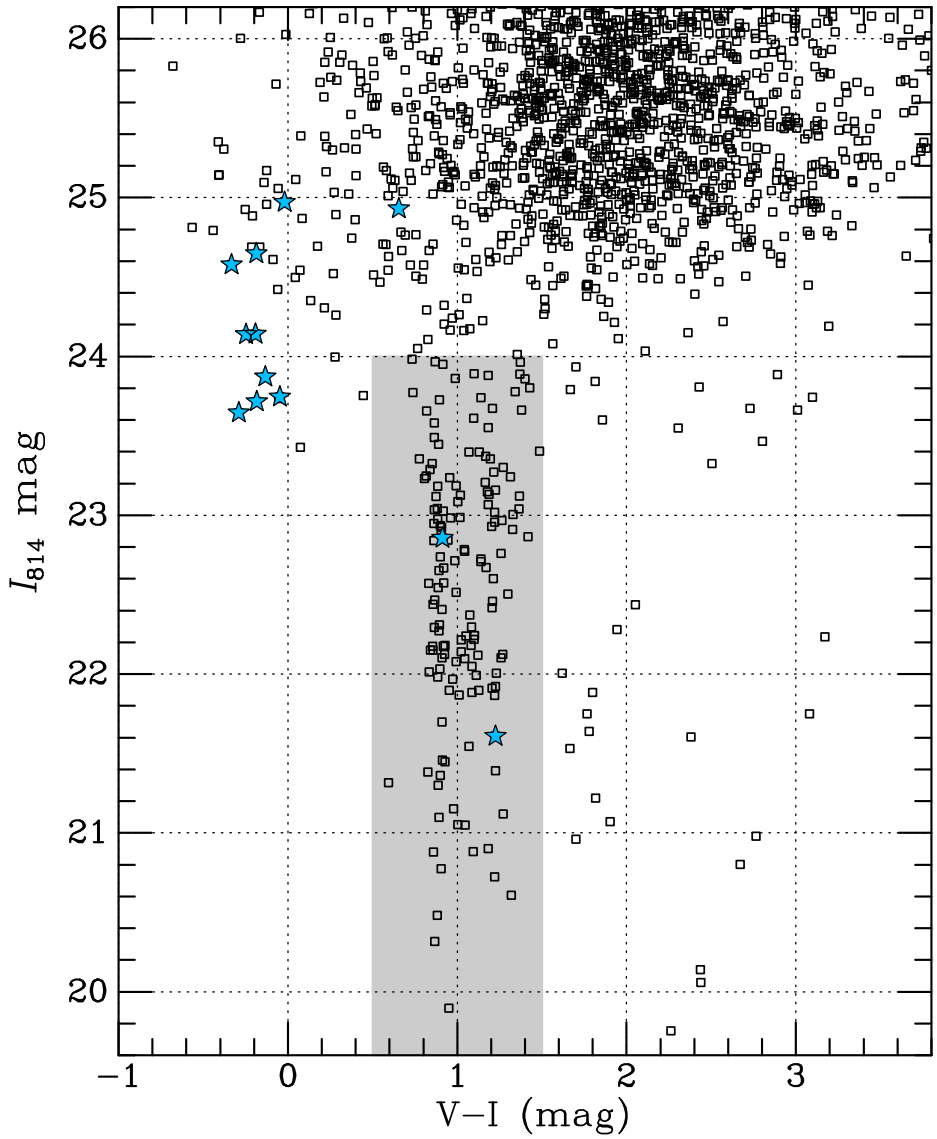

Figure 2.7 Color-magnitude diagram for compact sources (FWHM $< 0\farcs2$) in the galactocentric radial range $10'' < R_g < 108''$. The shaded region marks the broadest selection we use for GC candidates: $0.5 < (V-I) < 1.5$ and $I_{814} < 24$. The blue stars represent compact sources with $I_{814} < 25$ that lie within the H II regions identified by Meurer et al. (2006). The two such sources that lie within the region of the GC candidates are probably simple cases of projection. In general, objects with $(V-I) \approx 0 \pm 0.5$, $I_{814} \approx 23.5$–25.5 appear to be blue supergiants either in the H II regions or dispersed along the faint spiral arms; those with $(V-I) \approx 2$, $I_{814}23$ are likely Galactic M dwarfs. The large cloud of points with $(V-I) \approx 2 \pm 0.1$ and $I_{814} \gtrsim 25$ are (mostly blends of) the brightest evolved giants in NGC 1533.

associated with the H II region, since the projection is within the area of the largest H II region, and it is located at a radius where the surface density of GCs is fairly high. Thus, we treat these two objects the same as the other GC candidates in our analysis, and simply note that none of our results would change significantly if they were removed.

The selection for GC candidates was done for the catalogs from each pointing, then the two lists of GC candidates were merged, giving a total of 151 candidates. For objects in the overlapping region of the two rolls angles, the objects' magnitudes and colors were averaged. Table 2.2 lists the positions, $(V-I)$ colors, effective radii (discussed in the following section), I_{814} magnitudes, and field (roll 1, roll 2, or merge) for each object selected in this way. Figure 2.8 shows a histogram of the color distribution of the objects; for comparison, it also shows the resulting color distribution when the magnitude cutoff is made 2 mag fainter. With the fainter cutoff, there is sizable contamination from blends of the red giants and/or supergiants in NGC 1533.

Table 2.2. GC Candidates

ID Number	RA (J2000)	DEC (J2000)	$(V-I)_0$ (mag)	$\pm$ (mag)	R_{eff} (arcsec)	I_{814} (mag)	$\pm$ (mag)	field
13	62.478742	−56.109037	1.260	0.013	0.0207	22.759	0.024	merge
20	62.481901	−56.108821	1.341	0.024	0.0544	23.777	0.046	merge
30	62.494871	−56.107931	0.867	0.013	0.0307	22.467	0.014	merge
141	62.503620	−56.108303	1.082	0.014	0.0222	22.180	0.012	r2
175	62.469642	−56.111536	0.913	0.016	0.0340	22.856	0.034	merge
199	62.475854	−56.111165	0.863	0.011	0.0085	22.950	0.032	merge
219	62.456702	−56.113055	0.863	0.042	0.0159	23.580	0.058	merge
391	62.458113	−56.114010	0.855	0.011	0.0289	22.176	0.023	merge
424	62.477575	−56.112507	1.123	0.013	0.0377	22.120	0.019	merge
428	62.512621	−56.109436	1.299	0.017	0.0525	22.503	0.011	r2
443	62.468860	−56.113378	1.012	0.003	0.0237	21.869	0.022	merge
467	62.466586	−56.113788	1.086	0.011	0.0207	22.049	0.029	merge
472	62.470944	−56.113139	1.226	0.011	0.0277	21.610	0.018	merge
556	62.498873	−56.111763	0.816	0.011	0.0215	23.248	0.021	r2
566	62.486962	−56.112939	1.276	0.018	0.0592	23.898	0.054	r2

Table 2.2 (cont'd)

ID Number	RA (J2000)	DEC (J2000)	$(V-I)_0$ (mag)	$\pm$ (mag)	R_{eff} (arcsec)	I_{814} (mag)	$\pm$ (mag)	field
616	62.507189	−56.111401	0.987	0.021	0.0629	23.863	0.026	r2
785	62.488994	−56.114282	0.806	0.065	0.0433	23.231	0.060	merge
883	62.473735	−56.116447	0.901	0.018	0.0163	22.738	0.034	merge
1030	62.487940	−56.116245	1.093	0.012	0.0296	20.884	0.011	merge
1048	62.491160	−56.116023	0.869	0.024	0.0355	23.966	0.052	merge
1151	62.483266	−56.117620	0.950	0.014	0.0300	19.897	0.011	merge
1238	62.494429	−56.117187	0.895	0.014	0.0696	23.727	0.039	r2
1336	62.474199	−56.119748	1.220	0.012	0.0266	20.723	0.013	merge
1388	62.475712	−56.120119	0.905	0.014	0.0244	20.775	0.013	merge
1398	62.487527	−56.119145	0.907	0.012	0.0455	22.925	0.028	merge
1542	62.472319	−56.121682	1.070	0.037	0.0355	23.399	0.065	merge
1550	62.469259	−56.122013	1.088	0.017	0.0141	22.218	0.036	r2
1607	62.483549	−56.121258	0.901	0.011	0.0289	21.363	0.013	merge
1633	62.490568	−56.120816	1.270	0.017	0.0037	23.301	0.033	r2
1645	62.468214	−56.122742	1.460	0.010	0.0141	22.868	0.053	r2

Table 2.2 (cont'd)

ID Number	RA (J2000)	DEC (J2000)	$(V-I)_0$ (mag)	$\pm$ (mag)	R_{eff} (arcsec)	I_{814} (mag)	$\pm$ (mag)	field
1669	62.486759	−56.121398	0.858	0.012	0.0281	20.880	0.011	merge
1690	62.483049	−56.121813	1.205	0.012	0.0252	21.911	0.017	merge
1692	62.489449	−56.121244	1.326	0.015	0.0585	22.910	0.026	r2
1760	62.490182	−56.121732	1.141	0.010	0.0185	23.741	0.047	r2
1794	62.459528	−56.124760	1.046	0.013	0.0170	21.050	0.013	merge
1822	62.493954	−56.121881	0.900	0.007	0.0340	22.935	0.023	r2
1837	62.482462	−56.122994	0.839	0.021	0.0348	23.287	0.039	merge
1847	62.497809	−56.121721	0.834	0.011	0.0511	22.013	0.013	r2
1977	62.466685	−56.125414	1.269	0.007	0.0240	22.123	0.025	merge
1980	62.475828	−56.124632	0.892	0.011	0.1017	22.274	0.022	merge
2004	62.467446	−56.125627	1.042	0.021	0.0333	22.783	0.036	merge
2023	62.495436	−56.123193	1.183	0.018	0.0237	23.552	0.033	r2
2032	62.472654	−56.125346	0.928	0.007	0.0400	21.448	0.015	merge
2043	62.483985	−56.124394	0.893	0.012	0.0281	21.098	0.012	merge
2101	62.480199	−56.125032	0.882	0.019	0.1343	23.042	0.033	merge

Table 2.2 (cont'd)

ID Number	RA (J2000)	DEC (J2000)	$(V-I)_0$ (mag)	$\pm$ (mag)	R_{eff} (arcsec)	I_{814} (mag)	$\pm$ (mag)	field
2138	62.460701	−56.127096	1.367	0.017	0.0474	23.121	0.035	merge
2215	62.486362	−56.125426	0.819	0.066	0.0585	23.657	0.045	merge
2262	62.472163	−56.127100	0.831	0.012	0.0281	22.571	0.026	merge
2321	62.496776	−56.125300	0.857	0.013	0.0244	22.439	0.015	r2
2536	62.470591	−56.129244	0.884	0.010	0.0222	21.981	0.017	merge
2613	62.474279	−56.129425	0.994	0.015	0.0211	22.078	0.018	merge
2657	62.484181	−56.128924	1.222	0.013	0.0274	21.865	0.014	r2
2664	62.494131	−56.128090	1.215	0.019	0.0562	23.272	0.025	r2
2720	62.475693	−56.130236	1.004	0.170	0.0333	21.053	0.012	merge
2753	62.515850	−56.126848	1.195	0.021	0.0895	23.355	0.017	r2
2782	62.509445	−56.127683	1.129	0.020	0.0385	23.399	0.019	r2
2804	62.467737	−56.131626	0.826	0.011	0.0340	21.384	0.012	r2
2846	62.510464	−56.128097	0.864	0.014	0.0326	22.293	0.011	r2
2884	62.462936	−56.132600	0.918	0.011	0.0266	22.174	0.016	r2
2959	62.466327	−56.132967	1.023	0.013	0.0296	22.141	0.016	r2

Table 2.2 (cont'd)

ID Number	RA (J2000)	DEC (J2000)	$(V-I)_0$ (mag)	$\pm$ (mag)	R_{eff} (arcsec)	I_{814} (mag)	$\pm$ (mag)	field
3108	62.470197	−56.133570	0.890	0.010	0.0141	23.448	0.033	r2
3287	62.479226	−56.134192	0.841	0.011	0.0451	22.151	0.013	r2
3702	62.464106	−56.138694	0.896	0.013	0.0681	22.311	0.012	r2
4233	62.482340	−56.141013	0.739	0.018	0.0710	23.773	0.025	r2
4244	62.494051	−56.140087	0.861	0.016	0.0296	22.841	0.014	r2
4269	62.504504	−56.139280	0.875	0.018	0.0237	23.117	0.015	r2
4737	62.473405	−56.145470	0.912	0.013	0.0437	21.459	0.009	r2
4740	62.493197	−56.143711	1.069	0.015	0.0296	21.544	0.009	r2
4791	62.482879	−56.145036	0.961	0.020	0.0385	22.984	0.015	r2
2072	62.413458	−56.114438	0.775	0.016	0.0244	23.354	0.017	r1
2617	62.429086	−56.100548	1.128	0.013	0.0451	21.899	0.009	r1
2645	62.422291	−56.111412	1.225	0.012	0.0340	21.391	0.009	r1
2859	62.433442	−56.097663	1.207	0.029	0.0511	23.672	0.021	r1
3048	62.430437	−56.105507	1.103	0.013	0.0385	22.242	0.011	r1
3055	62.425954	−56.112310	0.956	0.018	0.0385	23.236	0.018	r1

Table 2.2 (cont'd)

ID Number	RA (J2000)	DEC (J2000)	$(V-I)_0$ (mag)	$\pm$ (mag)	R_{eff} (arcsec)	I_{814} (mag)	$\pm$ (mag)	field
3110	62.427170	−56.111496	0.864	0.017	0.0437	23.489	0.022	r1
3125	62.427697	−56.110888	1.018	0.017	0.0222	23.128	0.018	r1
3143	62.428683	−56.109900	0.866	0.010	0.0585	20.316	0.007	r1
3540	62.430444	−56.113735	0.925	0.012	0.0340	22.125	0.012	r1
3645	62.443910	−56.095340	0.914	0.025	0.0511	23.949	0.025	r1
3647	62.430762	−56.115511	1.139	0.015	0.0296	22.708	0.015	r1
3978	62.440401	−56.106818	1.015	0.016	0.0170	22.986	0.021	r1
4063	62.433704	−56.118506	0.920	0.011	0.0340	22.574	0.016	r1
4114	62.436845	−56.114726	1.074	0.012	0.0340	22.371	0.015	r1
4202	62.454829	−56.089105	0.927	0.013	0.0363	22.181	0.010	r1
4277	62.442072	−56.110460	1.099	0.010	0.0340	23.892	0.047	r1
4280	62.440208	−56.113842	1.271	0.012	0.0266	21.119	0.011	r1
4320	62.436274	−56.121193	1.004	0.013	0.0266	23.086	0.023	r1
4373	62.449126	−56.102981	0.885	0.007	0.0725	23.182	0.022	r1
4436	62.453844	−56.097291	0.919	0.013	0.0681	22.667	0.013	r1

Table 2.2 (cont'd)

ID Number	RA (J2000)	DEC (J2000)	$(V-I)_0$ (mag)	$\pm$ (mag)	R_{eff} (arcsec)	I_{814} (mag)	$\pm$ (mag)	field
4444	62.447418	−56.107243	1.044	0.013	0.0274	22.096	0.015	r1
4526	62.444006	−56.113942	1.260	0.011	0.0525	22.102	0.016	r1
4630	62.444749	−56.114977	1.205	0.013	0.0237	22.418	0.020	r1
4658	62.449950	−56.107424	1.203	0.013	0.0244	22.930	0.025	r1
4704	62.451416	−56.106083	1.098	0.007	0.0163	23.611	0.040	r1
4742	62.460552	−56.093062	1.112	0.013	0.0340	21.993	0.009	r1
4760	62.450792	−56.108034	1.379	0.025	0.0858	23.664	0.045	r1
4790	62.454256	−56.103414	0.909	0.012	0.0311	21.698	0.013	r1
4794	62.453328	−56.104755	1.171	0.015	0.0266	22.670	0.020	r1
4806	62.452688	−56.106034	1.164	0.013	0.0340	23.206	0.030	r1
4813	62.453102	−56.105470	1.167	0.012	0.0770	23.371	0.032	r1
4888	62.460404	−56.095814	1.182	0.028	0.0585	23.881	0.036	r1
4948	62.442253	−56.124977	1.024	0.011	0.0503	22.215	0.016	r1
5095	62.449093	−56.117356	0.884	0.016	0.0451	22.977	0.032	r1
5239	62.450679	−56.117956	1.045	0.006	0.0400	22.773	0.029	r1

Table 2.2 (cont'd)

ID Number	RA (J2000)	DEC (J2000)	$(V-I)_0$ (mag)	$\pm$ (mag)	R_{eff} (arcsec)	I_{814} (mag)	$\pm$ (mag)	field
5271	62.448478	−56.121895	1.364	0.017	0.1347	23.041	0.032	r1
5280	62.450171	−56.119649	1.188	0.006	0.0466	23.132	0.036	r1
5290	62.457697	−56.108462	0.974	0.008	0.0385	21.967	0.016	r1
5313	62.449563	−56.121180	1.400	0.029	0.0266	23.858	0.061	r1
5389	62.449014	−56.123932	0.882	0.011	0.0326	20.481	0.010	r1
5393	62.455059	−56.114635	1.214	0.009	0.0133	22.601	0.028	r1
5446	62.463440	−56.103252	1.140	0.013	0.0170	22.725	0.020	r1
5475	62.460226	−56.108876	1.226	0.008	0.0969	21.923	0.016	r1
5604	62.450771	−56.125846	1.230	0.011	0.0422	22.006	0.016	r1
5708	62.463336	−56.108916	0.905	0.015	0.0215	22.901	0.031	r1
5754	62.463867	−56.109087	1.221	0.003	0.1199	22.956	0.032	r1
5768	62.452947	−56.125993	0.952	0.019	0.0385	21.897	0.016	r1
5837	62.456743	−56.121757	0.887	0.010	0.0281	21.300	0.014	r1
5865	62.469218	−56.103303	1.208	0.012	0.0681	22.459	0.016	r1
5963	62.455278	−56.127144	0.887	0.007	0.0141	22.545	0.024	r1

Table 2.2 (cont'd)

ID Number	RA (J2000)	DEC (J2000)	$(V-I)_0$ (mag)	$\pm$ (mag)	R_{eff} (arcsec)	I_{814} (mag)	$\pm$ (mag)	field
6042	62.466243	−56.111291	1.341	0.009	0.0067	23.842	0.077	r1
6050	62.469475	−56.107693	1.184	0.011	0.0296	20.902	0.011	r1
6052	62.472359	−56.103277	1.100	0.013	0.0237	22.218	0.015	r1
6055	62.474468	−56.100142	0.918	0.014	0.0237	23.026	0.019	r1
6058	62.458180	−56.124987	1.226	0.009	0.0340	23.158	0.038	r1
6179	62.474633	−56.101859	1.084	0.013	0.0237	22.296	0.014	r1
6279	62.473238	−56.107092	1.177	0.010	0.0200	23.148	0.032	r1
6429	62.474914	−56.107999	1.263	0.013	0.0385	22.968	0.029	r1
6457	62.475410	−56.108026	0.856	0.008	0.0296	22.152	0.018	r1
6597	62.484653	−56.097083	1.222	0.019	0.0525	23.020	0.015	r1
6622	62.480808	−56.099170	1.087	0.013	0.0266	21.884	0.010	r1
6842	62.480776	−56.108464	0.986	0.008	0.0170	22.715	0.023	r1
6872	62.490483	−56.094283	0.853	0.018	0.0599	23.327	0.016	r1
6997	62.483392	−56.107559	1.183	0.014	0.0244	23.067	0.025	r1
7017	62.471658	−56.125870	0.971	0.006	0.0215	22.527	0.028	r1

Table 2.2 (cont'd)

ID Number	RA (J2000)	DEC (J2000)	$(V-I)_0$ (mag)	$\pm$ (mag)	R_{eff} (arcsec)	I_{814} (mag)	$\pm$ (mag)	field
7081	62.484164	−56.108342	0.910	0.009	0.0340	22.408	0.017	r1
7213	62.476729	−56.122510	0.841	0.022	0.0503	23.030	0.036	r1
7455	62.494309	−56.100625	0.945	0.019	0.0296	22.844	0.018	r1
7509	62.494724	−56.101300	0.892	0.014	0.0363	22.653	0.013	r1

The $(V-I)$ color distribution of the GC candidates (gray histogram in Figure 2.8) was tested for bimodality using the KMM (Kaye's Mixture Modeling) algorithm (McLachlan & Basford 1988; see also Ashman, Bird & Zepf 1994). The algorithm reports that the data are bimodal with essentially 100% confidence. It returns best-fit values for the color peaks of 0.921 and 1.226 mag. We also considered restricting the GC candidates to a narrower color range of $0.7 \leq (V-I) \leq 1.4$ (since the method is sensitive to outliers) and to alternative magnitude cutoffs of $I_{814} < 23$ and $I_{814} < 25$. The confidence of bimodality remained at 100% for all these combinations of magnitude and color cuts, except for the case with the faint magnitude cut $I_{814} < 25$ and color range of $0.5 \leq (V-I) \leq 1.5$, for which the confidence level was 98.8%. This fainter cutoff results in considerable contamination, yet still exhibits likely bimodality. We conclude that the GC color distribution in NGC 1533 is bimodal to a high level of confidence.

Recently there has been discussion in the literature of a correlation between magnitude and color for the blue component of the GC population, in the sense that the

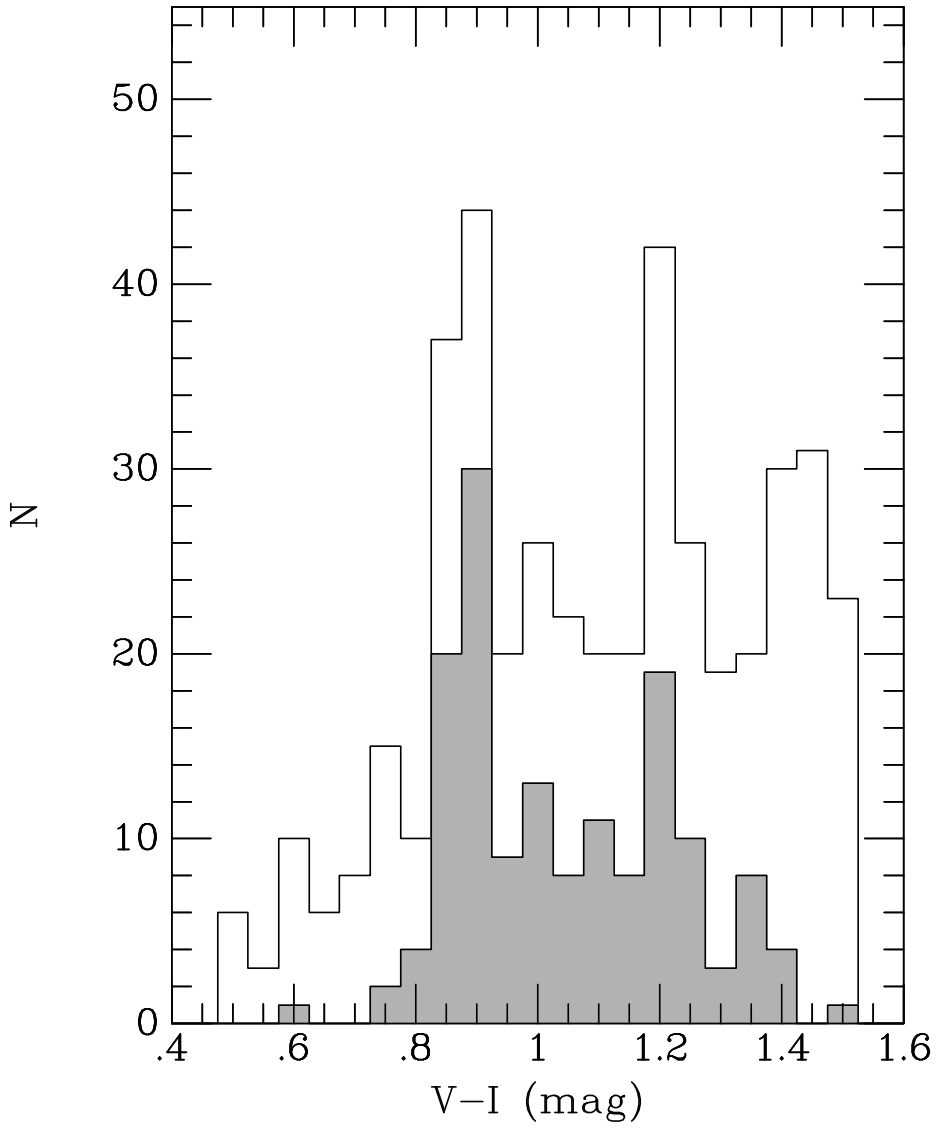

Figure 2.8 Histogram of candidate globular cluster ($V-I$) colors (converted from F814W and F606W as described in the text). The solid histogram uses an I-band magnitude cutoff $I < 24$, which is about $1\,\sigma$ beyond the peak of the GCLF. The open histogram uses a cutoff $I < 26$, and thus has a substantial contribution from the brightest giants in NGC 1533.

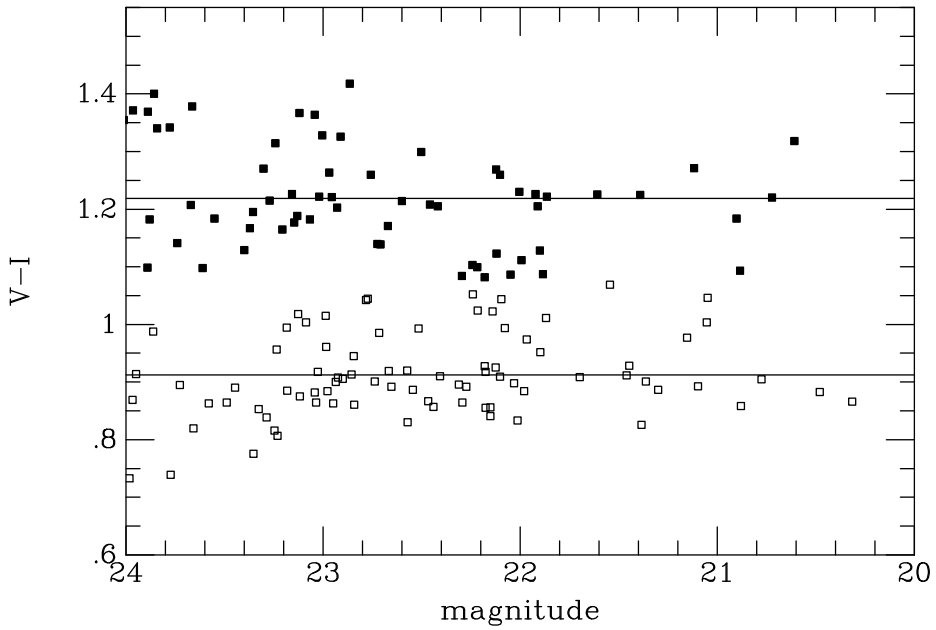

Figure 2.9 $(V-I)$ colors for GC candidates in the red (filled squares) and blue (open squares) peaks, as determined by the KMM algorithm, are plotted as a function of I_{814} magnitude. The solid lines show the average colors for the two groups. There is no significant slope in the color-magnitude relations of either the red or blue GCs when a cutoff magnitude of $I_{814} < 23$ is used.

blue GCs become redder at higher luminosities (Harris et al. 2006; Mieske et al. 2006). This has been dubbed "the blue tilt." As a simple test for this in NGC 1533, we split our catalog of GC candidates into red and blue groups using the $(V-I) = 1.07$ average between the two peaks from KMM as the dividing value. We then performed simple linear least-squares fits to test for a nonzero slope (see Figure 2.9). With a magnitude cutoff of $I_{814} < 23$, (just beyond the peak of the GCLF), we find slopes of $d(V-I)/dI = 0.003 \pm 0.012$ and $d(V-I)/dI = 0.012 \pm 0.021$ for the color-magnitude relations of the blue and red GC candidates, respectively; both are zero within the errors. If we use a cutoff magnitude of $I_{814} < 24$, then the slopes both differ from zero by $2\,\sigma$, but this occurs as a result of the increasing scatter at fainter magnitudes, coupled with the truncation of the other half the data (simple tests can reproduce this effect). When observed, the "tilt" occurs because the blue and red sequences converge at bright magnitudes, not diverge at faint magnitudes. There is no evidence of this effect in the present data set.

The lack of the blue tilt for NGC 1533 is not surprising, since past evidence for it comes from GCs in the brightest ellipticals in galaxy groups and clusters (Harris et al. 2006; Mieske et al. 2006). In such systems, the GCs reach higher luminosities and masses, both because the populations are richer and because the GCLFs are broader (Jordán et al. 2006). The simplest explanation for the tilt is that it results from self-enrichment: the most massive metal-poor GCs were able to retain some self-enriched gas while star formation was ongoing. Since the GCs in a small population like that of NGC 1533 do not reach such high masses, this effect may not have occurred. Similarly, if the tilt is due to mergers or accretion by GCs, it might only occur in the richest systems where these would be more common. It will be interesting to see if blue tilts are found in the GC systems of other intermediate-luminosity galaxies, and if so, whether those systems are unusually rich or have broad GCLFs.

2.6 Globular Cluster Sizes

2.6.1 GC Shape Analysis

The half-light radius of each GC candidate was obtained using the Ishape program (Larsen 1999). Ishape fits the 2-D shape of each object under the assumption that the object can be modeled by one of various analytic profiles convolved with the PSF. We fitted the GC candidates in each roll using the "KING30" profile, which is a King (1962) model with concentration parameter $c = 30$. Ishape reports the model FWHM in pixels (prior to PSF convolution), which we then converted to effective radius $R_{\rm eff}$ using the conversion factor of 1.48 given in Table 3 of the Ishape users' manual (Larsen 2005). We then converted to a physical size in parsecs using the distance derived in Sec. 2.4. From this analysis, 12 of the 151 GC candidates (7.9%) were found to be stellar, with zero intrinsic size, and were then removed from the catalog.

We fitted the GC candidates (to a fainter magnitude limit of $I_{814} < 26$) for the two different roll angles separately, and then compared the results for the ones in

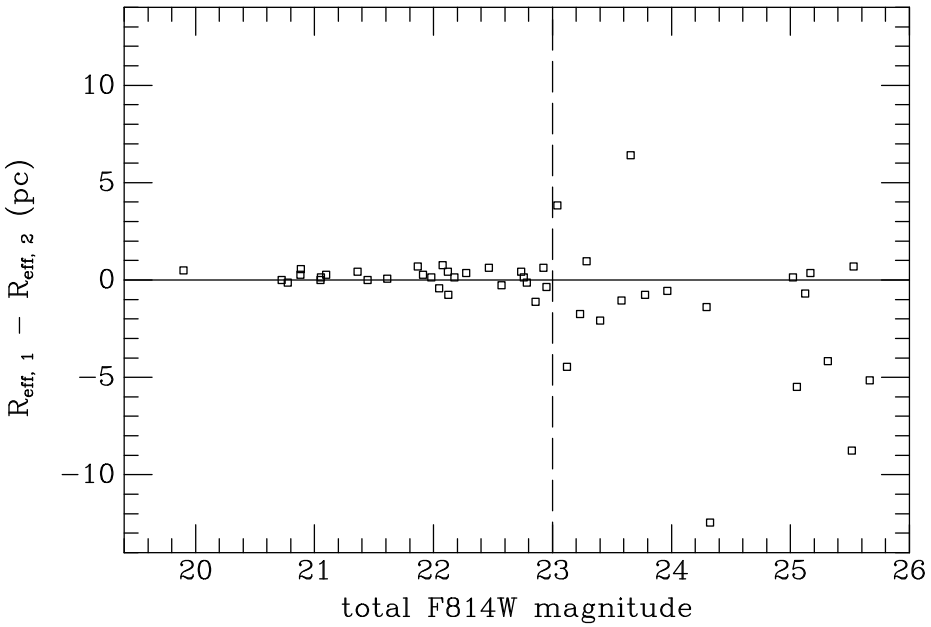

Figure 2.10 Differences in the $R_{\rm eff}$ values from Ishape for matched objects present in both the roll 1 and roll 2 observations are plotted as a function of I_{814} magnitude. There is an apparent abrupt transition from reliable to dubious measurement values at $I_{814} \approx 23$.

the overlapping region. This is an important test, as Ishape itself does not provide very robust size uncertainties. The manual states that the sizes should be accurate to about 10%, given sufficiently high signal-to-noise ($S/N \gtrsim 40$). Figure 2.10 shows that the agreement is good down to $I_{814} = 23$, where the scatter in the differences is 0.4 pc (or 0.3 pc error per measurement), but worsens abruptly at fainter magnitudes. The scatter is larger by a factor of 7.5 for objects with $23 < I_{814} < 24$, and by a factor of 10 for $23 < I_{814} < 26$. We therefore consider only objects with $I_{814} < 23$ as having reliable $R_{\rm eff}$ determinations, although we tabulate all the measurements in Table 2.2.

Figure 2.11 compares the effective radii from roll 1 to those from roll 2 for objects with $I_{814} < 23$ and present in both observations. The RMS scatter in the differences is 18.9%, indicating that the error per measurement is 13%. There is no significant offset in the $R_{\rm eff}$ values measured in the two different observations.

Some previous studies have found that $R_{\rm eff}$ depends on the color of the GC, with red GCs being smaller on average than blue GCs (Jordán et al. 2005; Larsen et al 2001). Figure 2.12 (left panel) shows $R_{\rm eff}$ vs $(V-I)$ for all GCs brighter than $I_{814} = 23$

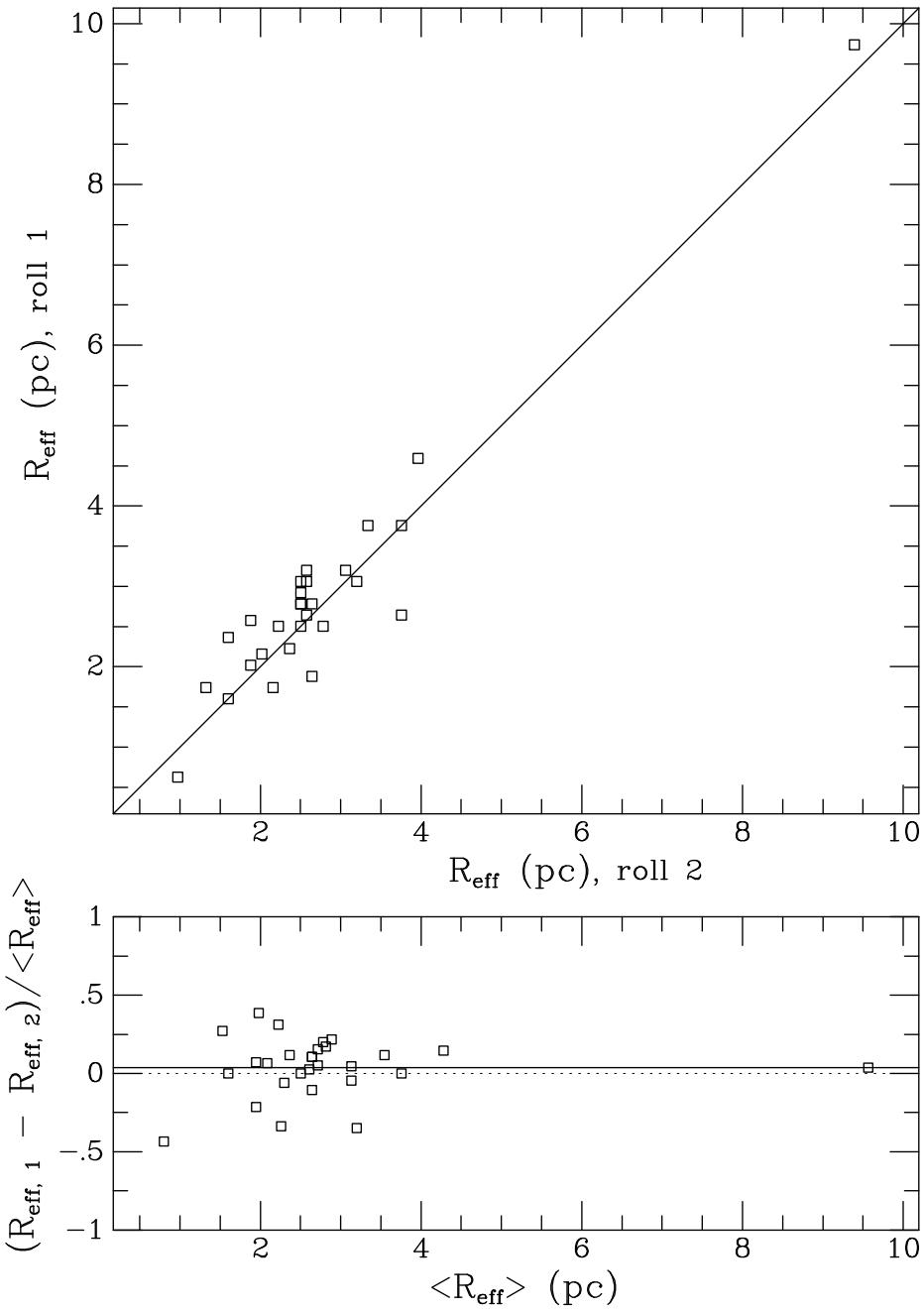

Figure 2.11 *Top:* Measured $R_{\rm eff}$ values for objects with $I_{814} < 23$ in roll 1 are plotted against the $R_{\rm eff}$ values for the same objects measured in roll 2. The plotted line is equality. *Bottom:* Fractional differences in the $R_{\rm eff}$ values are plotted as a function of the average value. The solid line shows the mean offset of 0.038 ± 0.036.

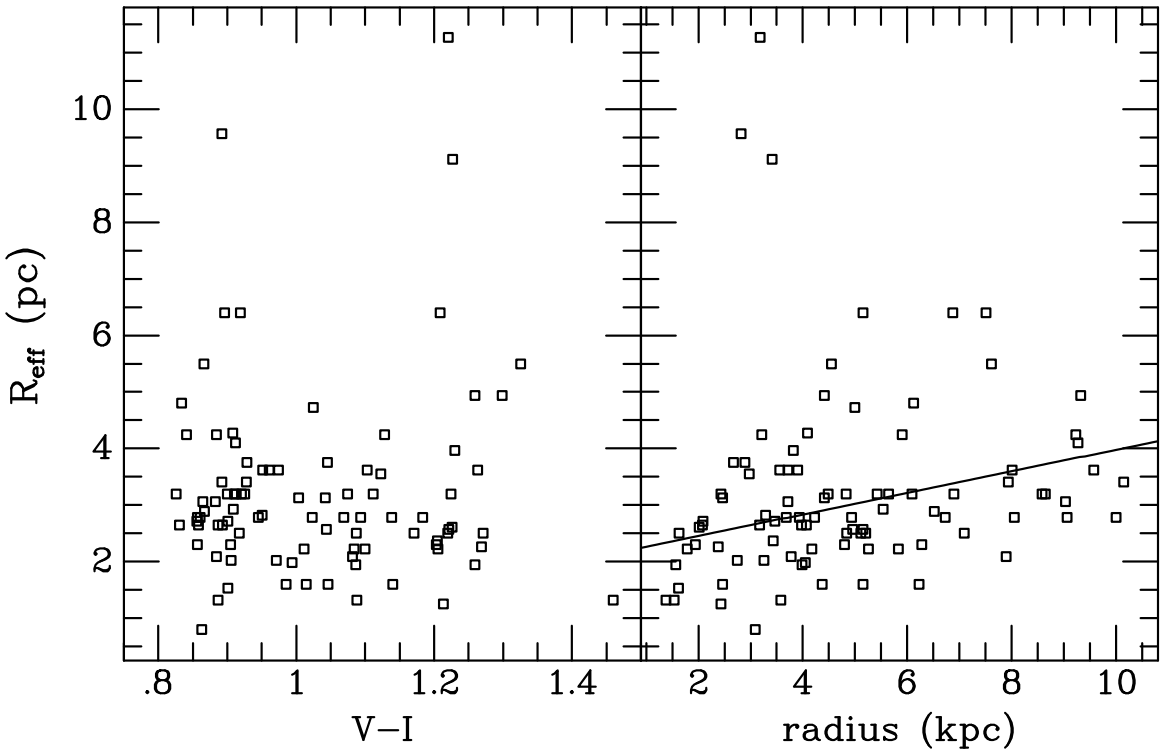

Figure 2.12 *Left:* GC effective radius is plotted versus GC color, showing no significant correlation. *Right:* GC effective radius is plotted versus radius from the center of NGC 1533. The line shows the correlation given in Eq. 2.5, which has a slope of ~ 0.2 pc/kpc.

in both roll angles (with the values averaged for objects in the overlap). We find no statistically significant trend of $R_{\rm eff}$ with color in the present data set. However, the sample consists of only 92 objects with robust $R_{\rm eff}$ measurements. If we calculate the median $R_{\rm eff}$ values for the 56 blue GCs and 36 red GCs (using the KMM splitting from above), we find $\langle R_{\rm eff} \rangle = 2.90 \pm 0.13$ and $\langle R_{\rm eff} \rangle = 2.59 \pm 0.18$ for the blue and red GCs, respectively. The uncertainties have been estimated by dividing the robust biweight scatter (Beers et al. 1990) by the square root of the number in each sample. Thus, we find that the red GCs are $11 \pm 8\%$ smaller than the blue ones, which is in the expected sense but not very significant.

On the other hand, we do find a correlation between $R_{\rm eff}$ and radial distance from center of NGC 1533 (Figure 2.12, right panel). The average size of the GCs increases with galactocentric radius. Omitting the 3 objects at radius $\sim 0\farcm5$ with $R_{\rm eff} > 9\,$pc

(which are more than $6\,\sigma$ outliers), we find the following relation:

$$R_{\rm eff} \;=\; (2.83 \pm 0.12) \;+\; (0.191 \pm 0.047)[(R_g/1\,{\rm kpc}) - 4]\ {\rm pc}, \tag{2.5}$$

where $R_{\rm eff}$ is in pc and galactocentric radius R_g is in kpc. Thus, we find a strong correlation between $R_{\rm eff}$ and radius R_g, significant at the $4\,\sigma$ level, but no significant correlation between $R_{\rm eff}$ and color. NGC 1533 is much more similar to the Milky Way in this regard (e.g., van den Bergh et al. 1991) than to the early-type galaxies in the Virgo cluster, where $R_{\rm eff}$ has only a mild dependence on R_g but a significant dependence on color (Jordan et al. 2005). It is tempting to associate this difference with environment, but first it is necessary to study the behavior of $R_{\rm eff}$ for the GCs of many more galaxies in loose group environments.

2.6.2 Distance from Half-Light Radius

Using the extensive ACS Virgo Cluster Survey data set, Jordan et al. (2005) have proposed a distance calibration based on the median half-light radius of the GC population of a galaxy. From Eq. 19 of that paper, the distance d in Mpc to the galaxy is estimated as

$$d = \frac{0.552 \pm 0.058}{\langle \hat{r}_h \rangle}\ {\rm Mpc}, \tag{2.6}$$

where $\langle \hat{r}_h \rangle$ is the corrected median half-light radius in arcseconds (their r_h corresponds to what we have called $R_{\rm eff}$, following the Ishape notation). Their definition of $\langle \hat{r}_h \rangle$ involves small corrections based on galaxy z-band surface brightness, galaxy $(g{-}z)$ color, and GC $(g{-}z)$ color. We do not have photometry in these bandpasses, and although we might estimate conversions from models, Jordán et al. note that the corrections are second-order; one can omit them for bright galaxies with broad GC color distributions (as in NGC 1533) and still obtain an accurate distance. Thus, we simply take $\langle \hat{r}_h \rangle$ as equal to the median $\langle R_{\rm eff} \rangle = 0\farcs0296 \pm 0\farcs0011$ for the 92 GC candidates in our catalog with $I_{814} < 23$. This gives a distance $d = 18.6 \pm 2.0$ Mpc, in accord with the distance of 19.4 ± 1.1 Mpc obtained from SBF in Sec. 2.4. The agreement in distance implies that the sizes of the GCs in NGC 1533 agree in the

median with those in the Virgo cluster and supports the use of GC half-light radii as distance indicators.

2.7 Globular Cluster Luminosity Function

We used the maximum likelihood code from Secker (1992) to fit the globular cluster luminosity function (GCLF) for 151 GC candidates down to a limit of $I_{814} = 24$. In order to do this, it is necessary to have a reasonable estimate of the background contamination. We searched the *HST* archive for possible background fields with similar Galactic latitudes taken through the same F606W+F814W filter combination to a similar depth. These fields were processed in the same way as the NGC 1533 fields, and the catalogs were subjected to the same selection according to their magnitude, color, and FWHM. Some of these fields were found to be anomalously rich, as they targeted distant rich clusters; these fields were excluded. In the end, we used four background comparison fields.

For a Gaussian GCLF, we find a turnover (peak) I_{814} magnitude $m_I^0 = 22.84^{+0.18}_{-0.24}$ and dispersion $\sigma_{\rm LF} = 1.10 \pm 0.15$ mag. This GCLF is plotted in Figure 2.13. The code also reports the confidence contours on the fit, as shown in Figure 2.14. We performed various tests by changing the selection of the data, including narrowing the color range to be between 0.7 and 1.4, varying the cutoff magnitude by ± 0.5 mag, and being more restrictive with the FWHM cut. These alternative selections changed m_I^0 by about ± 0.1 mag, and $\sigma_{\rm LF}$ by about ± 0.05 mag, both well within the quoted errors.

Our SBF distance together with the measured m_I^0 implies $M_I^0 = -8.6^{+0.22}_{-0.27}$ for NGC 1533. Conversely, the GCLF measurement provides another estimate of the distance, if we have a calibration for M_I^0. Harris (2001) gives a V-band calibration $\langle M_V^0 \rangle = -7.4 \pm 0.2$, where we use the quoted scatter as an estimate of the uncertainty. This zero point assumes a Virgo distance modulus of 30.97, which is 0.12 mag less than the calibration used for the ACS Virgo Cluster Survey and in this work. If we adjust for this offset and assume $\langle V-I \rangle = 1.07$ mag (Sec. 2.5; Kissler-Patig &

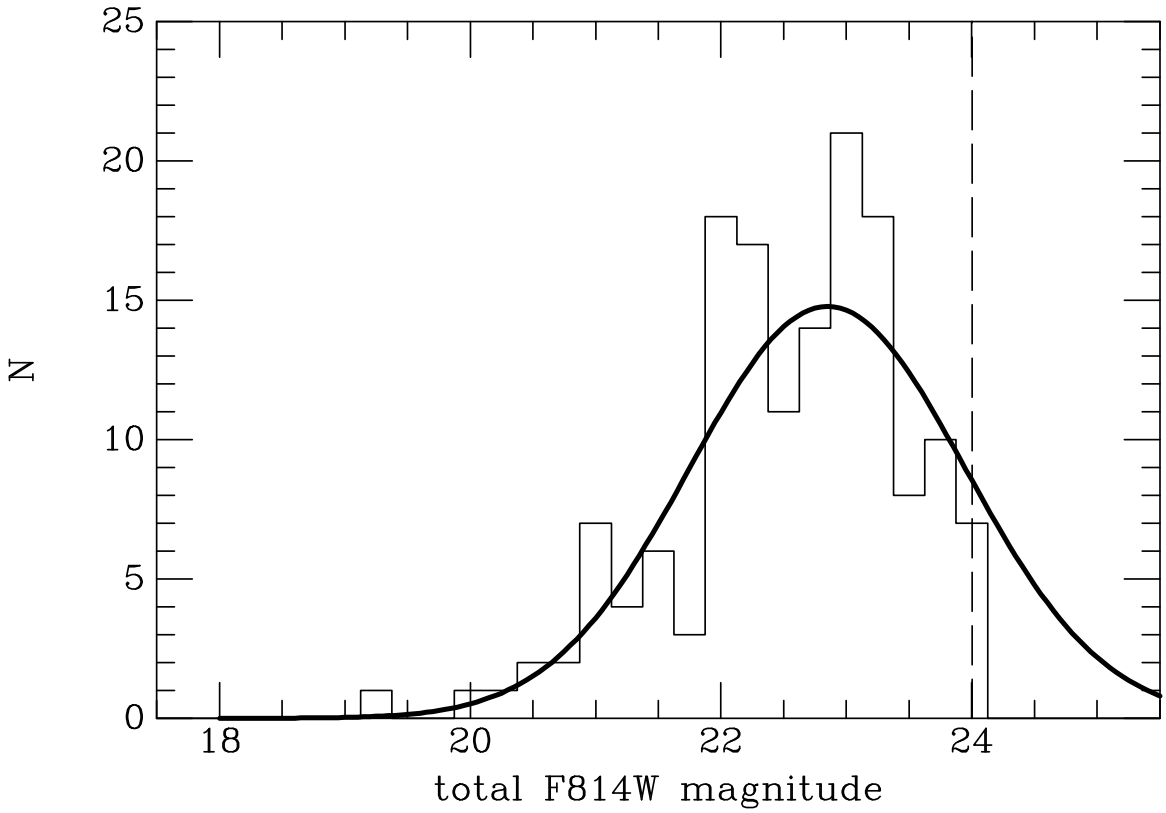

Figure 2.13 The GCLF of candidate globular clusters. The thick solid curve is a maximum likelihood fit to the (unbinned) GC magnitude distribution, represented by the histogram. The dashed line shows the limiting magnitude used for the fit.

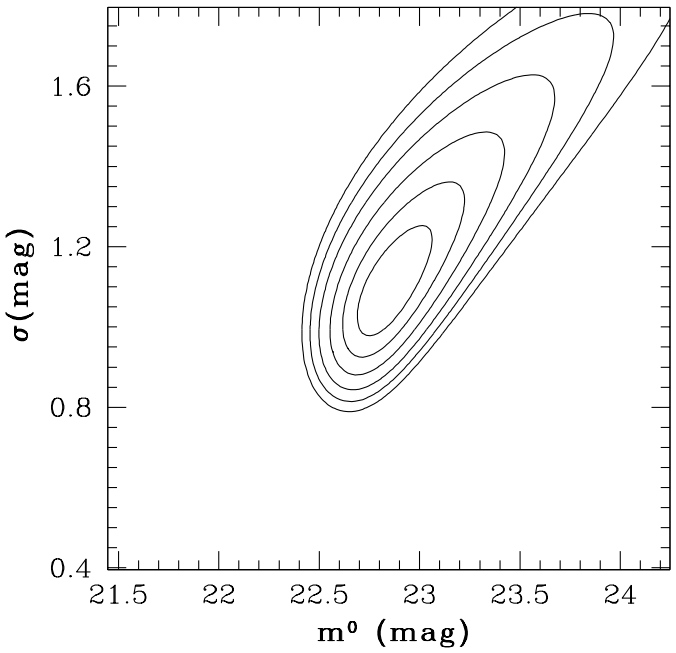

Figure 2.14 Probability contours on the GCLF width σ and turnover magnitude m_I^0 from the maximum likelihood fitting routine. The contours are drawn at significance steps of $0.5\,\sigma$, with the outermost being at $3\,\sigma$ (99.7% confidence).

Gebhardt 1999), then we have $\langle M_I^0 \rangle = -8.59$, giving $(m-M) = 31.41 \pm 0.29$ mag. This is consistent with the measured SBF distance and the distance estimated from the GC half-light radii. Note, however, that if we had used the value of $\langle M_V^0 \rangle$ given by Harris for S0 galaxies, or if we had converted from the value of $\langle M_z^0 \rangle$ given by Jordán et al. (2006), then the inferred distance modulus would have been larger by about 0.2 mag, although still in agreement within the errors.

Jordán et al. (2006) have found a correlation for Virgo galaxies of the GCLF width with galaxy B luminosity, and we can test whether or not NGC 1533 follows this trend. The total apparent B-band magnitude of NGC 1533 from the RC3 is 11.7. With our measured $(m-M)$, Eq. (2) from Jordán et al. (2006) predicts $\sigma_{\rm LF} = 1.09$ mag, in excellent agreement with our measured value of 1.10 ± 0.15 mag. We conclude that the GCLF of NGC 1533 is consistent within the uncertainties with those observed in Virgo.

Finally, we can estimate the value of the GC specific frequency $S_N = N_{\rm GC} \times 10^{0.4(M_V+15)}$ (Harris & van den Bergh 1981), where $N_{\rm GC}$ is the number of globulars and M_V is the absolute magnitude of the galaxy. The GCLF analysis indicates that the number of GCs integrated over luminosity is 163 ± 20 in the region analyzed. We used an outer radial limit of $1\farcm8$ for this study, but a significant portion of the area within this radius is missing as a result of the proximity of the galaxy to the image edge at both roll angles and the necessity of omitting the inner $10''$. If we make the reasonable assumption that the "missing" GCs roughly follow the galaxy light within $1\farcm8$, then we find a total population $N_{\rm GC} = 250 \pm 30$ within this radius. The total V magnitude of the galaxy within the same radius is $V = 10.75$, and using the measured distance modulus, we find $S_N = 1.3 \pm 0.2$. We expect this is very close to the "global" value, as $< 5\%$ of the light (based on the galaxy profile modeling), and few candidate GCs, are beyond this radius (which motivated the choice of radius). This result for NGC 1533 agrees well with the mean local $S_N = 1.0 \pm 0.6$ reported by Kundu & Whitmore (2001) from *HST*/WFPC2 imaging of nearby S0 galaxies.

2.8 Conclusions

We have analyzed deep F606W and F814W images of the galaxy NGC 1533 and its GC population taken at two roll angles with the ACS/WFC on *HST*. Although it is classified as an early-type barred lenticular galaxy, we found faint spiral structure once a smooth fit to the galaxy isophotes was subtracted. The color map shows faint dust features in the area around the bar and inner disk. Previous ground-based Hα imaging had shown that the galaxy disk contains several (~ 5) faint, compact H II regions. We find that all of these regions have luminous blue stars within them, although in some cases only one such star is evident. Four of these H II regions lie within one of the faint spiral arms, and a few other blue stars spread out within the arm. These observations suggest that NGC 1533 is in the late stages of a transition in morphology from type SBa to SB0.

From two-dimensional two-component parametric modeling of the galaxy surface brightness, we find a bulge-to-total ratio $B/T \approx 0.42$. The half-light radii of the bulge and disk are $\sim 7''$ and $\sim 46''$, respectively. We find a best-fitting Sérsic index $n = 2.0$ for the bulge, which can be reasonably approximated by an $r^{1/4}$ law in the 1-D profile. However, the disk has a relatively flat profile over a factor-of-three in radius, from $\sim 15''$ to $\sim 45''$, then steepens fairly abruptly beyond $\sim 50''$. This gives the disk a very low Sérsic index of $n \approx 0.4$, which might result from past high-speed interactions of NGC 1533 within the group environment.

Overall, the color of NGC 1533 is that of an evolved, red population, except in the few, small isolated regions where the blue stars occur. The bulge color is $(V-I) > 1.22$, similar to cluster ellipticals, and then there is a mild, but significant, linear color gradient throughout the disk. There is a gradual isophotal twist, and the isophotes increase in ellipticity from the bulge to a semi-major axis distance of $24''$, where ϵ goes above 0.4 before falling sharply again towards the round outer disk. The peak of the A_4 harmonic term, measuring "diskiness," actually occurs at a smaller semi-major axis of $21''$. This is because the pointed lens-like isophotes occur inside of the bar.

We measured the SBF amplitude in four broad radial annuli for each of the two observations at different roll angles. A gradient in the SBF amplitude is clearly detected

and follows the color gradient (the bluer outer regions have relatively brighter SBF). By matching our ACS photometry against ground-based $(V-I)$ data for this galaxy, we have accurately calibrated the SBF measurements to obtain distance moduli. We find excellent agreement among the different annuli but with an offset of 0.04 mag in distance between the two observations. However, the distance error is dominated by systematic uncertainty in the color and calibration zero point. We find a final distance modulus $(m-M) = 31.44 \pm 0.12$ mag, or $d = 19.4 \pm 1.1$ Mpc.

Candidate globular clusters were selected according to color, magnitude, radial position, and FWHM. Analysis of the color distribution of these objects with the KMM algorithm indicates with a very high degree of confidence that the distribution is bimodal. There is no evidence that the blue GCs become redder at bright magnitudes, the so-called "blue tilt." The absence of this effect in NGC 1533, an intermediate luminosity galaxy with a small GC population, is consistent with a self-enrichment explanation, since the GCs in such systems do not reach the high masses that they do in richer systems. The sizes of the GC candidates were measured using the Ishape software. By comparing the results from the two different roll angles, we found that the effective (half-light) radii $R_{\rm eff}$ have an accuracy of about 13% down to $I_{814} = 23$, but are not reliable beyond this. We did not find a significant trend of $R_{\rm eff}$ with GC color, although the red-peak GCs have a median $R_{\rm eff}$ smaller by $11 \pm 8\%$ than the blue-peak GCs.

However, we did find a significant $(4\,\sigma)$ trend of $R_{\rm eff}$ with galactocentric radius. In this respect, NGC 1533 is more like the Milky Way than the Virgo early-type galaxies. This may be an effect of the environment: since the sizes of the GCs are limited by the tidal field, and the density gradients will be steeper in small groups such as Dorado or the Local Group, GC sizes should have a stronger dependence on radius in such environments. The dominance of this radial effect may weaken or obscure any relation between size and color. More studies of size and color trends for the GCs of galaxies in loose groups are needed to verify this hypothesis, although this may be difficult because of the low GC populations in such systems. We then used the median half-light GC radius to obtain another estimate of the distance to NGC 1533. Following Jordán et al. (2005), we find $d = 18.6 \pm 2.0$ Mpc, in good agreement with

the SBF distance.

We modeled the I_{814}-band GCLF of NGC 1533 as a Gaussian using a maximum likelihood fitting routine. The best-fit peak magnitude $m_I^0 = 22.84^{+0.18}_{-0.24}$ corresponds to $M_I^0 \approx -8.6$ for the measured SBF distance, in good agreement with expectations based on other galaxies. The fitted Gaussian dispersion of $\sigma_{\rm LF} = 1.10 \pm 0.15$ mag is in accord with the relation between $\sigma_{\rm LF}$ and galaxy luminosity found recently by Jordán et al. (2006) for Virgo galaxies. Finally we estimate the GC specific frequency in the analysis region to be $S_N = 1.3 \pm 0.2$, typical for a disk galaxy. We conclude that the GCs in NGC 1533 have the same average size, color, and luminosity within the errors as the Virgo early-type galaxies, but the stronger dependence of size on galactocentric distance is more reminiscent of the Milky Way.

NGC 1533 represents an interesting class of transitional objects, both in terms of morphology and environment. A large, multi-band, systematic study of such systems with *HST*, similar to the ACS Virgo and Fornax Cluster surveys but focusing on group galaxies, has yet to be undertaken and must await either a revived ACS or Wide Field Camera 3. Such an effort would be extremely valuable in piecing together a more complete picture of the interplay between galaxy structure, globular cluster system properties, and environment.

Bibliography

[1] Ajhar, E. A., Lauer, T. R., Tonry, J. L., Blakeslee, J. P., Dressler, A., Holtzman, J. A., & Postman, M. 1997, AJ, 114, 626

[1] Ashman, K. M., Bird, C. M., & Zepf, S. E. 1994, AJ, 108, 2348

[1] Ashman, K. M., & Zepf, S. E. 1998, Globular Cluster Systems (New York: Cambridge University Press)

[4] Beers, T. C., Flynn, K., & Gebhardt, K. 1990, AJ, 100, 32

[8] Benítez, N., et al. 2004, ApJS, 150, 1

[6] Bernardi, M., Alonso, M.V., da Costa L.N., Willmer, C.N.A., Wegner, G., Pellegrini, P.S., Rité, and Maia, M.A.G. 2002, AJ, 123, 2990

[4] Bertin, E., & Arnouts, S. 1996, A&AS, 117, 393

[8] Blakeslee, J. P., Ajhar, E. A., & Tonry, J. L. 1999, Post-Hipparcos Cosmic Candles, 237, 181

[4] Blakeslee, J. P., Anderson, K. R., Meurer, G. R., Benítez, N., & Magee, D. 2003, Astronomical Data Analysis Software and Systems XII, 295, 257

[10] Blakeslee, J. P., Lucey, J. R., Tonry, J. L., Hudson, M. J., Narayanan, V. K., & Barris, B. J. 2002, MNRAS, 330, 443

[11] Blakeslee, J. P., Vazdekis, A., & Ajhar, E. A. 2001, MNRAS, 320, 193

[12] Brown, T. M., et al. 2005, AJ, 130, 1693

[13] Buta, R., Corwin, H., & Odewahn, S. 2006, The De Vaucouleurs Atlas of Galaxies (Cambridge: Cambridge Univ. Press)

[14] Cantiello, M., Blakeslee, J. P., Raimondo, G., Mei, S., Brocato, E., & Capaccioli, M. 2005, ApJ, 634, 239

[15] Cantiello, M., Raimondo, G., Brocato, E., & Capaccioli, M. 2003, AJ, 125, 2783

[16] Cantiello, M., Raimondo, G., Blakeslee, J. P., Brocato, E., & Capaccioli, M. 2007, ApJ, 662, 940

[17] Côté, P., Blakeslee, J.P., Ferrarese, L., Jordán, A., Mei, S., Merritt, D., Milosavljević, M., Peng, E.W., Tonry., J.L., & West, M.J. 2004, ApJS, 153, 223

[de Vaucouleurs et al. 1991] de Vaucouleurs, G., de Vaucouleurs, A., Corwin, H. G., Jr., Buta, R. J., Paturel, G., & Fouqué, P. 1991, Third Reference Catalog of Bright Galaxies (New York: Springer-Verlag) (RC3)

[18] Ferguson, H.C., & Sandage, A. 1990, AJ, 100, 1

[19] Ferrarese, L., et al. 2006, ApJS, 164, 334

[20] Firth, P., Evstigneeva, E.A., Jones, J.B., Drinkwater, M.J., Phillips, S., & Gregg, M.D. 2006, MNRAS, 372, 1856

[21] Freedman, W. L., et al. 2001, ApJ, 553, 47

[Gebhardt & Kissler-Patig 1999] Gebhardt, K. & Kissler-Patig, 1999, AJ, 118, 1526

[22] Harris, W. E. 2001, Saas-Fee Advanced Course 28: Star Clusters, 223

[10] Harris, W. E., & van den Bergh, S. 1981, AJ, 86, 1627

[12] Harris, W. E., Whitmore, B. C., Karakla, D., Okoń, W., Baum, W. A., Hanes, D. A., & Kavelaars, J. J. 2006, ApJ, 636, 90

[25] Jedrzejewski, R. I. 1987, MNRAS, 226, 747

[26] Jensen, J. B., Tonry, J. L., & Luppino, G. A. 1998, ApJ, 505, 111

[27] Jones, D.H., Saunders, W., Read, M., & Colless, M. 2005, PASA, 22, 277

[27] Jordán, A., et al. 2004, ApJS, 154, 509

[29] Jordán, A., et al. 2005, ApJ, 634, 1002

[30] Jordán, A., et al. 2006, ApJ, 651, L25

[31] Jordán, A., Blakeslee, J.P., Côté, P., Ferrarese, L., Infante, L., Mei, S., Merritt, D., Peng, E.W., Tonry., J.L., & West, M.J. 2007, ApJS, 169, 213

[32] Jorgensen, I. 1997, MNRAS, 288, 161

[33] Kilborn, V. A., Koribalski, B. S., Forbes, D. A., Barnes, D. G., & Musgrave, R. C. 2005, MNRAS, 356, 77

[34] Kissler-Patig, M., & Gebhardt, K. 1999, Astronomische Gesellschaft Meeting Abstracts, 15, 1

[35] Kundu, A., & Whitmore, B. C. 2001, AJ, 122, 1251

[14] King, I. 1962, AJ, 67, 471

[krist2003] Krist, J. 2003, ISR ACS-2003-06 (Baltimore: STScI)

[30] Larsen, S. S. 1999, A&AS, 139, 393

[Larsen & Richtler 2000] Larsen, S.S., & Richtler, T. 2000, A&A, 354, 836

[38] Larsen, S. S., Forbes, D. A., & Brodie, J. P. 2001, MNRAS, 327, 1116

[39] Laurikainen, E., Salo, H., Buta, R., Knapen, J., Speltincx, T., & Block, D. 2006, AJ, 132, 2634

[40] Liu, M. C., Charlot, S., & Graham, J. R. 2000, ApJ, 543, 644

[41] Mei, S., et al. 2005, ApJS, 156, 113

[42] McLachlan, G. J., & Basford, K. E. 1988, Mixture models. Inference and applications to clustering (Statistics: Textbooks and Monographs, New York: Dekker, 1988)

[43] Maoz, D., Barth, A.J., Sternberg, A., Filippenko, A.V., Ho, L.C., Macchetto, F.D., Rix, H.-W., & Schneider, D.P. 1996, AJ, 111, 2248

[44] Meurer, G.R., Heckman, T.M., Leitherer, C., Kinney, A., Robert, C., & Garnett, D.R. 1995 AJ, 110, 2665

[45] Meurer, G. R., et al. 2006, ApJS, 165, 307

[14] Mieske, S., et al. 2006, ApJ, 653, 193

[37] Peng, C. Y., Ho, L. C., Impey, C. D., & Rix, H. 2002, AJ, 124, 266

[9] Peng, E. W., et al. 2006, ApJ, 639, 95

[10] Ryan-Weber, E. V., et al. 2004, AJ, 127, 1431

[50] Sandage, A., & Brucato, R. 1979, AJ, 84, 472

[13] Schlegel, D. J., Finkbeiner, D. P., & Davis, M. 1998, ApJ, 500, 525

[52] Secker, J. 1992, AJ, 104, 1472

[40] Sérsic, J. L. 1968, Cordoba, Argentina: Observatorio Astronomico, 1968

[41] Sirianni, M., et al. 2005, PASP, 117, 1049

[45] Tonry, J. L., Blakeslee, J. P., Ajhar, E. A., & Dressler, A. 1997, ApJ, 475, 399

[56] Tonry, J. L., Dressler, A., Blakeslee, J. P., Ajhar, E. A., Fletcher, A. B., Luppino, G. A., Metzger, M. R., & Moore, C. B. 2001, ApJ, 546, 681

[57] van den Bergh, S., Morbey, C., & Pazder, J. 1991, ApJ, 375, 594

[58] West, M. J., Côté, P., Marzke, R. O., & Jordán, A. 2004, Nature, 427, 31

[59] Whitmore, B.C., & Schweizer, F. 1995, AJ, 109, 960

[60] Whitmore, B.C., Zhang, Q., Leitherer, C., Fall, S.M., Schweizer, F., & Miller, B.W. 1999, AJ, 118, 1551

Chapter 3

Ultra-Compact Dwarf Candidates Near the Lensing Galaxy in Abell S0740

This chapter was published under the same title in *The Astrophysical Journal*, Vol136, Issue 6, pp 2295-2305, (2008). The work presented in Chapter 3 was undertaken in collaboration with Dr. John Blakeslee.

Synopsis

We analyze three-band imaging data of the giant elliptical galaxy ESO 325-G004 from the *Hubble Space Telescope* Advanced Camera for Surveys (ACS). This is the nearest known strongly lensing galaxy, and it resides in the center of the poor cluster Abell S0740 at redshift $z = 0.034$. Based on magnitude, color, and size selection criteria, we identify a sample of 15 ultra-compact dwarf (UCD) galaxy candidates

within the ACS field. This is comparable to the numbers of UCDs found within similar regions in more nearby clusters (Virgo, Fornax, Hydra). We estimate circular half-light radii $R_{e,c}$ from 2-D Sérsic and King model fits and apply an upper cutoff of 100 pc for our UCD selection. The selected galaxies have typical Sérsic indices $n \approx 1.5$, while larger sources with $R_{e,c} > 100$ pc are more nearly exponential, perhaps indicating that the latter are dominated by background disk galaxies. Many of the UCD candidates are surrounded by a faint "fuzz" of halo light, which may be the remnants of stripped material, and there is some evidence for intrinsic flattening of the UCDs themselves. An apparent separation in size between the most compact UCDs with $R_{e,c} < 17$ pc and larger ones with $R_{e,c} > 40$ pc may hint at different formation mechanisms. We do not find any M32 analogues in this field. The colors of the UCD candidates span the range from blue to red globular clusters, although the brightest ones are predominantly red. The UCD candidates follow the flattened, elliptical distribution of the globular clusters, which in turn follow the galaxy halo light, suggesting a common evolution for these three components. Planned follow-up spectroscopy can determine which candidates are truly members of Abell S0740 and how similar they are in distribution to the globulars.

3.1 Introduction

A new class of stellar system has emerged in recent years. Due to the size of these objects, being larger than average globular clusters (GCs) and smaller than dwarf galaxies, they have been dubbed ultra-compact dwarf galaxies, or UCDs (Phillips et al. 2001). They are typically a few $\times 10^7$ $M_\odot$ in mass, with effective radii in the range 10-100 pc. First discovered in the Fornax Cluster (Hilker et al. 1999; Drinkwater et al. 2000), UCDs have now been found in significant numbers in the Virgo, Centaurus, and Hydra clusters (Haşegan et al. 2005; Mieske et al 2007; Wehner & Harris 2007), all systems within ~ 50 Mpc of the Local Group. They are apparently very rare outside of galaxy clusters (Evstigneeva et al. 2007b).

As they have absorption line spectra and appear to be transitional between GCs

and early-type dwarfs (cf. Haşegan et al. 2005), there are two basic ideas for the nature of UCDs: they are related to globulars, or to dwarf galaxies. More specifically, UCDs may be the largest members of the rich GC populations found inside galaxy clusters (Mieske et al. 2002), possibly growing to such large size through dissipational merging early in their lifetimes (Fellhauer & Kroupa 2002). Or, they may be the small, tidally stripped remains of nucleated dwarf galaxies on orbits that carried them too close to the center of the cluster potential (Bekki et al. 2001; Drinkwater et al. 2003). This latter explanation has come to be known as galaxy "threshing," but the idea has been around for many years. Bassino et al. (1994) numerically simulated the evolution of nucleated dwarfs in Virgo and showed that stripped nuclei could constitute a large fraction of M87's very rich GC system, while larger UCD-like remnants would occur farther out. Recent *Hubble Space Telescope* (*HST*) imaging has revealed nuclei in a much higher percentage of Virgo early-type dwarfs than previously thought (Côté et al. 2006). Thus, stripping of nucleated dwarfs may account for both UCDs and many of the GCs in the center of cluster potentials.

Some evidence based on the color-magnitude sequence of UCDs suggests that they may be an extension of the red GC component to brighter magnitudes (Wehner & Harris 2007). The UCDs in the Virgo and Fornax clusters also have spectroscopic metallicities and α-element enhancements consistent with their being the high-mass mass extreme of the red GC population (Evstigneeva et al. 2007a; Mieske et al. 2006), and less consistent with simple versions of the threshing model. Estigneeva et al. (2008) attempted to distinguish between the two formation scenarios on the basis of the structural properties of UCDs in the nearby Virgo and Fornax clusters measured using the *HST* High Resolution Channel. Even with such high resolution measurements, the data were consistent with either explanation, although more detailed predictions of the size evolution of the nuclei during threshing are needed to test this scenario. The relatively low velocity dispersions of cluster UCD populations are expected in either model (e.g., Bekki 2007). However, detailed comparison between the spatial distributions of large samples of UCDs and their possible nucleated dwarf progenitors in clusters may help uncover their evolutionary histories (e.g., Goerdt et al. 2008; Thomas et al. 2008).

Given the difficulty in distinguishing between the formation scenarios, further UCD surveys can provide valuable information on the properties of this new type of stellar system. A larger sample of groups and clusters is especially useful for constraining environmental effects on the formation of UCDs. Here, we present a search with *HST* for UCD candidates near ESO 325-G004, the central giant elliptical in Abell S0740. This is one of the systems in the supplementary list of poor clusters tabulated by Abell et al. (1989) that did not meet the lowest richness criteria of the original Abell (1958) catalogue. The cluster velocity dispersion is only ~ 300 km s^{-1} (see plot in Smith et al. 2005), similar to that of Fornax, where UCDs were first discovered. The absolute V magnitude of ESO 325-G004 is $M_V = -23.2$, making it about 60% more luminous than M87, or 2.5 times the luminosity of NGC 1399 in Fornax. At $z = 0.034$, ESO 325-G004 is also the closest known gravitational lens and has both dynamical and lensing mass estimates (Smith et al. 2005). This makes it an interesting target for UCD searches, since it is a very massive, dominant elliptical in a poor cluster or rich group environment.

The following section describes our data in detail. In § 3.3, we present our photometric and size measurements and discuss the selection of UCD candidates. The properties of the UCD candidates are discussed in § 3.4 and compared with those of GCs and other objects in the field. The final section summarizes the results. Throughout this paper, we use the WMAP 3-year cosmology results (Spergel et al. 2007) and assume a distance modulus for ESO 325-G004 of $(m-M) = 35.78$ mag, or a luminosity distance of 143 Mpc, and an angular scale of 0.65 kpc arcsec^{-1}. This translates to an image scale of about 33 pc pix^{-1} for our observations with Advanced Camera for Surveys Wide Field Channel (ACS/WFC).

3.2 Observations and Reductions

ESO 325-G004 was imaged with the ACS/WFC in the F475W, F625W, and F814W filters. Throughout this paper, we refer to magnitudes in these filters as g_{475}, r_{625}, and I_{814}, respectively. The galaxy was initially observed in F814W and F475W as part of

HST GO Program 10429 during January 2005. This program, which is conducting a surface brightness fluctuation survey in the Shapley supercluster region, is described in Blakeslee (2007). There were 22 F814W exposures of varying times totaling of 18,882 s, and three exposures in F475W of 367s each. In February 2006, further imaging of the ESO 325-G004 field was carried out by *HST* DD Program 10710 for a Hubble Heritage public release image.[1] This provided six additional exposures in each of the F475W and F625W filters. The total exposure times for this field were therefore 5901, 4650, and 18882 s in F475W, F625W, and F814W, respectively.

The images were processed with the Apsis pipeline (Blakeslee et al. 2003) to produce summed, geometrically corrected, cosmic ray cleaned images for each bandpass. Figure 3.1 shows a color composite image constructed from the data in the three bandpasses. Apsis corrects the astrometric zero point of the images to within an uncertainty of about $0\farcs1$. It also produces an RMS image giving the total noise for each pixel. We calibrated the photometry using the Vega-based ACS/WFC zero points for each filter from Sirianni et al. (2005): $m_{g475} = 26.168$, $m_{r625} = 25.731$, and $m_{I814} = 25.501$. We corrected the photometry for Galactic extinction using $E(B-V) = 0.0605$ mag (Schlegel et al. 1998) and the extinction ratios from Sirianni et al. (2005). We find the following extinction corrections in each band: $A_{475} = 0.217$ mag, and $A_{625} = 0.159$ mag, and $A_{814} = 0.109$ mag.

We modeled the main galaxy ESO 325-G004 using the elliprof software (Tonry et al. 1997), as well as several of the other smaller galaxies in the field to obtain a better fit. The small galaxy models were subtracted from the image, and bright stars, diffraction spikes, and other galaxies were masked so a final model of ESO 325-G004 could be made. This final model was then subtracted to create a residual image, which was used to find sources with the object detection software SExtractor (Bertin & Arnouts 1996). We used the Apsis RMS image, which includes the noise from the subtracted galaxies, for the SExtractor detection weighting. To the F814W RMS image, we also added additional noise to account for the galaxy surface brightness fluctuations, as described in more detail by Jordán et al. (2004) and Barber DeGraaff

[1] http://heritage.stsci.edu/2007/08/index.html

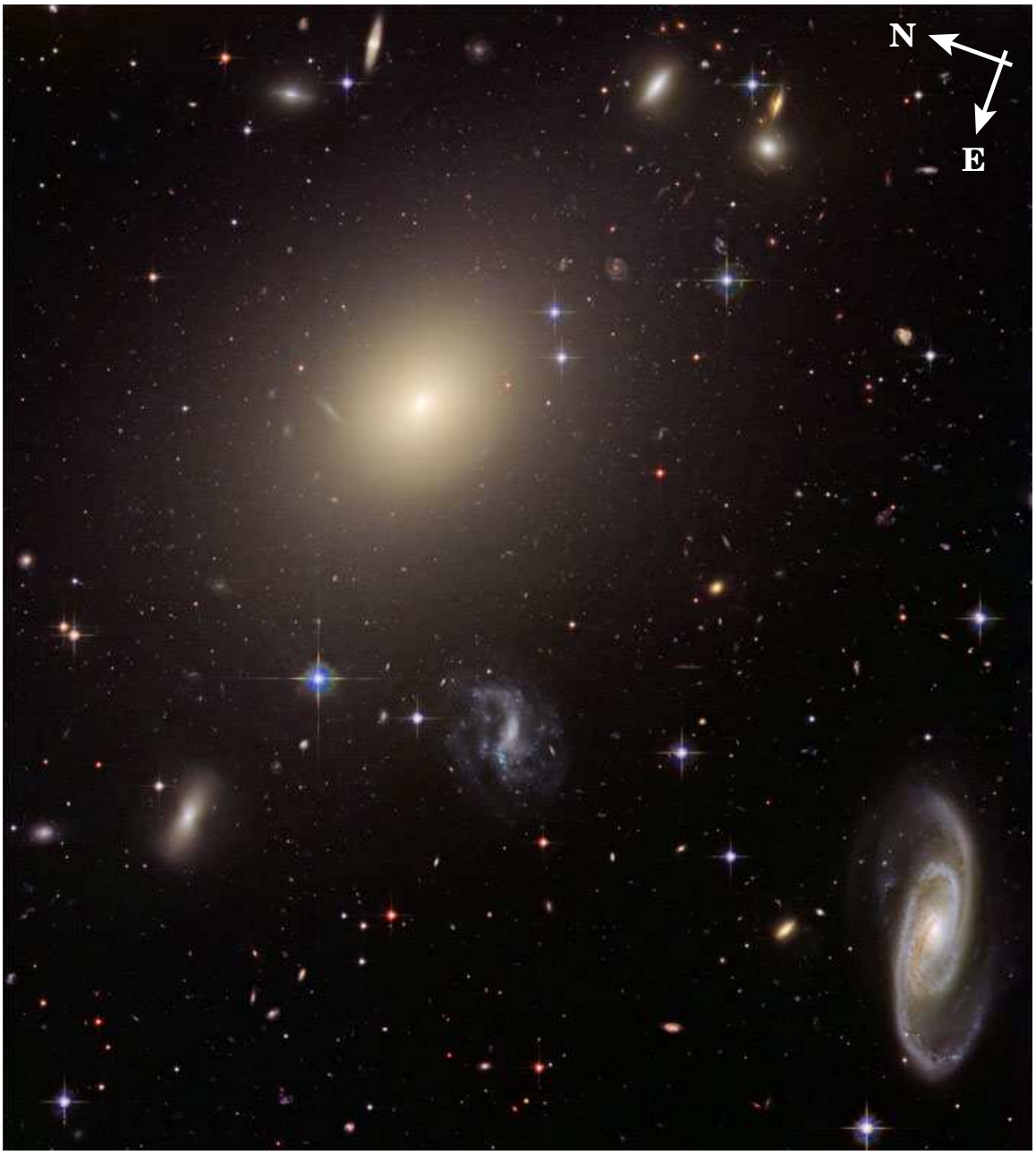

Figure 3.1 *Hubble Space Telescope* ACS/WFC image of ESO 325-G004, showing about $3\farcm0 \times 3\farcm3$ of the field at the observed orientation. This color composite was constructed by the Hubble Heritage Team (STScI/AURA) from our imaging in the F475W (g), F625W (r), and F814W (I) bandpasses.

et al. (2007). We used SExtractor in "dual image mode" with the much deeper F814W image as the detection image in each case, and individual filter images used for the photometry. This ensures that the same object centroids and measurement apertures are used for all the images, resulting in the most accurate color measurements (see Benítez et al. 2004). We adopt the SExtractor MAG_AUTO value for the total I_{814} magnitude and isophotal magnitudes to measure galaxy colors.

3.3 Sample Selection

3.3.1 Color and Magnitude Cuts

In order to search for UCDs in this field, we first applied cuts in color and magnitude to select a list of objects for size and shape measurements. Large numbers of GCs are visible in the image, but we expect the turnover, or peak luminosity, of the GC luminosity function (GCLF) to occur near $I_{814} \approx 27.5$. Therefore, only $\sim 1\%$ of the GCs should have magnitudes $I_{814} < 24$, which is about $2.7\,\sigma$ brighter than GCLF peak, and we chose $I_{814} = 24$ as the faint limit for UCD candidates. This corresponds to an absolute V magnitude $M_V \approx -10.8$, which typically marks the transition between GCs and UCDs (e.g., Haşegan et al. 2005). However, we performed the surface photometry fits and size measurements described below to a limit one magnitude fainter than this.

To derive color cuts, we calculated the color evolution for Bruzual & Charlot (2003) simple stellar population (SSP) models in the observed bandpasses at $z = 0.034$, as well as the colors of empirical galaxy templates from Benítez et al. (2004) and NGC 4889 in the Coma cluster, which we use as a template cD galaxy. Figure 3.2 shows the results of these calculations. The broader baseline ($g_{475}-I_{814}$) has more discriminating power, and we use it for our more stringent color selection criterion: $1.3 < (g_{475}-I_{814}) < 2.0$, which corresponds to $0.85 < V-I < 1.35$, based on the models. This range includes the photometrically transformed colors of *all* confirmed UCDs from previous studies (e.g., Mieske et al. 2004b, 2007; Haşegan et al. 2005,

Evstigneeva et al. 2008). The color cut spans the range from Sc-type spirals to the reddest giant ellipticals, and from intermediate age, very metal-poor models to metal-rich models. Note that the models do not include alpha-enhancement, and the absolute metallicity scale should be viewed as approximate; the empirical templates are the more useful comparison.

Additionally, we require $0.4 < (r_{625} - I_{814}) < 0.9$, a broad cut which simply ensures that the objects have reasonable colors for a galaxy at this redshift. We also attempted to use our multi-band imaging data to estimate photometric redshifts as part of the selection criteria, similar to Mieske et al. (2004a) who searched for UCD-like objects in the more distant cluster Abell 1689 and had the benefit of a fourth bandpass. However, we found that the photometric redshifts based on just these three bands were not very robust for objects in this low-redshift cluster. We therefore decided to use the simple color cuts highlighted in Figure 3.2. No additional objects would be included in our final sample of best UCD candidates if we relaxed the $(g_{475} - I_{814})$ color cut to a very red limit of 2.2.

The color-magnitude diagrams in Figure 3.3 illustrate our adopted photometric cuts as applied to the sample of objects detected in the ESO 325-G004 field. Figure 3.4 shows the color cuts in the $(r_{625} - I_{814})$ versus $(g_{475} - I_{814})$ plane for all objects with $I_{814} < 25$. We plot both the complete sample of objects (left panel), and the subset with SExtractor CLASS_STAR parameter greater than 0.85 (very compact or stellar objects; right panel). Although we do not use CLASS_STAR as a selection criterion, comparison of the plots indicates the location in this diagram of the likely GCs and UCD candidates.

3.3.2 Size and Shape Measurements

To measure object sizes, we used the programs Ishape (Larsen 1999) and Galfit (Peng et al. 2002) to model the 2-D profiles of objects in the very deep F814W image. Ishape is designed for modeling the light distributions of marginally resolved sources such as extragalactic GCs, while Galfit is intended for modeling resolved galaxy light distributions. It therefore seemed fitting to use both in a search for UCDs, which

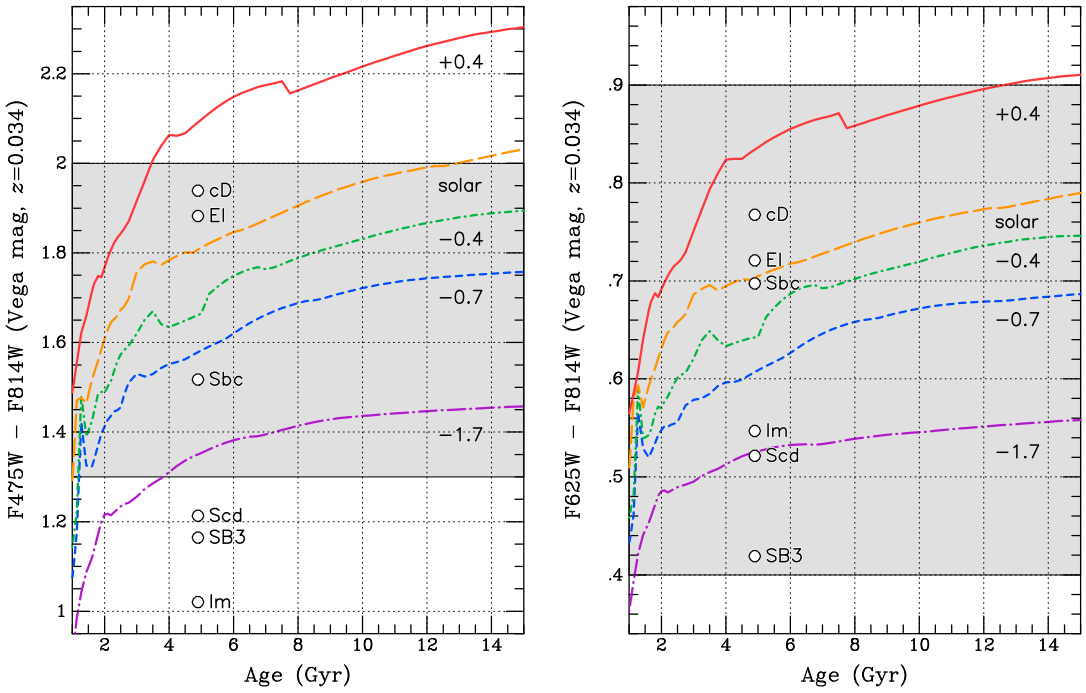

Figure 3.2 Predicted age evolution in the observed ACS colors at redshift z=0.034 for Bruzual & Charlot (2003) single-burst stellar population models with five different metallicities, labeled by their [Fe/H] values. We also show the expected colors at this redshift for six different empirical galaxy templates (see text) with arbitrary placement along the horizontal axis. The shaded areas delineate the color selection criteria for the UCD candidates. The broader baseline ($g_{475}-I_{814}$) color is used for the more stringent selection cut, based on the expected range of stellar populations in UCDs. The less-sensitive ($r_{625}-I_{814}$) cut is simply to ensure the objects have reasonable colors for galaxies at this redshift.

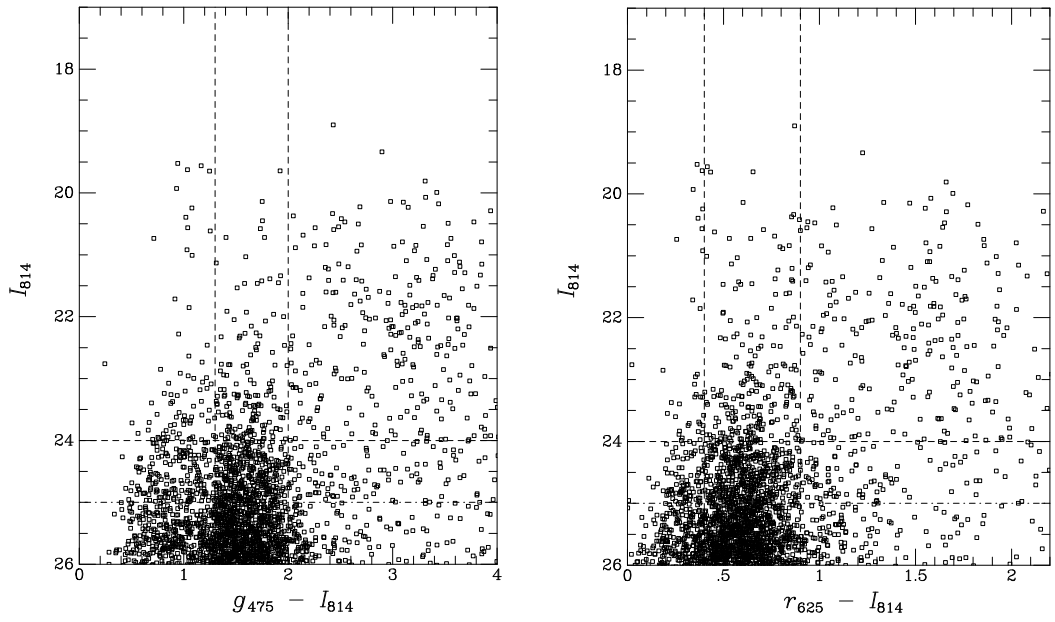

Figure 3.3 Color-magnitude diagrams for all objects detected in our images down to $I_{814} = 26$. The vertical dashed lines show the color cuts from Figure 3.2. The horizontal dashed line at $I_{814} = 24$ shows the faint limit we impose for UCD candidates; fainter than this, the objects at these colors are mainly globular clusters in ESO 325-G004. The dot-dashed horizontal line at $I_{814} = 25$ is the limit we use for the 2-D surface photometry fits.

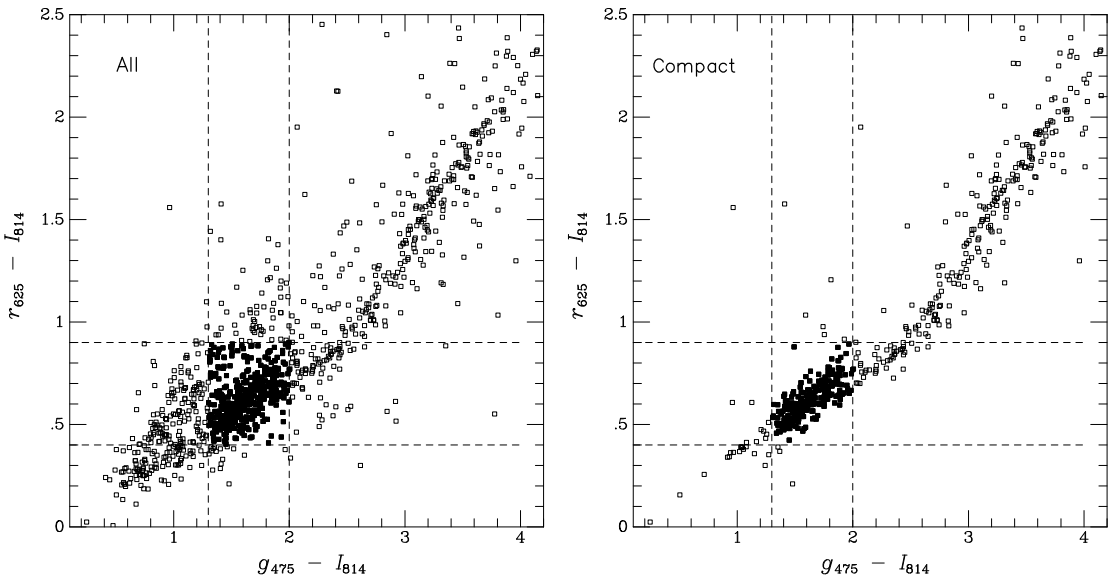

Figure 3.4 Color-color diagram of $r_{625}-I_{814}$ versus $g_{475} - I_{814}$ for objects in the ESO 325-G004 field with $17 < I_{814} < 25$ (the limit for the 2-D surface photometry fits). The left panel shows all objects in this magnitude range, while the right panel shows "compact" objects, having the SExtractor parameter CLASS_STAR > 0.85. We do not select based on CLASS_STAR, but the comparison illustrates the difference between "extended" and "compact" object sequences. The latter includes globular clusters and distant background objects, as well as stars. The color selection for the UCD candidates is delineated by the intersection of the horizontal and vertical dashed lines: $0.4 < r_{625} - I_{814} < 0.9$ and $1.3 < g_{475} - I_{814} < 2.0$, and solid points are used for objects within this region.

straddle the range between GCs and dwarf galaxies. For the Ishape fits, we used the "KING30" profile, a King (1962) model with concentration parameter $c = 30$, which works well for marginally resolved GCs (e.g., Larsen & Brodie 2000). For Galfit, we used a single Sérsic (1968) model, which has one more degree of freedom than KING30. Both programs are quite robust, with typical errors of 10-15% for compact but high signal-to-noise sources such as we have here (see Blakeslee et al. 2006; Barber DeGraaff et al. 2007). We fitted elliptical models, and use the circularized effective radius $R_{e,c} = R_e\sqrt{q} = R_e\sqrt{1-\epsilon}$, where R_e is the effective radius along the major axis, q is the fitted axis ratio, and ϵ is the ellipticity.

We modeled all objects in the field with $17 < I_{814} < 25$, within the color ranges given in § 3.3.1, and with SExtractor Kron radius $\leq$ 30 pix (1 kpc). The Kron radius selection removes objects much larger than the UCD and compact elliptical candidates that we are interested in; it should not exclude any objects in Abell S0740 with Sérsic-like profiles and half light radii below $\sim$500 pc (see Graham & Driver 2005). Figure 3.5 shows the magnitude-size diagrams using the $R_{e,c}$ values from Galfit (left panel) and Ishape (right panel), converted to parsecs using the adopted distance. The two panels are similar in overall appearance, except Ishape resolves many objects with $R_{e,c} < 10$ pc (0.3 pix) that are not resolved by Galfit; these are probably mainly globular clusters. In both cases, there are about a dozen bright, unresolved objects ($I_{814} < 23$, $R_{e,c} = 0$) that are most likely stars.

Figure 3.6 shows a direct comparison of Galfit and Ishape sizes for objects with $I_{814} < 24$, the magnitude limit for our UCD candidate selection. To this limit, the agreement is quite good, apart from the objects unresolved by Galfit (the agreement worsens for fainter objects). Ishape does not do as well for the sizes of larger objects, because it has a limited fit radius of only a few pixels and overestimates the sizes of larger objects by about 50%. The two worst outliers among the objects that are resolved by both software packages are irregular objects: #2228 is a blended double source, and #575 is a bright clump within a larger edge-on galaxy. For the final list of object sizes, we adopted the Galfit $R_{e,c}$ measurement if it was greater than 2 pix (66 pc); otherwise, we used the Ishape value for $R_{e,c}$.

Figure 3.7 plots the Sérsic index n against $R_{e,c}$ from the Galfit Sérsic model fits.

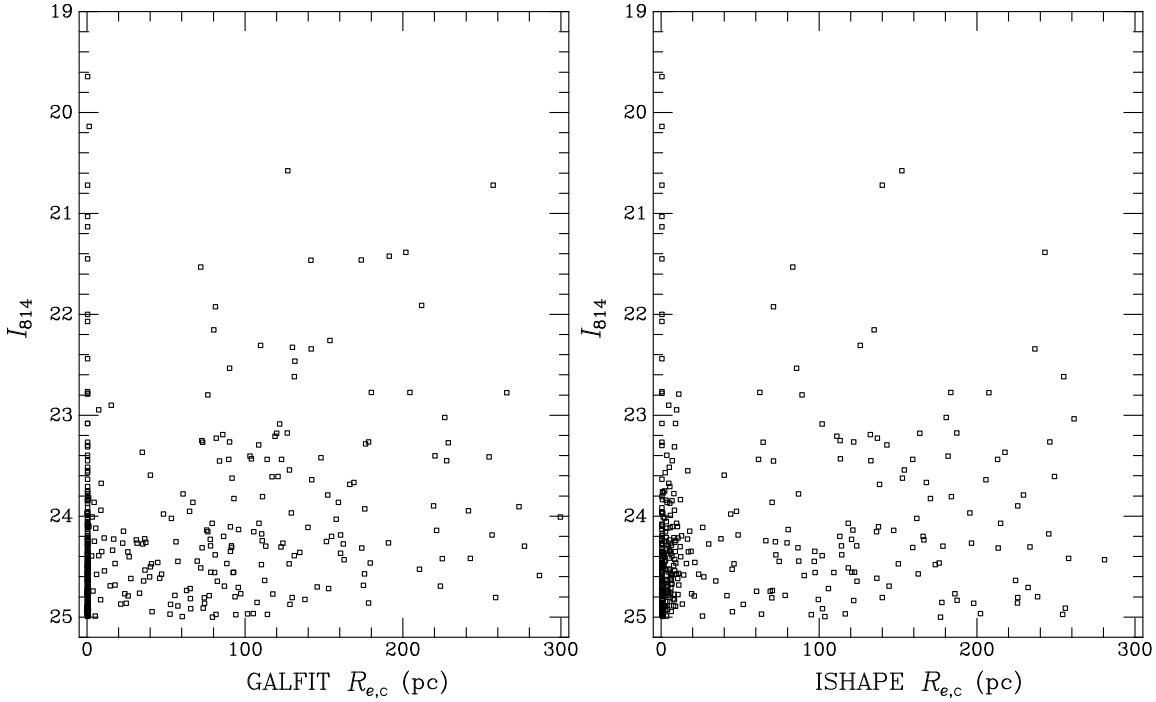

Figure 3.5 Magnitude-size diagrams for the selected sample of objects in the ESO 325-G004 field with $I_{814} < 25$ and the color cuts given in the preceding figures. We use SExtractor MAG_AUTO for I_{814} and circular half-light radii $R_{e,c}$ from the Galfit Sérsic model (left) and Ishape King model (right) fits. Note that $R_{e,c} = R_{e,c}\sqrt{1-\epsilon}$, where $R_{e,c}$ is the fitted half-light radius along the major axis, ϵ is the fitted ellipticity, and $(1-\epsilon)$ the axis ratio. The image scale at the distance of ESO 325-G004 is 33 pc pix^{-1}.

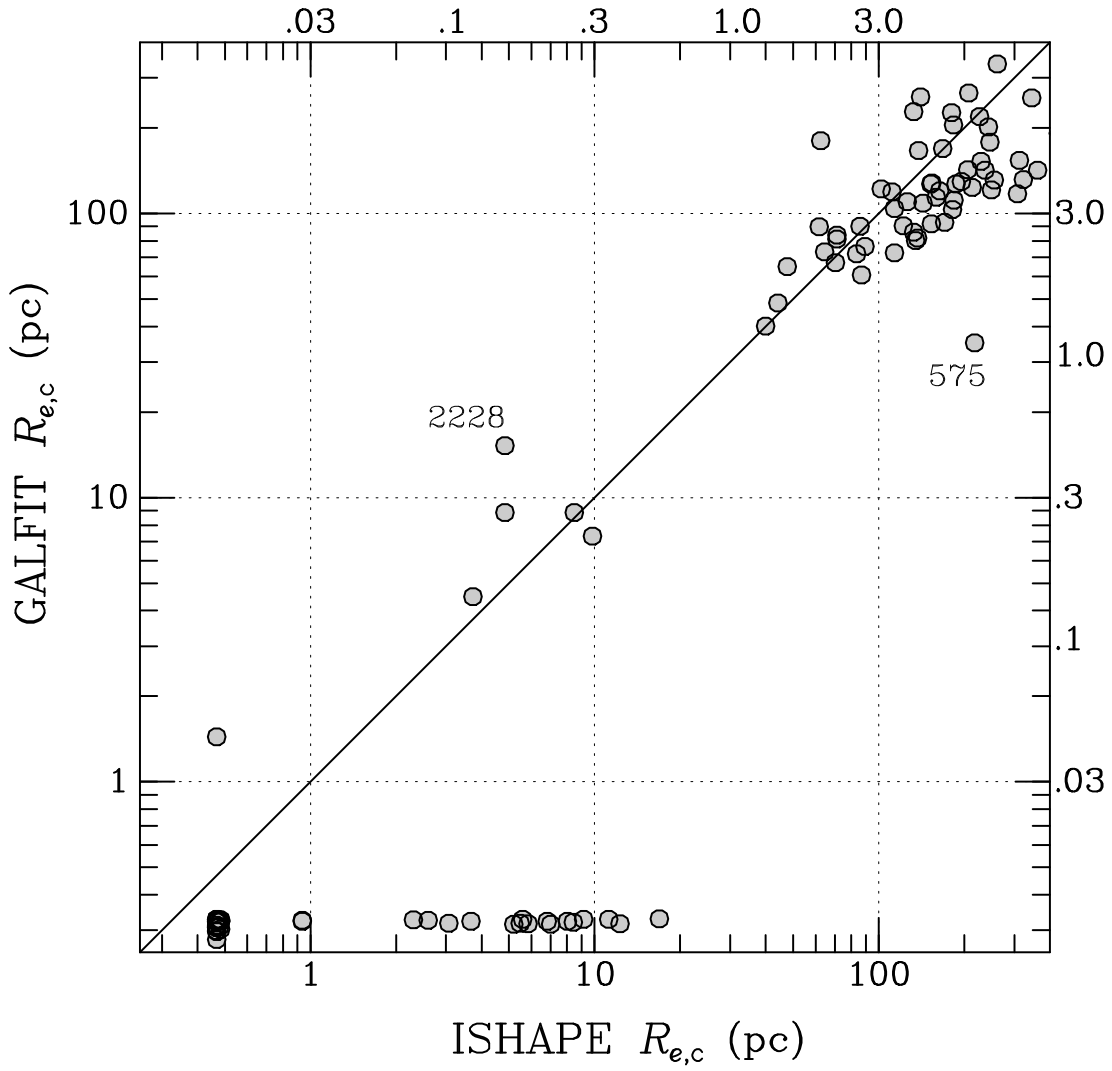

Figure 3.6 Comparison between the circular half-light radii $R_{e,c}$ found from the Galfit and Ishape fits for objects with $I_{814} < 24$, the magnitude limit for the UCD selection. Sizes in pixels are plotted along the right and top edges of the figure (assuming 33 pc per pixel). Ishape is designed for marginally resolved sources and can measure sizes for smaller objects, while Galfit can perform more detailed analyses of larger objects. Two moderate outliers are marked: 2228 is a blend of two objects and 575 is an edge-on galaxy having a bright subclump; the programs model different regions in these two composite sources. Otherwise, the two programs agree fairly well, with the exception of objects with $R_{e,c} \lesssim 10\,\mathrm{pc}$ (0.3 pix) which Galfit mostly fails to resolve.

Interestingly, the mean n value appears to be lower for objects with $R_{e,c} > 100$ pc. The biweight mean (to reduce the effect of outliers) is $\langle n \rangle = 1.47 \pm 0.15$ for objects with $R_{e,c}$= 10-100 pc, and $\langle n \rangle = 1.07 \pm 0.07$ for $R_{e,c} > 100$ pc, a 2.4-σ difference. (This includes all objects fitted by Galfit with sizes in this range, even when the Ishape model was used for the final size.) The biweight scatters in n for the two groups are 0.66 and 0.51, respectively. In comparison, the median Sérsic index for the 21 Virgo and Fornax UCDs analyzed by Evstigneeva et al. (2008) was 2.2, with a large range. There is a good correspondence between Sérsic indices measured by Galfit and morphological type (Blakeslee et al. 2006). Thus, Figure 3.7 may indicate that the larger objects in the ESO 325-G004 field are dominated by background galaxies with exponential profiles, while the ones in the 10-100 pc range include a sizable fraction of UCDs. Follow-up spectroscopy is necessary to confirm if this is actually the case.

3.4 Properties of UCD candidates

For the final sample of most likely UCD candidates, we select all objects with $I_{814} < 24$, $1.3 < (g_{475} - I_{814}) < 2.0$, $0.4 < (r_{625} - I_{814}) < 0.9$, $10\,\mathrm{pc} < R_{e,c} < 100\,\mathrm{pc}$, and $\epsilon < 0.5$ (to eliminate disks and other very elongated objects). Cut-out images of the 15 UCDs candidates meeting these criteria are displayed in Figure 3.8. We removed one object, #575, from the sample because it appears to be a subclump of a very elongated galaxy (although it could be a projection). All of the remaining UCD candidates appear to be genuine compact, but nonstellar, early-type galaxies having colors consistent with being members of Abell S0740. When examined closely, many of these objects also show a faint "fuzz" of halo light at radii $r > 4\ R_{e,c}$ and surface brightness levels $\mu_I \approx 24.0$-24.5 mag arcsec^{-1}, which is well in excess of PSF blurring effects.

In Figure 3.9, we show an additional set of 26 compact galaxies meeting all of the UCD selection criteria except that they have larger sizes in the range 100-300 pc; we also include object #575 in this figure. Although some of these galaxies appear simply to be larger UCD candidates, and we label these as compact ellipticals (cE), others

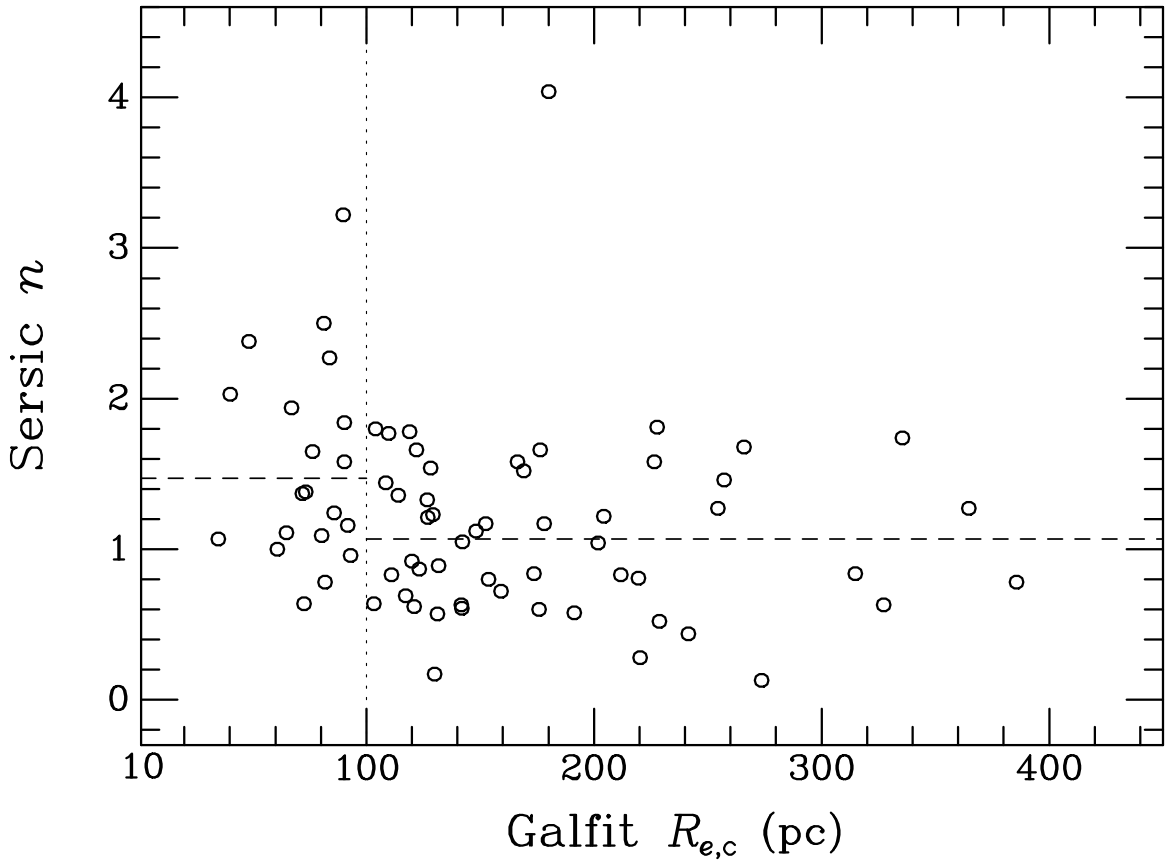

Figure 3.7 Sérsic index n is plotted against the circularized half light radius $R_{e,c}$ for the Galfit Sérsic model fits. The dashed lines show the biweight mean values of 1.47 ± 0.15 and 1.07 ± 0.07 for the objects with $10 < R_{e,c} < 100$ pc and $100 < R_{e,c} < 400$ pc, respectively.

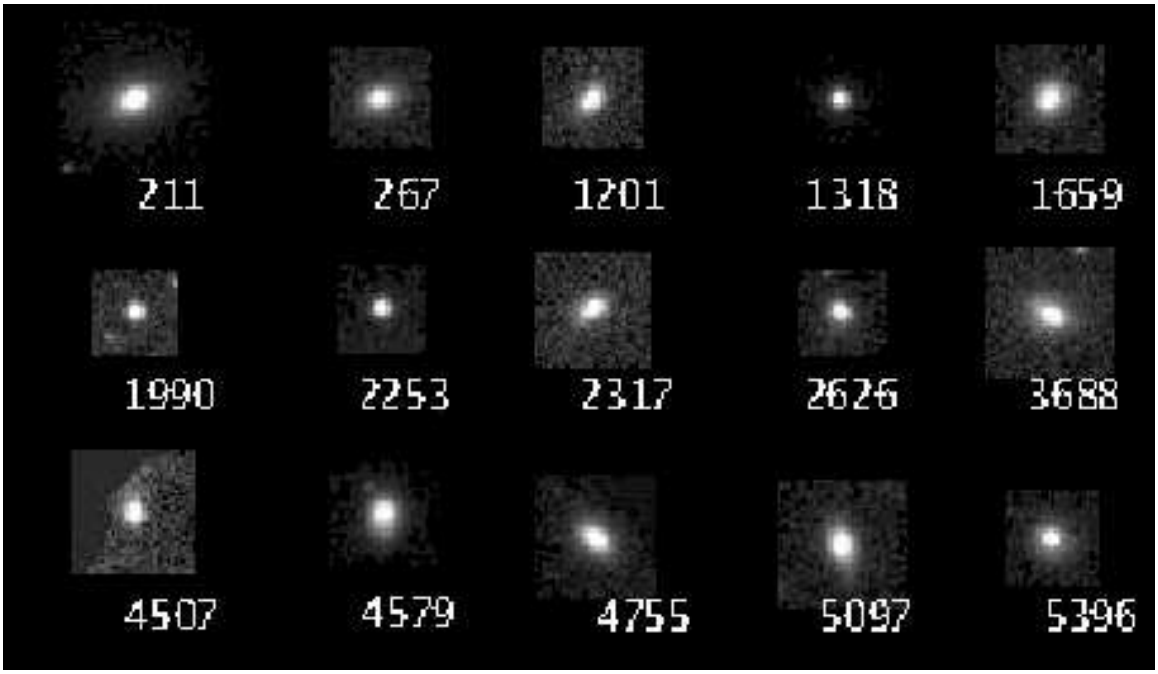

Figure 3.8 F814W band images of the candidate ultra-compact dwarf galaxies in the field of ESO 325-G004. These objects meet the color selection criteria, have $I_{814} < 24$, half-light radii in the range 10 to 100 pc, and ellipticity $\epsilon < 0.5$. One other source (575, shown in the following figure) ostensibly meeting these criteria was rejected as a subcomponent of an elongated edge-on galaxy. Faint halos of light are visible here around objects 211, 3688, 4579, and some others; most have such halo light when examined closely. Object 4507 is near the edge of a masked region.

are irregular galaxies, and a few appear to be small background spirals. Table 3.1 lists the positions, magnitudes, colors, and sizes of the 41 objects in Figures 3.8 and 3.9. Magnitudes and colors are corrected for extinction as described above. The last column of Table 3.1 reports our classifications for these objects as UCD (all objects in Fig. 3.8), cE, Sp (spiral), S0 (disky galaxy without obvious spiral structure), Irr (irregular), or clump (subcomponent of an irregular or interacting system).

The ellipticity distributions of the 15 UCD candidates and other objects in the field within the same magnitude and color ranges are shown in Figure 3.10. The UCDs have a mean $\epsilon = 0.32$ and a range from 0.16 to 0.46. The UCD sample selection excludes objects with $\epsilon > 0.5$, but it is interesting that none has $\epsilon \leq 0.15$. This may reflect intrinsic flattening in the UCDs, since there are many objects in the larger sample that are found to have lower ellipticity values.

Figure 3.11 shows the positions of the UCD candidates, larger compact galaxies, globular clusters candidates with $I_{814} < 25$, and other objects in the field meeting our color and magnitude cuts. Elliptical isophotes of ESO 325-G004 are also drawn at three radii. The galaxy is very regular. It has a mean ellipticity $\epsilon = 0.23 \pm 0.03$ and is oriented $45° \pm 2°$ counter-clockwise from the $+x$ direction in the observed frame, which translates to a position angle east of north of PA $= 66° \pm 2°$. (The errorbars reflect the rms scatter among the fitted isophotes from the galaxy modeling in Sec. 3.2.) A more detailed analysis of the GC population is in preparation, but we find a best-fit PA $= 71° \pm 20°$ for the GC distribution, in close agreement with the major axis of the galaxy isophotes. It is also noteworthy that 2/3 of the UCD candidates fall along the galaxy's major axis, within a region covering about 40% of the image. Although not statistically very significant, the UCD alignment along this direction suggests a link between the UCD and GC populations, and in turn with the stellar halo of the central elliptical. We ran a 2-D Kolmogorov-Smirnov test and found that the spatial distributions of the GCs and UCD candidates were at least consistent with being the same. It will be important to see what fraction of the UCDs lie along the major axis once a spectroscopically confirmed sample is available.

In the previous section, we examined the magnitude-size diagrams for the $R_{e,\mathrm{c}}$ values measured separately by Galfit and Ishape. Figure 3.12 presents our final

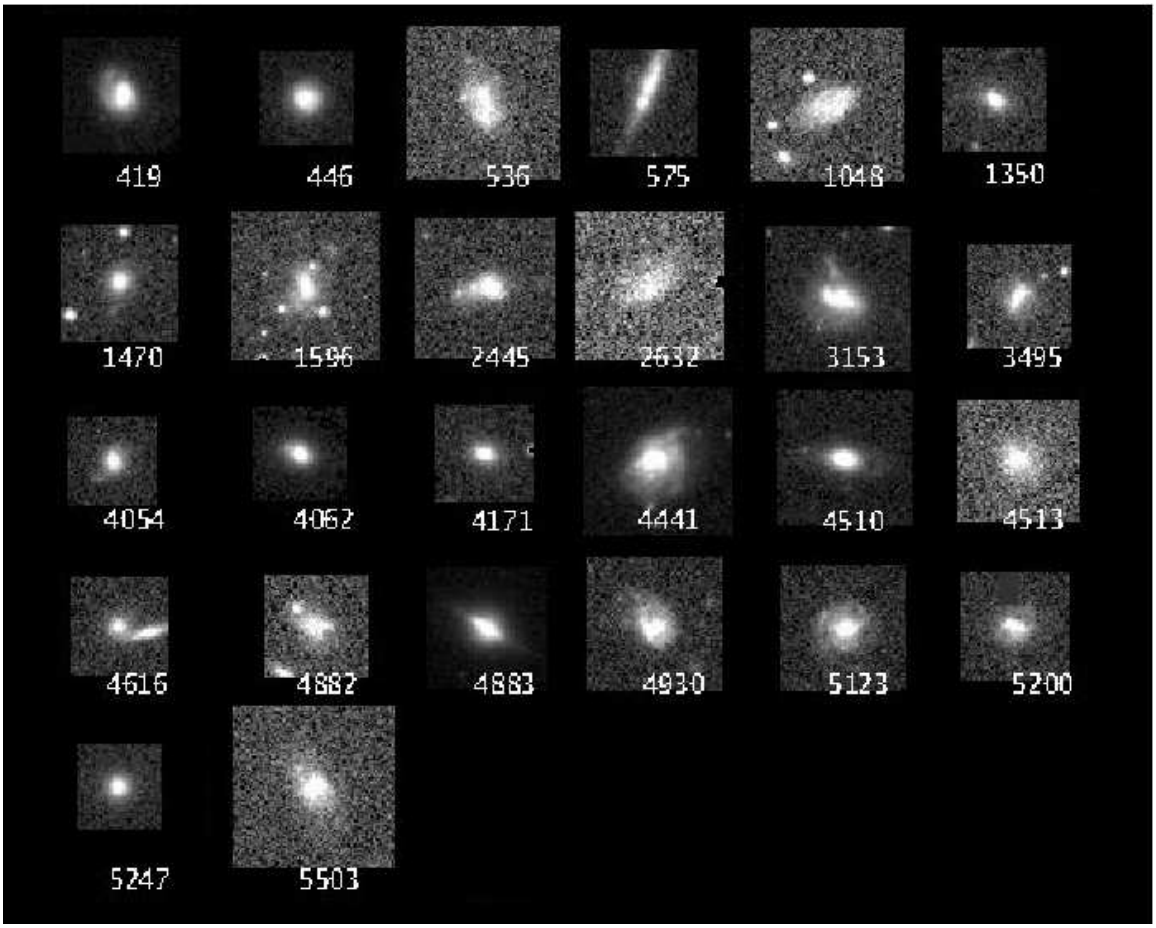

Figure 3.9 F814W band images of objects in the field of ESO 325-G004 meeting all the selection criteria for UCDs, except having slightly larger sizes in the range 100 to 300 pc (plus object 575, noted in the caption to Fig. 3.8). These objects are more irregular in appearance; some appear to be background spiral galaxies.

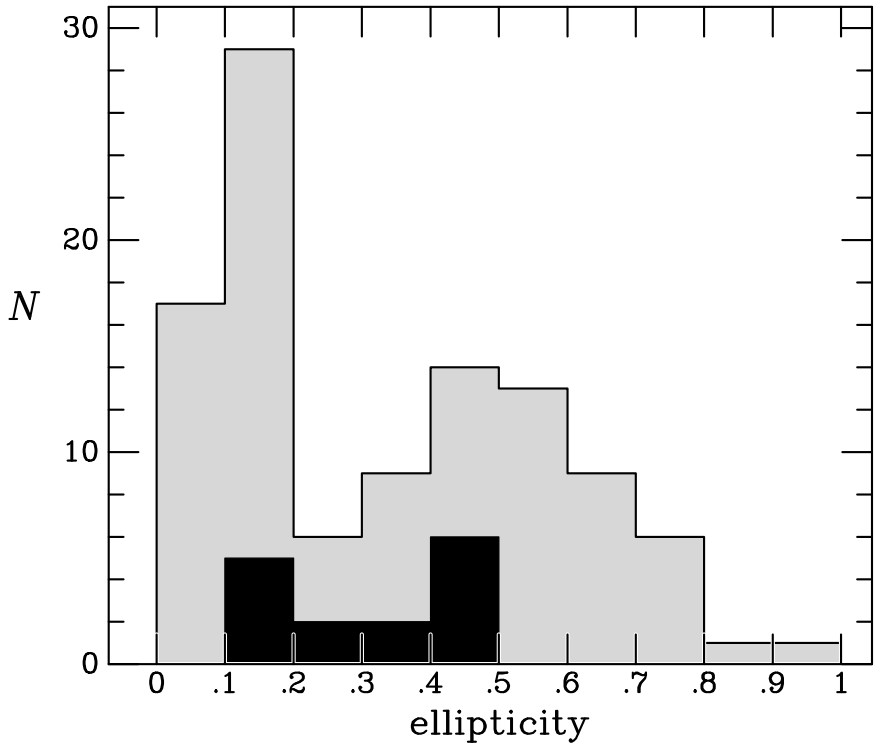

Figure 3.10 Ellipiticity ϵ distributions for the final sample of 15 UCD candidates (black histogram) and all other fitted objects (gray histogram) in the same magnitude and color ranges ($I_{814} < 24$ and color cuts from Fig. 3.2). The larger sample is clearly bimodal with stellar/GC and extended components. The UCDs also show two peaks near $\epsilon \approx 0.17$ and $\epsilon \approx 0.45$, although these have only 5 and 6 objects, respectively, and are subject to small number statistics. None of the UCD candidates has an ellipticity $\epsilon < 0.16$.

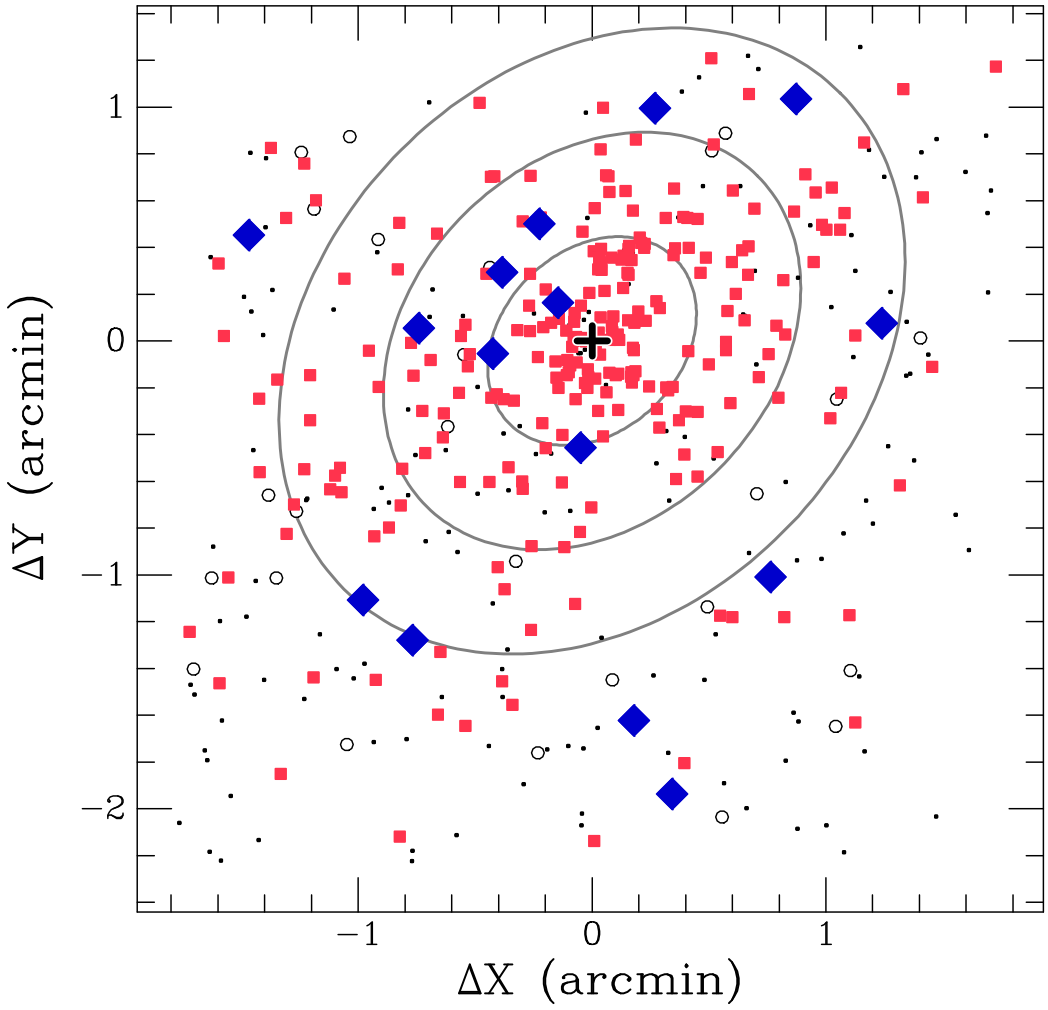

Figure 3.11 Locations of the 15 UCD candidates (blue diamonds), bright globular cluster candidates with $I_{814} < 25$ and $R_{e,c} < 10\,\mathrm{pc}$ (red squares), larger compact galaxies from Fig. 3.9 (open circles), and all other objects in the field with $17 < I_{814} < 25$ and meeting our color cuts (small dots). The orientation is the same as in Fig. 3.1, although here we represent the full $\sim 3\farcm4 \times 3\farcm4$ field. The contours show elliptical isophotes of ESO 325-G004 with major axes of $0\farcm5$, $1\farcm0$, and $1\farcm5$. The GCs preferentially align along the galaxy's major axis. Two-thirds of the UCD candidates in the field also fall along this direction.

magnitude-size diagram using the merged $R_{e,c}$ values as described above. The UCD candidates are marked as large filled diamonds, compact sources meeting the UCD selection requirements but having $R_{e,c}$ in the 100-300 pc range are shown as gray circles, and all other objects that were modeled are shown as open squares. Taking the UCDs by themselves, or the sample of UCD and larger compact galaxies together, there is a weak tendency for larger objects to be brighter. Formally, our best fit relation for the UCD candidates implies $R_{e,c} \propto L^{0.38\pm0.32}$, but this becomes $R_{e,c} \propto L^{0.53\pm0.25}$ if we omit the most compact candidate with $R_{e,c} = 11$ pc. This is consistent with the better determined relation of $R_{e,c} \propto L^{0.68\pm0.13}$ from Evstigeeva et al. (2008) using a sample of confirmed UCDs measured at much higher physical resolution.

There is also an apparent separation in Figure 3.12 between the three smallest UCDs at $R_{e,c} < 17$ pc and the other 12 at $R_{e,c} > 40$ pc. The first group is very similar to the GCs, while the latter group appears to blend smoothly with the larger dwarf galaxies. This may indicate the presence of two distinct types of objects in our UCD candidate sample, and possibly two different origins for UCDs in general. However, there is a 17% probability of a gap as large as the observed one occurring by chance in this sample. To our knowledge, no similar gaps have been reported in previous UCD studies. Again, spectroscopic confirmation and larger samples of UCDs in diverse environments are needed to assess the possibility of two distinct populations. Figure 3.12 also indicates the location that M32 would have in this diagram if it were at the distance of ESO 325-G004, using data from Kent (1987). There are no objects near this position in our sample. We inspected the images visually to determine if we were somehow missing such objects in our selection. One small elliptical located $1\farcm0$ approximately due south of ESO 325-G004 (at the "4 o'clock" position in Fig. 3.1) has size and magnitude very close to the expected values for M32. However, its colors, $(g_{475}-I_{814}) = 2.81$ and $(r_{625}-I_{814}) = 0.93$, are outside our selection range and indicate a higher redshift of $z \approx 0.3$. Thus, we find no M32-like galaxies in this Abell S0740 field.

Figure 3.13 presents the final color-magnitude diagram for the UCD candidates, larger compact galaxies, and GC candidates. The dashed lines indicate the expected locations of the peaks typically found in GC color distributions (e.g., Peng et al.

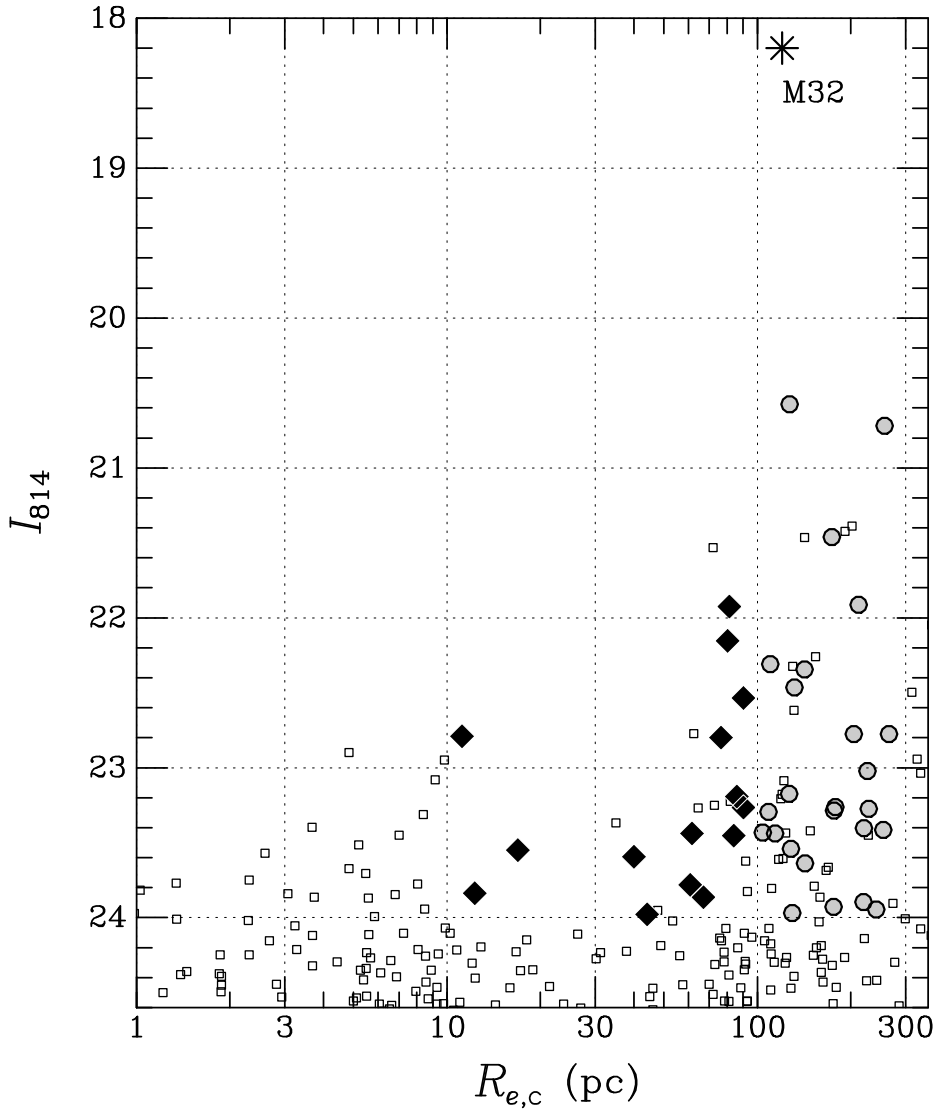

Figure 3.12 F814W magnitude versus size for UCD candidates (filled diamonds), larger compact galaxies in the 100-300 pc range (circles) and all other objects (open squares) in the ESO 325-G004 field that meet our color selection criteria and are within the plotted magnitude and size limits. Objects with $R_{e,c} < 10$ pc are designated globular cluster candidates, while the UCD candidates are chosen as having $R_{e,c} = 10$ to 100 pc and ellipticity < 0.5. However, there may be a separation between the most compact UCD candidates with $R_{e,c} < 20$ pc, similar to large globular clusters, and those with $R_{e,c} \gtrsim 40$ pc, which may be true compact dwarfs. Completely unresolved objects with $R_{e,c} \approx 0$ fall off the edge of this logarithmic plot. We show the expected location for M32 at this distance; no similar galaxies are found in our sample.

2006). Past studies have found that UCDs tended to be slightly redder than the average for the GC population (Wehner & Harris 2007; Evstigneeva et al. 2008). Wehner & Harris described the color-magnitude sequence for their (unresolved) UCD candidates as an extension of the red GC subpopulation to higher luminosities. We also find that the UCDs in Figure 3.13 are weighted towards redder colors, especially the brightest ones. We note that several of the compact galaxies with $R_{e,c} > 100$ pc fall intriguingly close to the expected peaks of the GC color distribution, but the interpretation for these objects is unclear until we have spectroscopic redshifts.

The $\sim 3\farcm4 \times 3\farcm4$ coverage of our images translates to about 125×125 kpc. We find that our sample of 15 UCD candidates is reasonable compared with the numbers found over similar magnitude limits in other clusters. In the Fornax cluster, only 4 objects are found within a similar radius of NGC 1399 (Mieske et al. 2004b; Jones et al. 2006). The number in Virgo is complicated by the enormous GC population around M87, and the lack of a complete high-resolution imaging survey of the core region. Jones et al. (2006) and Evstigneeva et al. (2008) indicate $\sim$5 UCDs within this distance of M87, but an additional five were found by Haşegan et al. (2005) in a physical area 70 times smaller than our own. Therefore, there may be dozens of UCDs clustered close to M87. Perhaps the most comparable survey to ours is that by Wehner & Harris (2007) who tabulated 29 UCD candidates in a $5\farcm5$ field in the center of the Hydra cluster, to about the same absolute magnitude limit. The physical area covered by their imaging is roughly half of ours; so, we might expect to find $\sim$60 candidates based on this extrapolation. However, Wehner & Harris used ground-based imaging and were not able to select based on objects sizes; if we had not made the lower $R_{e,c}$ size cut, we would have a much larger sample of 58 candidates, although the majority of these would be stars and bright GCs. We also note that our sample size is roughly comparable to the numbers within similar radii in the "Fornax" and "Virgo" numerical models presented by Bekki et al. (2003).

Finally, we provide estimates of the stellar masses of the UCD candidates and compact galaxies in Figures 3.8 and 3.9. We calculated the masses of each of the candidates using relations between mass-to-light ratio M/L_V and $(g_{475}-I_{814})$ based on the SSP models from Figure 3.2. The M/L_V values we find for the UCD candidates

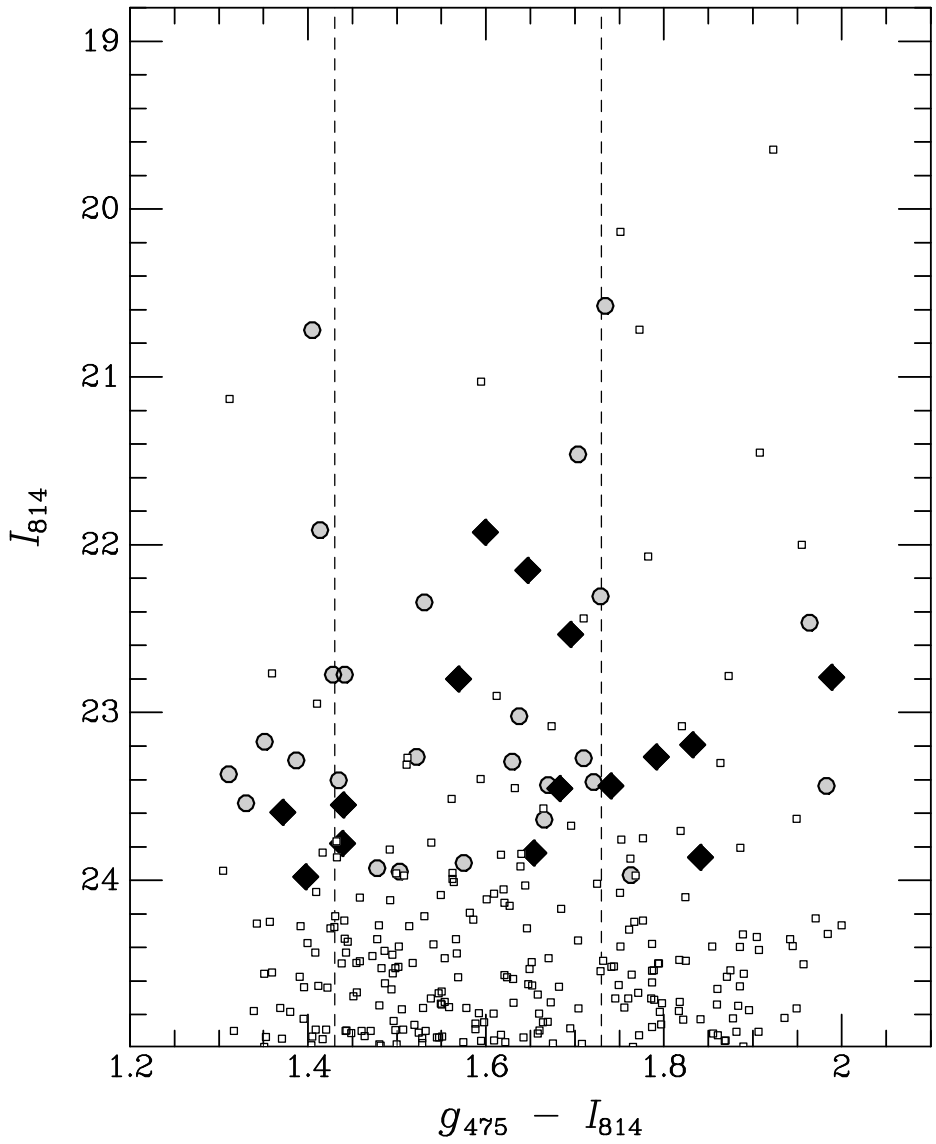

Figure 3.13 Color-magnitude diagram for UCD candidates (diamonds), globular cluster candidates (small squares) and larger compact galaxies from Fig. 3.9 (circles). The dashed lines indicate the expected locations of the characteristic peaks in the globular cluster color distribution. The UCD candidates are weighted toward the red peak location. It is interesting that most of the brightest larger objects (circles at $I_{814} \lesssim 22.8$) lie near the dashed lines. The bright objects marked as globular cluster candidates (squares at $I_{814} \lesssim 22.8$) are all unresolved and may be predominantly stars (they all fall off the left edge of Fig. 3.12).

range from $\sim$0.5 to 3.5, which are likely uncertain by about 30-50%, based on the scatter in the models. The same uncertainty is inherent in the stellar mass estimates, which we give in Table 3.1. The values for the UCD candidates range from 6×10^6 to 10^8 $M_\odot$, with a median of 3.4×10^7 $M_\odot$. This agrees well with the dynamically derived masses of $\sim$(2-9) $\times 10^7$ $M_\odot$ from Evstigneeva et al. 2007a, a range that includes 73% of our candidates. Similarly, Hilker et al. (2007) found dynamical masses of 1.8 to 9.5×10^7 $M_\odot$ for five bright Fornax UCDs. The two objects with the largest masses in Table 3.1 (#419 and #4883) have $R_{e,c}$ values too large for inclusion in the UCD sample, and both have structure indicating they are probably background objects (see Fig. 3.9). We conclude that our mass estimates are reasonable for UCDs.

3.5 Summary

We have presented an analysis of three-band ACS/WFC imaging to search for possible UCDs near the lensing galaxy ESO 325-G004 in Abell S0740. This is an interesting target for a UCD search because it is a massive central elliptical in a poor cluster environment with a velocity dispersion similar to that of Fornax. We selected objects based on their having magnitudes brighter than 99% of the expected GCs population, color appropriate for an early-type or population II system at this redshift, ellipticity less than 0.5, and circular half-light radii in the 10-100 pc range. The radii were measured using both the Galfit and Ishape programs. We found 15 good UCD candidates meeting the selection criteria, comparable to the expectations from previous searches.

In addition, we presented a sample of larger compact galaxies with radii in the range 100-300 pc, if they are located within the cluster. These objects appear to be a mix of irregular background galaxies and larger versions of the cluster UCDs. We did not find any counterparts of M32 in this field. The mean Sérsic index for the UCD candidates is around 1.5, which is marginally higher than the value $\sim$1 found for the larger compact galaxies. This may indicate that the latter objects are dominated by background disk-like galaxies, while the former group is mainly

comprised of UCDs in the cluster. Most of the UCD candidates and larger compact galaxies have visible surrounding halo light, consistent with galaxy threshing models. There is also evidence that most UCDs are intrinsically flattened, as none of the 15 UCD candidates has a fitted ellipticity $\epsilon < 0.16$.

The magnitude-size and color-magnitude diagrams show general continuity in the distributions of these parameters from GCs to the UCDs candidates. For our limited sample of UCD candidates, we find $R_{e,c} \sim L^{0.5}$. This is an intriguing proportionality, as it implies a roughly constant surface brightness for UCDs of different sizes. The better determined relation from Evstigneeva et al. (2008) is somewhat steeper, but consistent within the errors. There may be a bifurcation in the UCDs between those with sizes similar to GCs and larger ones with $R_{e,c} > 40$ pc, suggesting different origins for these two groups. However, because of the small number of objects, the significance of the observed gap in $R_{e,c}$ is only 83%. Therefore, although suggestive, it remains inconclusive. The colors of UCD candidates are weighted towards the red compared to the expected $(g_{475}-I_{814})$ GC color distribution. Several of the bright compact galaxies with sizes in the 100-300 pc range have colors near the expected peaks of the GC color distribution. It would be useful to know if these objects are also in the cluster, and what may be their relation to the UCDs.

The majority of UCD candidates align along the major axis of ESO 325-G004, similar to the spatial distribution of the bright GCs. Because of the small numbers involved, this result is not highly significant, but follow-up spectroscopy can provide a confirmed sample of UCDs; it will be interesting to see if these are mainly along the galaxy's major axis. These findings may appear to support a scenario in which the UCDs are the high-luminosity extension of the GC system. However, as discussed in the Introduction, the true situation is probably more complex, and many red GCs may actually have their origin as stripped nucleated dwarfs, clouding the distinction between the main UCD formation scenarios. It would be useful to discover how the number of UCDs in complete surveys of many different clusters scales with the GC population of the central galaxy. We are currently completing a more detailed analysis of the GC population in this cluster and other similar fields from the same *HST* program. We also plan to obtain spectroscopy for all our UCD candidates to

see what fraction of them are indeed associated with ESO 325-G004. The additional information from these studies should provide further insight into the origin of UCDs and their connection to the GC populations.

Table 3.1. UCD Candidates and Compact Galaxies

ID	RA (J2000)	Dec (J2000)	I_{814}	±	$r-I$	±	$g-I$	±	b/a[a]	q[b]	$R_{e,c}$[c] (pc)	Mass[d] ($M_\odot$)	type[e]
211	205.86130	-38.18323	21.926	0.011	0.497	0.015	1.599	0.019	0.67	0.62	81.3	8.7e+07	UCD
267	205.86669	-38.17410	23.438	0.014	0.631	0.029	1.740	0.043	0.75	0.68	61.6	3.4e+07	UCD
419	205.86652	-38.17941	21.461	0.011	0.498	0.014	1.704	0.018	0.82	0.80	173.6	1.9e+08	Sp
446	205.87906	-38.15454	22.343	0.012	0.510	0.017	1.531	0.022	0.97	0.96	141.9	4.6e+07	S0
536	205.88198	-38.15171	23.273	0.019	0.734	0.048	1.710	0.056	0.66	0.57	228.7	3.6e+07	Irr
575	205.86844	-38.17896	23.368	0.017	0.829	0.042	1.311	0.038	0.69	0.93	35.0	8.0e+06	clump
1048	205.88637	-38.15403	23.403	0.020	0.829	0.048	1.434	0.045	0.57	0.56	220.3	1.2e+07	Irr
1201	205.88024	-38.16939	23.780	0.018	0.680	0.036	1.439	0.042	0.72	0.58	60.8	8.6e+06	UCD
1318	205.89067	-38.15035	22.791	0.012	0.747	0.027	1.988	0.030	0.92	0.84	11.2	1.2e+08	UCD
1350	205.88684	-38.15907	23.433	0.017	0.825	0.038	1.670	0.049	0.71	0.56	104.0	2.8e+07	cE
1470	205.87982	-38.17601	23.175	0.019	0.490	0.031	1.351	0.037	0.72	0.82	126.7	1.1e+07	cE
1596	205.88554	-38.16720	23.022	0.018	0.610	0.031	1.637	0.045	0.60	0.56	226.5	3.6e+07	Irr
1659	205.88557	-38.16813	23.265	0.015	0.829	0.030	1.792	0.041	0.87	0.81	90.3	4.7e+07	UCD
1990	205.88631	-38.17262	23.837	0.017	0.567	0.033	1.654	0.042	0.96	0.81	12.3	1.8e+07	UCD
2253	205.87746	-38.19469	23.551	0.014	0.522	0.027	1.440	0.034	0.99	0.83	16.9	1.1e+07	UCD
2317	205.89302	-38.16406	23.863	0.019	0.655	0.037	1.841	0.060	0.71	0.55	67.1	3.1e+07	UCD

Table 3.1 (cont'd)

ID	RA (J2000)	Dec (J2000)	I_{814}	±	$r-I$	±	$g-I$	±	b/a[a]	q[b]	$R_{e,c}$[c] (pc)	Mass[d] ($M_\odot$)	type[e]
2445	205.87746	-38.19764	23.264	0.018	0.579	0.032	1.522	0.045	0.53	0.58	178.2	1.9e+07	Irr
2626	205.89274	-38.16961	23.594	0.016	0.660	0.031	1.372	0.034	0.88	0.70	40.0	7.9e+06	UCD
2632	205.89377	-38.16771	23.947	0.033	0.876	0.087	1.503	0.093	0.51	0.56	241.5	9.5e+06	Irr
3153	205.88536	-38.19365	21.912	0.012	0.499	0.016	1.413	0.020	0.87	0.66	211.8	4.4e+07	Irr
3495	205.90039	-38.16848	23.638	0.021	0.692	0.043	1.665	0.059	0.73	0.59	142.2	2.3e+07	Irr
3688	205.89787	-38.17786	22.535	0.015	0.640	0.022	1.695	0.034	0.77	0.54	90.2	6.9e+07	UCD
4054	205.89599	-38.19076	23.541	0.018	0.549	0.033	1.330	0.041	0.75	0.80	128.1	7.2e+06	Sp
4062	205.91205	-38.15832	22.308	0.011	0.554	0.022	1.729	0.024	0.76	0.65	109.9	9.4e+07	cE
4171	205.91251	-38.16059	23.294	0.015	0.513	0.037	1.630	0.042	0.73	0.62	108.6	2.7e+07	cE
4441	205.90959	-38.17646	20.721	0.010	0.531	0.012	1.405	0.013	0.78	0.76	257.2	1.3e+08	Sp/Irr
4507	205.90258	-38.19380	23.979	0.020	0.664	0.044	1.397	0.052	0.68	0.54	44.1	6.1e+06	UCD
4510	205.91878	-38.16098	22.464	0.012	0.795	0.029	1.964	0.035	0.50	0.56	131.6	1.5e+08	cE
4513	205.92092	-38.15667	23.897	0.028	0.543	0.075	1.575	0.083	0.85	0.89	219.5	1.3e+07	Irr
4579	205.91782	-38.16729	22.154	0.011	0.767	0.017	1.647	0.020	0.76	0.77	80.2	8.3e+07	UCD
4616	205.90719	-38.19038	23.969	0.026	0.625	0.055	1.763	0.084	0.85	0.90	129.3	2.3e+07	clump
4755	205.91962	-38.17162	22.799	0.012	0.534	0.020	1.569	0.028	0.73	0.54	76.4	3.5e+07	UCD

Table 3.1 (cont'd)

ID	RA (J2000)	Dec (J2000)	I_{814}	±	$r-I$	±	$g-I$	±	b/a[a]	q[b]	$R_{e,c}$[c] (pc)	Mass[d] ($M_\odot$)	type[e]
4882	205.92918	-38.15779	23.928	0.025	0.509	0.065	1.478	0.069	0.79	0.76	175.8	8.8e+06	Irr
4883	205.90786	-38.20153	20.577	0.010	0.709	0.012	1.734	0.013	0.69	0.54	127.1	4.7e+08	S0
4930	205.91646	-38.18593	22.775	0.015	0.512	0.024	1.441	0.031	0.73	0.82	204.4	2.2e+07	Irr
5097	205.91919	-38.18841	23.193	0.014	0.860	0.030	1.832	0.042	0.64	0.59	85.9	5.6e+07	UCD
5123	205.91309	-38.20199	22.776	0.015	0.773	0.029	1.428	0.033	0.90	0.90	265.8	2.1e+07	Sp
5200	205.93059	-38.16994	23.284	0.017	0.863	0.054	1.387	0.040	0.84	0.62	176.4	1.1e+07	Irr
5247	205.92507	-38.18285	23.438	0.017	0.693	0.045	1.983	0.061	0.93	0.98	114.0	6.5e+07	cE
5396	205.92415	-38.19283	23.454	0.014	0.544	0.036	1.683	0.042	0.92	0.83	83.9	2.8e+07	UCD
5503	205.92445	-38.19675	23.414	0.023	0.489	0.056	1.721	0.071	0.66	0.72	254.5	3.3e+07	Irr

[a]Axis ratio measured by SExtractor; no PSF correction.

[b]Intrinsic axis ratio $q = 1 - \epsilon$ from our 2-D modeling with PSF correction.

[c]Fitted circularized effective radius $R_{e,c} = R_e\sqrt{q}$.

[d]Photometrically derived stellar mass estimate.

[e]Morphological type from our visual inspection. All objects in Fig. 3.8 are type UCD; see text for further details.

Bibliography

[1] Abell, G. O. 1958, ApJS, 3, 211

[2] Abell, G. O., Corwin, H. G., Jr., & Olowin, R. P. 1989, ApJS, 70, 1

[3] Barber DeGraaff, R., Blakeslee, J. P., Meurer, G. R., & Putman, M. E. 2007, ApJ, 671, 1624

[4] Bassino, L. P., Muzzio, J. C., & Rabolli, M. 1994, ApJ, 431, 634

[5] Bekki, K. 2007, MNRAS, 380, 1177

[6] Bekki, K., Couch, W. J., & Drinkwater, M. J. 2001, ApJ, 552, L105

[7] Bekki, K., Couch, W. J., Drinkwater, M. J., & Shioya, Y. 2003, MNRAS, 344, 399

[8] Benítez, N., et al. 2004, ApJS, 150, 1

[4] Bertin, E., & Arnouts, S. 1996, A&AS, 117, 393

[10] Blakeslee, J. P. 2007, Cosmic Frontiers, ASP Conference Series, 379, 99

[4] Blakeslee, J. P., Anderson, K. R., Meurer, G. R., Benítez, N., & Magee, D. 2003, Astronomical Data Analysis Software and Systems XII, 295, 257

[12] Blakeslee, J. P., et al. 2006, ApJ, 644, 30

[13] Bruzual, G. & Charlot, S. 2003, MNRAS, 344, 1000

[14] Côté, P., et al. 2006, ApJS, 165, 57

[15] Drinkwater, M. J., Gregg, M. D., Hilker, M., Bekki, K., Couch, W. J., Ferguson, H. C., Jones, J. B., & Phillipps, S. 2003, Nature, 423, 519

[16] Drinkwater, M. J., Jones, J. B., Gregg, M. D., & Phillipps, S. 2000, PASA, 17, 227

[17] Evstigneeva, E. A., Drinkwater, M. J., Jurek, R., Firth, P., Jones, J. B., Gregg, M. D., & Phillipps, S. 2007a, MNRAS, 378, 1036

[18] Evstigneeva, E. A., Gregg, M. D., Drinkwater, M. J., & Hilker, M. 2007b, AJ, 133, 1722

[19] Evstigneeva, E. A., et al. 2008, AJ, 136, 461

[20] Fellhauer, M. & Kroupa, P. 2002, MNRAS, 330, 642

[21] Goerdt, T., Moore, B., Kazantzidis, S., Kaufmann, T., Macciò, A. V., & Stadel, J. 2008, MNRAS, 385, 2136

[22] Graham, A. W., & Driver, S. P. 2005, PASA, 22, 118

[23] Haşegan, M., et al. 2005, ApJ, 627, 203

[24] Hilker, M., Baumgardt, H., Infante, L., Drinkwater, M., Evstigneeva, E., & Gregg, M. 2007, A&A, 463, 119

[25] Hilker, M., Infante, L., Vieira, G., Kissler-Patig, M., & Richtler, T. 1999, A&AS, 134, 75

[26] Jones, J. B., et al. 2006, AJ, 131, 312

[27] Jordán, A., Blakeslee, J. P., Peng, E. W., Mei, S., Côté, P., Ferrarese, L., Tonry, J. L., Merritt, D., Milosavljević, M., & West, M. J. 2004, ApJS, 154, 509

[28] Kent, S. M. 1987, AJ, 94, 306

[14] King, I. 1962, AJ, 67, 471

[30] Larsen, S. S. 1999, A&AS, 139, 393

[31] Larsen, S. S., & Brodie, J. P. 2000, AJ, 120, 2938

[32] Mieske, S., Hilker, M., & Infante, L. 2002, A&A, 383, 823

[33] Mieske, S., Hilker, M., & Infante, L. 2004b, A&A, 418, 445

[34] Mieske, S., Hilker, M., Infante, L., & Jordán, A. 2006, AJ, 131, 2442

[35] Mieske, S., Hilker, M., Jordán, A., Infante, L., & Kissler-Patig, M. 2007, A&A, 472, 111

[36] Mieske, S., et al. 2004a, AJ, 128, 1529

[37] Peng, C. Y., Ho, L. C., Impey, C. D., & Rix, H. 2002, AJ, 124, 266

[9] Peng, E. W., Jordán, A., Côté, P., Blakeslee, J P., Ferrarese, L., Mei, S., West, M. J., Merritt, D., Milosavljević, M., & Tonry, J. L. 2006, ApJ, 639, 95

[39] Phillipps, S., Drinkwater, M. J., Gregg, M. D., & Jones, J. B. 2001, ApJ, 560, 201

[Schlegel et al. 1998] Schlegel, D. J., Finkbeiner, D. P., & Davis, M. 1998, ApJ, 500, 525

[40] Sérsic, J. L. 1968, Atlas de Galaxias Australes (Cordoba: Observatorio Astronomico)

[41] Sirianni, M., et al. 2005, PASP, 117, 1049

[17] Smith, R. J., Blakeslee, J. P., Lucey, J. R., & Tonry, J. 2005, ApJ, 625, L103

[43] Spergel, D. N., et al. 2007, ApJS, 170, 377

[44] Thomas, P. A., Drinkwater, M. J., & Evstigneeva, E. 2008, MNRAS, 389, 102

[45] Tonry, J. L., Blakeslee, J. P., Ajhar, E. A., & Dressler, A. 1997, ApJ, 475, 399

[46] Wehner, E. M. H. & Harris, W. E. 2007, ApJ, 668, L35

Chapter 4

Introduction to the Shapley Supercluster and Data Analysis

The work presented in Chapters 4, 5 and 6 was undertaken in collaboration with Dr. John Blakeslee. The DAOphot analysis in this chapter was also undertaken in collaboration with Dr. William Harris.

4.1 Motivation for Survey Data

In January 2005, the HST GO Program 10429 obtained F814W band imaging of 11 galaxies in the Shapley Supercluster. To better understand the motivations of this program, we must first discuss the location and motions of the local cluster of galaxies to which the Milky Way belongs.

4.1.1 Local Group Motion

The Local Group consists of a cluster of about 30 gravitationally bound galaxy members with the Milky Way galaxy as the second largest member and the Andromeda Galaxy, M31, being the largest. The membership criterion is being within a radial distance of 1.5 Mpc ($\sim$ 5 million light years) of the cluster's center between the Milky Way and M31. Membership is vague, and has been updated in recent years (van den Berg, 2000). This update is due to the Local Group being gravitationally bound to other nearby groups and by the difficulty in knowing what members are free to leave the bound Local Group. In Chapter 1, we discussed Hubble's Law and the motion of the galaxies in the universe. However, there are deviations from the Hubble Flow called peculiar velocities. These peculiar velocities result from the influence of nearby mass concentrations. The nearest large cluster of galaxies, the Virgo cluster, creates a motion in a direction apart from the expected Hubble expansion, of 250km/s. This is called the Virgocentric infall. The Local Group and the Virgo cluster are members of a larger bound group called the Local Supercluster, where Virgo is more concentrated at the Local Supercluster's center and the Local Group is located in a more outlying region (Binney 1998).

4.1.2 Great Attractor

A more significant departure from the Hubble flow is a velocity of about 600km/s motion relative to the Cosmic Radiation Background (CMB) our local group of galaxies experiences. To explain this motion, astronomers speculated the cause to be a huge concentration of mass in the direction of Centaurus and called it the Great Attractor. It was initially hard to investigate due to the fact that Centaurus lies close to the Milky Way's galactic plane where there is a large amount of extinction from dust. The Hydra-Centaurus supercluster was ruled out as the Great Attractor in Lynden-Bell et al. (1988). They concluded that the primary source of this $\sim$ 600km/s motion was 40% further away. Lynden-Bell et al. also found that the Hydra-Centaurus supercluster was, itself, falling toward the Great Attractor at velocities greater than

1000 km/s. This finding remains a controversial finding and the identity of the Great Attractor is still debated. HST GO Program 10429 was submitted to investigate a large mass concentration in the direction of Centaurus, the Shapley Supercluster.

4.1.3 Shapley Supercluster

Located in the Southern Hemisphere and centered at a distance of $\sim$ 150-200 Mpc (490-650 million light years), the Shapley Supercluster (SSC) constitutes the densest part of the nearby universe. First discovered in 1930 by Harlow Shapley during a survey of galaxies in the southern hemisphere, he mentions a cloud of galaxies in Centaurus that appears to be the most populous yet discovered. Figure 4.1 gives a good visual representation of SSC's distance from the Milky Way and the distribution of the cluster members. It is the richest supercluster in the direction (and distance) of the Great Attractor. If the peculiar velocities for SSC members can be calculated then a more accurate mass density map can be created for the SSC. Also this survey's main goal was to obtain SBF distances to several galaxies within the SSC, which recently became possible because of the ACS (section 4.3.1). This data was also intended to be used to further the study of globular clusters in this rich, dense environment.

The following is a list of the clusters targeted and the galaxy members imaged:

A1736a: ESO509-g008, ESO509-g020, ESO509-g067

A3558: ESO444-g046, 2masxj13275493-3132187 (PGC47197),
2masxj13272961-3123237 (PGC47154), 2masxj13280261-3145207 (PGC88857)

A3571: ESO383-g076, 2masxj13481399-3322547 (PGC84052)

A3570: ESO325-g016 & AS0740: ESO325-g004

The galaxies with names that begin with *2masxj* will further be simplified in this study as *2mj* with the last 7 digits left off. For example, 2masxj13275493-313287 will be called 2mj13275493. Table 4.1 is a list containing a few galaxy properties, obtained from various sources, of each of the 11 galaxies in this study. The first and second columns are the name of the galaxy and cluster the galaxy belongs to, respectively. The next two columns are the right ascension (RA) and declination (Dec). The following column is the class of galaxy obtained from the NASA/IPAC

Table 4.1. Galaxy Properties

galaxy	Abell	RA	Dec	class	cz (km/s)	Δ cz	M_V	σ
ESO509-G008	A1736a	13:26:44.10	-27:26:21.8	E	10555	139	-22.8	292
ESO509-G020	A1736a	13:28:00.15	-27:21:15.5	E	10195	-221	-22.5	315
ESO509-G067	A1736a	13:34:47.80	-27:07:37.4	E	10396	-20	-22.7	N/A
ESO325-G016	A3570	13:46:24.00	-37:58:15.6	compact	11309	337	-22.0	276
ESO325-G004	AS0740	13:43:33.20	-38:10:33.7	SA0/cD	10164	-26	-22.8	310
ESO383-G076	A3571	13:47:28.40	-32:51:53.0	cD5	11567	-109	-23.6	380
2MJ13481399	A3571	13:48:14.00	-33:22:54.7	cD/S0	12205	529	-21.9	232
ESO444-G046	A3558	13:27:56.86	-31:29:44.6	cd4	14061	-246	-23.8	275
2MJ13275493	A3558	13:27:54.95	-31:32:18.7	E	15481	1174	-22.4	323
2MJ13272961	A3558	13:27:29.63	-31:23:24.2	E	14281	-26	-22.9	335
2MJ13280261	A3558	13:28:02.62	-31:45:20.8	E	12857	-1450	-22.1	284

Extragalactic Database, NED (see Chapter 1 for definition of galaxy class). The cz column lists the radial velocities of each galaxy. The Δ cz value is difference between each galaxy's radial velocity and the cluster's mean radial velocity (listed in table 4.2). M_V is the absolute magnitude of each galaxy obtained from I band values corrected for extinction and coverted to V band. The last column is the velocity dispersion of the each galaxy, which could not be found all galaxies (Smith 2000).

4.2 Abell Clusters in Study

In this section I will briefly describe each cluster and the members in this survey. The Abell Clusters in this survey are A3558, A3570, A3571, A1736a and AS0740. The brightest cluster galaxy (BCG) was targeted in each of the five clusters. Table 4.2

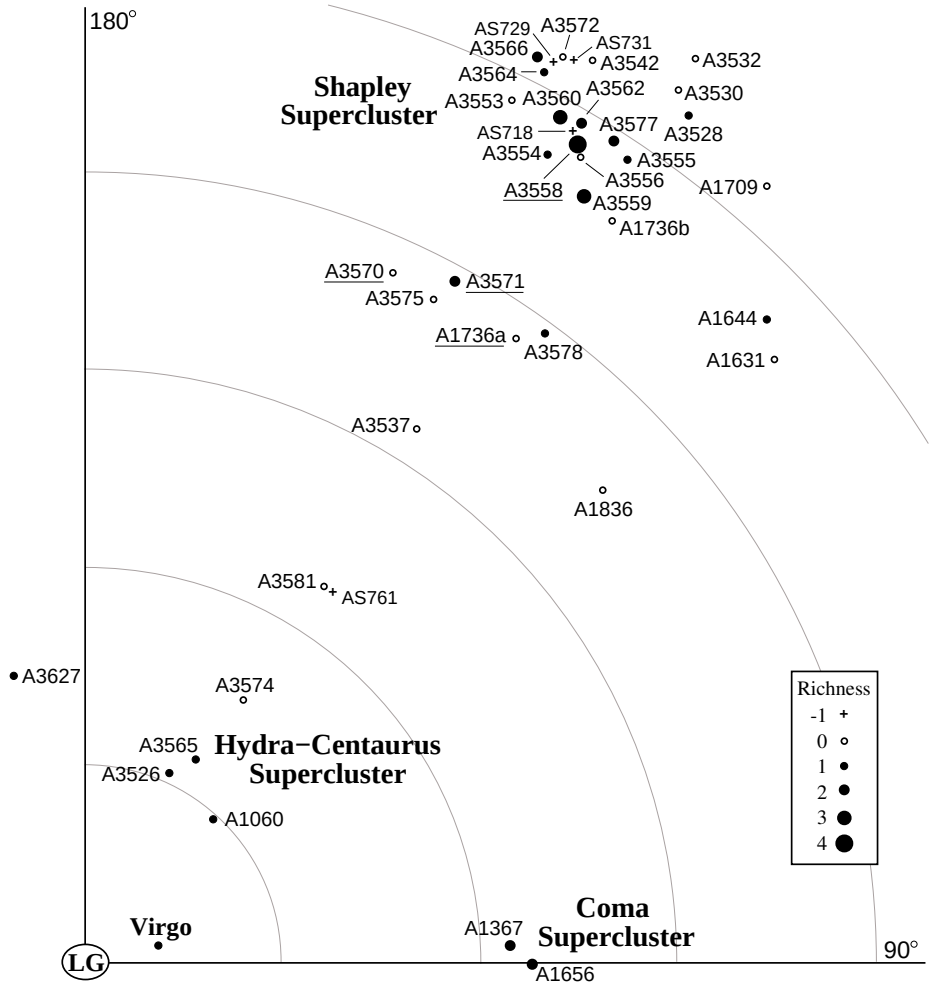

Figure 4.1 Map of the Shapley Supercluster location relative to the Local Group. The semicircular lines are spaced at 3000 km/s intervals.

Table 4.2. Cluster Properties

cluster	z	cz	$(m-M)$	σ	$\pm$	BM	A.C.	R_e (arcmin)	L_X (10^{44})	$\pm$
A1736a	0.0350	10416	35.89	381	0	III	41	–	–	–
A3570	0.0379	10972	35.93	460	0	I-II	31	6.0	0.191	–
AS0740	0.0350	10190	35.78	330	10	I-II	2	–	–	–
A3571	0.0397	11676	36.08	853	45	I	126	3.5	4.91	0.25
A3558	0.0477	14307	36.52	902	27	II	226	6.0	5.56	0.18

contained the following cluster properties: cluster name, redshift (z), radial velocity (cz), distance modulus, velocity dispersion (σ), error for velocity dispersion, Bautz-Morgan Type, Abell count, effective radius of cluster (R_e) and the x-ray luminosity ($L_X \times 10^{44}$ erg/s). The velocity dispersion of each cluster is the standard deviation of all the member radial velocities. Each σ was obtained from the following sources: Fadda et al. (1996), Struble et al. (1991), Schindler et al. (2000), Smith et al. (2000, 2001, & 2005) and Y.-Y. Zhang et al. (2011). However, we directly calculated the velocity dispersion for AS0740 using the radial velocities from all of the member galaxies. The Abell count is a measure of the richness of the cluster where as Bautz-Morgan type is a measure of the kind of galaxies reside in the cluster instead of the just the number (see Chapter 1). The effective radii and x-ray luminosities for only three clusters were available in Böhringer et al. (2004).

4.2.1 A3558

Also called the Shapley 8, being the eighth rich cluster in a list published by Shapley in 1933, Abell 3558 is a popular cluster to study due to it being a massive core Shapley cluster. The BCG is ESO444-g046 and located at very near the center

of the cluster.

4.2.2 A3570

Abell 3570 is a poor cluster whose BCG is ESO325-g016.

4.2.3 A3571

Abell 3571 is a cluster dominated by a massive elliptical, the BCG, ESO383-g076. The BCG is located very near the x-ray center of A3570.

4.2.4 A1736a

Abell 1736 is at a redshift of 0.0350, which can be read in Table 4.2, however, there is confusion in labeling this cluster. There is another cluster named A1736b which is at a redshift of 0.0458. In some papers the cluster at redshift 0.0350 is called A1736b and the other is called A1736a or just A1736. Therefore, one is never quite sure which cluster the study is referring to until the redshift is listed. This cluster is fairly poor and not dominated by any single massive galaxy. The BCG is ESO509-g008.

4.2.5 AS0740

This cluster contains the nearest known lensing galaxy with Chapter 3 of this thesis discussing a search for Ultra Compact Dwarfs (UCDs). AS0740 is a poor cluster with ESO325-g004 as the BCG. The richness of the cluster is the reason it exists in the Abell supplementary list published by Abell, Corwin and Olowin in 1989. AS0740 did not meet the original richness criteria. The BCG is also at the cluster's X-ray center (Smith 2011) and can be viewed in Figure 4.2, which is a X-ray contour map of AS0740.

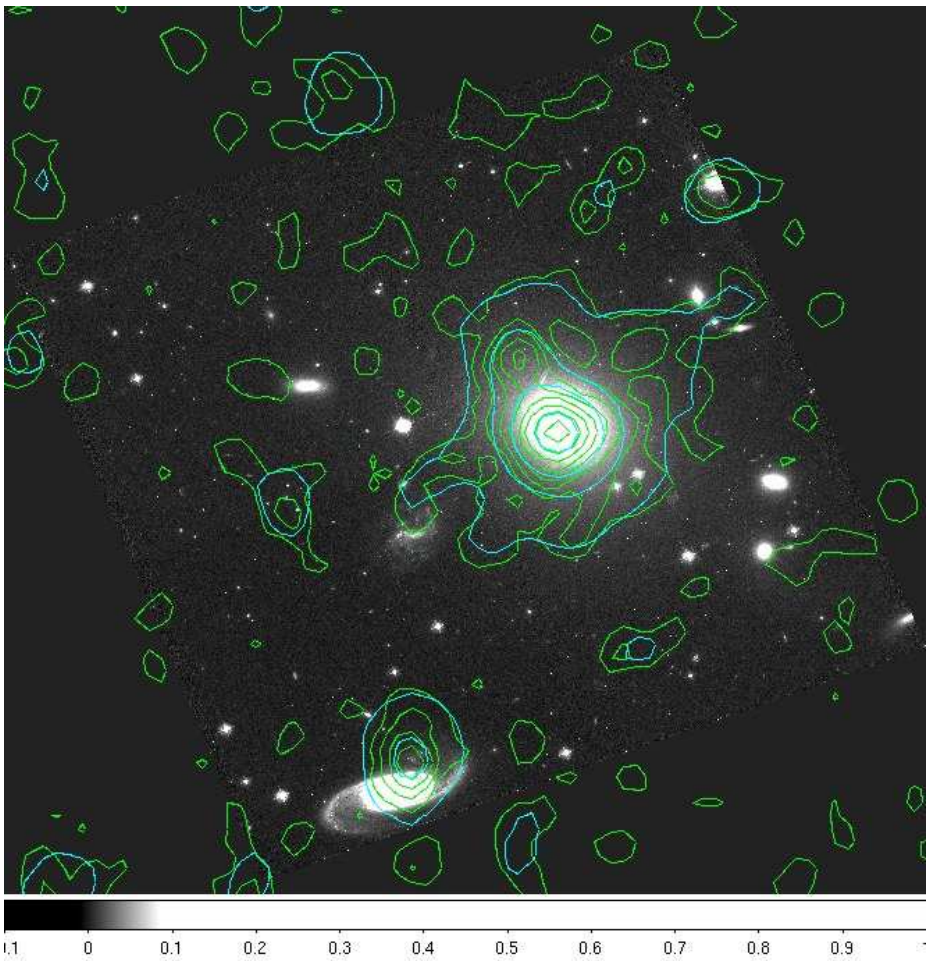

Figure 4.2 X-ray map of AS0740, courtesy R. Smith

4.3 Data Analysis

4.3.1 ACS/WFC

The Advanced Camera for Surveys (ACS) was installed on the HST in March 2002. ACS has three channels, the High Resolution Channel, the Wide Field Channel (WFC) and the Solar Blind Channel (SBF). One of the two photometric channels, WFC, was used to image the 11 galaxies in this study. The resolution is 20 pix/arcsec with a field of 202 arcsec $\times$ 202 arcsec. The image scale for this survey was 33.4 pc/pix - 43.4 pc/pix. ACS went offline a few times and currently has only two channels in operation, WFC and SBC (Ford 2003; ACS/HST updates).

4.3.2 Observations

The various galaxies were imaged with ACS/WFC in F814W during 114 orbits, with the exception of ESO325-g004, which was imaged in the additional filters F475W and F625W. As previously stated, the HST GO Program 10429 was designed to collect data on the following galaxies to calculate SBF distances: ESO509-g008, ESO509-g020, ESO509-g067, ESO444-g046, 2mj13275493, 2mj13272961, 2mj13280261, ESO383-g076, 2mj13481399, ESO325-g016, and ESO325-g004. The exposure times of these images were 18567s, 18567s, 18567s, 34210s, 35550s, 35550s, 35550s, 21081s, 21081s, 18882s and 18882s, respectively. These more precise distances would give us a better understanding of the supercluster's significance to the Local Group's relative motion to the CMB. These images were processed with the *Apsis* pipeline detailed in Blakeslee et al. (2003). This pipeline is used to sum the exposures, geometrically correct orientation, and remove cosmic rays from the images. Mosaics of the images produced can be found in Figure 4.3 and Figure 4.4.

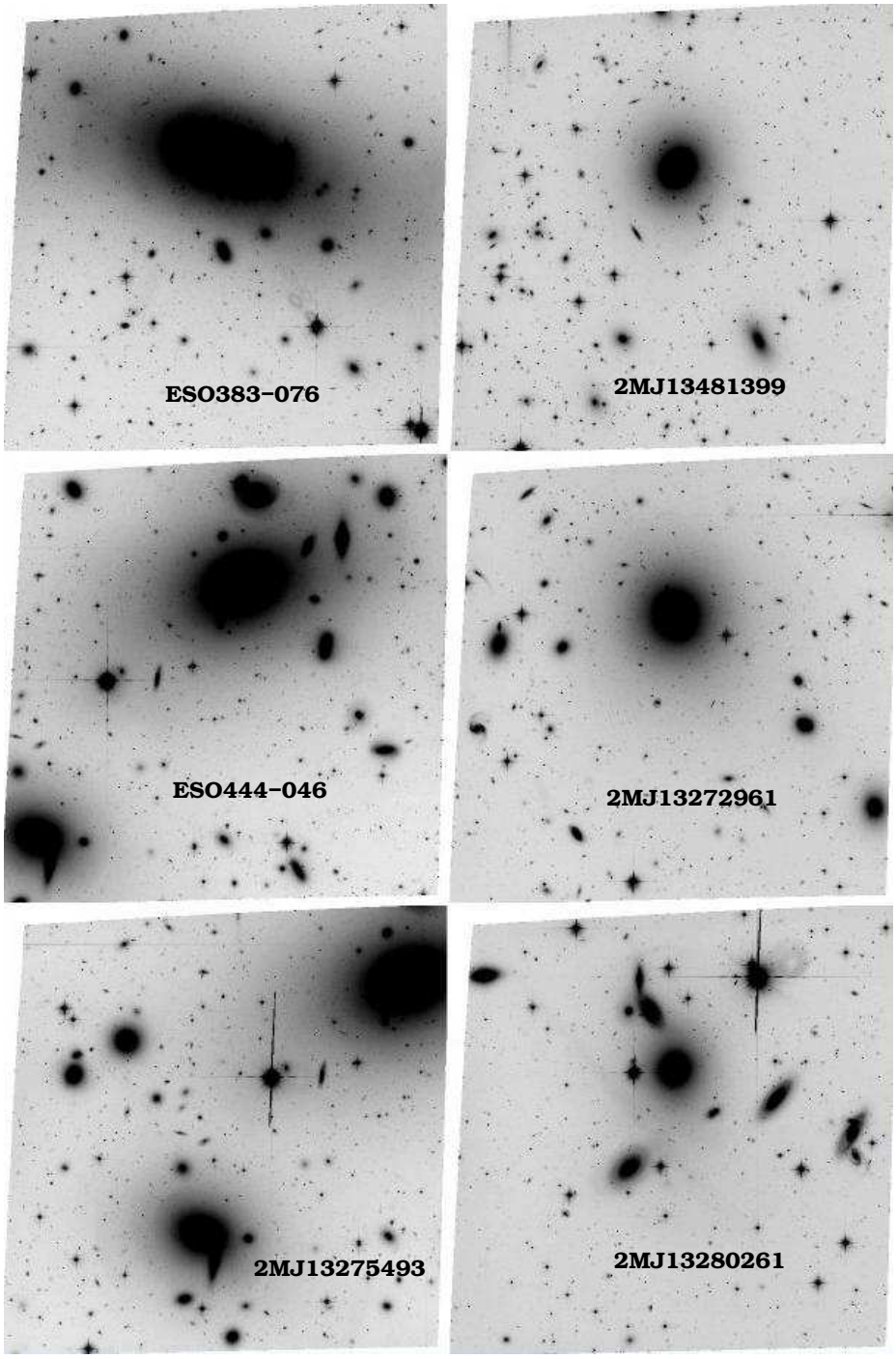

Figure 4.3 Mosaic of 6 of the 11 galaxies in this study.

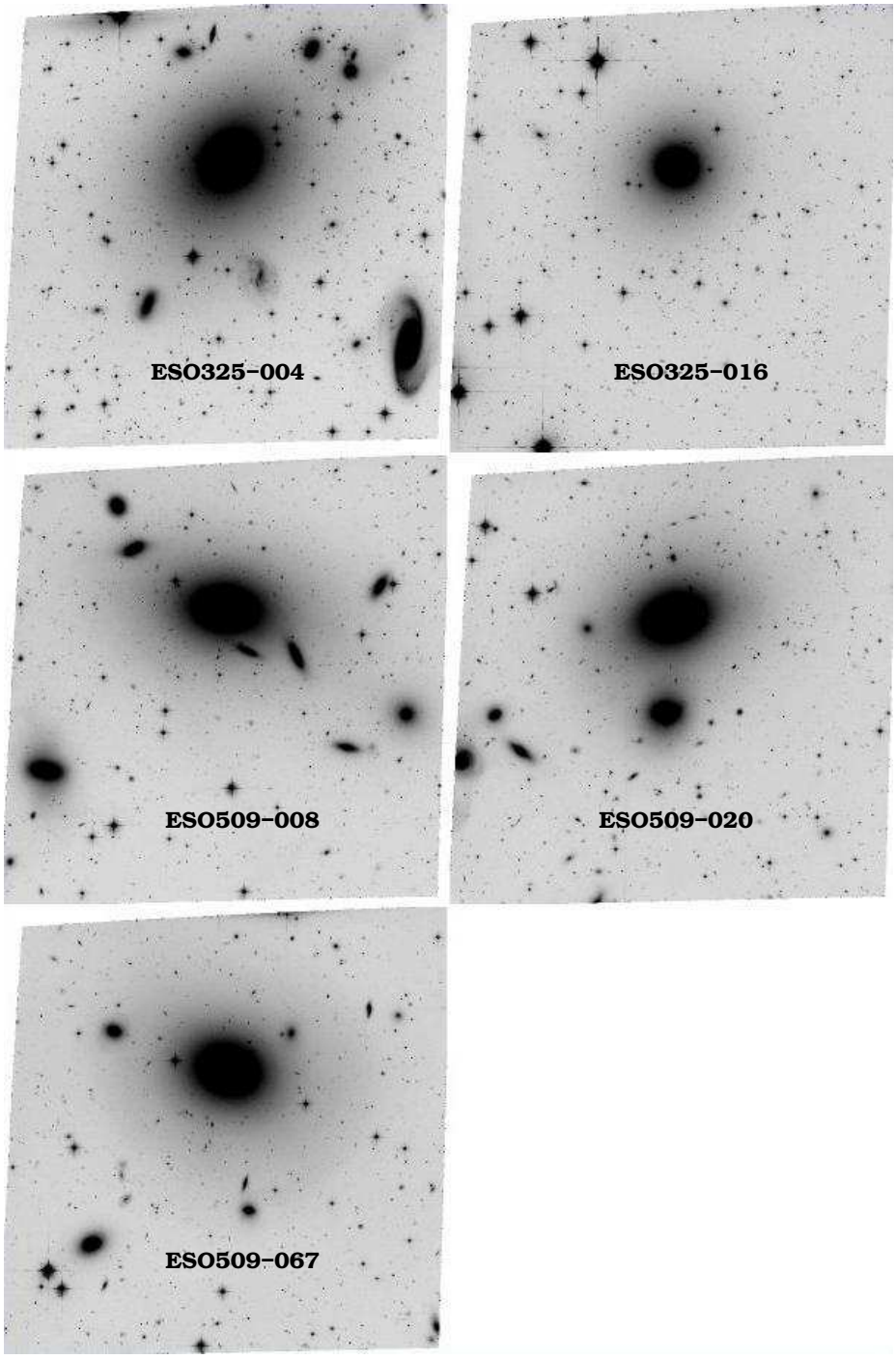

Figure 4.4 Mosaic of 5 of the 11 galaxies in this study.

4.3.3 Reductions in IRAF/DAOphot

The object detection process for the 11 galaxies was done primarily with IRAF / DAOphot and is detailed below.

DAOphot (Stetson 1987) is an object detection software program used to perform stellar photometry, measuring flux or intensity, in crowded fields. This software package was used within IRAF, which stands for Image Reduction and Analysis Facility. IRAF is a software system that contains tools for a large amount of astronomical data reduction (some examples include optical imaging and spectra). The process that leads to the final catalog of GC candidates was a lengthy one with many steps. The tasks or algorithms used are in the DAOphot package in IRAF. The first step was to set all the parameters before any task is done. This object detection software looks for star-like objects or point sources and at this distance all the GCs are points.

The first task is called *daofind* and is an algorithm that detects sources and produces a list of stars from the input image. Figures 4.3 and 4.4 show the 11 galaxy input images. *Daofind* searches for point sources within the image that meet the parameters the user assigns, such as, fwhmpsf, sigma, threshold, datamin, and datamax. The image is then convolved with a fitted Gaussian and the resulting maxima (from the parameters) are the objects detected. *Daofind* computes centers, estimated magnitudes, sharpness and roundness for the selected stars. Sharpness is defined as the ratio of the amplitude of the best fitting delta function at the position of a detected object to the amplitude of the best fitting Gaussian at the same position (Stetson 1987). Roundness is computed by fitting a one-dimensional Gaussian function of full width at half-maximum fwhmpsf to the x and y marginal pixel distributions (Stetson 1987). The output file of the *daofind* task is called image.coo, where image is replaced by whatever name belongs to the input image. The image used in this task was the rescaled image of the galaxy. The rescaled image was the original image divided by its exposure time and then multiplying by 2680 so that the parameters in *datapars*, *daopars*, and *findpars* (parameter files) are uniform.

The second task is *phot* and is run on the same rescaled image. This algorithm computes initial magnitudes, centers, and sky values from the list compiled by *daofind*.

The values in the star list *phot* creates are used as starting values for the next steps in the DAOphot process. *Phot* first reads in the image.coo file and computes sky values by looking at fluctuations in the sky background within a defined annulus of pixels. It then computes an instrumental magnitude and error using the aperture radii specified in the parameter files. The *phot* output file is called image.mag.

Next, the *pstselect* task creates a list of bright, isolated objects as good star candidates to create a point spread function (psf) model, used in the following task, *psf*. The *pstselect* algorithm reads in an image file and the image.mag file. It first sorts the stars in the list by magnitude, with the brightest stars at the top of the list. It then selects the maxnpsf number of brightest stars. In this case we defined maxnpsf = 100 in the parameter files. *Pstselect* makes sure none of these stars are saturated, have any bad pixels and have no close, bright neighbors. The output file is named image.pst and contained a list of bright stars their id, x and y coordinates, magnitudes and sky values of the selected stars.

Once the list of 100 objects is selected, we interactively look at each object using the *psf* task to see if it can contribute to a psf model. This psf model will be used by the allstar to compute magnitudes using psf fitting instead of apertures like in phot. The psf algorithm uses image.pst. and displays the contour, radial, and 3D mesh plot of each star in the list. From these plots one chooses which of the stars in the list will be accepted. Doing this task interactively is essential to the fitting since a significant number of the stars in the 100 star list turn out not to be point sources. Once all the stars in the list have either been accepted or rejected, the remaining stars are compiled and are fitted to a analytic function. Since auto was chosen in the parameter file, the following functions are tried until one fits best: gauss, moffat25,

moffat15, penny1, penny2, and lorentz.

$$
\begin{aligned}
z &= \frac{x^2}{p1^2} + \frac{y^2}{p2^2} \\
gauss &= A * exp(-0.5z) \\
z &= \frac{x^2}{p1^2} + \frac{y^2}{p2^2} + xyp3 \\
moffat15 &= \frac{A}{(1+z)^{1.5}} \\
moffat25 &= \frac{A}{(1+z)^{2.5}} \\
z &= \frac{x^2}{p1^2} + \frac{y^2}{p2^2} + xyp3 \\
lorentz &= \frac{A}{1.0+z} \\
z &= \frac{x^2}{p1^2} + \frac{y^2}{p2^2} \\
e &= \frac{x^2}{p1^2} + \frac{y^2}{p2^2} + xyp4 \\
penny1 &= \frac{A*(1-p3)}{1.0+z} + p3 * exp(-0.693 * e) \\
z &= \frac{x^2}{p1^2} + \frac{y^2}{p2^2} + xyp5 \\
e &= \frac{x^2}{p1^2} + \frac{y^2}{p2^2} + xyp4 \\
penny2 &= \frac{A*(1-p3)}{1.0+z} + p3 * exp(-0.693 * e)
\end{aligned}
\tag{4.1}
$$

The psf model can vary with respect to its position in the image. This is controlled by the parameter varorder. We used varorder of 2, which modeled a psf that varies quadratically with position. Psf produces a list of the stars, another image.pst file, a list of grouped stars (on the basis of position and signal-to-noise), image.psg, and an image of the created psf model.

Once a psf model is made, the *allstar* task is run. This task fits the psf model to each object it finds in the image and assigns a magnitude and error to that object and to the sky. It also calculates a χ and sharpness value. The definition of sharpness is a measure of the difference between the observed width of the object and the width of the psf model (Stetson 1987). The definition of χ is the ratio of the observed

pixel-to-pixel scatter in the fit residuals to the expected scatter calculated from a predictive model based on measured detector features (Sabbi et al. 2008). *Allstar* produces a subtracted image where all the objects the program found are removed from the original image.

This first sequence of tasks is done to make an image to use in the median process. This process is designed to create a smoothed image from the subtracted image. This will smooth the edges of the areas where the objects were removed. This leaves an image that is mostly devoid of all unresolved objects. Once this smoothed image is subtracted from the original image most of the large objects will be masked or erased. Now we have something we call a flat image (which is like the masked image mentioned in the NGC1533 chapter on data reduction). This image has all the big objects removed and now we are free to try to detect objects (our GC candidates) without the distraction of large foreground stars or background galaxies. Again the first run's sole purpose was to get this flat image, which will be used, in the data detection process.

The sequence of *daofind*, *phot* and *allstar* is run again. The process is exactly like the first run with the exception of not having to perform *pstselect* or *psf* because we can use the psf model found in the first run. However, even though *daofind* and *phot* are run with the flat image, *allstar* is run with the original rescale image. The .mag output file from *phot* will help *allstar* avoid all the non-star-like objects in the image (as mentioned earlier). This time we are running it to actually catalog our objects. Using our flat image we get a .mag file and an .als file. We use the subtracted image from this *allstar* process for our last and final run. When this .sub.fits image is subtracted from the flat image, we get an image that only has the objects missed in the object detection in this run (we call it sub.flat.fits). This final run is to detect and get photometry for any missed star-like objects. *Daofind* and *phot* are run with the sub.flat.fits. The .mag files from run 2 and run 3 are combined and then given to *allstar* for this final run. This combined .mag file has all the objects found in round 2 and then in round 3 (where we are trying to find any candidates that were missed in round 2). The .als file (called _3.als) of this last run of *allstar* is our final catalog of candidates. The task *pdump* is used to create a more condensed and cleaned up

final list. It consists of id, xc, yc, mag, magerr, sharp and chi (χ). We called this final catalog _3.dat. Once we have this photometry file we do a similar process to get completeness.

4.3.4 Magnitude Correction

The magnitudes need to be corrected for extinction and aperture effects for the ACS camera as in Sirianni et al. (2005), as well as for the DAOphot fitting aperture.

Extinction & Photometric Corrections

Galactic Extinction is the effect that causes the magnitude of a stellar object to dim due to photons being scattered and absorbed by the dust in the interstellar medium. The parameter A is called the galactic extinction and is defined as the difference between the magnitude that is observed, m, and the magnitude that would be observed in the absence of dust, m_o and can be written in the following equation,

$$A_X = (m - m_o)_X \tag{4.2}$$

where X is the X-band, the filter in which the magnitude is measured.

If extinction is known in two filters then a value defined as the difference is called reddening or color excess E(X-Y) and is described in the following equation,

$$E(X - Y) = [m(X) - m(Y)] - [m_o(X) - m_o(y)] = A_X - A_Y \tag{4.3}$$

where X is the X-band and Y is the Y-band (Binney 1998).

The E(B-V) are available in NED based on the dust maps of Schlegel et al. (1998) for each galaxy and are listed in Table 4.3 at the end of this section. These values needed to be converted to A_I since our images were taken in the F814W bandpass and therefore give magnitudes in the I-band. This conversion is done using data from Siranni et al. 2004. They give a value of 1.8 for the F814W filter and early-type galaxy. Thus, A_I can be obtained for each galaxy the following way:

$$E(X - Y) * 1.8 = A_I \tag{4.4}$$

There is also an aperture correction of -0.09 for an aperture of r = 5pix (0.25 arcsec) using ACS in the F814W filter (Sirianni 2005).

Aperture correction within DAOphot

Since all of the magnitudes are coming from psf fitting of objects during the *allstar* task, we need to calculate what aperture correction must to be applied in order to obtain total magnitudes. We do this by making a list omitting the brightest 1000 stars in the final allstar catalog. This list is used in the task *substar*, which produces an image that subtracts all objects in the list, leaving only the 1000 brightest stars. The *phot* task is run on this image using an aperture of 10 pixels in diameter (which corresponds to an aperture of 0.5 arcsec). Comparing the .mag file that phot produces to the image3.dat file from the final allstar run will give the difference between the psf fitted magnitudes and the aperture 10pix magnitudes. The following Figures 4.5-4.7, show plots of the difference in magnitude values (aperture magnitude from the brightest stars minus *allstar* magnitude verses the *allstar* magnitude. The correlation shown in Figures 4.5- 4.7 give the aperture correction that needs to be applied to each magnitude value. The median difference is labeled in each plot next to the galaxy name.

Table 4.3 contains the aperture correction (Sirriani aperture correction plus DAOphot aperture correction from previous plots) in the first column, with the second column listing the E(B-V) values from NED. The third column in the extinction values in the I-band. The last column is the total correction, apercor + A_I.

4.3.5 Completeness

By adding a known number of artificial stars (with given magnitudes) to the image and then running the same detection and measurement process, one can see the fraction of objects the software does not detect. The percentage of objects detected as a function of magnitude is called completeness function. The completeness progressively decreases as you get to fainter and fainter objects (higher magnitudes, see

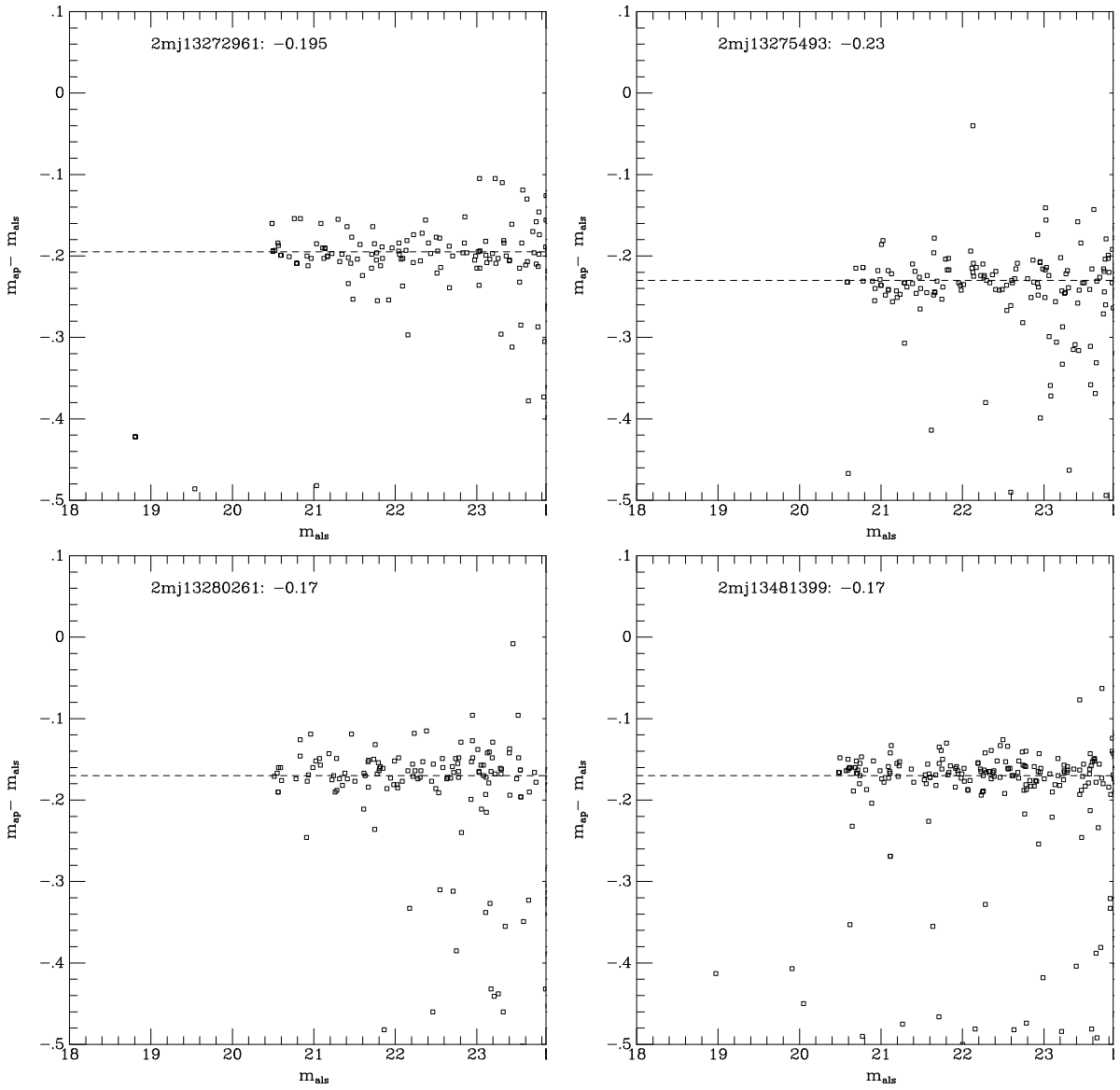

Figure 4.5 Aperture Corrections for 2mj13272961, 2mj13275493, 2mj13280261 and 2mj13481399

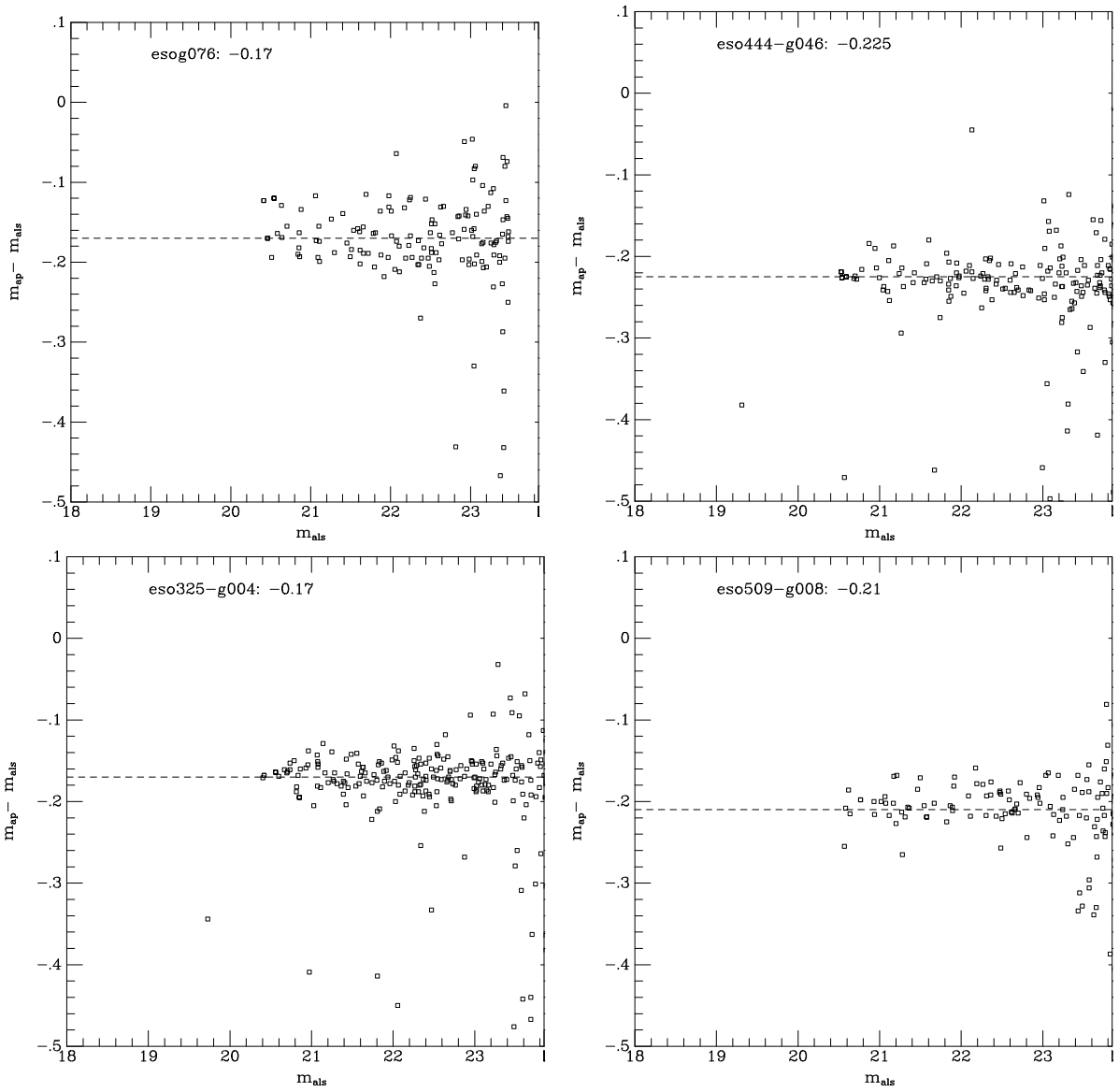

Figure 4.6 Aperture Corrections for ESO383-g076, ESO444-g046, ESO325-g004, and ESO509-g008

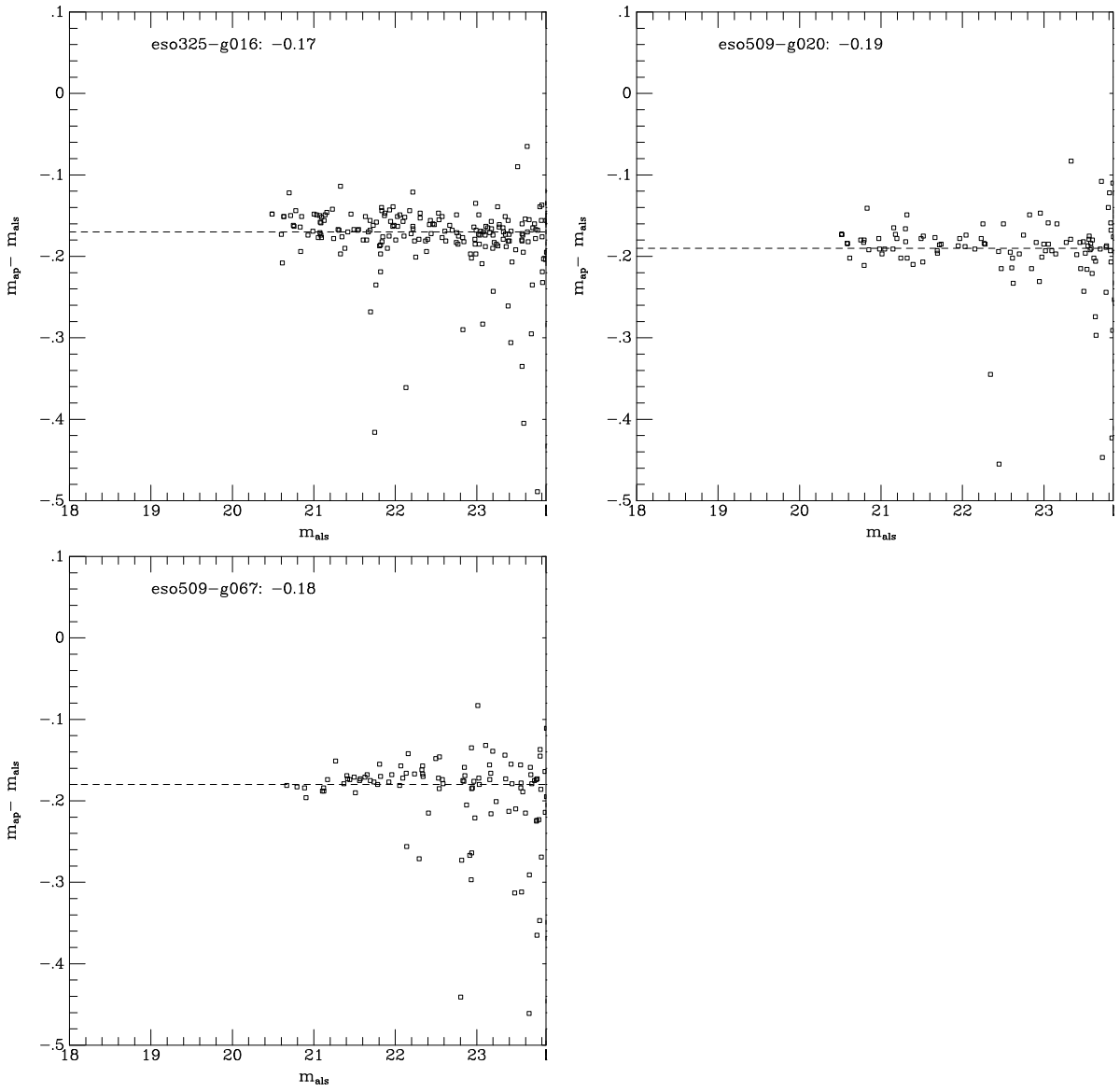

Figure 4.7 Aperture Corrections for ESO325-g016, ESO509-g020, and ESO509-g067

Table 4.3. Magnitude Correction

galaxy	apercor	E(B-V)	A_I	total correction
ESO509-G008	-0.30	-0.054	-0.097	-0.397
ESO509-G020	-0.28	-0.057	-0.103	-0.363
ESO509-G067	-0.27	-0.068	-0.122	-0.392
ESO325-G016	-0.26	-0.078	-0.140	-0.400
ESO325-G004	-0.26	-0.060	-0.108	-0.368
ESO383-G076	-0.26	-0.054	-0.097	-0.357
2MJ13481399	-0.26	-0.055	-0.099	-0.359
ESO444-G046	-0.32	-0.050	-0.090	-0.410
2MJ13275493	-0.32	-0.050	-0.090	-0.410
2MJ13272961	-0.29	-0.060	-0.108	-0.398
2MJ13280261	-0.26	-0.051	-0.092	-0.352
b1608	-0.29	-0.030	-0.054	-0.344
class0218	-0.24	-0.069	-0.123	-0.363
field-14	-0.30	-0.015	-0.028	-0.328
gdds-sa02	-0.28	-0.024	-0.043	-0.323

Chapter 1).

The task in DAOphot used to add additional artificial stars is called *addstar*. *Addstar* also produces a list of the magnitudes and positions of the added artificial stars. This file is called an image.art file. We do two runs of daofind, phot and allstar to get a final catalog of objects detected. We only do two runs instead of the three, which is explained in the previous section. The first run was just done to get the flat image, which we then use here for the final two runs. The final catalog is called add3.dat (created by using *pdump* on the final allstar file). Once we have the add3.dat files we can compare this final list to the list of stars added to the image. We can now see the number of added objects actually detected.

This information was binned by magnitude. The bins range from magnitude 20 to 29 by increments of 0.5. The image.art file and the add3.dat file are binned individually by magnitude. Then we can make a file where each bin will have number detected divided by the number inserted into the image. This file is called completeness.bin and used in a python script called pritchfit.py to obtain essential parameters, α and m_0 (the magnitude when completeness reaches 50 percent; not to be confused with the m_0 in the extinction section) for a completeness curve that follows this equation:

$$f = 0.5(\frac{\alpha(m - m_0)}{\sqrt[2]{[1 + \alpha^2(m - m_0)]}}) \tag{4.5}$$

The output for pritchfit.py is an α and m_O and a file with a list of values for the completeness with errors. Once these values are plotted with the data from the completeness.bin file, we obtain the completeness curves. These curves are the presented in following Figures 4.8- 4.10, showing f verses magnitude.

The values obtained to create these plots are listed in Table 4.4 where the columns match the parameters in equation 4.5.

4.3.6 Background

At this distance, our GC candidates are point sources therefore to make sure we are not counting foreground stars or background galaxies, we use "background"

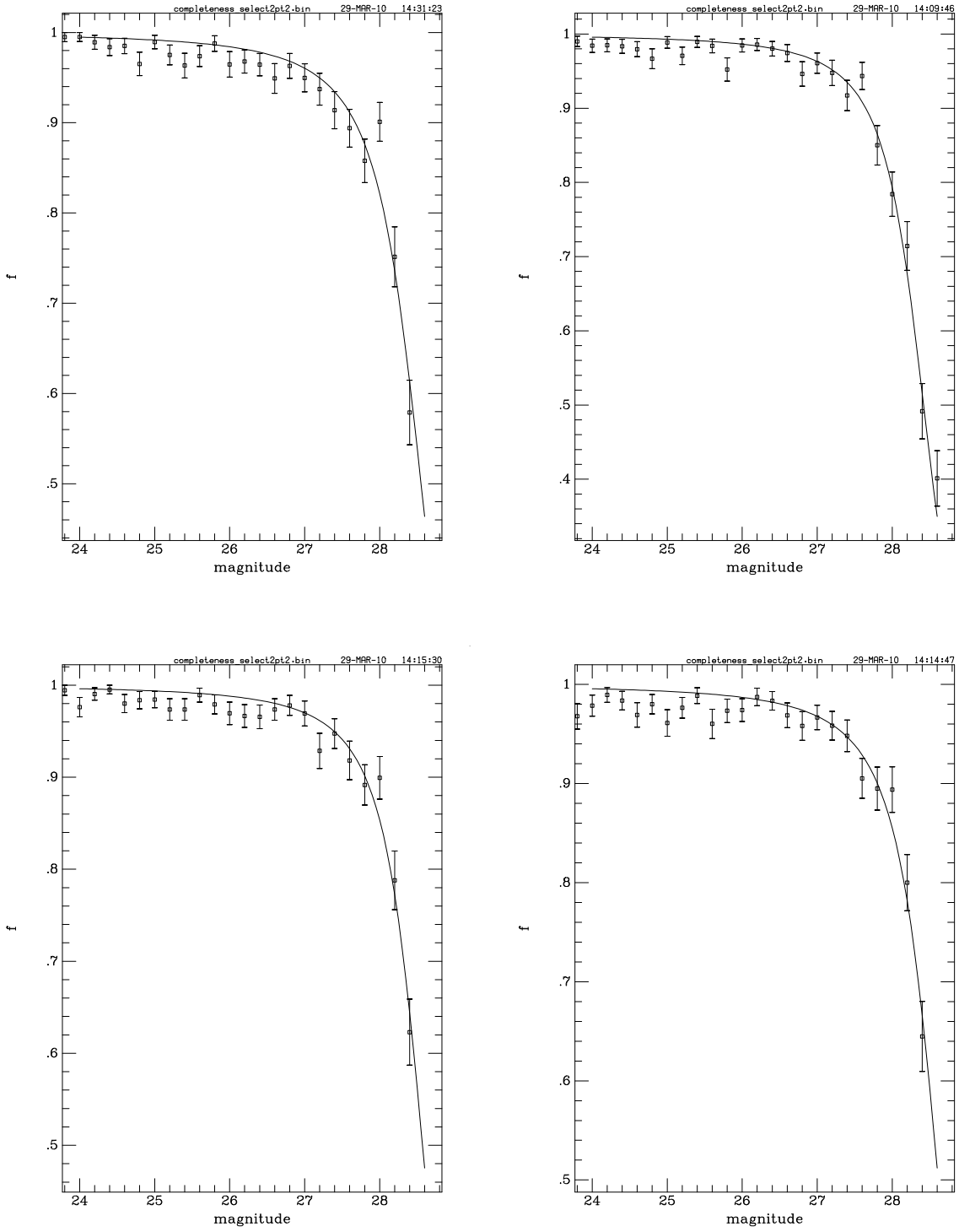

Figure 4.8 Completeness Curves for 2mj13275493, 2mj13481399 (top row), 2mj13272961, and 2mj13280261 (bottom row) plotted with percentage of detected objects versus magnitude.

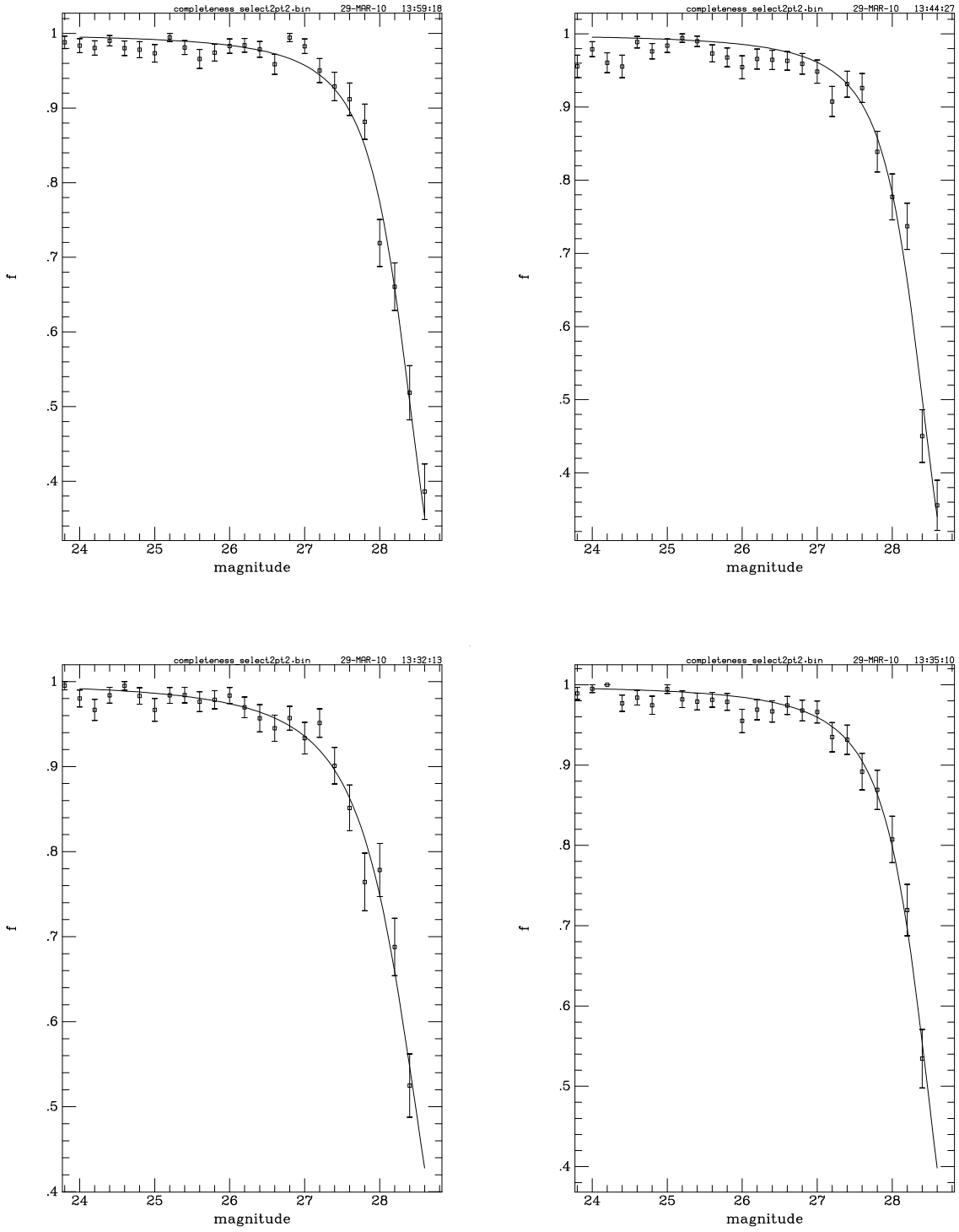

Figure 4.9 Completeness Curves for ESO383-g076, ESO444-g046 (top row), ESO325-g004, and ESO509-g008 (bottom row) plotted with percentage of detected objects versus magnitude.

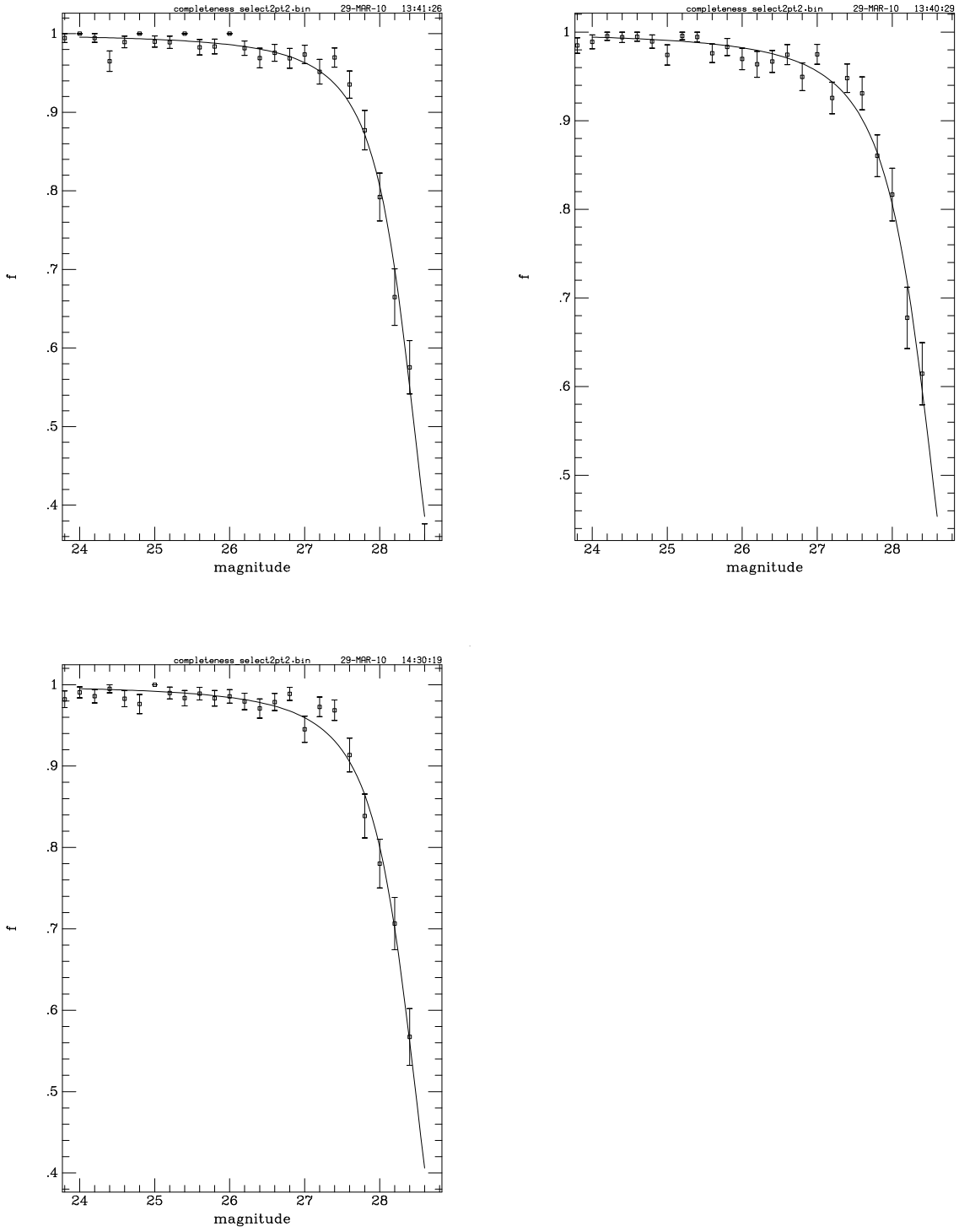

Figure 4.10 Completeness Curves for ESO325-g016, ESO509-g020 (top row), and ESO509-g067 plotted with percentage of detected objects versus magnitude.

Table 4.4. Completeness

galaxy	α	m_0
ESO509-G008	1.588	28.4688
ESO509-G020	1.443	28.5352
ESO509-G067	1.574	28.4783
ESO325-G016	1.684	28.4603
ESO325-G004	1.201	28.4785
ESO383-G076	1.607	28.4080
2MJ13481399	1.731	28.4179
ESO444-G046	1.703	28.4020
2MJ13275493	1.520	28.5520
2MJ13272961	1.749	28.5716
2MJ13280261	1.642	28.6145
allbckgnd	1.973	28.5156

fields with similar galactic latitudes taken through the same F814W filter. We run the "background" fields though the same data analysis (DAOphot and selection and listed in Table 4.3 for magnitude correction) and then subtract just the number of objects detected in that magnitude range from the GC candidates detected to get a background corrected number of objects. The following Figure 4.11 is that of each field's histogram of N galaxies verses I band magnitude. The dotted line represents ~ 28.5 as our initial faint magnitude cutoff. This choice is supported by the completeness curves in 4.8-4.10 that show the magnitude in which completeness falls to 50% at around 28.5 for each galaxy.

4.3.7 Selection

Sharpness and χ

To better narrow down the lists of objects obtained from DAOphot, we chose to cut the data files with respect to two parameters, χ and sharpness from the final allstar output file image3.als (defined in section 4.3.3). Since we only have data in one filter for all but one galaxy, size and color cannot be used to help discern which objects are good GC candidates in our list of detected objects. Once χ and sharpness were plotted against magnitude and each other, correlations were found. Figures 4.12-4.15 show these correlations for 4 different galaxies. The plots of the top row are the values obtained without masking out the uneven edges of each image. Since the galaxy images are summed from several dithered exposures the edges can be very noisy. Noise can cause many false detections at the edges of the image. Once they are masked stronger correlations can be seen (bottom row of Figures 4.12- 4.15). These plots also show that the fainter the magnitude, the more non-point sources detected. DAOphot's manual suggests the values for χ and sharpness are good indicators of whether a detected object is a point source (star) or not. χ should be ~ 1 or it is not a star. This is why the range of $\chi < 2$ was chosen. It also suggests that stars should have a sharpness value of ~ 0, and deviates greatly from 0 if they are cosmic rays or other bad pixels in the image. Beaulieu et al. (2001) used a sharpness range of

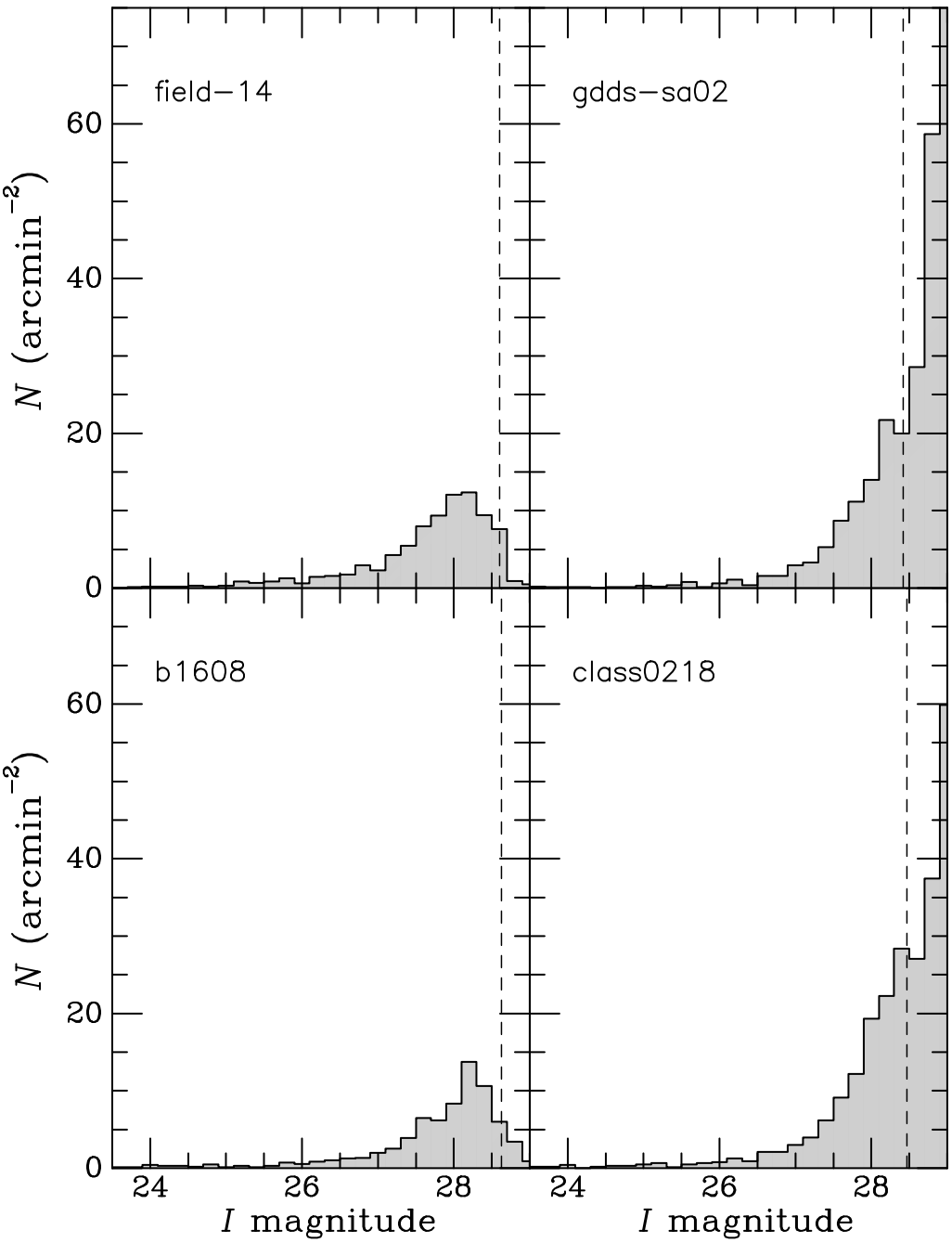

Figure 4.11 Number of objects in each "background" field. The vertical dotted line is where completeness goes to zero.

-0.2 to 3.0, which seemed reasonable compared to our own plots. Sabbi et al. (2008) chose $\chi < 4$ and a range of -.5 < sharpness < .5 for the F814w filter. Looking at the histograms of sharpness verses magnitude, Figures 4.16- 4.18, the scatter around zero is from -0.2 to 3.0 with some plots showing another bump at 0.5. We decided on the selection range of sharpness -0.2 to 3.0 for our GC candidates.

Magnitude

A magnitude cut of 23.5 to 27.5 was applied to select GC candidates. The faint cut is 27.5 because past this magnitude we cannot get reasonable completeness, the completeness falling below 90% around 27.5 (see Figures 4.8- 4.10). The famous globular cluster luminosity function, discussed in Chapter 1 and the following section, shows at these distances GCs will not have magnitudes much brighter than 23.5, which is the basis for our bright cut.

4.4 GCLF

In Chapter 1 it was explained that the Globular Cluster Luminosity Function (GCLF) was assumed to be universal for globular cluster systems. Our data does not go far enough beyond the turnover (peak of Gaussian luminosity function) to give a reliable fit. Therefore, our data cannot be used for distance measurements. However, it is interesting to plot the GCLF that is available and see if an extrapolated turnover corresponds to the known distances to these Abell clusters.

Using distance moduli for each cluster from NED and M_I = -8.5 mag (Harris et al. 2009), a value for the turnover magnitudes, m_0 from equation 1.6, was calculated for each cluster: A3558 = 28.02, A3570 = 27.43, A3571= 27.58, A1736a = 27.39, and AS0740 = 27.28. In Figures 4.19- 4.21) show the "background" population in red and the detected GCs in black. These histograms match the first half of the Gaussian curve and when the background is taken into account, the turnover magnitudes seem to match the values obtained from NED.

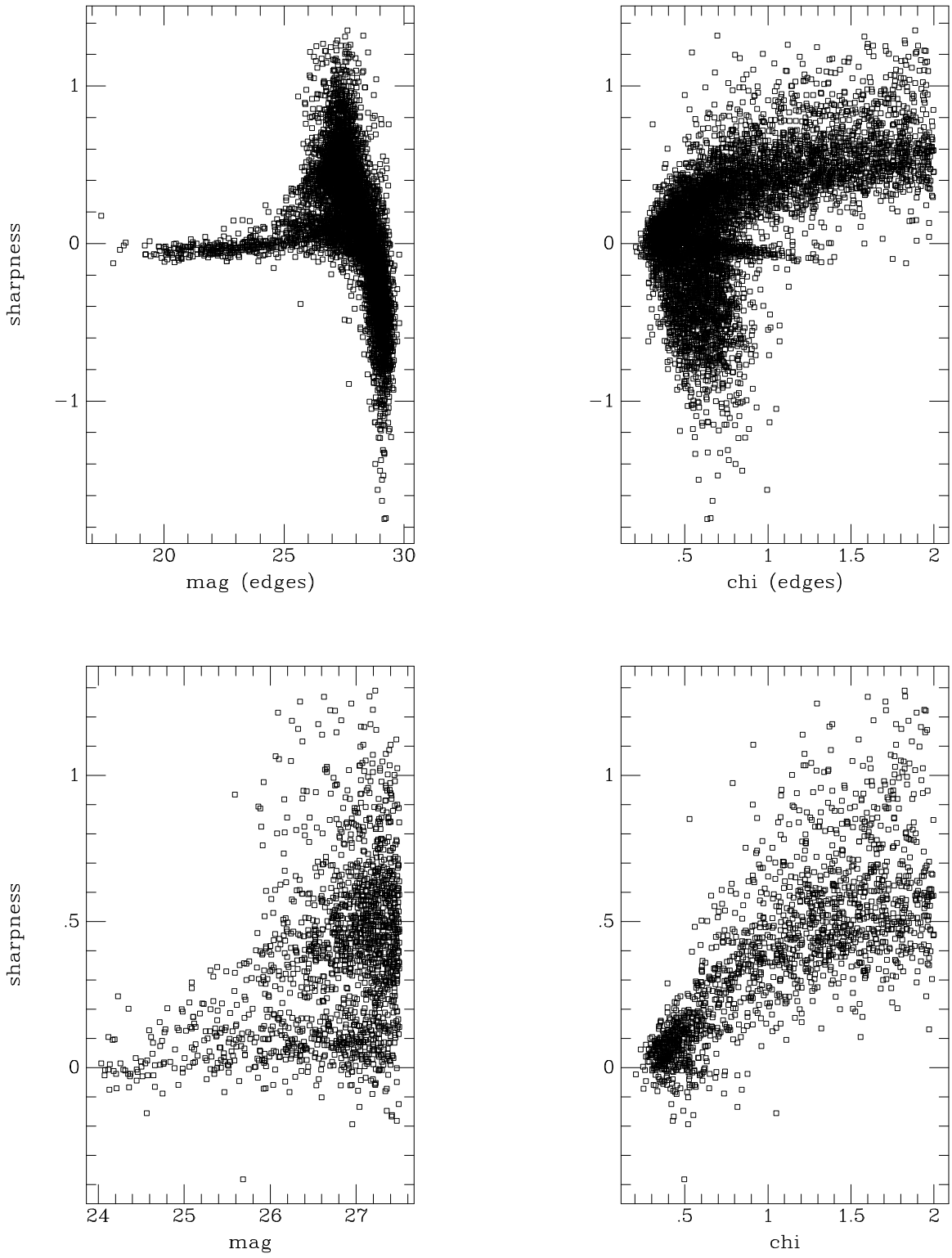

Figure 4.12 2mj13481399 sharpness vs magnitude and *chi* with and without edges cut

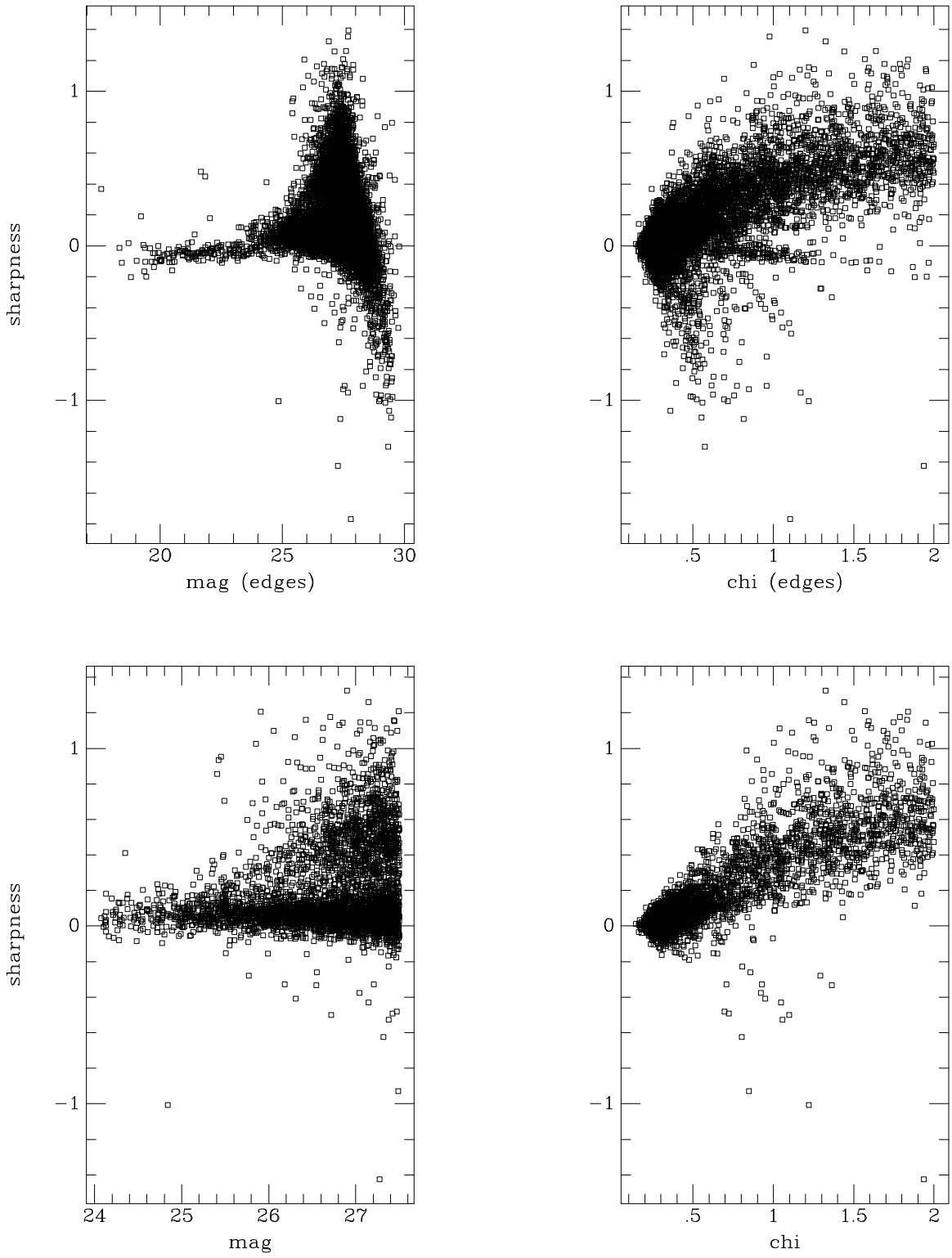

Figure 4.13 2mj13272961 sharpness vs magnitude and *chi* with and without edges cut

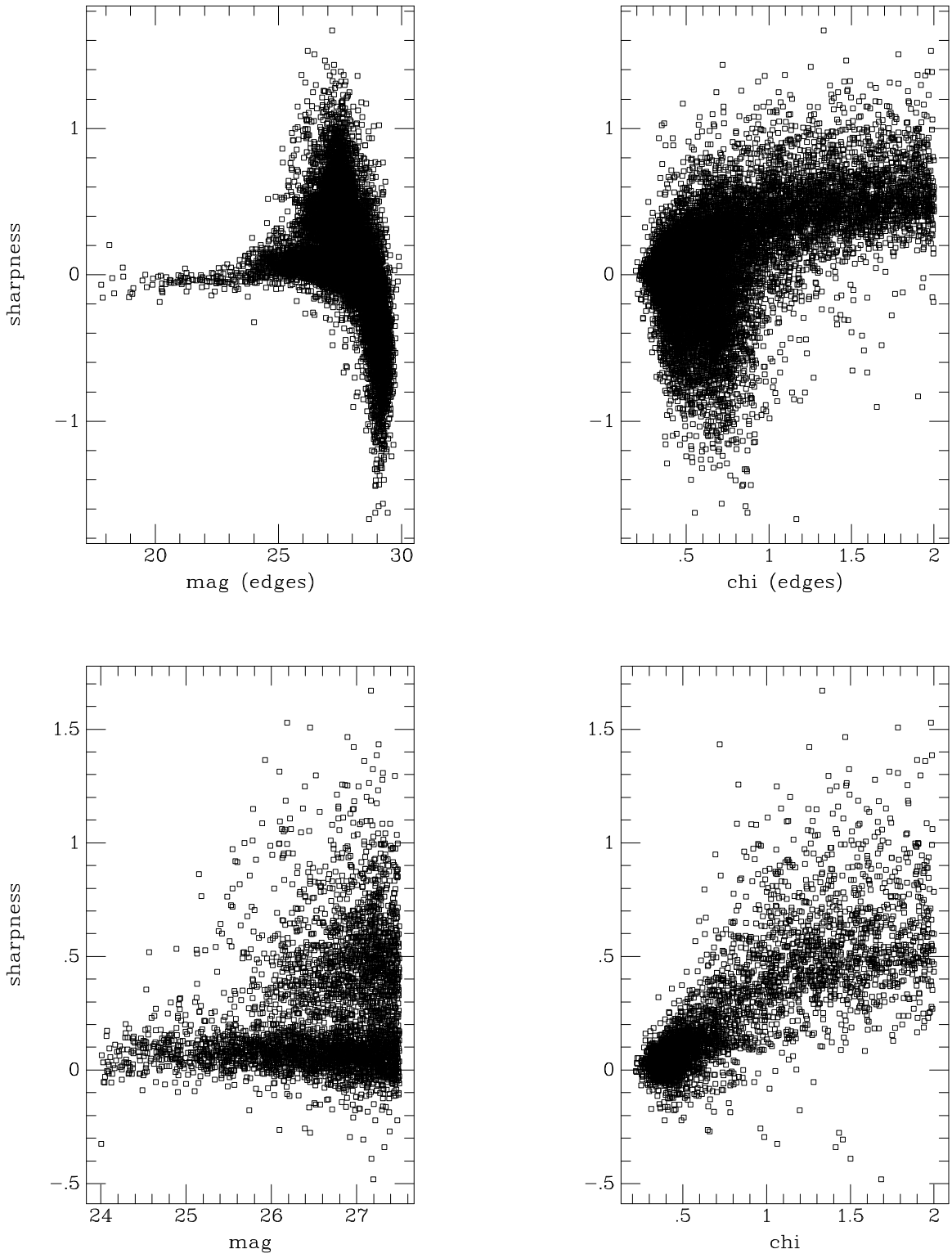

Figure 4.14 eso509-g008 sharpness vs magnitude and *chi* with and without edges cut

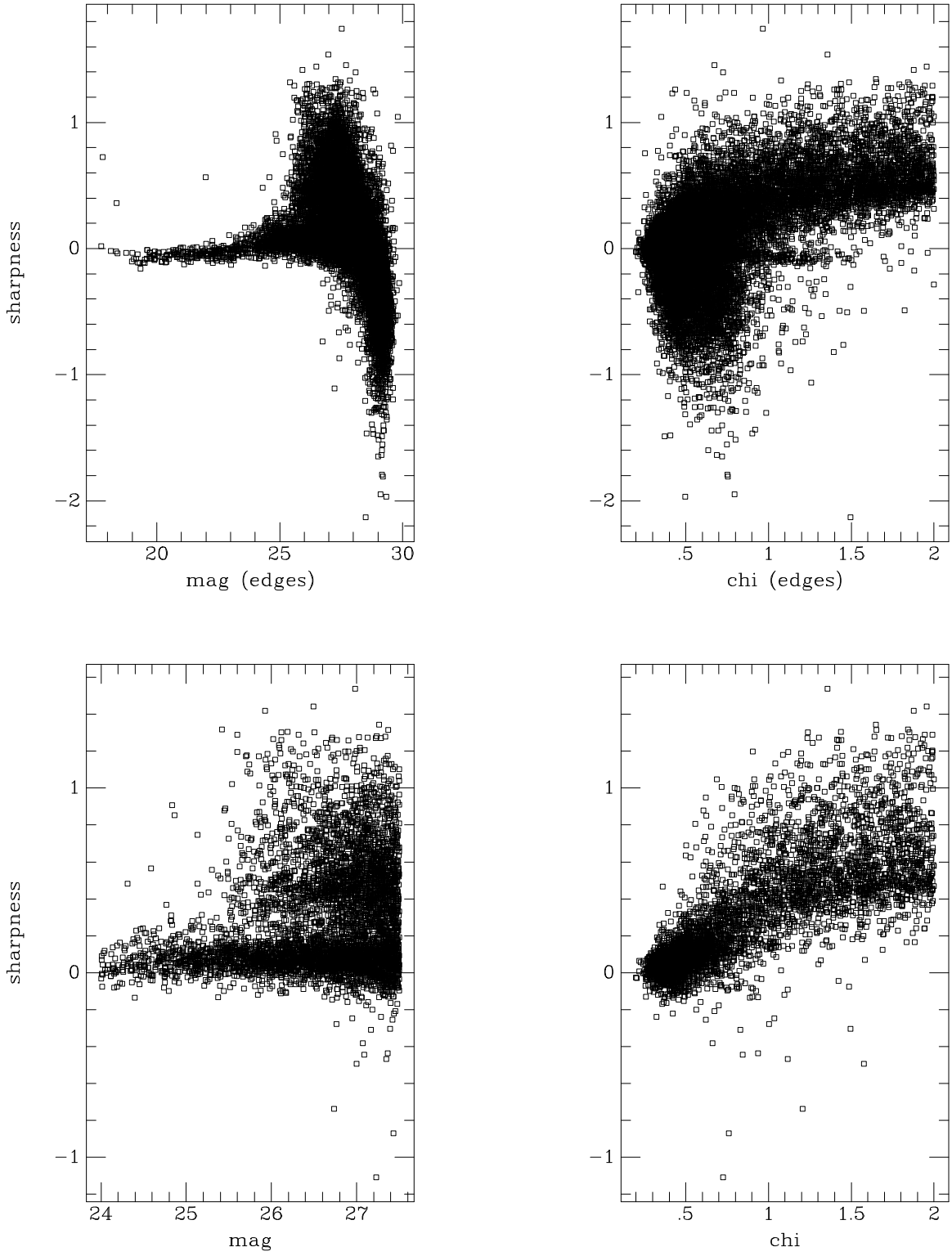

Figure 4.15 eso325-g004 sharpness vs magnitude and *chi* with and without edges cut

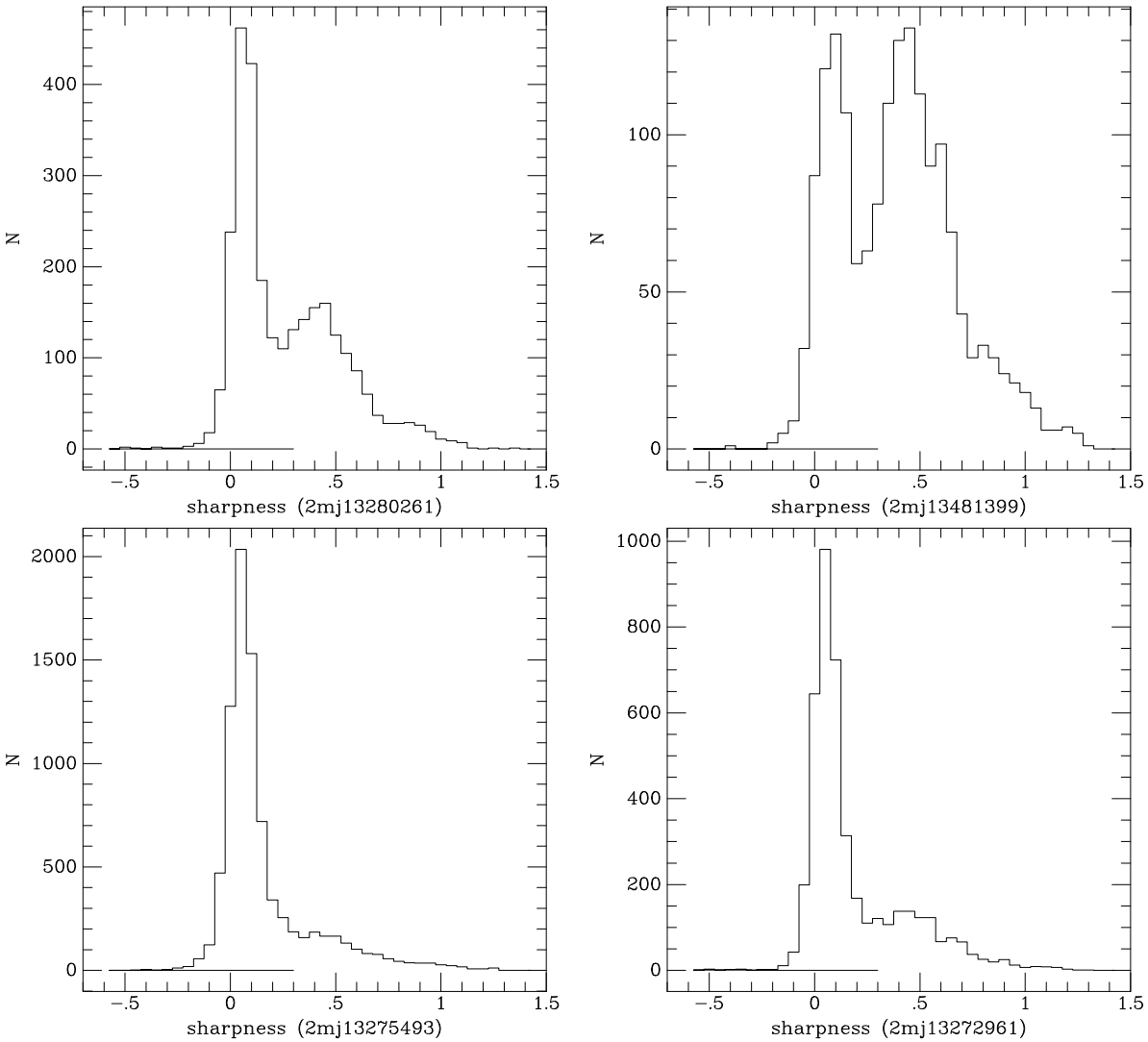

Figure 4.16 Sharpness histograms

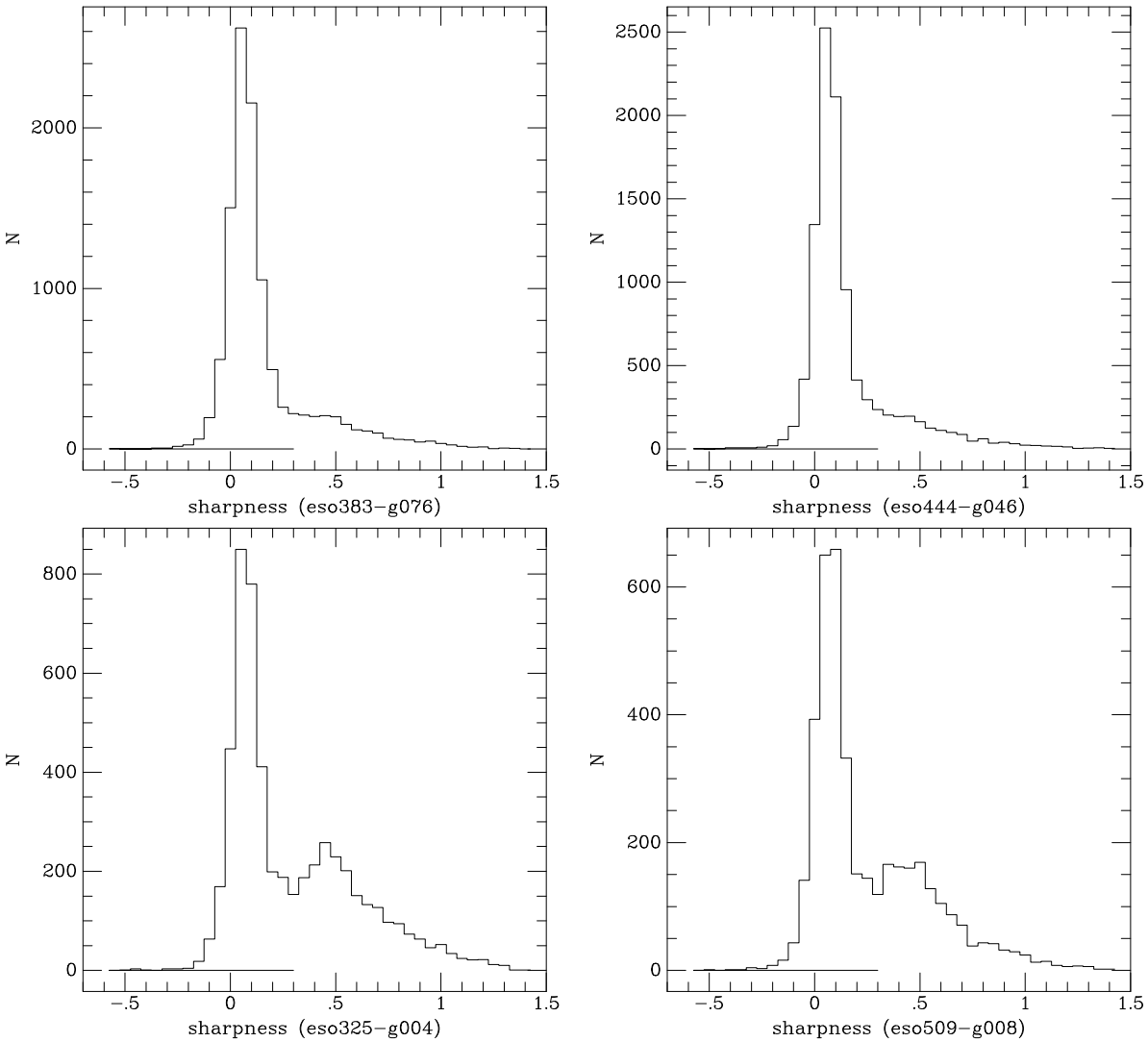

Figure 4.17 Sharpness histograms

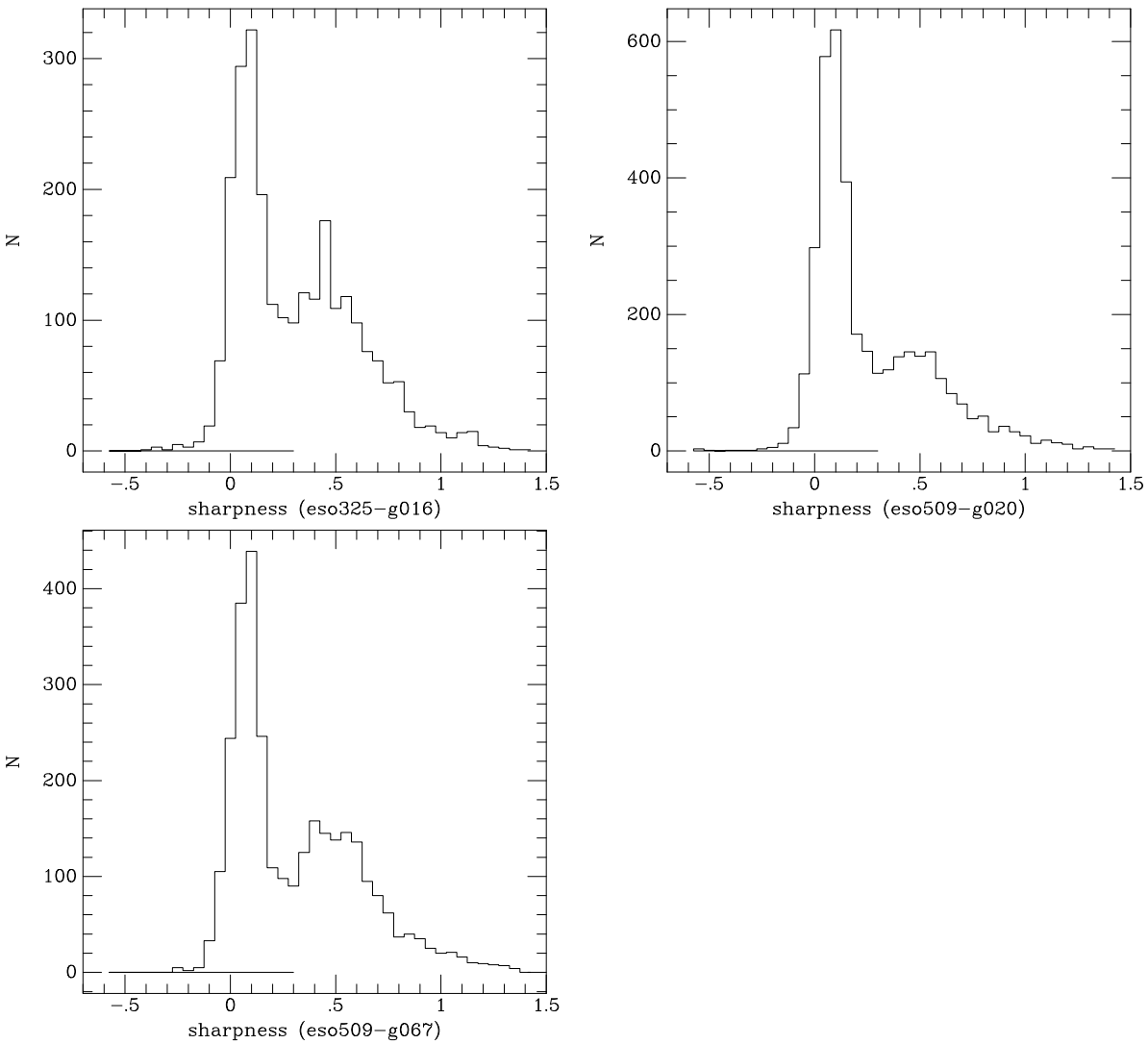

Figure 4.18 Sharpness histograms

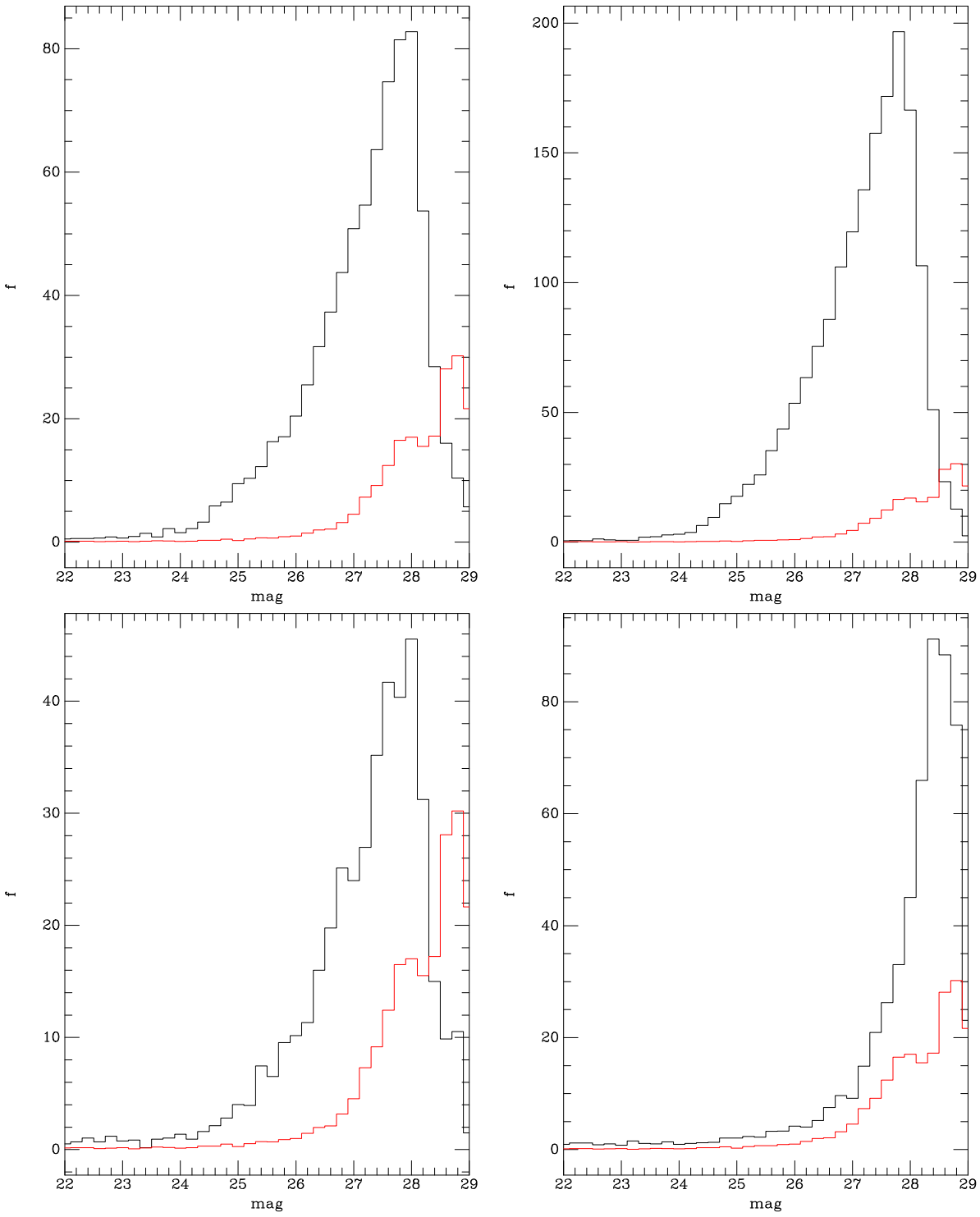

Figure 4.19 GCLF for 2mj13272961, 2mj13275493, 2mj13280261 and 2mj13481399. The red line presents the background population. The black line represents the total number of detected point sources after completeness correction.

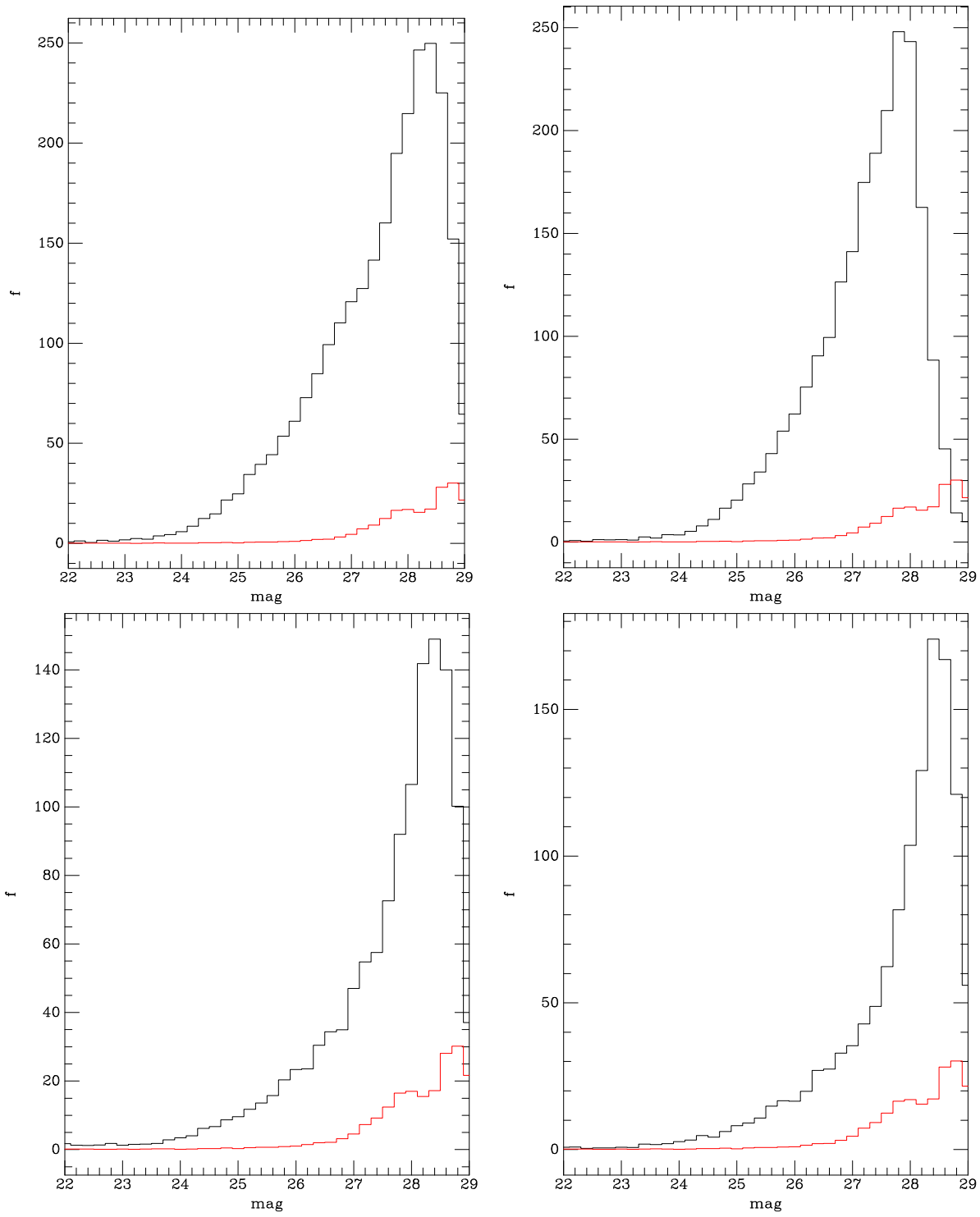

Figure 4.20 GCLF for ESO383-g076, ESO444-g046, ESO325-g004, and ESO509-g008. The red line presents the background population. The black line represents the total number of detected point sources after completeness correction.

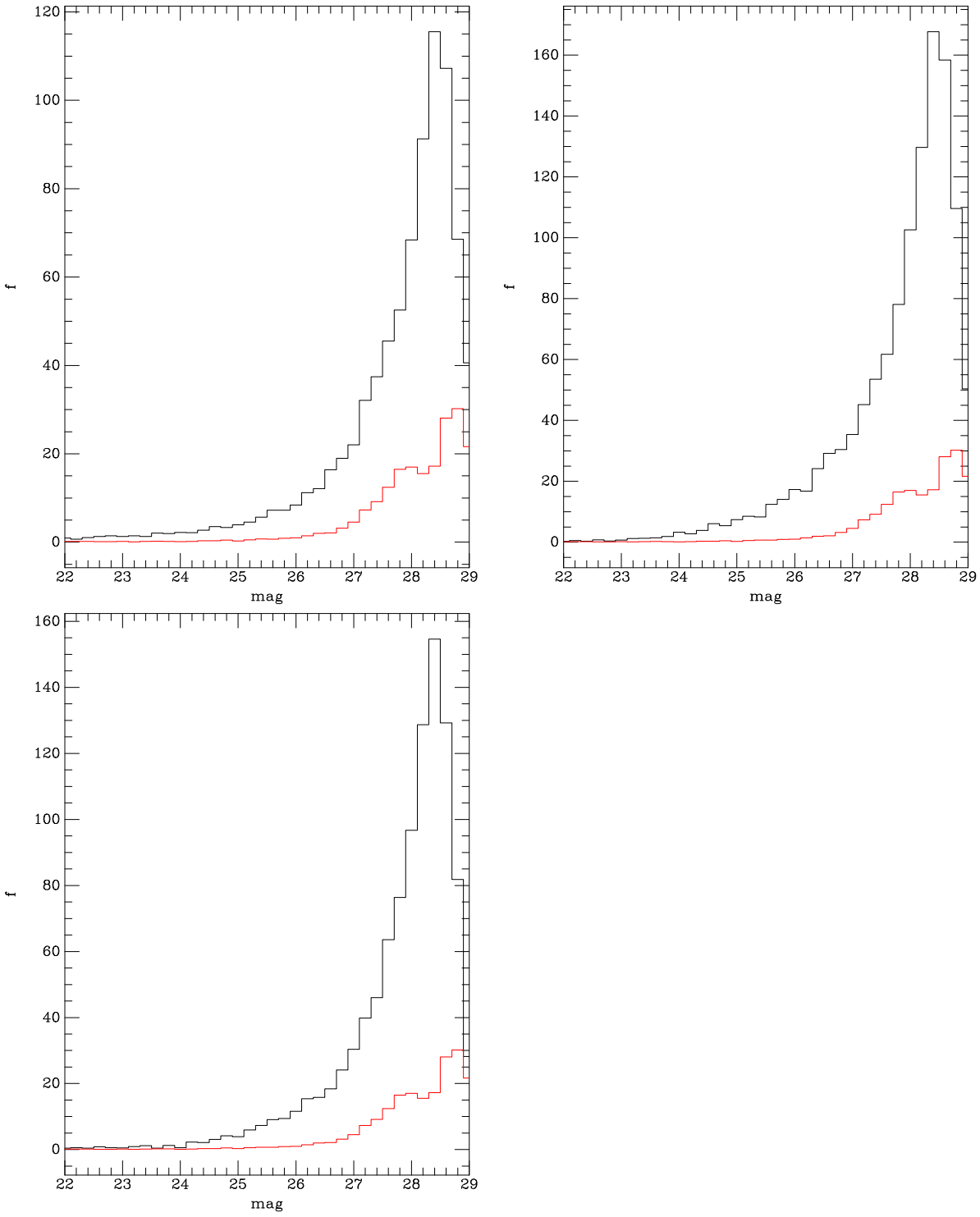

Figure 4.21 GCLF for ESO325-g016, ESO509-g020, and ESO509-g067. The red line presents the background population. The black line represents the total number of detected point sources after completeness correction.

Bibliography

[1] Beaulieu, S. F., Gilmore, G., Elson, R. A. W., Johnson, R. A., Santiago, B., Sigurdsson, S., & Tanvir, N. 2001, AJ, 121, 2618

[7] Binney, J., & Merrifield, M. 1998, Galactic astronomy / James Binney and Michael Merrifield. Princeton, NJ : Princeton University Press, 1998. (Princeton series in astrophysics) QB857 .B522 1998

[3] Blakeslee, J. 2004, HST Proposal, 10429

[4] Blakeslee, J. P., Anderson, K. R., Meurer, G. R., Benítez, N., & Magee, D. 2003, Astronomical Data Analysis Software and Systems XII, 295, 257

[4] Böhringer, H., et al. 2004, A&A, 425, 367

[6] Fadda, D., Girardi, M., Giuricin, G., Mardirossian, F., & Mezzetti, M. 1996, ApJ, 473, 670

[7] Ford, H. C., et al. 2003, Proc. SPIE, 4854, 81

[8] Harris, W. E. 2009, ApJ, 703, 939

[9] Lynden-Bell, D., Faber, S. M., Burstein, D., Davies, R. L., Dressler, A., Terlevich, R. J., & Wegner, G. 1988, ApJ, 326, 19

[10] Postman, M., & Lauer, T. R. 1995, ApJ, 440, 28

[11] Sabbi, E., Gallagher, J. S., Smith, L. J., de Mello, D. F., & Mountain, M. 2008, ApJ, 676, L113

[12] Schindler, S. 2000, A&AS, 142, 433

[13] Schlegel, D. J., Finkbeiner, D. P., & Davis, M. 1998, ApJ, 500, 525

[14] Shapley, H. 1930, Harvard College Observatory Bulletin, 874, 9

[15] Smith, R. J., Lucey, J. R., Hudson, M. J., Schlegel, D. J., & Davies, R. L. 2000, MNRAS, 313, 469

[16] Smith, R. J., Lucey, J. R., Schlegel, D. J., Hudson, M. J., Baggley, G., & Davies, R. L. 2001, MNRAS, 327, 249

[17] Smith, R. J., Blakeslee, J. P., Lucey, J. R., & Tonry, J. 2005, ApJ, 625, L103

[18] Stetson, P. B. 1987, PASP, 99, 191

[19] Struble, M. F., & Rood, H. J. 1991, ApJS, 77, 363

[20] van den Bergh, S. 2000, PASP, 112, 529

[23] Zhang, Y.-Y., Andernach, H., Caretta, C. A., Reiprich, T. H., Böhringer, H., Puchwein, E., Sijacki, D., & Girardi, M. 2011, A&A, 526, A105

Chapter 5

Shapley Supercluster Results

5.1 Number of Globular Clusters Counted

5.1.1 Completeness and "Background" Correction

To obtain the total population of GCs for each of the 11 galaxies studied, we must perform the proper corrections. DAOphot detects objects in the image and using various cuts, described in Chapter 4, a list of detected objects is recorded. The number of GC candidates in this detected list is then scaled to produce the total number of GCs associated to the host galaxy corrected for completeness and area.

The completeness procedure is performed due to our detection software missing a certain number of objects depending on the object's magnitude. When objects become too faint they are more difficult to detect, therefore, efficiency in detection decreases with increasing magnitude. This exercise calculates the percentage of objects the software is detecting within magnitude bins. We can then use the completeness correction curves to scale the detected objects to total number of GCs in the image. There are also a number of background objects and foreground objects in the field, so there needs to be a "background" correction. As discussed in Chapter

4, the HST archive was searched for images taken in the same filter, F814W, and at similar Galactic latitude. We picked four background fields and performed the same data reduction described in the DATA section (DAOPhot). The background detection lists were subject to the same selection in χ, sharpness and magnitude as the catalogs for the 11 Shapley Supercluster galaxies. Once these selections were applied, the background field catalogs were combined into one file. The "background" object list was then binned by magnitude, as were the detected objects in the 11 galaxies. By subtracting the binned background file from the binned galaxy file, we completed another correction to obtain a value for the total number of GCs. A python script was created to take into account the correction for completeness, background and magnitude (luminosity function). The next correction to get total number of GCs associated with a host galaxy is a consequence of the initial magnitude cut and the subject of the next section.

5.1.2 Magnitude Range and the GCLF Correction

In Chapter 4, we discuss the selection criteria for GC candidates. One selection was magnitude cuts due to the inability to detect objects much fainter than the turnover, which is 27.5 ± 0.5 depending on the Abell cluster distance. Since we are detecting objects only in a magnitude range of $m_{bright} = 23.5$ to $m_{faint} = 27.5$, we are limiting our search for GC candidates. The globular luminosity function (see Chap 1 for full description) shows us that magnitudes of a GC population follow a Gaussian curve with m_0 as the peak magnitude and σ equal to the standard deviation. This shape can be seen in Figure 5.1. The GCs with magnitude above and below our range, whose existence is suggested by this Gaussian curve, need to be counted in the total number of GCs. These additional globular clusters are taken into account by considering a ratio of areas in luminosity space. If we are counting only a fraction of the total number of GCs, that fraction is equal to the ratio of the corresponding areas under the Gaussian curve or integral and may be represented in the following way,

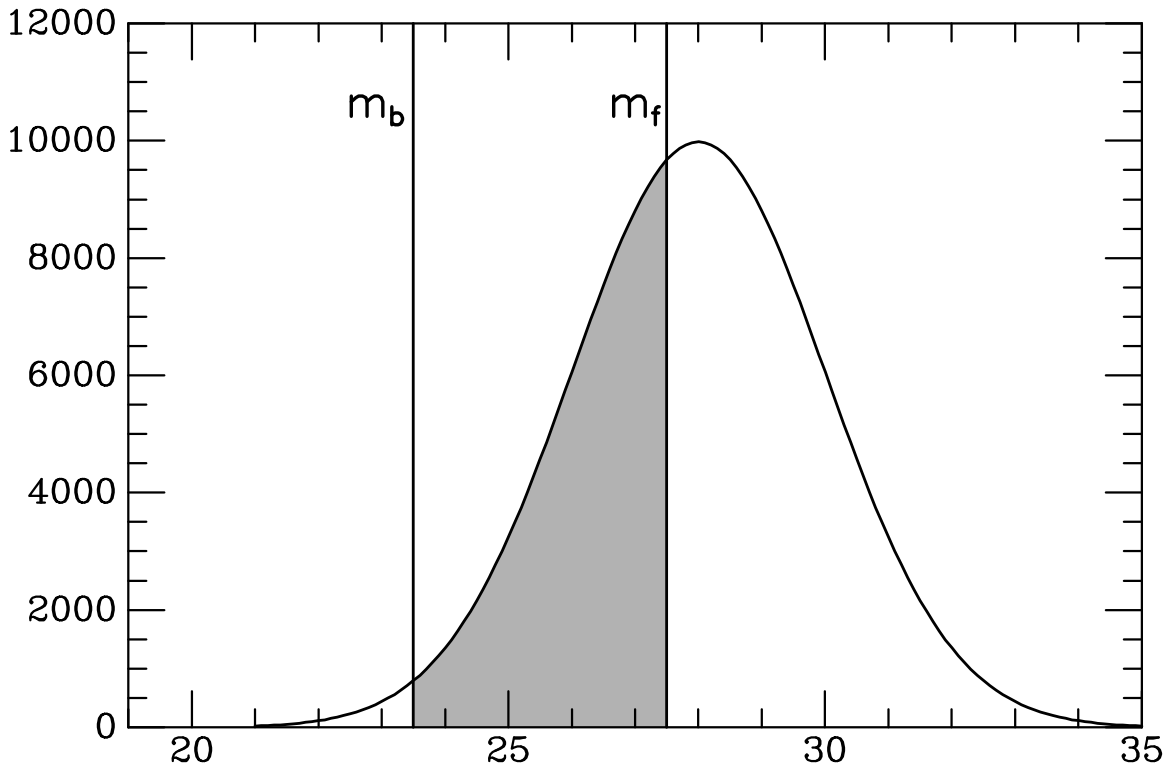

Figure 5.1 The vertical lines are the locations of the $m_{bright} = 23.5$ and $m_{faint} = 27.5$. The peak of this Gaussian curve is called m_0.

$$\frac{N_{count}}{N_{tot}} = \%\text{ counted} = \frac{\text{area under curve between magnitude selection range}}{\text{total area under Guassian curve}} \quad (5.1)$$

where N_{count} is the value of the number of GCs associated with the host galaxy after completeness and background corrections are applied. If we take the total area under the curve to be one, we can calculate the total number of GCs, N_{tot}, using the following equation,

$$\frac{N_{count}}{N_{tot}} = \frac{1}{2}[erf(a) - erf(b)] \quad (5.2)$$

where the 1/2 is from the symmetry of the Gaussian and the erf(x) is the error function, a fractional integral of a Gaussian over the range -x to x in units of sigma. Here the values a and b are obtained by the difference in magnitudes divided by sigma, a = $\frac{m_0 - m_{bright}}{\sigma}$ and b = $\frac{m_0 - m_{faint}}{\sigma}$

5.2 Distribution of GCs and a Radial Correction

The corrections in the previous section were applied to obtain a more realistic total number of GCs associated with the host galaxy. However, the image does not display the whole GC population, so there must be a radial correction. There is also the possibility of the GC population of close neighboring galaxies overlapping.

5.2.1 Distribution of Detected GCs

Here the distribution of the GC candidates, selected from only detection software output lists, can be seen. In the following plots, Figures 5.2 - 5.7, the GCs detected are more concentrated toward the center of the host galaxy. The number in each radial bin is plotted against mean radius of each bin. When the detected objects are plotted using their x,y coordinates, the GC population follows an approximately round distribution about the center of the host galaxy (Figures 5.8 - 5.10). However,

there are some slight exceptions. The two largest galaxies ESO383-G076 and ESO444-G046 seem to have a band of GCs across the center. This band can be seen in Figure 5.9. Here the x,y coordinates of each GC are plotted. In Figure 5.10, ESO509-G020 seems to have GC candidates that are associated with a close neighbor. This contamination from the BCG is discussed in section 5.2.3.

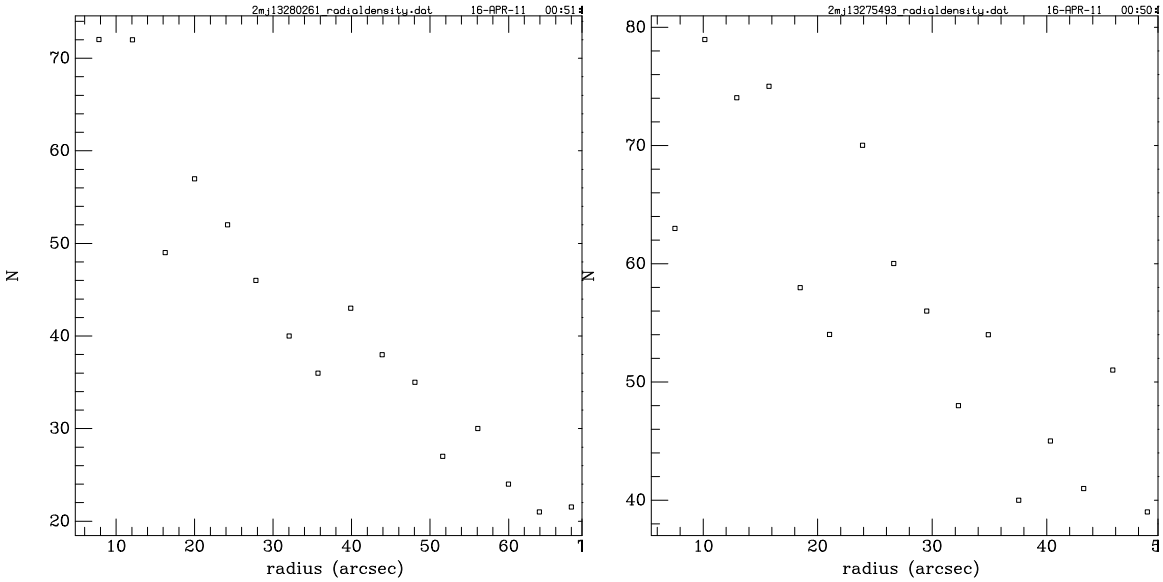

Figure 5.2 Plot of number detected versus radius, in arcseconds, taken from center of host galaxy. Here we show plots for galaxies 2mj13280261 (top) and 2mj13275493 (bottom).

5.2.2 Radial Factor

For our last correction to total number, we acknowledge that the host galaxy has globular clusters that do not lie in the scope of the image. To get an accurate number of GCs that are associated with the galaxy, we need to investigate the globular cluster radial distribution. We so far have not accounted for GC candidates beyond some radius from the center of the host galaxy, or maximum galactic radius, within the image. To get an accurate number of GCs that are associated with the galaxy, we need to investigate the globular cluster distribution. The GC's radial number density, number of GC candidates per area, can be extrapolated from the number of

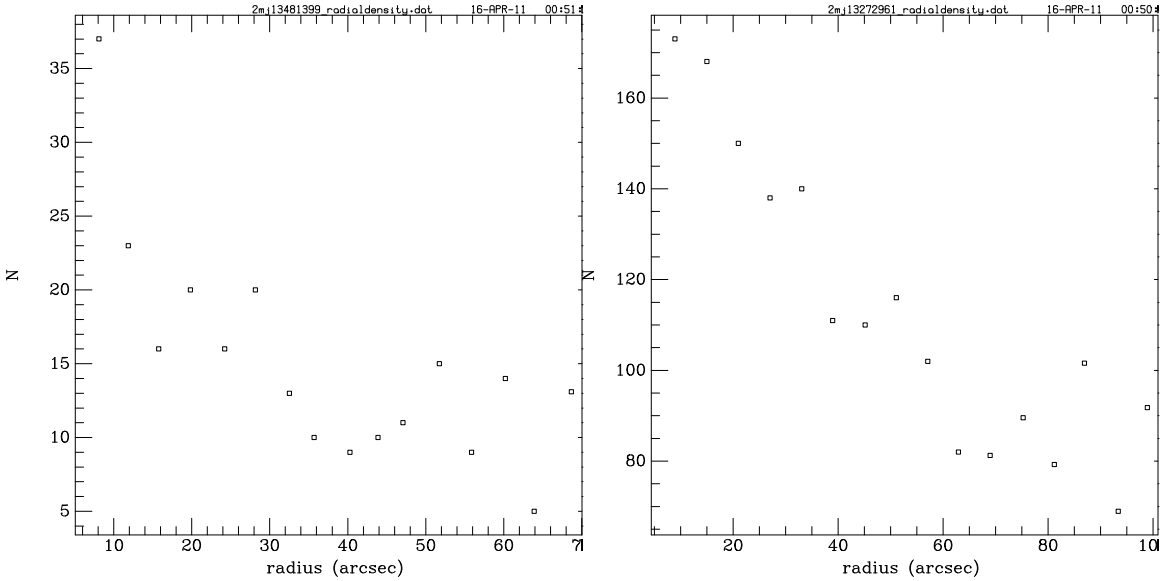

Figure 5.3 Plot of number detected versus radius, in arcseconds, taken from center of host galaxy. Here we show plots for galaxies 2mj13481399 (top) and 2mj13272961 (bottom).

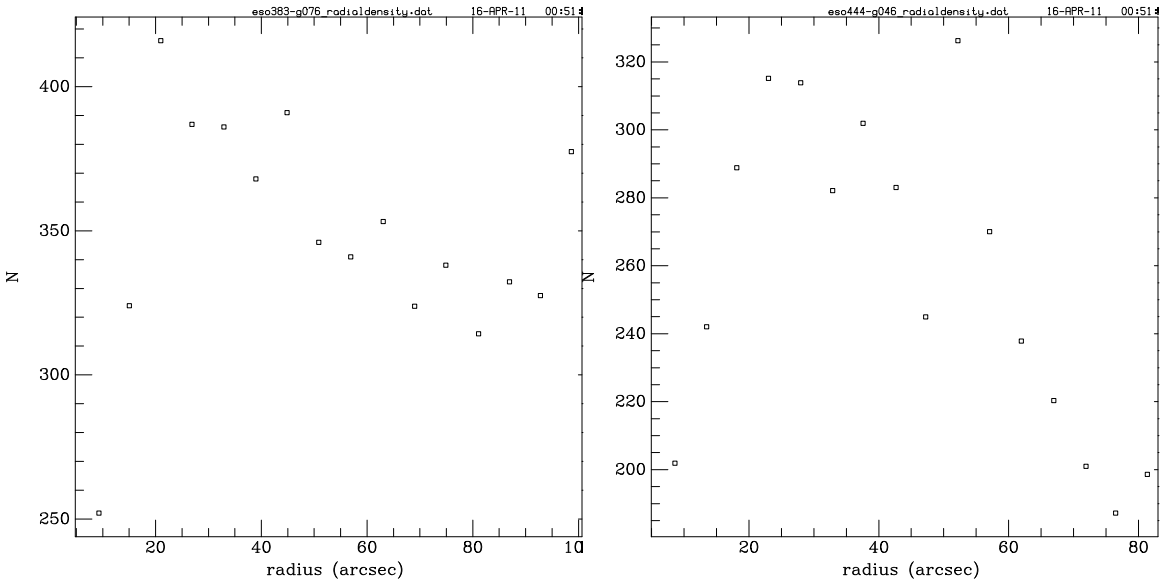

Figure 5.4 Plot of number detected versus radius, in arcseconds, taken from center of host galaxy. Here we show plots for galaxies ESO383-G076 (top) and ESO444-G046 (bottom).

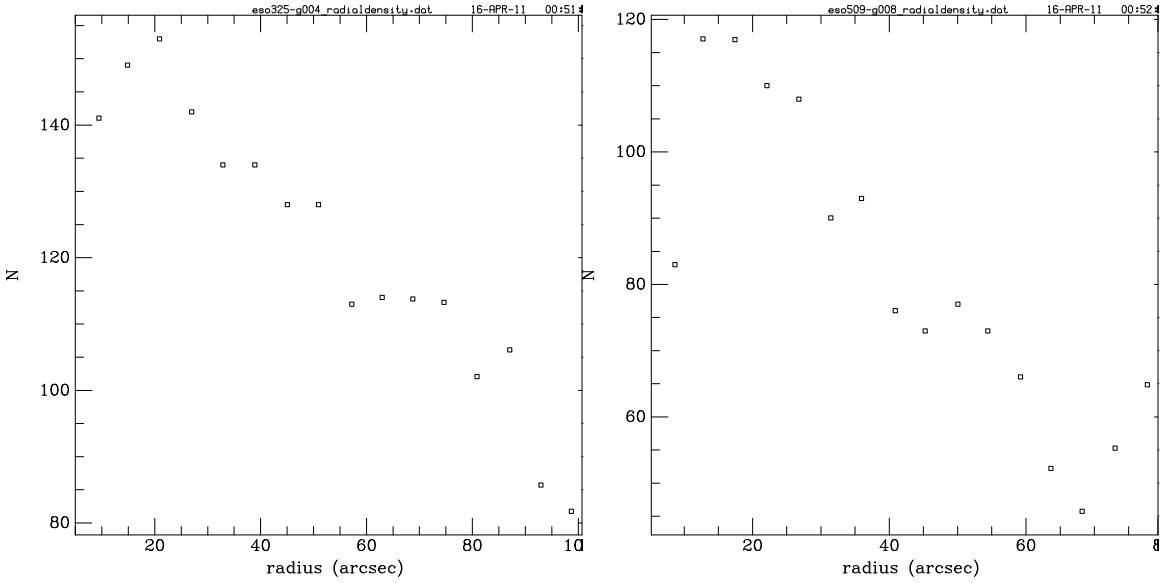

Figure 5.5 Plot of number detected versus radius, in arcseconds, taken from center of host galaxy. Here we show plots for galaxies ESO325-G004 (top) and ESO509-G008 (bottom).

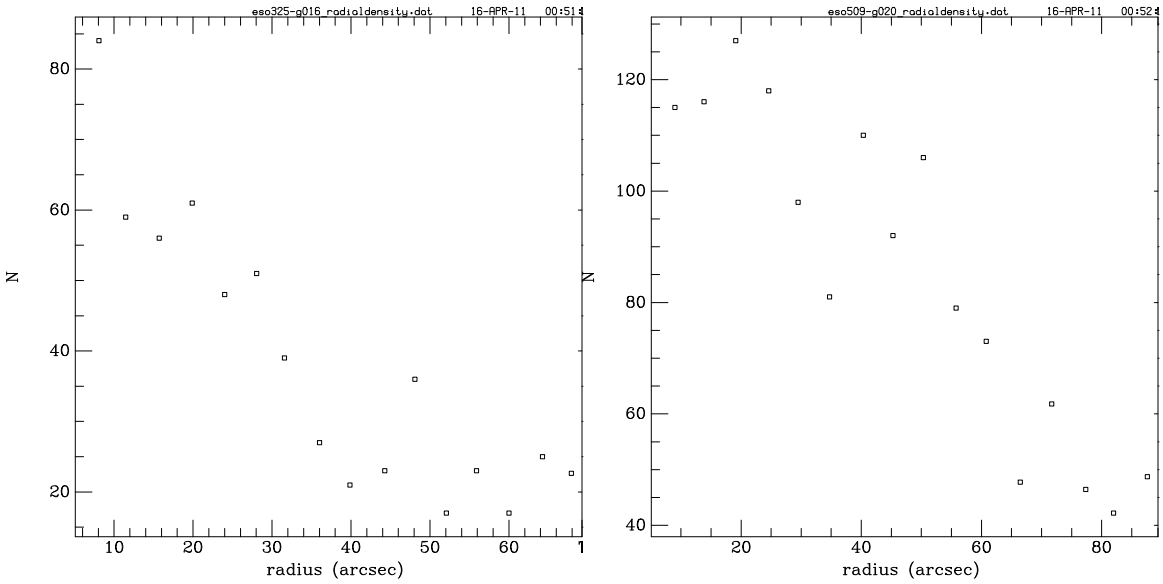

Figure 5.6 Plot of number detected versus radius, in arcseconds, taken from center of host galaxy. Here we show plots for galaxies ESO325-G016 (top) and ESO509-G020 (bottom).

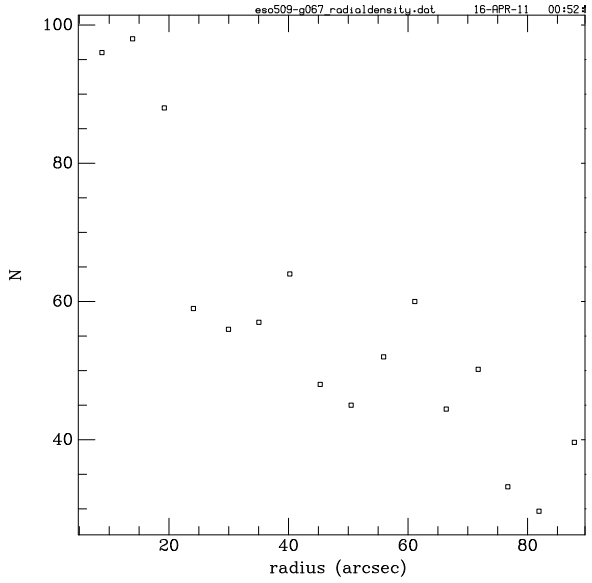

Figure 5.7 Plot of number detected versus radius, in arcseconds, taken from center of host galaxy. Here we show the plot for the galaxy ESO509-G067.

detected objects and their radial values. We first bin the list of detected objects, per galaxy, by galactic radius. We start the binning at a minimum radius of 120 pixels (6 arcsec), to avoid the core of the galaxy which is prone to falsely detected objects, and a maximum radius, which varies by galaxy. These maximum radii correspond to a reasonable radius that includes most of the galaxy's GC population without going too far beyond the edges of the field and are listed in Table 5.1. The maximum and minimum radii were used in plotting Figures 5.8 - 5.10.

Another factor in choosing maximum radius is trying to exclude any neighboring galaxy's GC population. In the image of galaxy ESO444-G046 (Figure 4.3), we see that galaxy 2maxj13275493 is present in the field. This is also true in the reverse; Galaxy ESO444-G046 is present in the image taken of 2maxj13275493. We revisit this issue in the following section, contamination.

The following radial density plots, Figures 5.11 - 5.16, represent the log of the number density, calculated as the number of candidates per unit area in $arcesec^2$ in each annulus, versus the log of the mean of the outer and inner radii of each annulus. Each radius annuli has the thickness of 120 pix (6 arcsec). The relation between log(number density, σ_r) and log(r) is approximately linear, indicating that

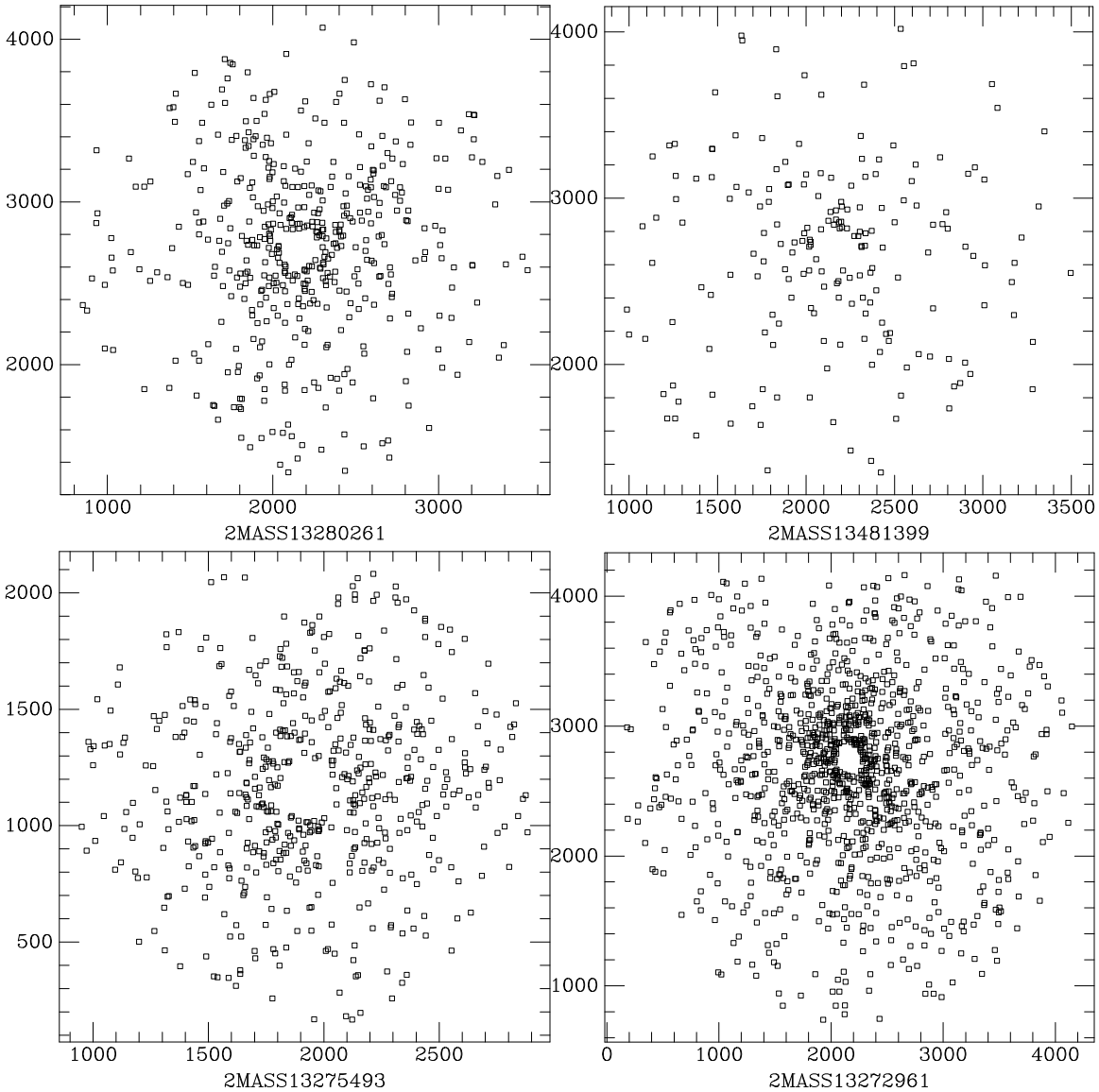

Figure 5.8 Distribution of number detected using x,y coordinates in pixel space. Here we show plots for galaxies 2mj13280261, 2mj13481399, 2mj13275493 and 2mj13272961.

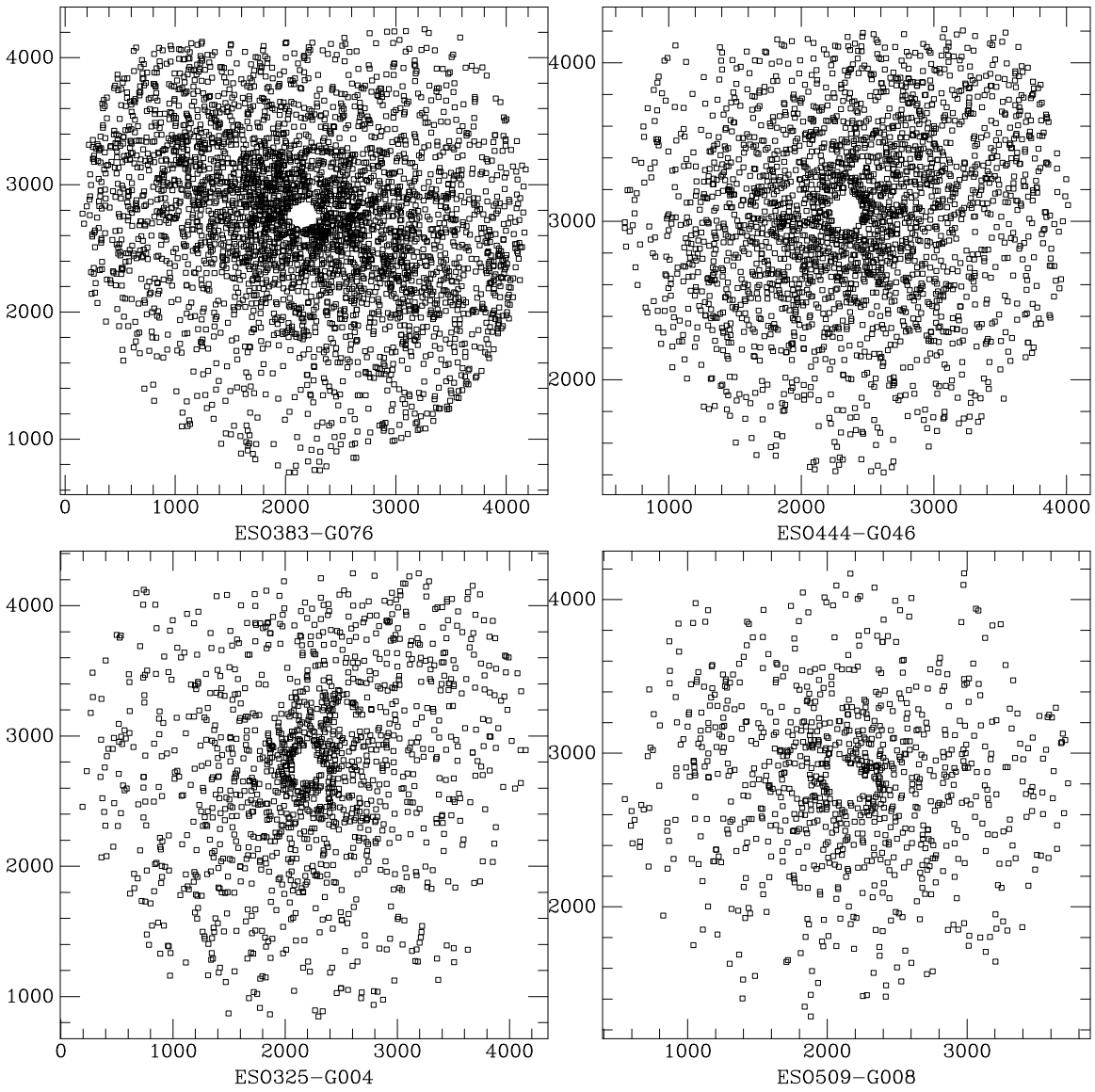

Figure 5.9 Distribution of number detected using x,y coordinates in pixel space. Here we show plots for galaxies ESO383-G076, ESO444-G046, ESO325-G004 and ESO509-G008.

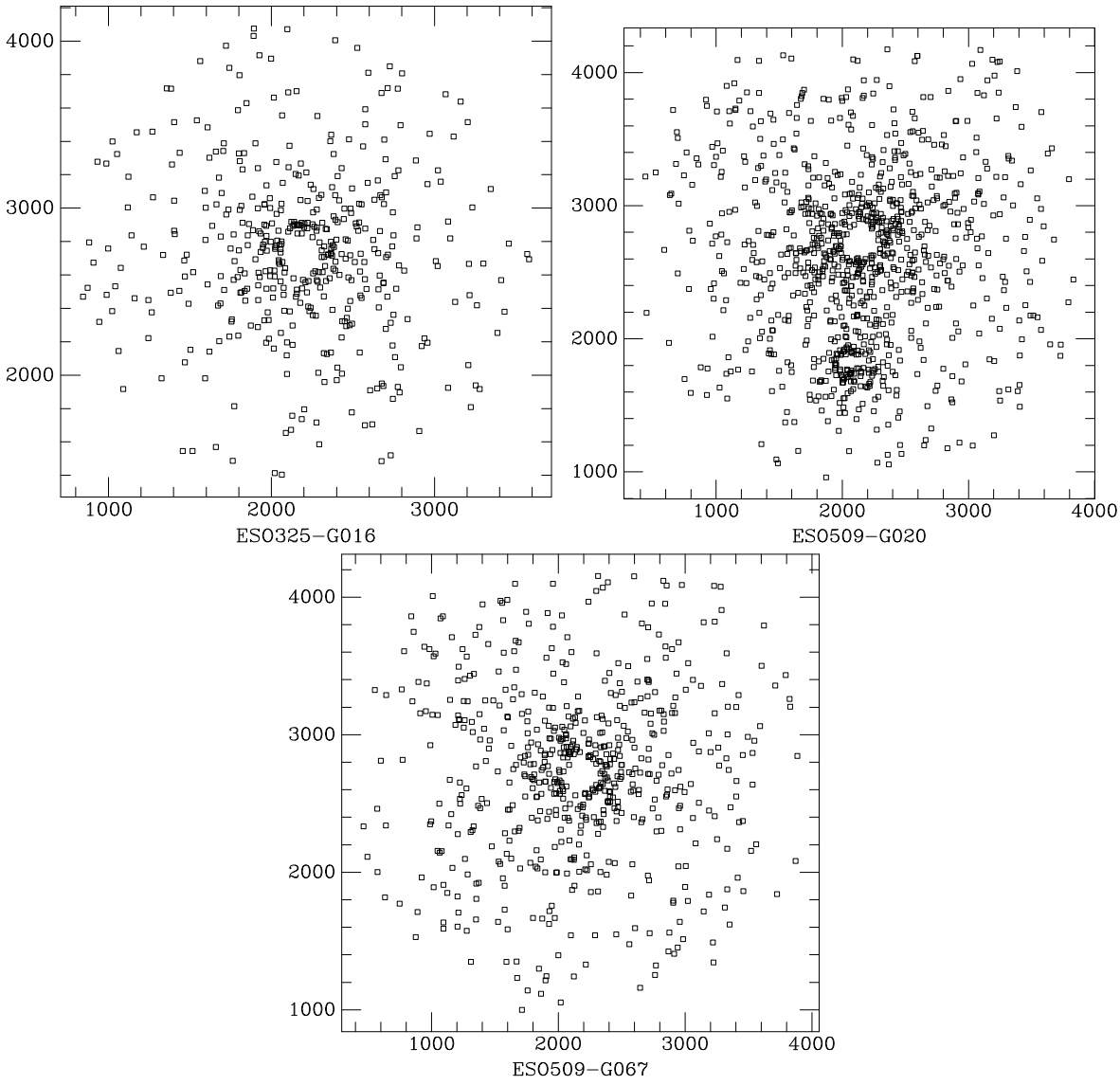

Figure 5.10 Distribution of number detected using x,y coordinates in pixel space. Here we show plots for galaxies ESO325-G016, ESO509-G020 and ESO509-G067.

Table 5.1. Radial Data

galaxy	cluster	R_{100}(arcsec)	b	a	r_{min} pix	r_{max} pix
eso383-g076	A3571	138.3	1.229	1.151	20	2040
2mj13481399	A3571	138.3	1.030	1.949	0	1400
eso444-g046	A3558	115.3	2.041	1.653	35	1680
2mj13272961	A3558	115.3	1.234	1.480	10	2040
2mj13275493	A3558	115.3	1.147	1.460	10	1000
2mj13280261	A3558	115.3	1.327	1.771	10	1400
eso325-g004	AS0740	149.7	1.167	1.405	20	2040
eso325-g016	A3570	149.7	1.708	2.055	20	1400
eso509-g008	A1736a	149.7	1.530	1.692	20	1600
eso509-g020	A1736a	149.7	1.849	1.897	20	1800
eso509-g067	A1736a	149.7	1.165	1.612	15	1800

GCs follow a power law density distribution. The number densities are corrected for "background".

The best fit lines in each of the radial density plots have the form,

$$\log(\sigma_r) = b - a(\log(r)) \tag{5.3}$$

The values of the minimum and maximum galactic radius used in this calculation are listed in Table 5.1 as well as the parameters for the linear fits in the radial density plots. The first column in the galaxy name and the second is the Abell cluster name followed by the distance in arcseconds that equals 100 kpc. The next two columns are the fitting parameters in equation 5.3 followed by the minimum and maximum radii in pixels. The resolution for ACS is 20 pix/arcsec.

If you take the integral of the radial density σ_r with respect to radius with limits from maximum radius to some large radius (100 kpc) to make sure we are including

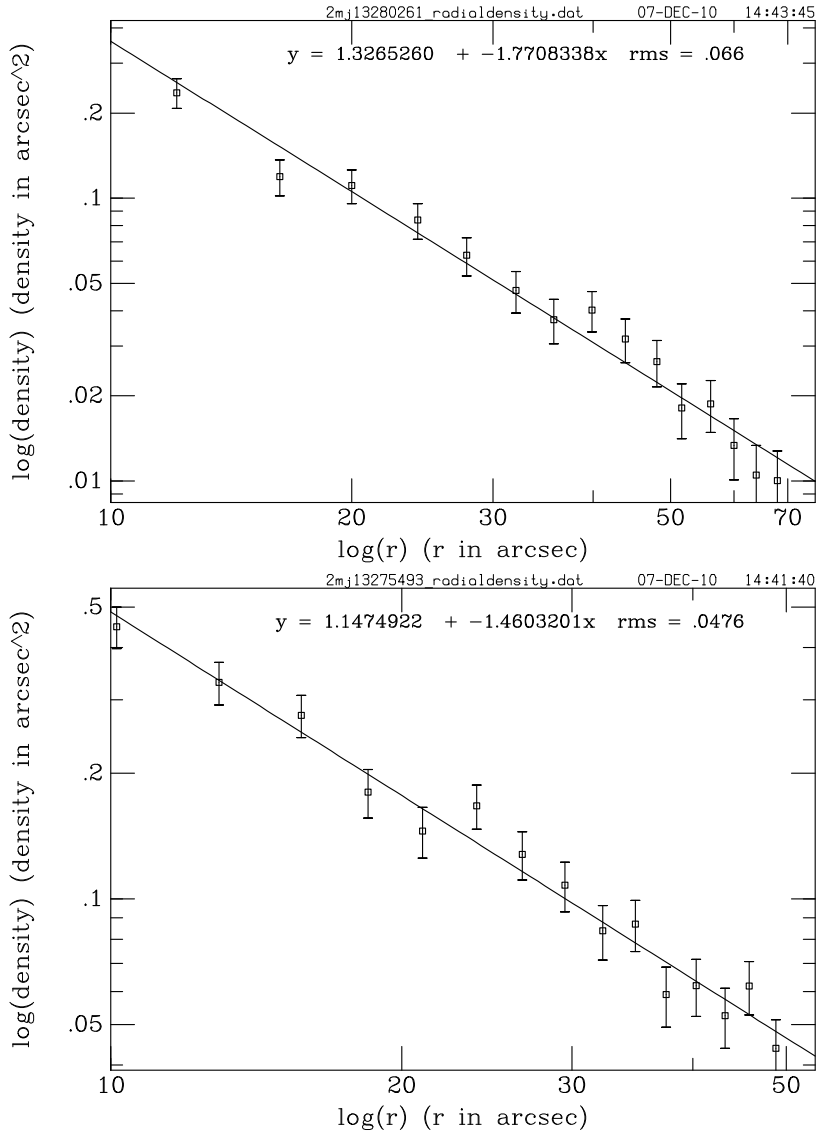

Figure 5.11 Radial density plots of 2mj13280261 and 2mj13275493. A log-log plot of radial density in $arcseconds^{-2}$ versus radial bin in arcseconds (20 pix/arcsec).

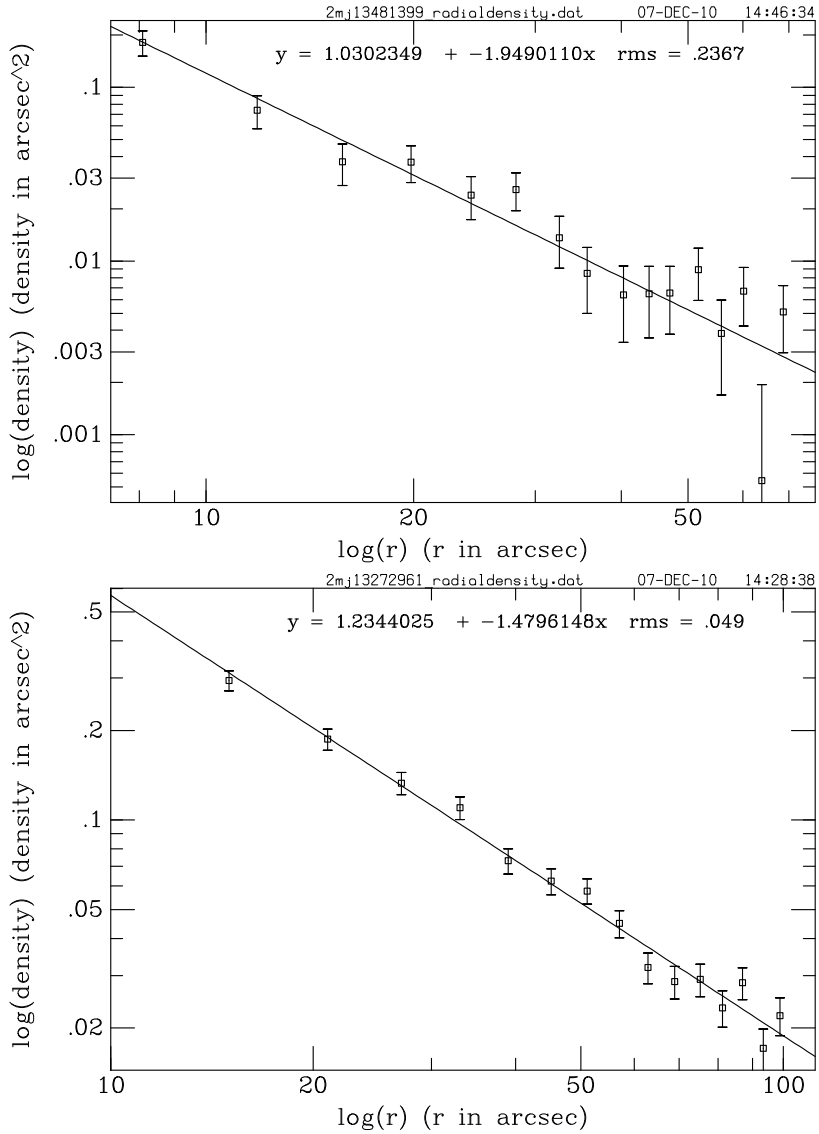

Figure 5.12 Radial density plots of 2mj13481399 and 2mj13272961. A log-log plot of radial density in $arcseconds^{-2}$ versus radial bin in arcseconds (20 pix/arcsec).

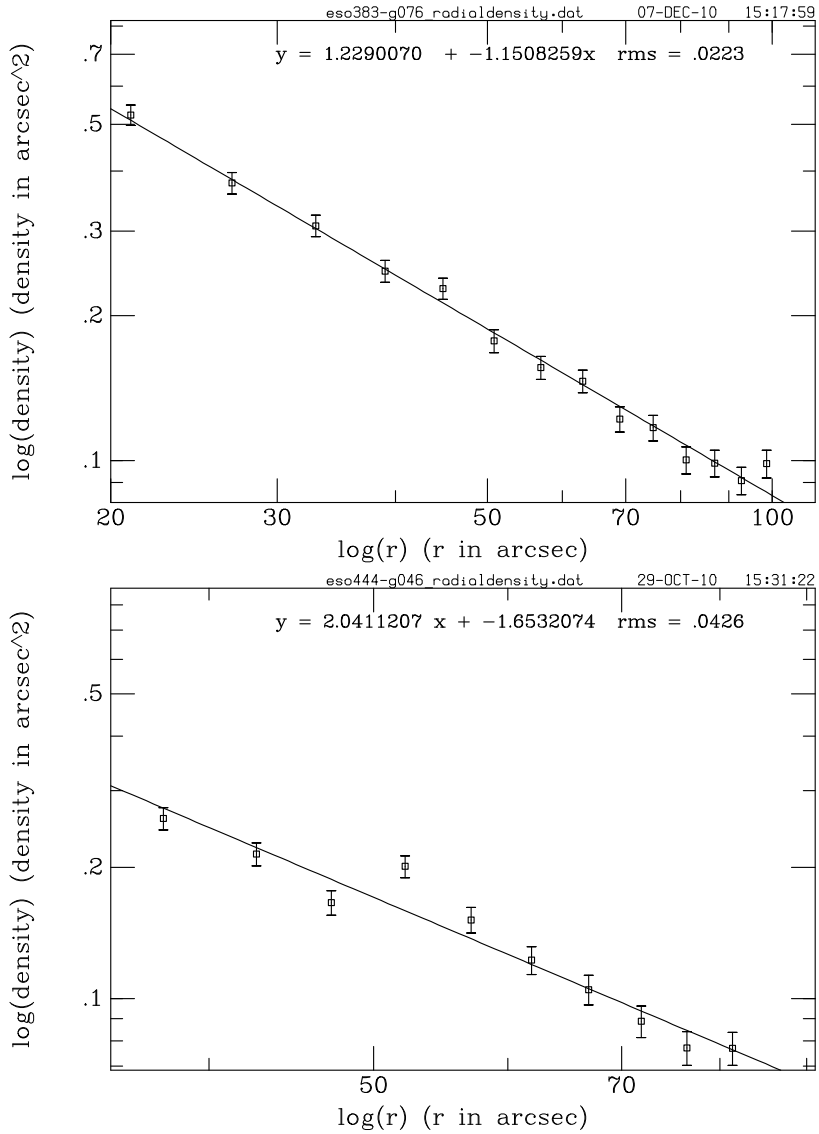

Figure 5.13 Radial density plots of ESO383-G076 and ESO444-G046. A log-log plot of radial density in $arcseconds^{-2}$ versus radial bin in arcseconds (20 pix/arcsec).

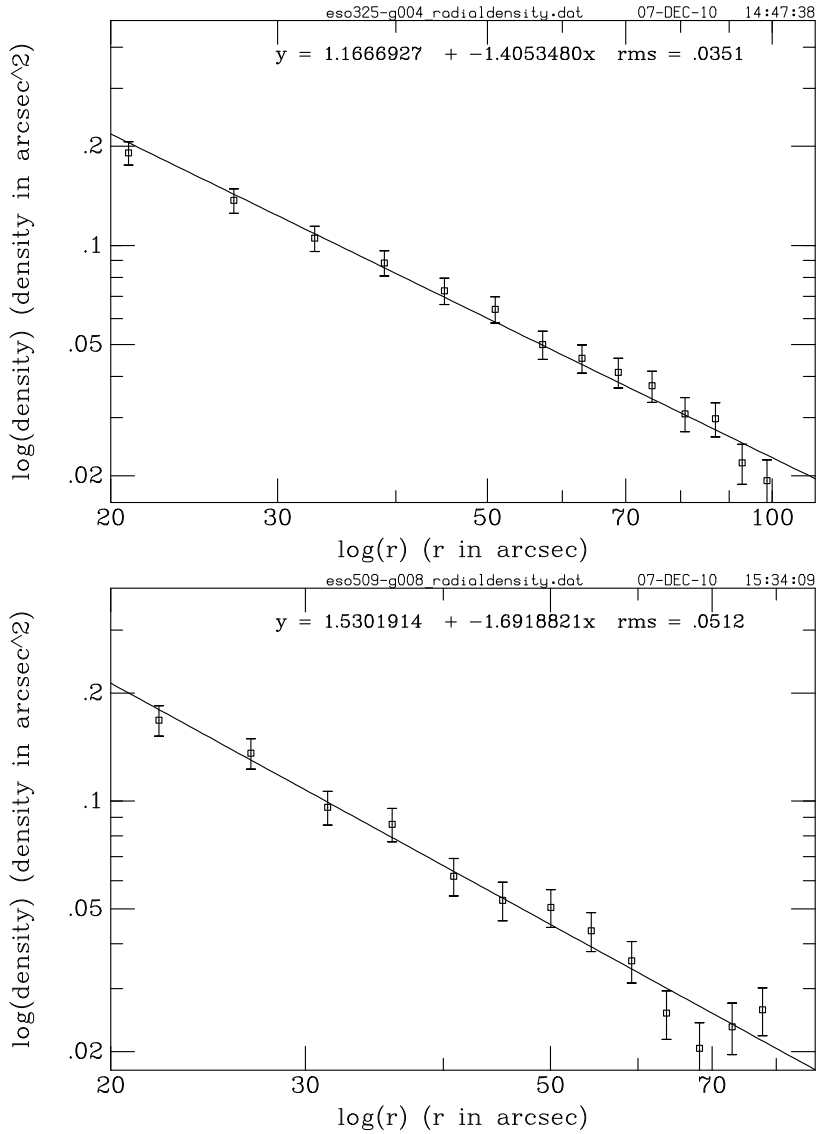

Figure 5.14 Radial density plots of ESO325-G004 and ESO509-G008. A log-log plot of radial density in $arcseconds^{-2}$ versus radial bin in arcseconds(20 pix/arcsec).

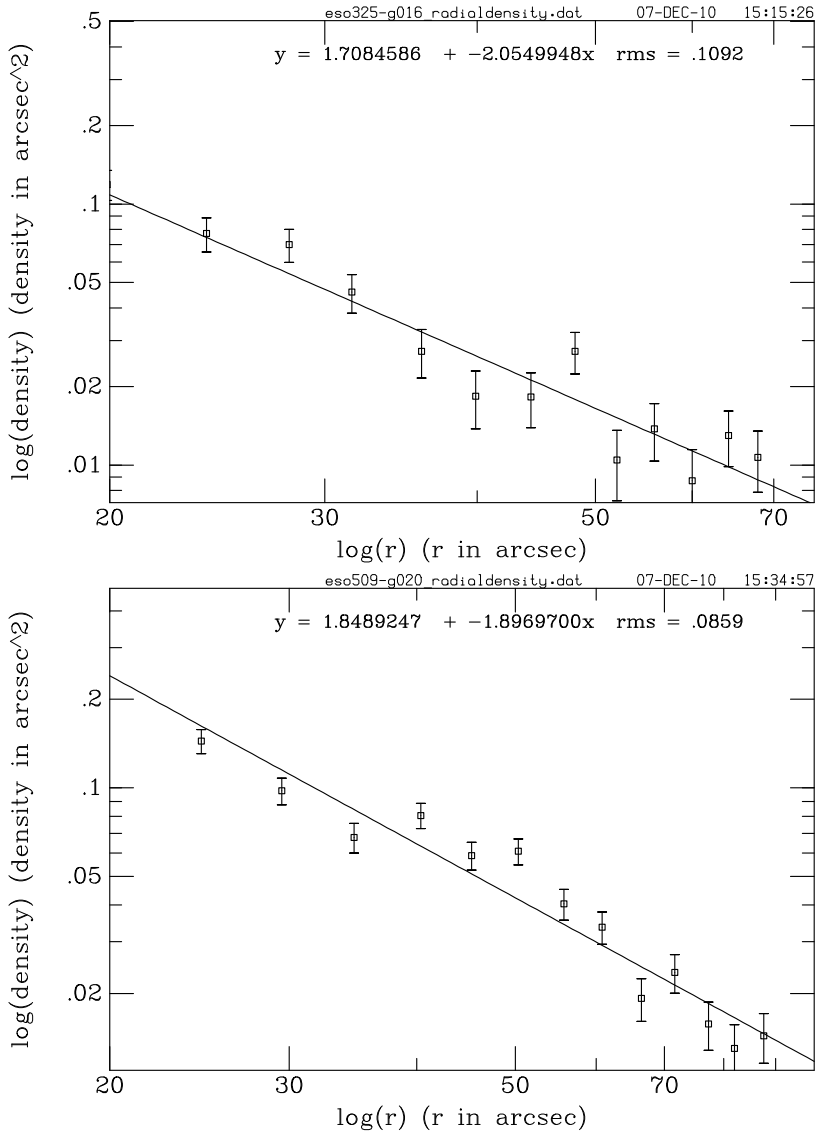

Figure 5.15 Radial density plots of ESO325-G016, ESO509-G020, and ESO509-G067. A log-log plot of radial density in $arcseconds^{-2}$ versus radial bin in arcseconds (20 pix/arcsec).

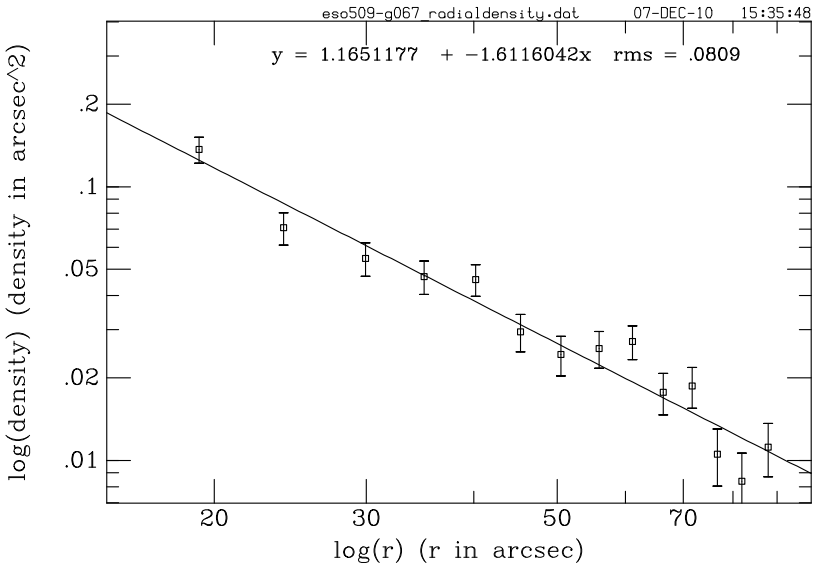

Figure 5.16 Radial density plots of ESO509-G067. A log-log plot of radial density in $arcseconds^{-2}$ versus radial bin in arcseconds (20 pix/arcsec).

most of the GCs that belong to the host galaxy in question (more for smaller galaxies), then the solution is the number of GCs the detection is missing in this radial range. Taking all integrals out to 100 kpc gives a well defined outer limit. This equation can be written in the following way,

$$2\pi \int_{r_{max}}^{100kpc} \sigma_r dr = 2\pi \int r^a 10^b dr \tag{5.4}$$

where the a, b and r_{max} values are from Table 5.1. The solution to the integral is called "total extra" and we can add this "extra" number of GCs to the total number of GCs counted in each radius annuli. If this sum is divided by the total number actually counted. This value is the radial factor and can be written as:

$$\text{Radial Area Factor} = \frac{\text{total in annuli} + \text{total extra}}{\text{total counted}} \tag{5.5}$$

Table 5.2 lists the total number of GCs counted in each radius annuli, N_{count}, the radial factor calculated with equation 5.5, and the resulting total number of GCs, N_{tot}. Each number value is displayed with an error value.

Table 5.2. Radial Factor

galaxy	N_{count}	±	N_{tot}	±	radial factor
ESO509-G008	3633.8	395.6	5450.7	593.5	1.50
ESO509-G020	3909.4	425.0	5238.6	569.6	1.34
ESO509-G067	2571.4	282.5	3600.0	395.7	1.40
ESO325-G004	5280.8	534.9	7551.5	765.0	1.43
ESO325-G016	1732.9	197.6	2408.8	274.8	1.39
ESO383-G076	18788.6	2247.2	27619.3	3303.3	1.47
2MJ13481399	639.8	84.7	850.9	112.8	1.33
ESO444-G046	19444.0	2988.6	27027.1	4154.1	1.39
2MJ13275493	4852.6	752.7	9268.4	1437.7	1.91
2MJ13272961	8209.9	1267.2	9769.8	1508.0	1.19
2MJ13280261	3275.7	511.1	4389.4	684.9	1.34

5.2.3 Contamination

In the previous sections we have shown that the proximity of 2mj13275493 to ES0444-G046, the brightest cluster galaxy (BCG) of A3558, made it so both could be seen in each others' field. This made the issue of maximum radius, discussed in the "radial factor" section, problematic. Perhaps the N_{tot} in 2mj13275493 is 'contaminated' with GCs that belong to the BCG of A3558. We came to the conclusion that the issue of contamination, in this study, would affect only members of Abell 3558. Looking at Table 5.3, we can see the A3558 members are the last four galaxies. We can also see the distance of galaxies in this study, relative to their BCGs, are less than 1 Mpc only in this cluster, with the exception of ES0509-G020. All the galaxies with offset values of zero in Table 5.3 are the BCGs of the cluster. In A3558, the BCG, ES0444-G046, is a giant elliptical and about twice as big as the BCG in A1736a, ES0509-G008. ES0509-G008 is approximately the same size as the other A1736a members (see Table 5.7 for galaxy size, R_I)). This is the reason why A1736a is given the BM type III in Table 4.2 (see Chapter 1 for BM type definition). Since we do not survey all members in A1736a, there is a possibility there is another galaxy of comparable size to ES0509-G008 even closer to ES0509-G020, therefore taking into account the GC contamination from ES0509-G008, just because it is the BCG by being only slighter brighter than the other members, would not be consistent. Contamination in this study is considering contamination from a central, massive BCG.

To calculate contamination, we first look at the radial density of the BCG at the distance of the neighbor galaxy. Looking at the radial density plots we see that the density drops off as you get further and further from the BCG center. Since at the distance of neighboring members of the cluster we are venturing into such low densities, we take the radial density to be constant over the detection area of the neighboring galaxy. We use equation 5.3 to calculate the radial density of the BCG at this distance. We then subtract this constant density from the densities in each radial bin already calculated during the initial radial factor process. This new binned file has to be corrected for "contamination", and when plotted can give us new fitting parameters to our radial density plots (see Figures 5.17 and 5.18). The values are

Table 5.3. Galaxy Offsets from BCG

Galaxy	Abell Cluster	RA (J2000)	Dec (J2000)	geom. scale (kpc/arcsec)	offset (arcsec)	offset (kpc)
ESO509-G008	A1736a	13:26:44.10	-27:26:21.8	0.668	0	0
ESO509-G020	A1736a	13:28:00.15	-27:21:15.5	0.668	1057.7	706.5
ESO509-G067	A1736a	13:34:47.80	-27:07:37.4	0.668	6546.8	4373.3
ESO325-G016	A3570	13:46:24.00	-37:58:15.6	0.668	0	0
ESO325-G004	AS0740	13:43:33.20	-38:10:33.7	0.668	0	0
ESO383-G076	A3571	13:47:28.40	-32:51:53.0	0.723	0	0
2MJ13481399	A3571	13:48:14.00	-33:22:54.7	0.723	1947.169	1407.8
ESO444-G046	A3558	13:27:56.86	-31:29:44.6	0.867	0	0
2MJ13275493	A3558	13:27:54.95	-31:32:18.7	0.867	156.9	136.0
2MJ13272961	A3558	13:27:29.63	-31:23:24.2	0.867	514.6	446.2
2MJ13280261	A3558	13:28:02.62	-31:45:20.8	0.867	939.9	814.9

Table 5.4. Radial Data for Contamination

galaxy	cluster	R_{100}(arcsec)	b	a	r_{min} pix	r_{max} pix
2mj13272961	A3558	115.3	1.372	1.586	10	2040
2mj13275493	A3558	115.3	1.647	1.916	10	1000
2mj13280261	A3558	115.3	1.415	1.843	10	1400

Table 5.5. Radial Factor: Contamination from A3558 BCG

galaxy	N_{count}	±	N_{tot}	±	radial factor
2MJ13275493	3594.2	753.5	5576.2	1169.1	1.55
2MJ13272961	7466.7	1267.5	8831.0	1499.1	1.18
2MJ13280261	3146.9	511.2	4153.5	674.7	1.32

recorded in Table 5.4, which is a correction to Table 5.1.

Once the corrected a and b are obtained they can be used in equation 5.4 and equation 5.5 is used to find a brand new radial factor. The new radial factors can be seen in Table 5.5.

5.3 Specific Frequency

The idea that more luminous galaxies should contain more globular clusters seems to be a logical conclusion and this idea is what gave birth to a galaxy quantity called specific frequency, S_N. This quantity measures the number of globular clusters

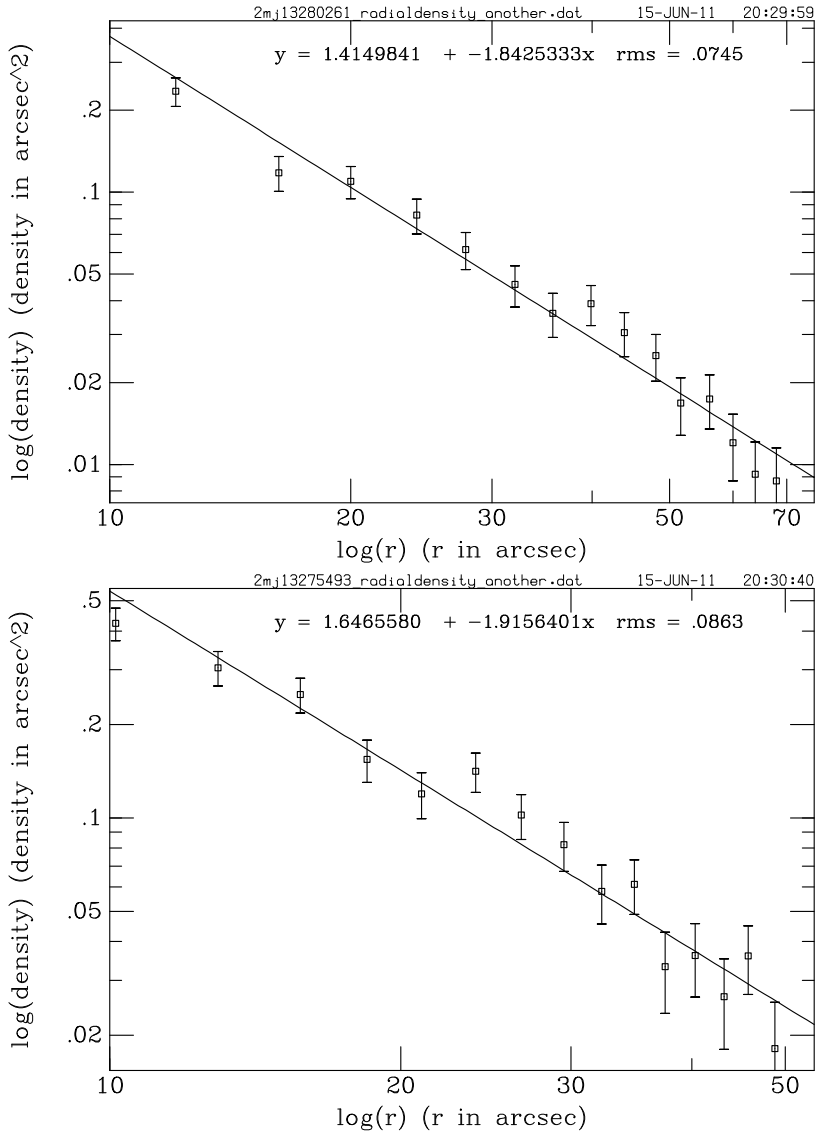

Figure 5.17 Radial density plots of 2mj13280261 and 2mj13275493 after the contamination correction was applied. A log-log plot of radial density in $arcseconds^{-2}$ versus radial bin in arcseconds.

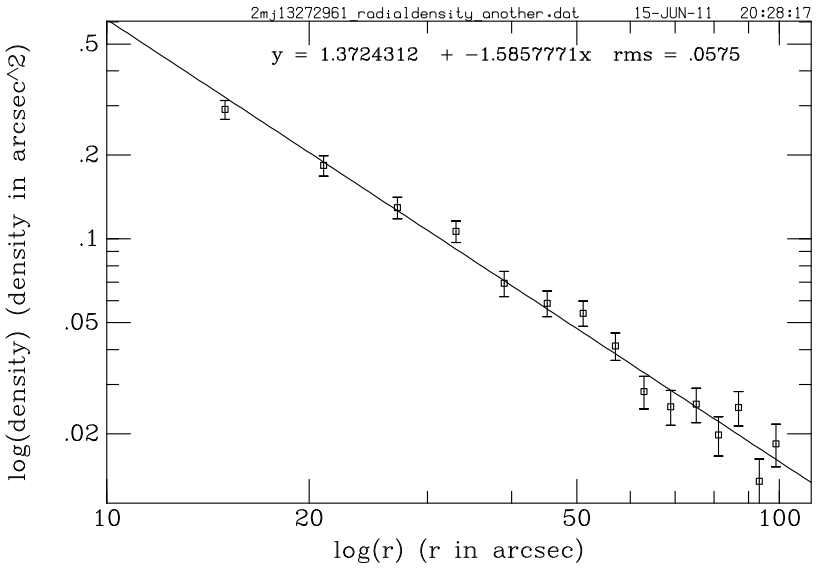

Figure 5.18 Radial density plots of 2mj13272961 after the contamination correction was applied. A log-log plot of radial density in $arcseconds^{-2}$ versus radial bin in arcseconds.

relative to the host galaxy's luminosity and was first stated in a paper by Harris & van de Bergh in 1981. The equation for S_N is,

$$S_N = N_{tot} 10^{-0.4(M_V+15)} \tag{5.6}$$

where M_V is the absolute magnitude, in the V-band, discussed in Chapter 1 and listed in Table 4.1. N_{tot} is listed in Tables 5.2 and 5.5.

Once S_N was introduced, it was used to infer properties about the host galaxy and the GC system itself. This was discussed in the previous NGC1533 section. It was assumed that S_N should be constant for different galaxy types. Spiral galaxies have been shown to have specific frequencies of ∼1 - 2. The specific frequency of the Milky Way is roughly one. Ellipticals were thought to have S_N values of ∼3-6. However, a few problems arise from these assumptions. One is that the theory that elliptical galaxies are formed by the merger of two spiral galaxies (discussed in Chapter 1) should not change the S_N value too dramatically, if no GCs are created in the merger. However, since ellipticals have greater S_N values, additional GCs are being formed. Also, not only are the S_N values of ellipticals greater, 3-6, they actually

Table 5.6. Specific Frequency

galaxy	M_V	N_{count}	±	N_{tot}	±	S_N	±	$radialfactor$
ESO509-G008	-22.773	3633.8	395.6	5450.7	593.5	4.240	0.627	1.50
ESO509-G020	-22.528	3909.4	425.0	5238.6	569.6	5.104	0.754	1.34
ESO509-G067	-22.659	2571.4	282.5	3600.0	395.7	3.109	0.462	1.40
ESO325-G004	-22.774	5280.8	534.9	7551.5	765.0	5.867	0.835	1.43
ESO325-G016	-22.028	1732.9	197.6	2408.8	274.8	3.720	0.564	1.39
ESO383-G076	-23.573	18788.6	2247.2	27619.3	3303.3	10.284	1.603	1.47
2MJ13481399	-21.906	639.8	84.7	850.9	112.8	1.470	0.244	1.33
ESO444-G046	-23.805	19444.0	2988.6	27027.1	4154.1	8.125	1.490	1.39
2MJ13275493	-22.425	3594.2	753.5	5576.2	1169.1	5.975	1.388	1.55
2MJ13272961	-22.874	7466.7	1267.5	8831.0	1499.1	6.258	1.233	1.18
2MJ13280261	-22.107	3146.9	511.2	4153.5	674.7	5.966	1.138	1.32

range from 7-11 for giant ellipticals, which is the case in our study and Peng et al. (2011). Even larger values up to 20 are given in earlier studies such as West et al. (1995).

The S_N values for the 11 Shapley galaxies in this study were calculated using the total number of GCs obtained after all corrections: completeness, "background", GCLF, radial, and contamination. Table 5.6 lists the galaxy name, the absolute magnitude in the V-band, $N_{counted}$ with error, N_{tot} with error, S_N with error and the radial factor.

5.3.1 S_N Correlation between Galaxy and Cluster Properties

The S_N values in Table 5.6 can be plotted versus various galaxy and cluster properties in Tables 4.1 and 4.2 and studied for correlations. To give a quantitative

value for visual trends, we use the Spearman and Pearson estimates for the significance of the correlation. These estimates are described in Numerical Recipes (Press et al. 1992). When Pearson's r (also called the linear correlation coefficient) equals 1, it is said to be in "complete positive correlation" where the data points form a linear relation with a positive slope. The Pearson's r ranges from -1 to 1, with negative values relating to negative slopes for the trend line. The Spearman rank correlation coefficient also ranges from -1 or 1 and like Pearson's value represents correlation when the value is very near 1. For the rest of the thesis, we will call the Spearman rank correlation coefficient, s correlation, and Pearson's r, p correlation.

Galaxy Properties

In this section we investigate how S_N scales with M_V, radial velocity, cz and velocity dispersion of the host galaxy (see Table 4.1). As discussed in the magnitude section of Chapter 1, M_V is the absolute V-band magnitude of the host galaxy. It can be calculated from the distance modulus, DM, and the apparent magnitude, m_V, of the galaxy. The distance modulus, DM = m_V - M_V, used for each galaxy is that of the associated cluster to avoid any effect from the internal velocities of the member galaxies. The distance modulus can be calculated by assuming standard cosmological parameters, $H_0 = 73$ km/s Mpc^{-1}. Peng et al. (2008) mentioned a relation between M_V and Specific frequency with low and high magnitudes increasing in S_N with intermediate magnitudes having lower S_N, forming a kind of U shape. Looking at Figure 5.19, which only contains 11 galaxies, we do not see a slight U shape. However, we do see a trend of increasing S_N with increasing magnitude. The s correlation is 0.98 and the p correlation is > 0.99. The trend is less apparent when looking at the BCGs, the circles in the plot; however, it does reduce the sample points. When one considers that the outliers are galaxy members farther away from the cluster center, the idea of GCs being associated with the galaxy and/or the cluster can materialize.

There should be no correlation between radial velocity and S_N. A possible correlation in a S_N versus cz plot would be from some systematic error. When S_N is compared to radial velocity, cz, of each galaxy in Figure 5.20, no trend can be seen.

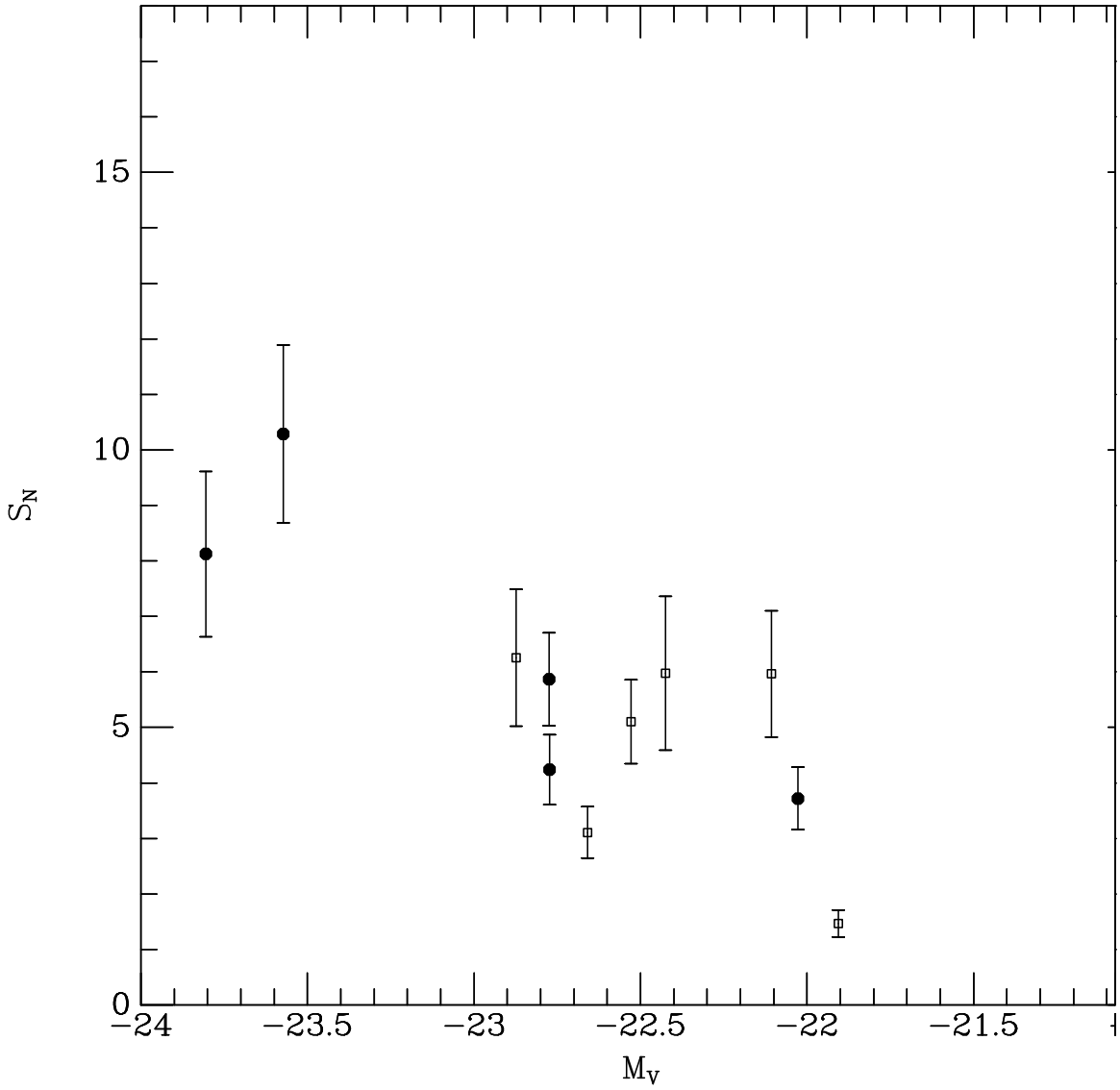

Figure 5.19 Specific frequency versus absolute V-band magnitude. A downward linear trend can be seen. The BCGs are represented by solid circles.

The BCGs were plotted as circles in the plot but there is also no correlation between S_N of the BCGs.

Velocity dispersions for 10 out of 11 galaxies were found in the literature and recorded in Table 4.1. The velocity dispersion of galaxies is usually derived from analyzing shifts and broadening of the absorption lines in galaxy spectra. The variations in the absorption lines are due to the orbital motions of the stars that reside in the galaxy and therefore contribute to the galaxy spectrum (Binney 1998). Figure 5.21 shows an approximately linear trend with greater values of galaxy velocity dispersion, σ_{gal}, corresponding to greater S_N values. The s correlation is 0.97 and the p correlation is 0.94.

Using the virial theorem, in 3D space, the velocity dispersion can be related to the galaxy mass the following way,

$$\frac{1}{2}m(3\sigma)^2 = \frac{GmM(R)}{R} \tag{5.7}$$

where the m is mass of a single star (negligible compared to the mass of the galaxy), M is the mass of the galaxy (or star cluster in question), and G is the gravitational constant. Since a correlation between specific frequency and the mass of galaxy is reasonable (bigger galaxy, more GCs), and σ depends on the mass, the trend in Figure 5.21 is not surprising. Equation 5.7 claims that σ_{gal}^2 is proportional to $\frac{M(R)}{R}$, but the functional form of $M(R)$ is uncertain. However, virial analyses (e.g., Cappellari et al. 2006; Mo, van den Bosch & White 2010) indicate that a galaxy's gravitating mass is proportional to $\sigma^2 R_e$, where σ is the central stellar velocity dispersion, and R_e is the effective radius. For similar types of galaxies, effective radii are closely related to the isophotal radii, which are much easier to measure observationally. Table 5.7 presents values of the isophotal radius R_I, which is the linear size in arcsec out to an I-band isophote of 22.5 mag/arcsec^2. These values were retrieved from the Hyperleda website, a database for physics of galaxies (http://leda.univ-lyon1.fr/). The R_I values in arcsec are then converted to a physical size in kpc, taking into account the cluster distances. The conversion factors for the clusters are included in Table 5.7. The Table also repeats the S_N values for each galaxy.

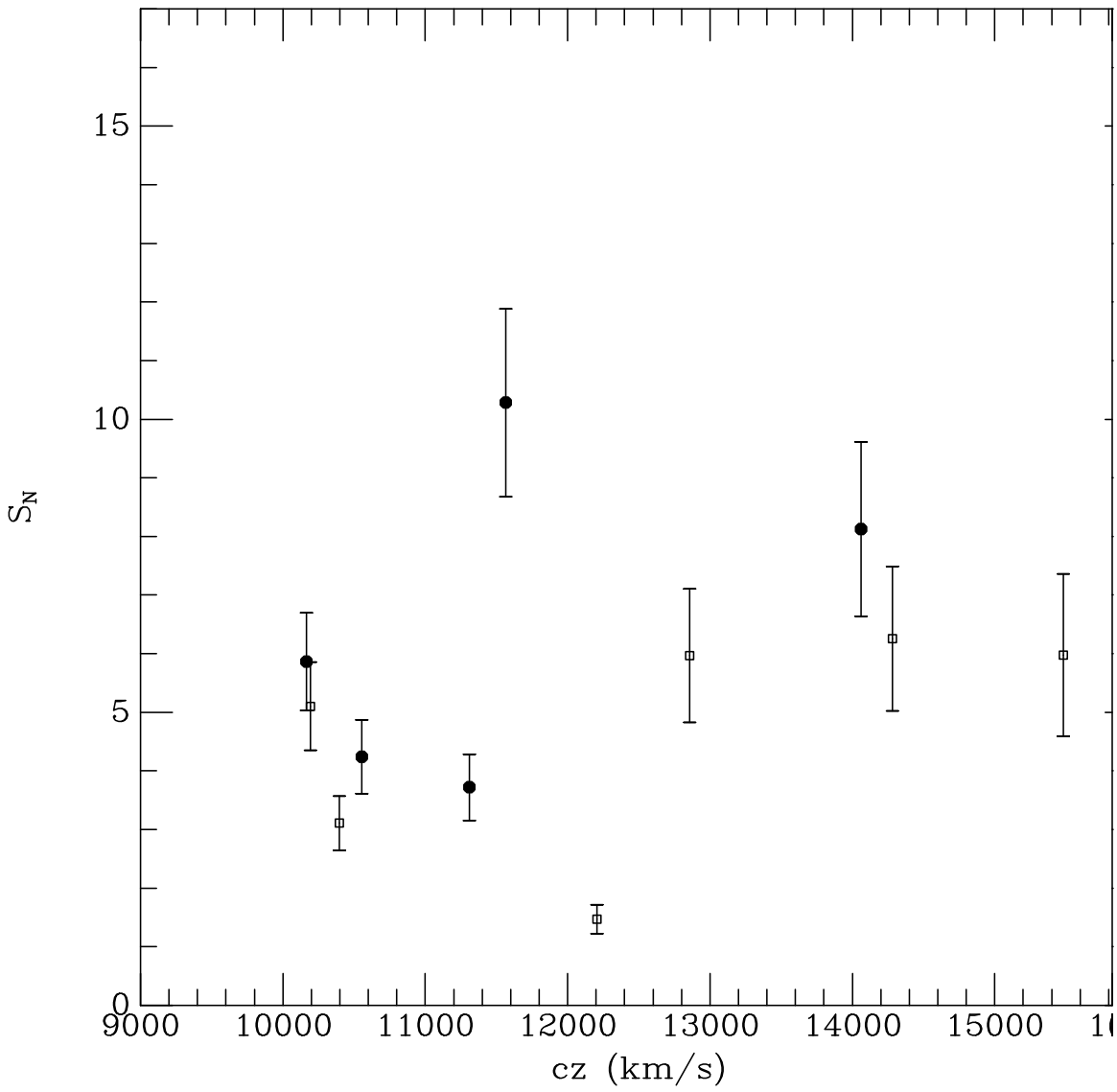

Figure 5.20 Specific frequency versus radial velocity, cz in km/s ($c = 3 \times 10^8$ m/s and z = redshift). The BCGs are represented by solid circles.

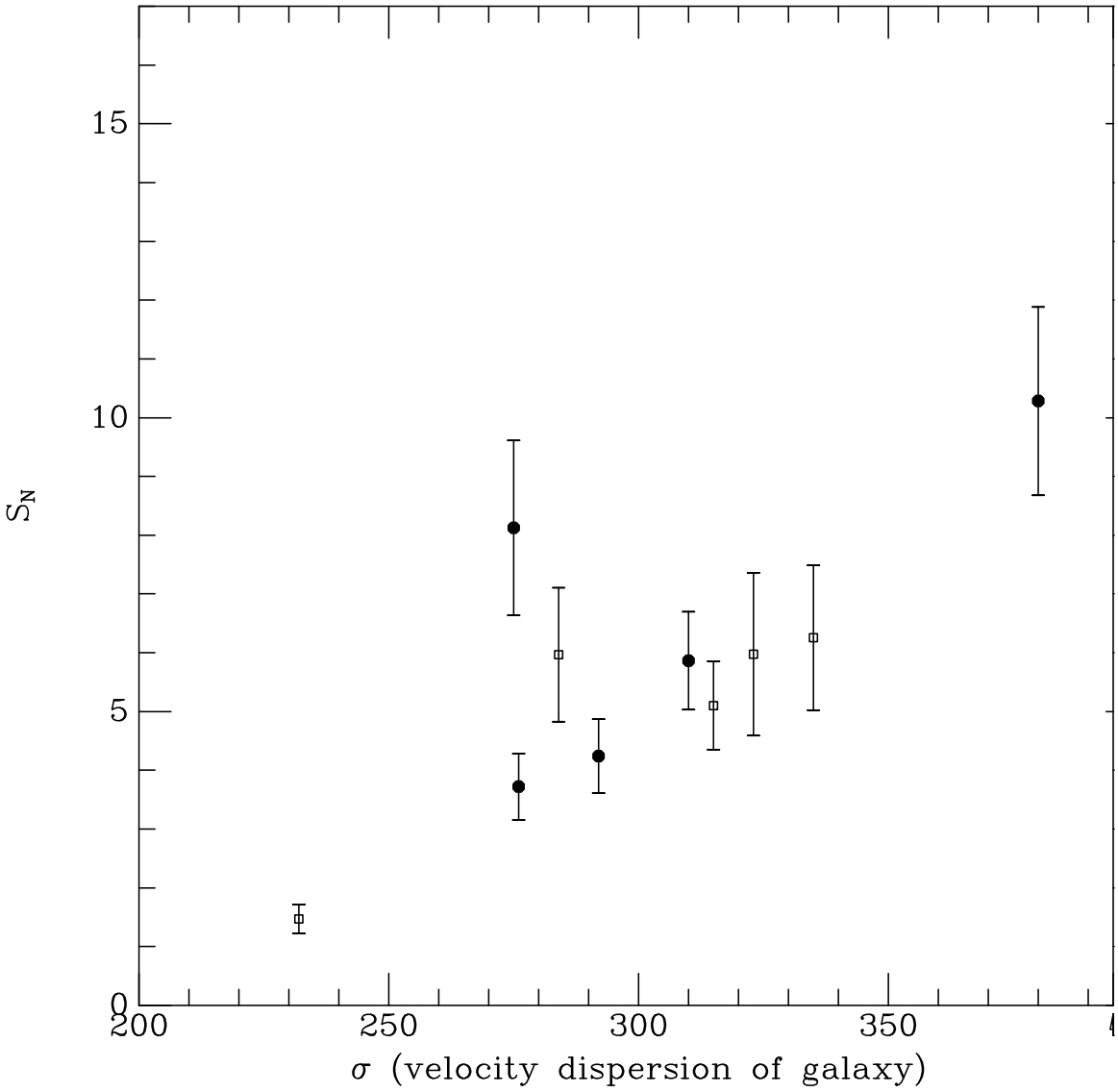

Figure 5.21 Specific frequency versus galaxy velocity dispersion, σ_{gal}. An approximately linear trend can be seen with increasing σ_{gal} corresponding to greater S_N values. The BCG data are represented by solid circles.

Table 5.7. R_I Data

galaxy	S_N	$\pm$	kpc/arcsec	R_I(arcsec)	R_I (kpc)
ESO509-G008	4.240	0.627	0.668	37.8	25.3
ESO509-G020	5.104	0.754	0.668	26.7	17.8
ESO509-G067	3.109	0.462	0.668	36.1	24.1
ESO325-G016	3.720	0.564	0.668	20.8	13.9
ESO325-G004	5.867	0.835	0.668	31.4	21.0
ESO383-G076	10.284	1.603	0.723	82.6	59.7
2MJ13481399	1.470	0.244	0.723	21.0	15.2
ESO444-G046	8.125	1.490	0.867	58.5	50.7
2MJ13275493	5.975	1.388	0.867	23.3	20.2
2MJ13272961	6.258	1.233	0.867	25.5	22.1
2MJ13280261	5.966	1.138	0.867	19.4	16.8

Figure 5.22 shows that both S_N and the total number of GCs depend on the galaxy mass. The top panel of Figure 5.22 plots specific frequency versus the log of the product of galaxy velocity dispersion squared σ_{gal}^2 and R_I, which should be proportional to the galaxy mass. The bottom panel shows a log-log plot of N_{tot} versus the same quantity along the x-axis as in the top panel.

Cluster Properties

Now we will look at the correlation between S_N and the properties of the cluster in which the host galaxy resides. The cluster properties recorded in Table 4.2 are, the cluster velocity dispersions, the type of cluster, and the Abell count, or richness, of the cluster. The velocity dispersion of a cluster, σ, is the standard deviation of the radial velocities, cz, of all the cluster members. As Chap 4 states, these σ values are obtained from various sources of literature except for AS0740 which was calculated by collecting the radial velocities of all members. The cluster velocity dispersion for ESO509-G067 could not be found. We see a slight trend upward in the S_N versus velocity dispersion plot, Figure 5.23. The s correlation is 0.92 and the p correlation is 0.78. These values can not confirm strong correlation. However, this trend would be even more prominent if 2MJ13481399 point was excluded. 2MJ13481399 is interesting in the sense that its low GC population, which is the main factor for a small S_N of 1.47, may be due to its distant location to the cluster center. This issue will be revisited in section 5.5. If the galaxy had a bigger GC population then it would fall in the upward trend. The other galaxy in this study that occupies the same cluster as 2MJ13481399 is ESO383-G076 and it has a much more abundant GC population. This upward trend is discussed in Blakeslee et al. (1999), Elmgreen (1999), Harris et al. (1998) and is even more present in the BCGs. When considering only the BCGs in Figure 5.23, the p correlation rises significantly to 0.92, which makes sense since most of the BCGs are located at the cluster center (see section 5.5).

As stated in Chapter 1, the Bautz-Morgan Type, BM type, is related to the morphology of the cluster. A cluster with a BM type of I has a single supergiant cD galaxy and a BM type of III indicates a cluster where the one member is no bigger

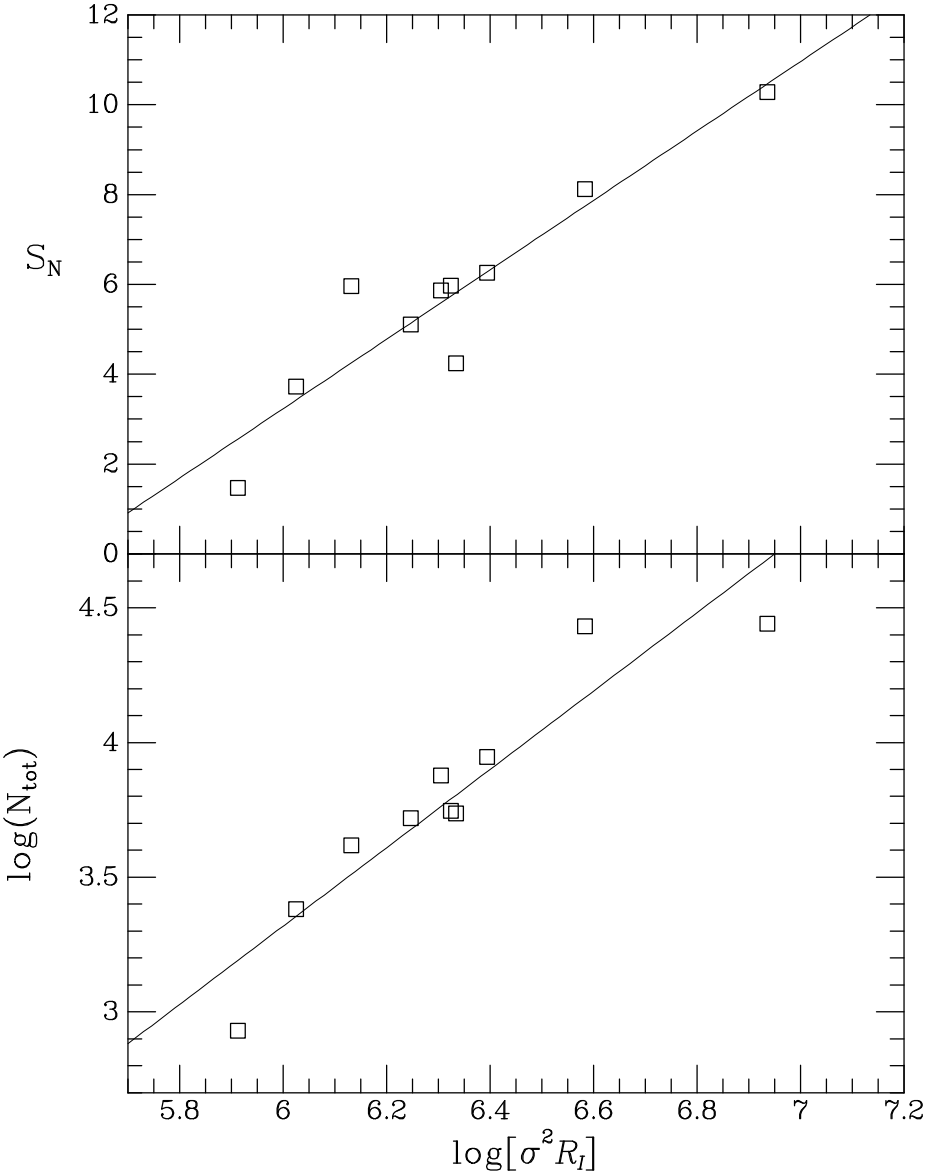

Figure 5.22 Top: Specific frequency versus the log of the product of galaxy velocity dispersion squared, σ^2_{gal}, and R_I. A approximately linear trend can be seen corresponding to greater S_N values. Bottom: This plot has the same x-axis with the log of N_{tot} as the new y-axis.

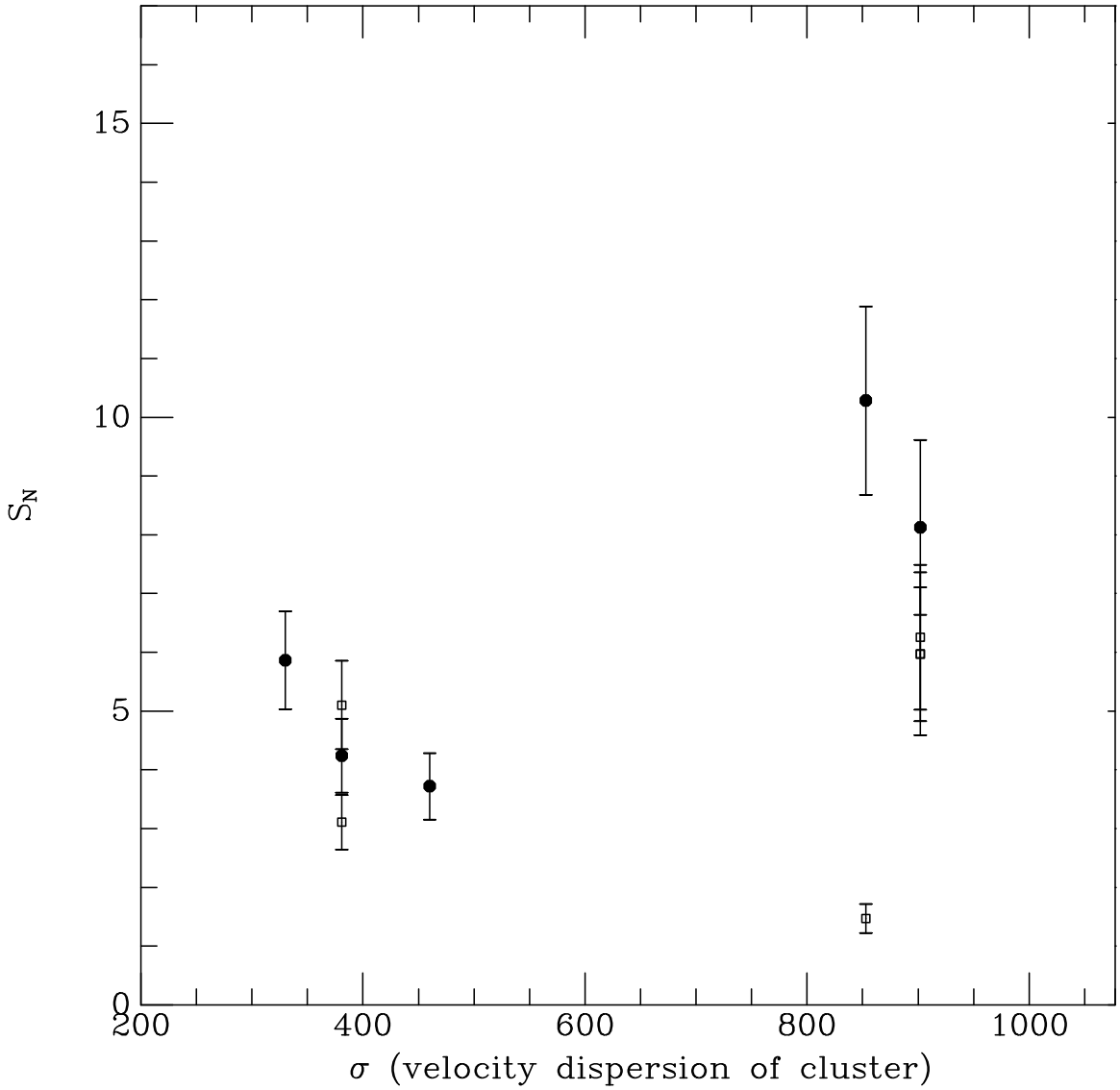

Figure 5.23 Specific frequency versus cluster velocity dispersion. The BCGs are plotted as solid circles. Value could not be found for ESO509-G067.

than any other member. Variations in between are given BM type values that range in this order I-II, II, II-III. McLaughlin et al. (1994) and Harris et al. (1995) claim higher BM types, II-III and III, have higher S_N values. However, Blakeslee & Tonry (1995) concluded that there was no correlation between BM type and S_N values. In our sample, Figure 5.24 shows that whatever weak correlation exists, it is opposite of what McLaughlin and Harris found. The trend, corresponding to an s correlation of 0.93 and p correlation of 0.77, in the following plots seem to have the higher BM types with the smaller S_N values. However, the galaxies associated with a cluster with BM type I, seem to have a wide range of S_N values. Taking into account the error in S_N, the correlation is less pronounced. Overall, the correlation is very weak compared to the relation that McLaughlin and Harris discussed and therefore, it is more likely that there is no correlation.

The last cluster property to compare is the cluster richness, quantified by the Abell count (Abell 1958). The Abell count assigned to each cluster is simply the number of cluster members that Abell used in order to determine the richness class, which ranges from 0 to 4.

A very slight trend upward can be seen between S_N and Abell count in Figure 5.25. The s correlation is 0.93 and the p correlation is 0.78. This correlation suggests a possible dependence of S_N on cluster richness. The greater the number of galaxies, the greater the S_N value.

The correlations between S_N and cluster properties seem to exist and become more pronounced when plotting only centrally located BCGs. This result may point to the possibility of GC populations also being associated with the host cluster as well as the host galaxy itself. This relation between S_N and host cluster is discussed later in section 5.5.

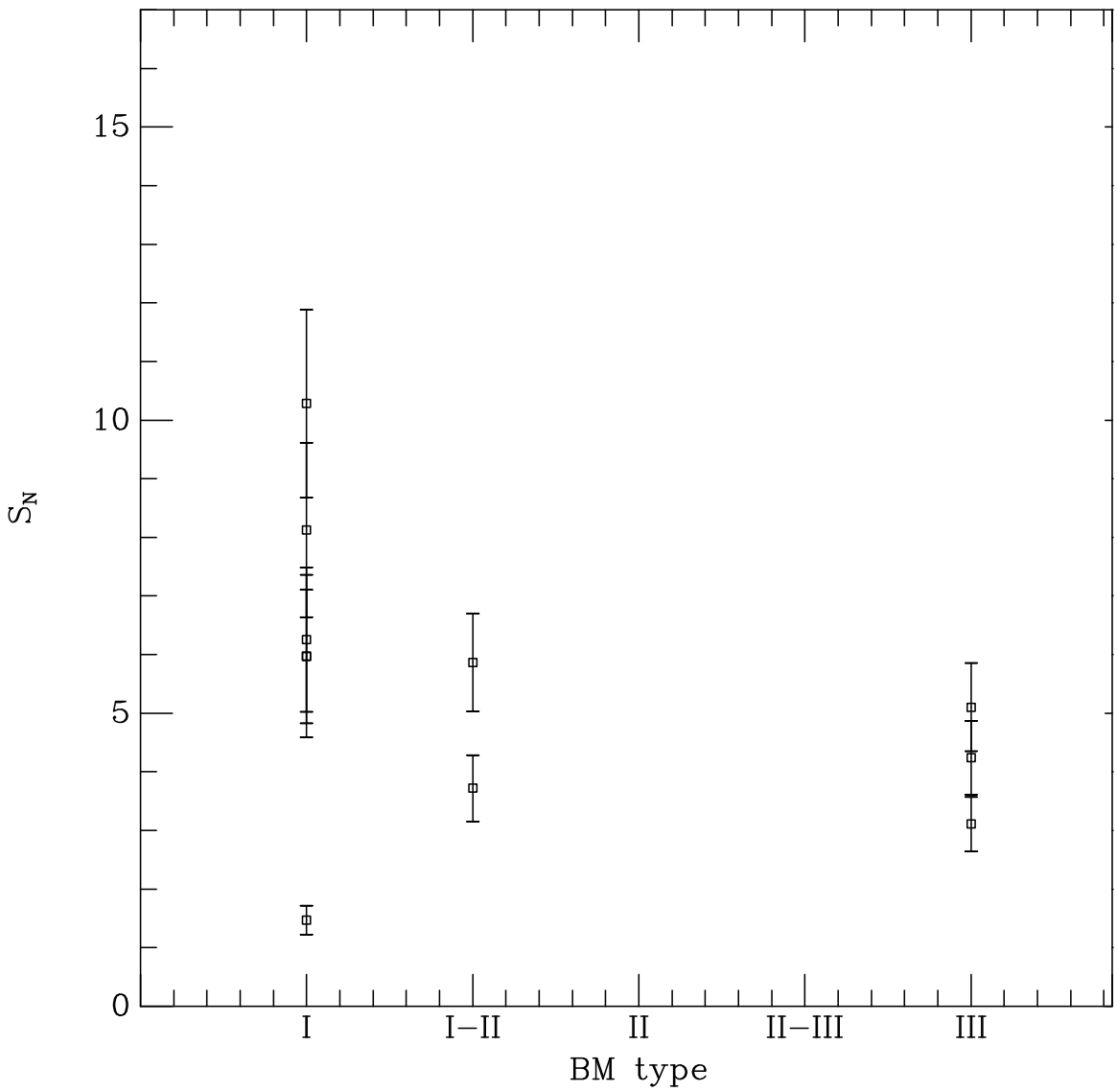

Figure 5.24 Specific frequency versus BM type. We conclude there is no trend considering error in S_N. The BCGs are plotted as solid circles.

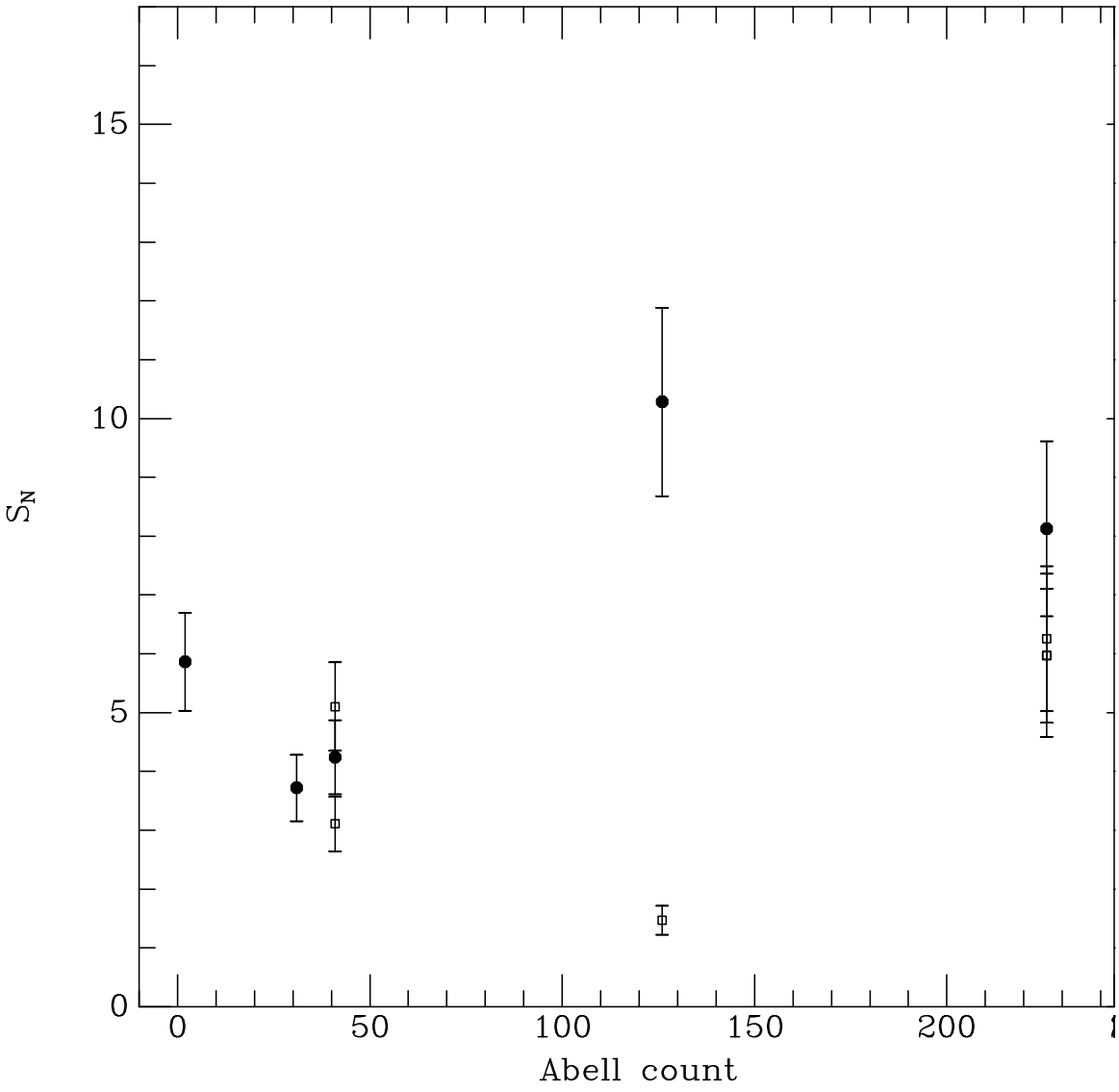

Figure 5.25 Specific frequency versus Abell count. The Abell catalog lists galaxy count used in estimateing the richness class of each cluster. The BCGs are represented by solid circles.

5.4 Total Number of GCs and Host Galaxy Luminosity Relation

Early on in galactic astronomy, it was thought that the number of GCs should roughly scale with the host galaxy's stellar luminosity, which was discussed earlier as one of the notions that helped develop the equation for specific frequency. However, the S_N versus M_V plot (Figure 5.19) showed a slight downward trend that led us to investigate a more fundamental idea of just total number of GCs, N, versus optical luminosity of the galaxy, L. We can obtain absolute luminosity, L_V, using our M_V values (listed in Table 5.6)and the following equation,

$$M_V = -2.5 log L_V + C \tag{5.8}$$

where C is the M_V value of the sun, 4.83. When equation 5.8 is solved for log(L_V), one finds it is proportional to -0.4*M_V. To look for a correlation, we plot log(N) versus log(L_V) in Figure 5.26.

We see a good relation between log(N) and log(L_V) described by the following equation:

$$log N = -10.7 + 1.59 log L_V \tag{5.9}$$

which scales with luminosity to the power of 1.6.

5.5 Intracluster Globular Clusters

The formation scenario described in Chapter 1 discussed the problem with the simple notion that if ellipticals are merged spirals then they should have S_N values the same as spiral galaxies, S_N ∼2. Peng et al. (2008) shows that there are indeed ellipticals with this value but there also exist a wide range of S_N values that get into the teens. This issue of high S_N values was studied in West et al, (1995), where they believed the issue had to do with "Intracluster Globular Clusters" (IGCs). They

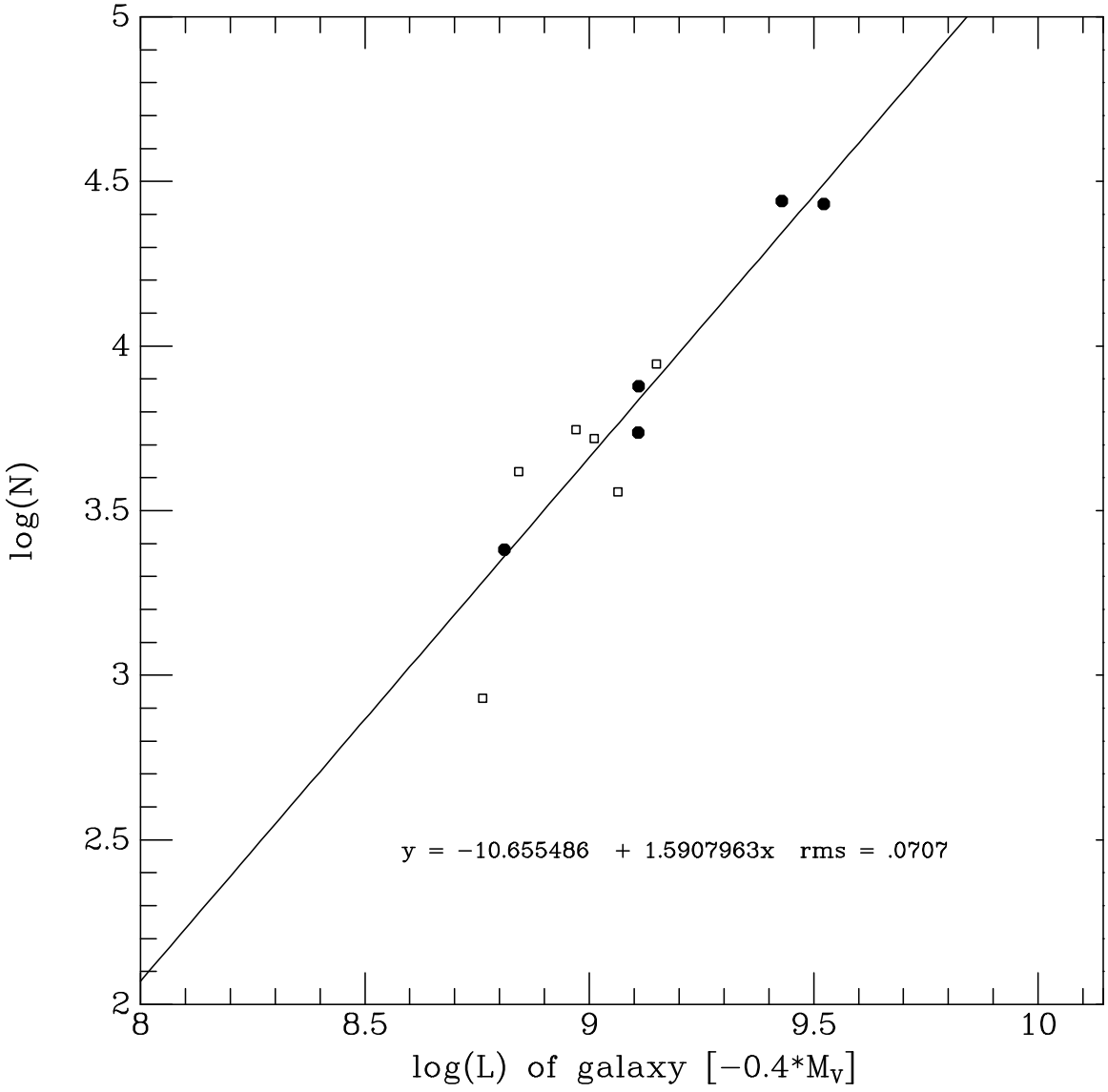

Figure 5.26 Luminosity is estimated by -0.4*M_V and we see a relation between the luminosity of the host galaxy and the number of globular clusters. The equation logN = -10.7 + 1.59(logL) is displayed with the circles representing the BCGs of each cluster.

claimed that galaxies do not just have GCs associated with them but the cluster itself had GCs bound to the cluster potential. West started with the following assumptions:

1. There existed a populations of IGCs in all galaxy clusters. The total number of IGCs depends on the cluster mass.

2. The distribution of IGCs follows the mass distribution. The mass density "which satisfactorily describes the projected distribution of galaxies and the dark matter component indicated by gravitational lens studies in King (1962)" (West 1995) can be written as,

$$\Sigma(r) = \frac{\Sigma_0}{1 + \frac{r^2}{r_c^2}} \tag{5.10}$$

where Σ_0 is the central density, r is the distance from galaxy center and r_c is the core radius of the cluster.

3. BCGs galaxies develop a GC population that creates a S_N $\sim$4.

4. Depending on where the galaxy is located in the cluster, it can be surrounded by a halo of IGCs.

However, this study was done in 1995 and since then there have been ellipticals with values as low as $\sim$2, so assumption 3 must be modified. Some examples of low S_N values are present in Peng et al. (2008) and the study of the Shapley Supercluster presented in this thesis (see Table 5.6). Therefore, we will be using a base S_N of $\sim$ 2, which is used to calculate the number of "excess GCs" for each galaxy. If we start with the equation for S_N and set specific frequency to 2, we can calculate a number of GCs expected for that value of S_N $\sim$2, $2 \times 10^{-0.4(MV+15)}$. So the number of excess GCs, N_{excess}, is the total number of GCs we calculate in our study minus the expected number and is calculated the following way,

$$N_{excess} = N_t - 2 \times 10^{-0.4(M_V+15)} \tag{5.11}$$

where N_{excess} is the number of "excess GCs."

Combining assumptions 1 and 2, West gets a good estimate of the projected

density, Σ_{IGC}, of the IGCs and writes the following equation,

$$\Sigma_{IGC} \propto \frac{M_{cl}}{1+\frac{r^2}{r_c^2}} \tag{5.12}$$

where M_{cl} is the mass of the cluster. Obtaining the mass of the cluster is difficult using optical data but with the "assumption that the hot X-ray gas is in hydrostatic equilibrium in the gravitational potential well, the X-ray temperature is expected to be linearly proportional to the total cluster mass, $T_X \propto M_{cl}$" (West 1995). Since the X-ray temperature values were not available for the galaxies in our study, we made the additional relation between X-ray temperature and X-ray luminosity, $T_X \propto L_X$ and use values for L_X obtained in Böhringer et al. (2004) and Zhang et al. (2011). Using this substitution, we get the equation:

$$\Sigma_{IGC} \propto \frac{L_X}{1+\frac{r^2}{r_c^2}} \tag{5.13}$$

This idea of Intracluster GCs suggests that galaxies close to the center, in many cases the BCGs, will have a large number of excess GCs and inversely the larger the galaxy's distance from the cluster center, r, will result in a lower N_{excess}. Plotting N_{excess} versus $\frac{L_X}{1+\frac{r^2}{r_c^2}}$, the local IGC density, will show if this correlation exists. The data is listed in Table 5.8, where the offset column lists the distance of the galaxy to the cluster center. All distances in this Table are in arcminutes. As stated above, the X-ray luminosity for A1736a could not be found. Figure 5.27 relates to the total number before contamination since we want to examine if the total number of globular clusters is affected by a population of GCs associated with the cluster and not by one or another galaxy around it.

Figure 5.27, like the plots in West et al. (1995) and Blakeslee & Tonry (1995), does show a strong correlation between N_{excess} and IGC density. If the BCG is centrally located, the contamination technique (section 5.2.3) is almost identical to a possible IGC population, which would be centered around that BCG. Further studies in IGCs have found that this population is bimodal in color (Peng et al. 2011).

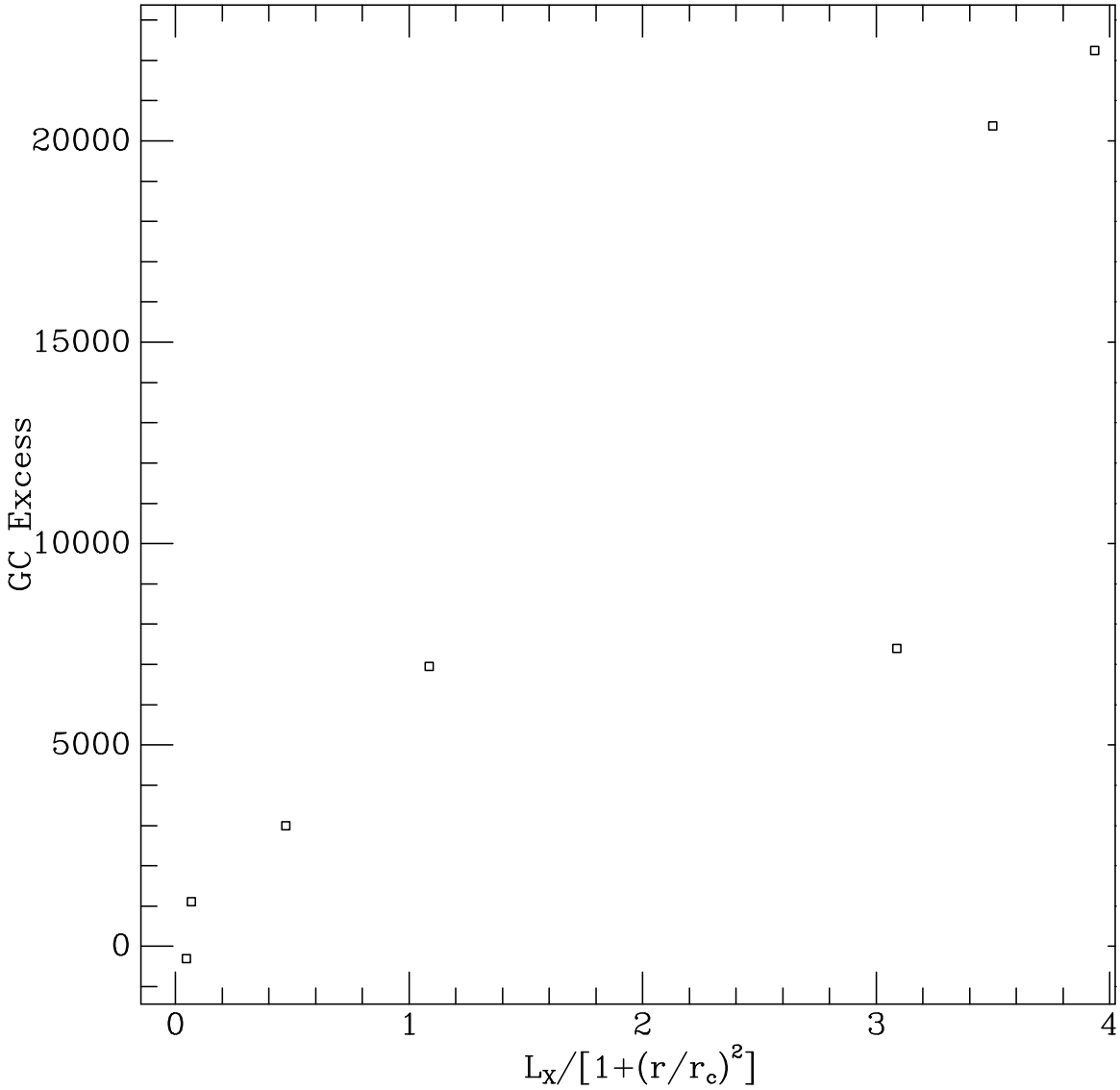

Figure 5.27 GC excess versus a ratio involving X-ray luminosity and core radius of the galaxy cluster.

Table 5.8. Intracluster Data

galaxy	cluster	r_c (arcmin)	L_X E44 erg/s	offset (arcmin)	N_{tot}	$\pm$	excess	$\frac{L_X}{1+\frac{r^2}{r_c^2}}$
ESO325-G016	A3570	6.0	0.191	8.077	2408.8	274.8	1113.9	0.0679
ESO444-G046	A3558	6.0	5.56	0.443	27027.1	4154.1	20373.9	3.4990
2MJ13275493	A3558	6.0	5.56	2.236	9268.4	1437.7	7401.9	3.0889
2MJ13272961	A3558	6.0	5.56	8.986	9769.8	1508.0	6947.3	1.0849
2MJ13280261	A3558	6.0	5.56	15.239	4389.4	684.9	2996.8	0.4722
ESO383-G076	A3571	3.5	4.91	0.917	27619.3	3303.3	22246.1	3.9360
2MJ13481399	A3571	3.5	4.91	33.330	850.9	112.8	-306.4	0.0459

5.6 Conclusion

We present a brief introduction of the Shapley Supercluster and its connection to the Great Attractor. The motivation for the imaging of the 11 galaxies in this survey was to obtain velocities of each of these galaxies to further investigate the motion toward the Great Attractor. We then list properties, from the literature, of each galaxy imaged and the cluster in which they reside.

The data analysis using DAOphot was described in detail, from source detection to the final corrections that needed to be applied to get a total number of globular clusters. The total number of GCs associated with each galaxy, in Table 5.6, has been corrected for completeness, background, luminosity function, radial distribution and contamination from the central BCG in A3558. Table 5.6 also shows the largest specific frequency, 10.3, to belong to ESO383-G076. This is most massive galaxy in our survey (see Table 5.7) and along with the next largest galaxy ESO444-G046, may be the largest GC populations studied at ∼23,000 - 30,000 (taking into account error). However, their largest S_N values may have something to do with distance from cluster center. In Table 5.8, the total numbers are corrected for completeness,

background, radial affects but not contamination. We can see that the numbers all scale with the distance from the cluster center.

We find that both galaxy and cluster properties correlate with S_N. Our S_N values strongly correlate with velocity dispersion of the host galaxy, which is predicted using the virial theorem. Since mass is proportional to $\sigma^2 R_e$, we find a strong correlation of S_N with the dynamical mass of the galaxy in Figure 5.22. This finding agrees with the correlation between S_N and mass of the central black hole in Harris & Harris (2011) because the central black hole mass has been found to correlate with galaxy mass in Ferrarese (2002) and Ferrarese et al.(2006).

We find, in our 11 galaxy sample, the relation between total number of GCs and optical galaxy luminosity varies as,

$$N_{tot} \propto L_V^{1.6} \tag{5.14}$$

where the power 1.6 suggests that the number of GCs can not be scaled with the host galaxy luminosity. This result may suggest that GCs are not entirely associated with the host galaxy.

The range of specific frequency values may point to GC association to host cluster as well the host galaxy. Cross referencing Table 5.8 and Table 5.7, we see that the galaxies with the highest S_N values were not only the biggest galaxies, ESO383-G076 and ESO444-G046, but the most centrally located. There are two factors here so the association with the cluster is not conclusive. However, the galaxy with the lowest specific frequency of 1.47 $\pm$ 0.24 is 2MJ13481399, which is the galaxy that is the furthest away from its host cluster center. The notion that number of GCs scales with size of galaxy may not be totally accurate because 2MJ13481399 is not the smallest galaxy in the survey. The smallest galaxy is ESO325-G016 and its S_N value is 3.72 $\pm$ 0.56. This is the third smallest specific frequency. The galaxy ESO509-G067, almost twice as big as ESO325-G016, has a lower S_N of 3.11 $\pm$ 0.46. Taking into account error, the S_N values of ESO325-G016 and ESO509-G067 may be equivalent, but the great difference in size suggests that environment as well as size plays a role in GC population and consequently formation.

Another interesting finding is the evidence, seen in Figure 5.27, for Intracluster GCs in four of our five Abell clusters. Abell 1736a lacked L_X data. Interacluster GCs (IGCs) may be the solution to phenomenon in the previous paragraph. The large numbers of GCs for ESO383-G076 and ESO444-G046 may be due to the addition of IGCs, since both are within 1 arcmin of their cluster centers. The idea that clusters have GC populations associated with them, gives clues into formation scenarios. IGCs might be produced during mergers. They may be a result of tidally stripped GCs that become attracted to the cluster potential or newly formed during the merger. More studies need to be done on GC systems in clusters of varying richness.

Bibliography

[1] Abell, G. O. 1958, ApJS, 3, 211

[2] Blakeslee, J. P., & Tonry, J. L. 1995, ApJ, 442, 579

[7] Binney, J., & Merrifield, M. 1998, Galactic astronomy / James Binney and Michael Merrifield. Princeton, NJ : Princeton University Press, 1998. (Princeton series in astrophysics) QB857 .B522 1998

[4] Böhringer, H., et al. 2004, A&A, 425, 367

[6] Brodie, J. P., & Strader, J. 2006, ARA&A, 44, 193

[6] Cappellari, M., et al. 2006, MNRAS, 366, 1126

[7] Elmegreen, B. G. 1999, Ap&SS, 269, 469

[8] Ferrarese, L. 2002, ApJ, 578, 90

[9] Ferrarese, L., et al. 2006, ApJ, 644, L21

[10] Harris, W. E., & van den Bergh, S. 1981, AJ, 86, 1627

[11] Harris, W. E., Pritchet, C. J., & McClure, R. D. 1995, ApJ, 441, 120

[12] Harris, W. E., Harris, G. L. H., & McLaughlin, D. E. 1998, AJ, 115, 1801

[13] Harris, G. L. H., & Harris, W. E. 2011, MNRAS, 410, 2347

[14] King, I. 1962, AJ, 67, 471

[15] Peng, E. W., et al. 2008, ApJ, 681, 197

[16] Peng, E. W., et al. 2011, ApJ, 730, 23

[17] Press, W. H., Teukolsky, S. A., Vetterling, W. T., & Flannery, B. P. 1992, Cambridge: University Press, —c1992, 2nd ed.,

[18] McLaughlin, D. E., Harris, W. E., & Hanes, D. A. 1994, ApJ, 422, 486

[19] Mo, H., van den Bosch, F. C., & White, S. 2010, Galaxy Formation and Evolution, Cambridge University Press, 2010. ISBN: 9780521857932,

[20] van den Bergh, S., & Harris, W. E. 1982, AJ, 87, 494

[21] West, M. J., Cote, P., Jones, C., Forman, W., & Marzke, R. O. 1995, ApJ, 453, L77

[22] West, M. J., Jordán, A., Blakeslee, J. P., Côté, P., Gregg, M. D., Takamiya, M., & Marzke, R. O. 2011, A&A, 528, A115

[23] Zhang, Y.-Y., Andernach, H., Caretta, C. A., Reiprich, T. H., Böhringer, H., Puchwein, E., Sijacki, D., & Girardi, M. 2011, A&A, 526, A105

Chapter 6

Three Band Imaging of the Globular Cluster Subpopulations of ESO325-G004

6.1 Data and Selection

ESO325-G004's UCD population was the subject of Chapter 3. As discussed in that chapter, out of the 11 galaxies in the survey, ESO325-G004 was imaged with the ACS/WFC in the F475W, F625W and F814W filters due to interest for a Hubble Heritage public release image. Object detection and subsequent data reduction by DAOphot in Chapter 4 was combined with object detection by SExtractor to obtain the best GC candidates for this host galaxy. The SExtrator data was processed previously for a study of Ultra Compact Dwarf objects discussed in Chapter 3. SExtractor detects objects by finding peaks in the image and neighboring pixels that are significantly above the local background. This detection software has a variation of

apertures to measure the magnitude of image objects. The aperture we used was "AUTO", which gives magnitudes called "magauto". Magauto is measured using a kron-like elliptical aperture. This kron-like aperture is a flexible aperture that tries to capture most of the flux from a detected object (Bertin & Arnouts 1996).

The two catalogs were merged using the x,y coordinates. The merged catalog was then subjected to further selection for GC candidates. It was then possible to select GC candidates based on color using the ranges from Chapter 3, $1.3 \leq g_{475}$-$I_{814} \leq 2.0$ and $0.4 \leq r_{625}$-$I_{814} \leq 0.9$. This selection is explained in detail in 3.3.1 where color cuts from other studies in V-I correspond to the range used for g_{475}-I_{814} . These color ranges were also picked using Bruzual-Charlot single-burst stellar population models. The cut for r_{625}-I_{814} encompasses all metallicities in Figure 3.2.

After the Sextrator GC candidates and the DAOphot candidates were merged, we compared the I_{814} magnitude found from each program. Figure 6.1 shows the magnitudes plotted against each other in the top plot. One can see a shift up from the one-to-one line. The bottom plot in Figure 6.1 plots the difference in mag auto verses the DAOphot magnitude. The shift in the upper plot is represented as an offset of about 0.2 in the bottom of Figure 6.1. Each magnitude was corrected for extinction, however, the DAOphot I_{814} magnitude needed a further aperture correction (detailed in Chapter 4). Since SExtractor measured magnitude in the "AUTO" aperture, this offset may be due to the difference in aperture used in the measurement.

Figure 6.1 also shows that for magnitudes greater than 25.5, there is less correlation. This is consistent with noise affecting detection at fainter magnitudes. Therefore, for the rest of this chapter, we will look at data with a magnitude cut of 25.5. The sharpness and χ cuts are the same as described in Chapter 4 and correspond to the DAOphot magnitudes.

6.2 Color Bimodality

The common detection of color bimodality in GC populations was discussed in Chapter 1, 2 and 3. Figure 6.2 shows no bimodality in r_{625}-I_{814} due to the similarity

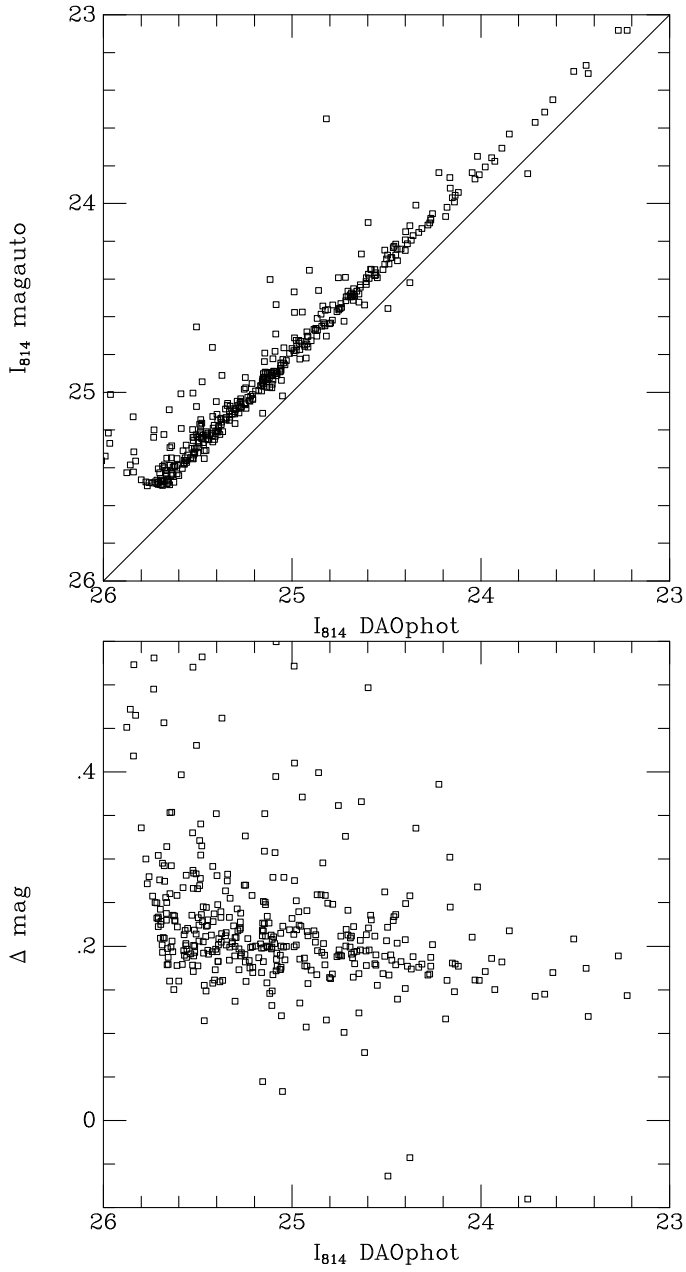

Figure 6.1 Top: Magauto from SExtractor verses magnitude from DAOphot. Both are F814W magnitudes. The line presents a one-to-one relation. The data is shifted. Bottom: This plot shows an offset of 0.2 between the magnitude from SExtractor and the magnitude from DAOphot. The F814W magnitude from DAOphot is the greater value (fainter).

between r_{625} and I_{814} being both filters on the red end of the spectrum. Bimodality is observed in Figure 6.3 which shows number of GC candidates verses g_{475}-I_{814} but not in r_{625}-I_{814} . Therefore, the statement in the globular cluster review, Brodie & Strader (2006), that "no massive elliptical (E) galaxy has been convincingly shown to lack GC subpopulations" is supported by the system of GCs of ESO325-G004.

The g_{475}-I_{814} histogram, Figure 6.3, was tested for bimodality using the KMM (Kaye's Mixture Modeling) algorithm which compares data to discern if it can be best described by a single or double Gaussian (Ashman et al. 1994). This also was mentioned in the NGC1533 study in Chapter 2. The algorithm found the g_{475}-I_{814} color data to be best described by a double Gaussian with $> 99\%$ confidence. It gave values for the two color peaks, 1.489 and 1.785 mag. We will call the 1.489 mag peak, the blue peak and the 1.785 mag peak, the red peak. When looking at Figure 6.3, a minimum at ~ 1.7 can be seen. This figure binned the number of GCs in g_{475}-I_{814} magnitude intervals of 0.05. The file that created Figure 6.3 had the lowest number of GCs in the 1.70 color bin. Binning the data by smaller g_{475}-I_{814} intervals such as 0.01 and 0.025, we found that the bin with the lowest number of GCs was still 1.70. Therefore, g_{475}-$I_{814} = 1.70$ is taken to be the minimum between the blue and red peak and the color data was split between blue and red using this value. The blue GCs are candidates with $1.30 \leq g_{475}$-$I_{814} < 1.70$ and the red GCs are candidates with $1.70 \leq g_{475}$-$I_{814} \leq 2.00$. KMM claims the blue population is 59.2% and the red population is 40.8% of the total detected GC population, 405, in ESO325-G004. However, when the data file is split into two catalogs, using 1.70 as the dividing value, the numbers are actually 274 blue GCs (67.7%) and 131 red GCs (32.3%).

6.3 Distribution

The Milky Way GC subpopulations, briefly mentioned in section 1.7.1, do tend to depend on the radius from the galactic center (galactic radius), with the "Halo" containing more metal-poor, blue GCs and the disk and bulge corresponding to more metal-rich, red GCs (Zinn 1985; Côté 1999) . Even though the Milky Way is a spiral

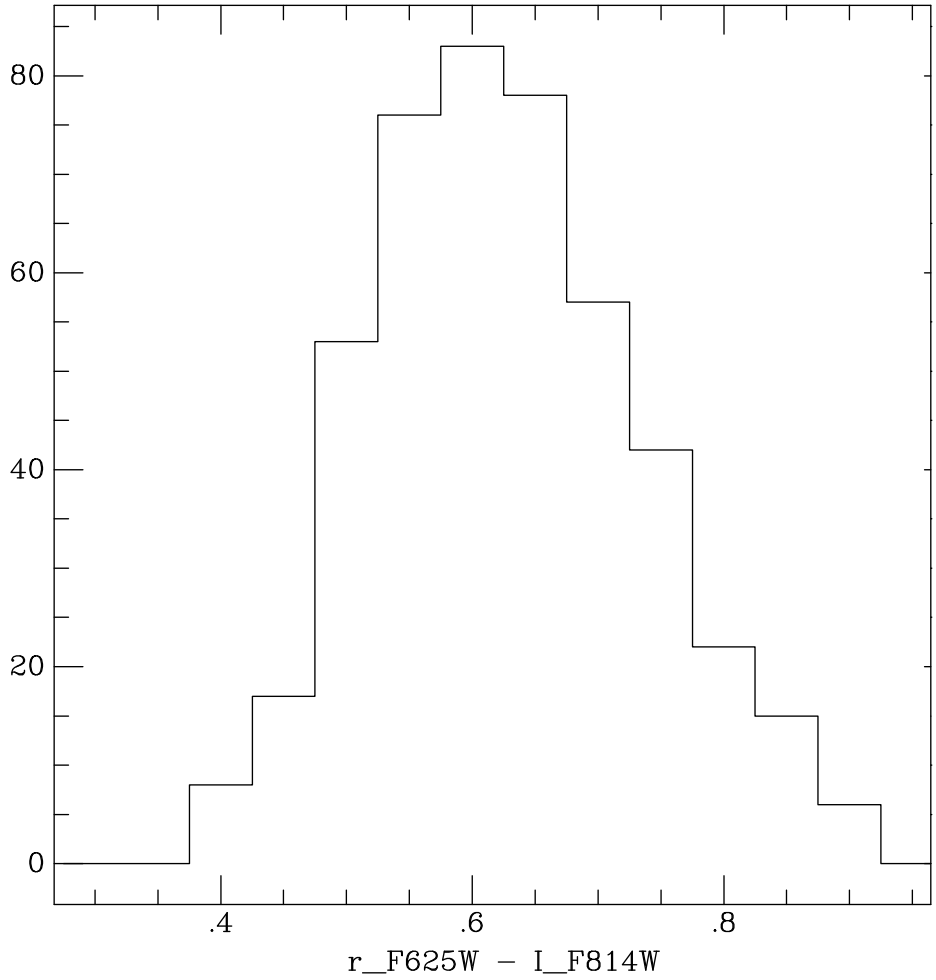

Figure 6.2 Since r and I are filters that are both on the red end, bimodality is not observed in this color, r_{625}-I_{814} . These data have been cut in magnitude from 23 to 25.5.

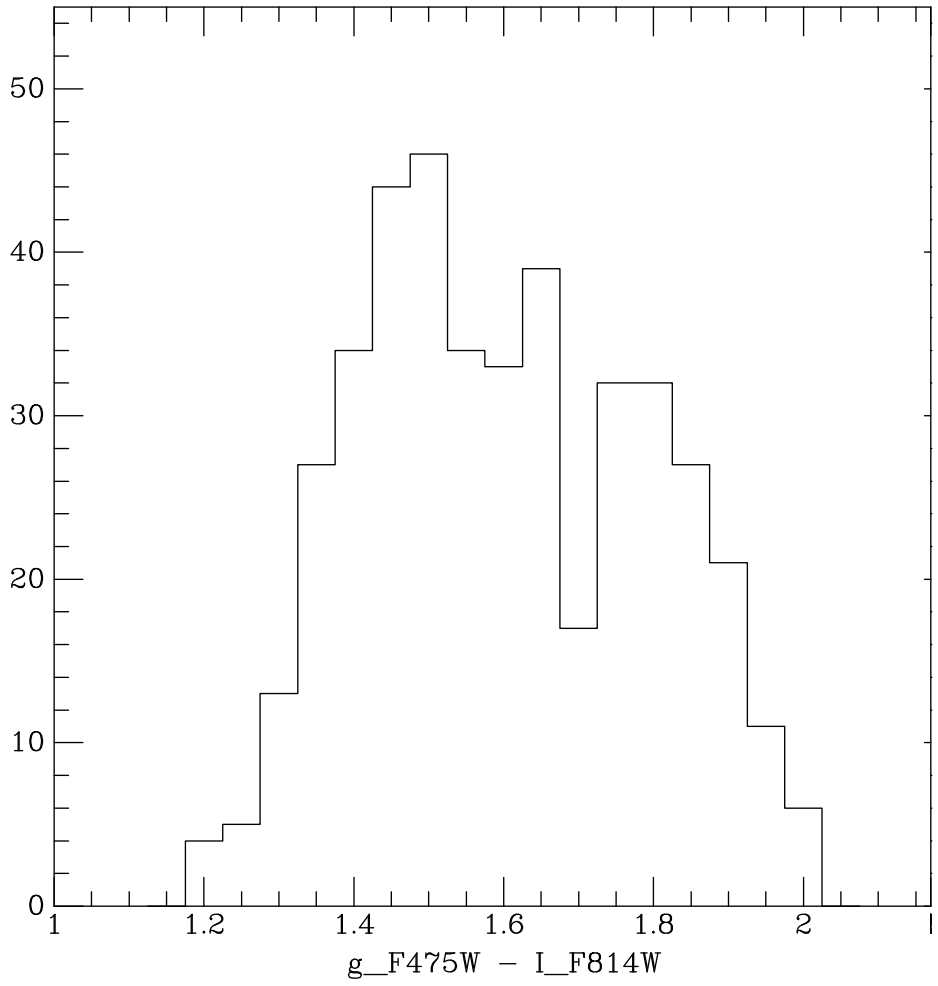

Figure 6.3 Bimodality is seen in this magnitude verse g_{475}-I_{814} plot. These data have been cut in magnitude from 23 to 25.5.

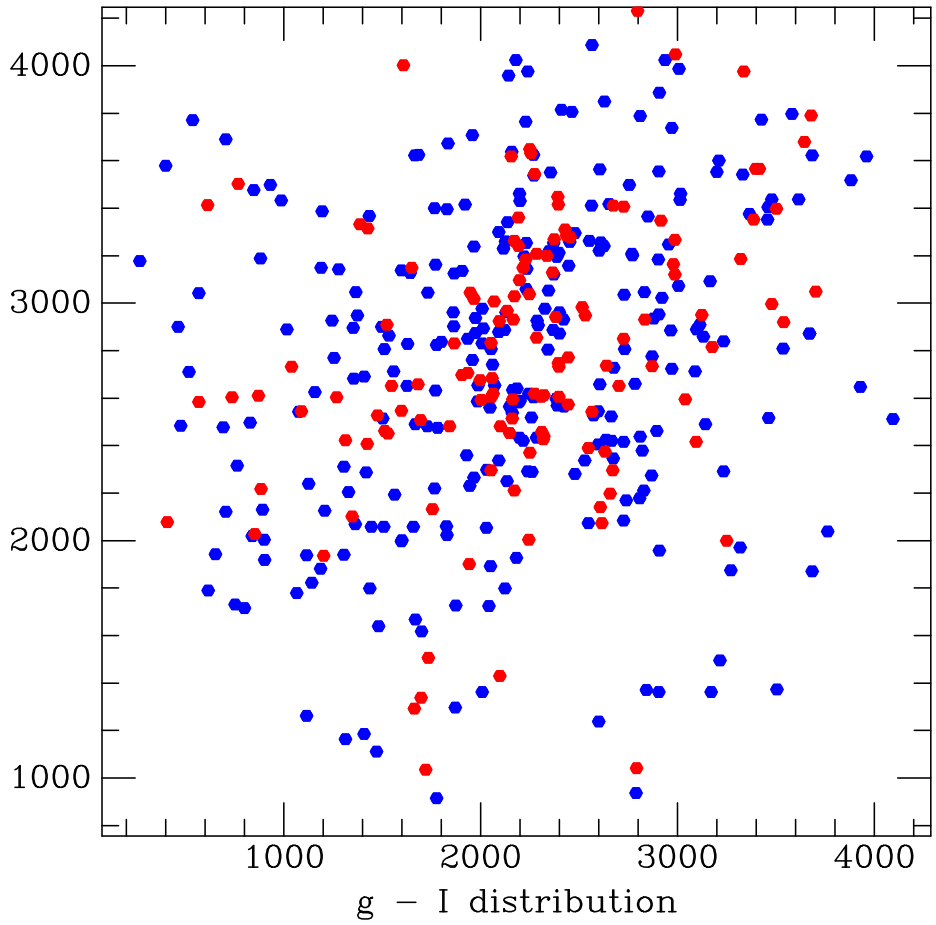

Figure 6.4 Distribution of ESO325-G004 GC subpopulations in pixel space (20 pix/arcsec)

and our study contains only ellipticals, it might be interesting to plot the two GC subpopulations of ESO325-G004 to see if there is any correlation between color and galactic radius. Figure 6.4 represents the blue and red subpopulations plotted with their x,y coordinates in pixels. The blue GCs are plotted with blue points and the red GCs are plotted with red. This Figure seems to show a concentration of red GC candidates near the center of ESO325-G004. To further verify that this is the case, Figure 6.5 shows the number density of GC's for the blue (bottom plot) and red (top plot) subpopulations verses galactic radius.

In section 5.2.2, the log-log plots of number density verses mean binned radius

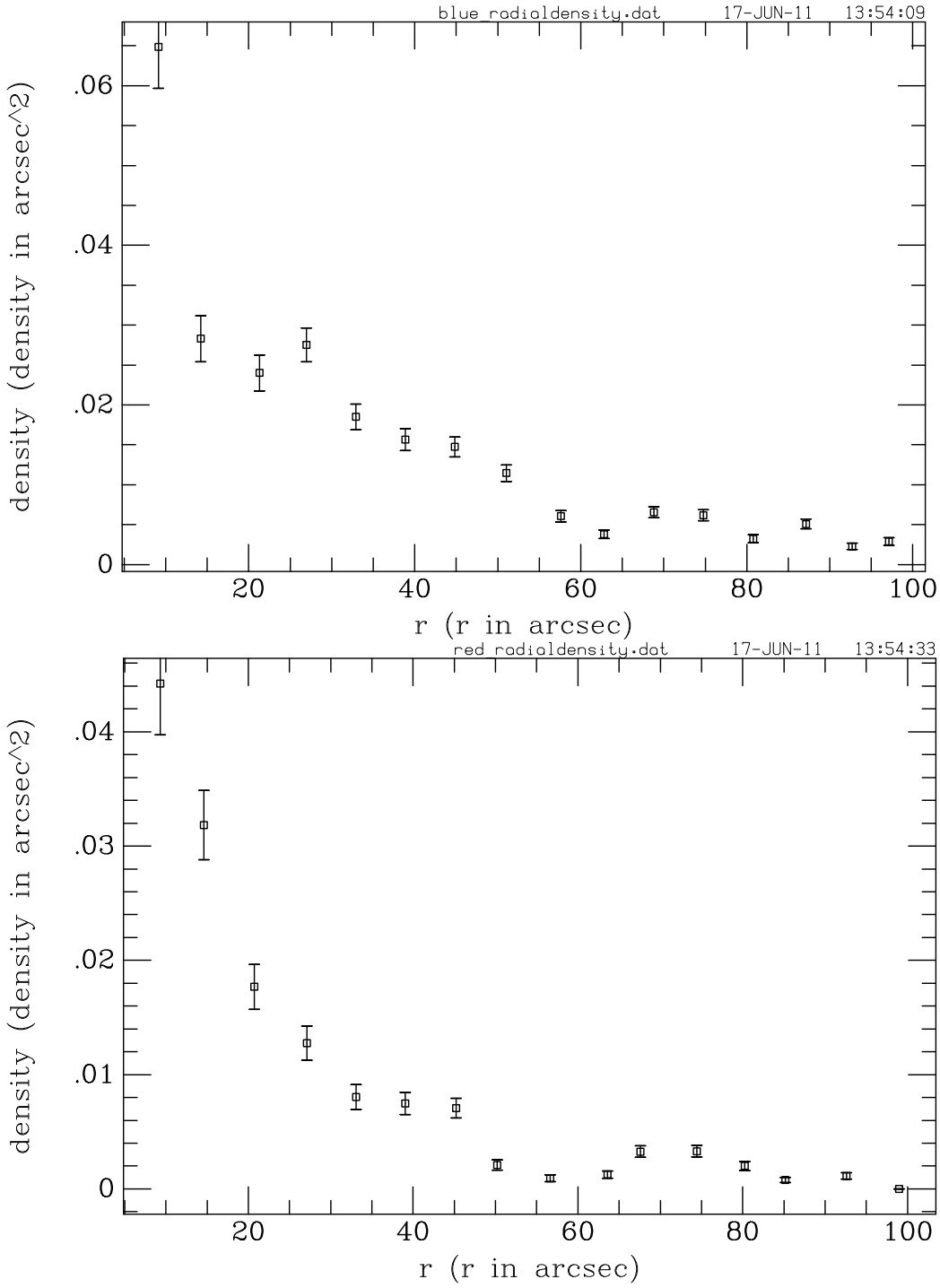

Figure 6.5 The top plot is number of Blue GCs per area verses radius from ESO325-G004 center in pixels. The bottom plot is the same plot but with Red GCs.

gave us an idea of how GC population would decrease with distance from galaxy center. Figure 6.6 shows the GC concentration of the red and blue populations in the form of a linear relation. In each plot we see the equation for the line listed. The slope for the blue population, displayed in the top log-log plot, is -1.31. Compared to the slope for the red population, -1.75, we see that the red population is verified to be more concentrated towards the center of the host galaxy. The radial densities plotted in figure 6.6 are not corrected for background since we cannot select by color for the background fields. However, since each subpopulation was plotted in the same manner, the overall trends, such as if the red population is more centrally located, are still visible.

The scenario of self-enrichment causing a bimodal GC population was discussed in Chapter 1. The observation of more centrally located red GCs may be a relic of galaxy formation. Enriched gas sank down towards the center of the galaxy and the star clusters that formed there became more metal rich than the clusters that formed in the halo (Ashman & Zepf 1998).

6.4 Blue Tilt

In Chapter 2, we discussed the correlation between GC magnitude and color. In recent studies, the blue GC subpopulation tends to become redder at higher luminosity. This occurrence is called the "Blue Tilt" (Harris et al. 2006; Mieske et al. 2006). Unlike the study done on NGC1533, we do see a slight "blue tilt" here in Figure 6.7, where the y-axis is g_{475}-I_{814} and the x-axis is I_{814} from DAOphot. The GC candidates are broken up into the blue and red population and are represented by circles of matching color. Figure 8 in the paper Bailin & Harris (2009) is an i magnitude verses g - i color plot has a very similar shape to our Figure 6.7. In this paper Bailin & Harris give a quantitative model for the color - metallicity relation and relate their self-enrichment models, for globular clusters, to the "blue tilt" observed in Harris et al. (2006). They claim that self-enrichment is the primary driver for the "blue tilt" and overlay the model prediction with the i magnitude verses g - i data in Figure 8.

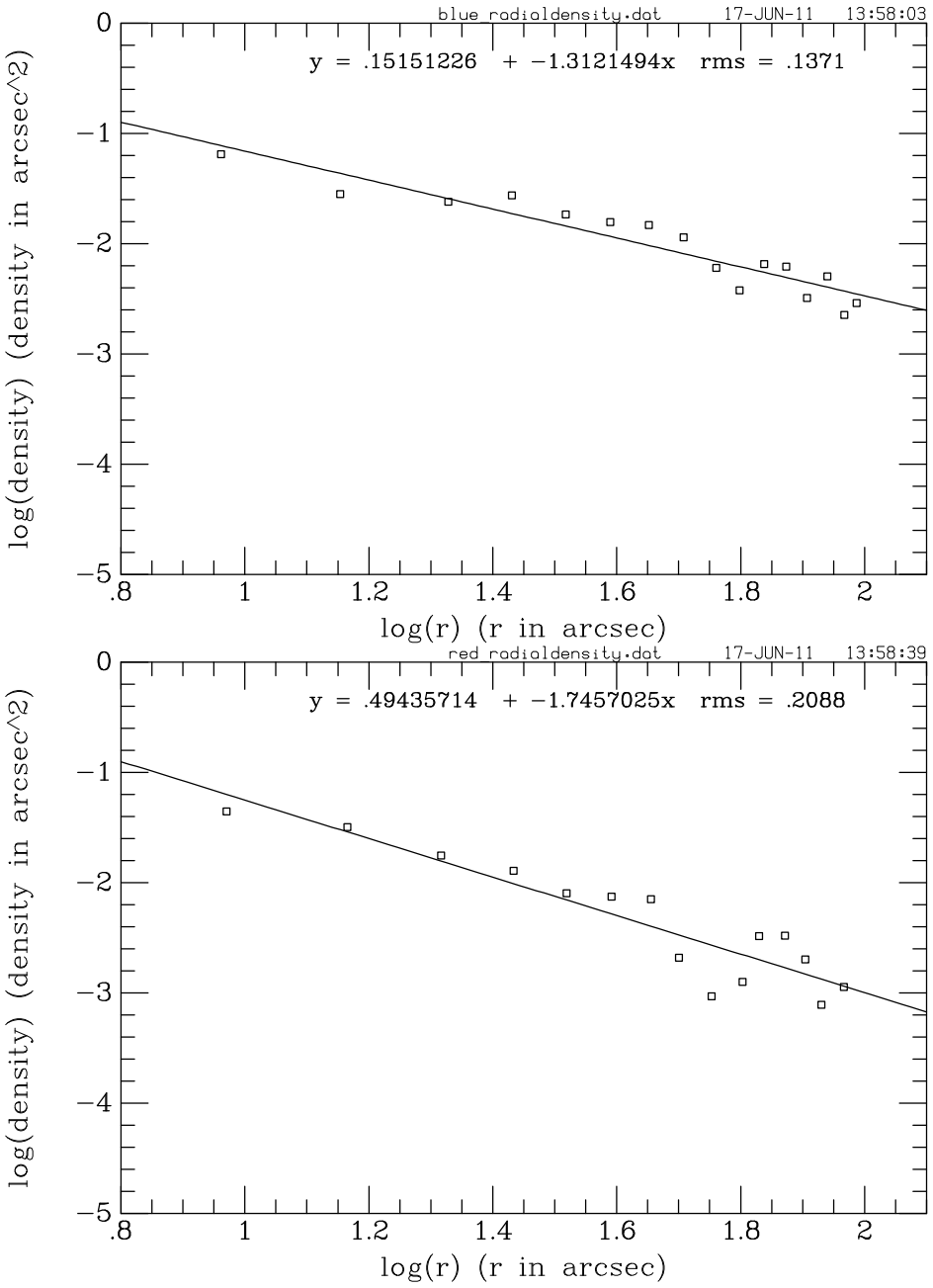

Figure 6.6 The top plot is the log-log plot of number density of Blue GCs verses radius from ESO325-G004 center in pixels. The bottom plot is the same plot but with Red GCs.

It shows a curve, that contains the GC candidates, which is fairly flat starting from 24 magnitude and climbing steeper towards brighter magnitudes (< 24) ending at the red peak vertical line in g - i. The blue GCs in Figure 6.7 seem consistent with this curve. Harris et al. (2006) claims that for very bright galaxies the GC population starts to become less obviously bimodal at $M_I < -10.5$. In our study this M_I value corresponds to an I_{814} of 25.3. Since Figure 6.7 is subject to a color cut, it is hard to confirm that our slight "blue tilt" starts around 25.3 mag.

This suggests that the slight "blue tilt" here is due to self-enrichment, which Bailin & Harris (2009) claim only creates the "blue tilt" at masses of 10^6 $M_\odot$. This is the reason evidence of the "blue tilt" comes from GCs in bright ellipticals in galaxy groups or clusters. ESO325-G004 seems to meet these requirements. Harris et al. (2006) mentions that the blue and red peaks merge into a single broad peak but since there are only about 15 objects brighter than 24 mag, it is difficult to make verify in our data set. Also, as discussed in chapter 2, if the "tilt" is due to mergers, it may only be a stronger occurrence that accompanies richer systems. If the galaxy is in a poor cluster, as is ESO325-G004, it would be another reason why a "tilt" is slight.

The "blue tilt" has been detected by Peng et al. (2009) and Harris et al. (2009). If the assumption is made that blue candidates are metal-poor, as stated in chapter 2 and Blakeslee et al. (2010), the simplest explanation for the "tilt" is self-enrichment, where the most massive metal-poor GCs were able to keep a small portion of self-enriched gas while star formation continues. However, the quick relation between color and metallicity of a globular cluster, which is so often used in studies involving bimodal color GC distributions, is under investigation (Yoon et al. 2006; Cantiello & Blakeslee 2007; Blakeslee et al. 2010) to see if this simple assumption that blue equals metal poor and red equals metal rich is reasonable.

6.5 Metallicity-Color Relation

A common occurrence of bimodality in the color distributions of GC populations can be perceived to be a reflection of metallicity (see Chapter 1, section 1.7.1)

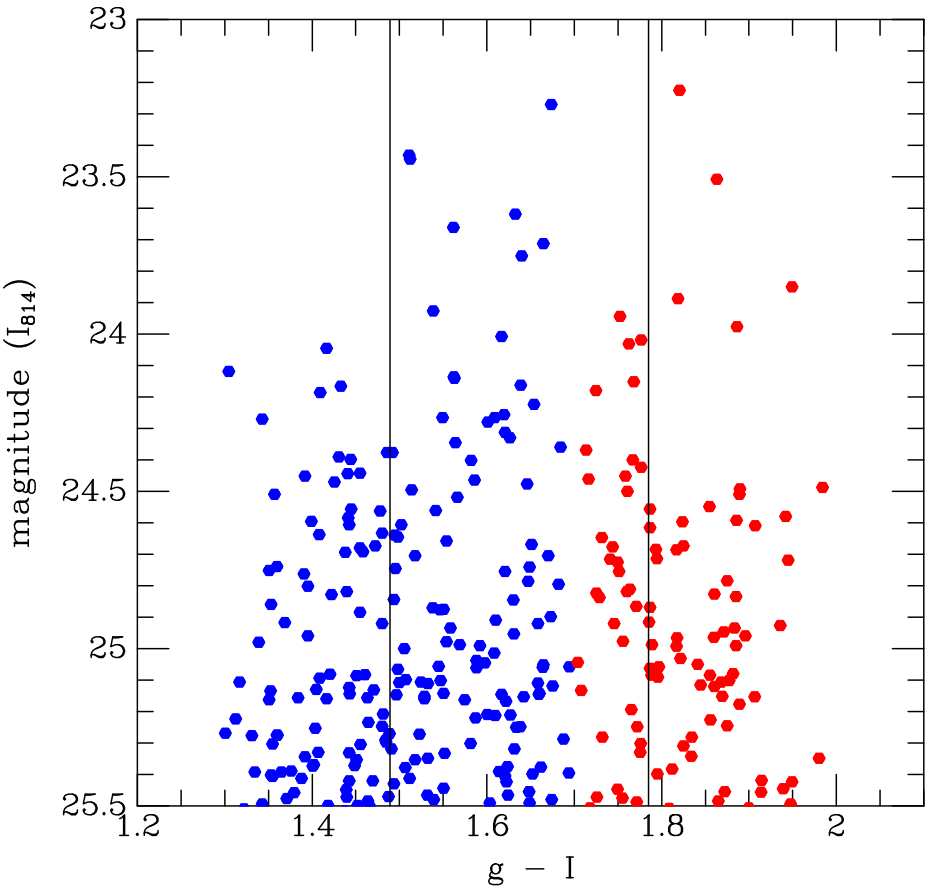

Figure 6.7 The peaks of the g_{475}-I_{814} color, blue and red, GC candidates were determined by KMM algorithm to be 1.489 and 1.785. The magnitude range, x-axis, is from 23 to 25.5 to match the histograms.

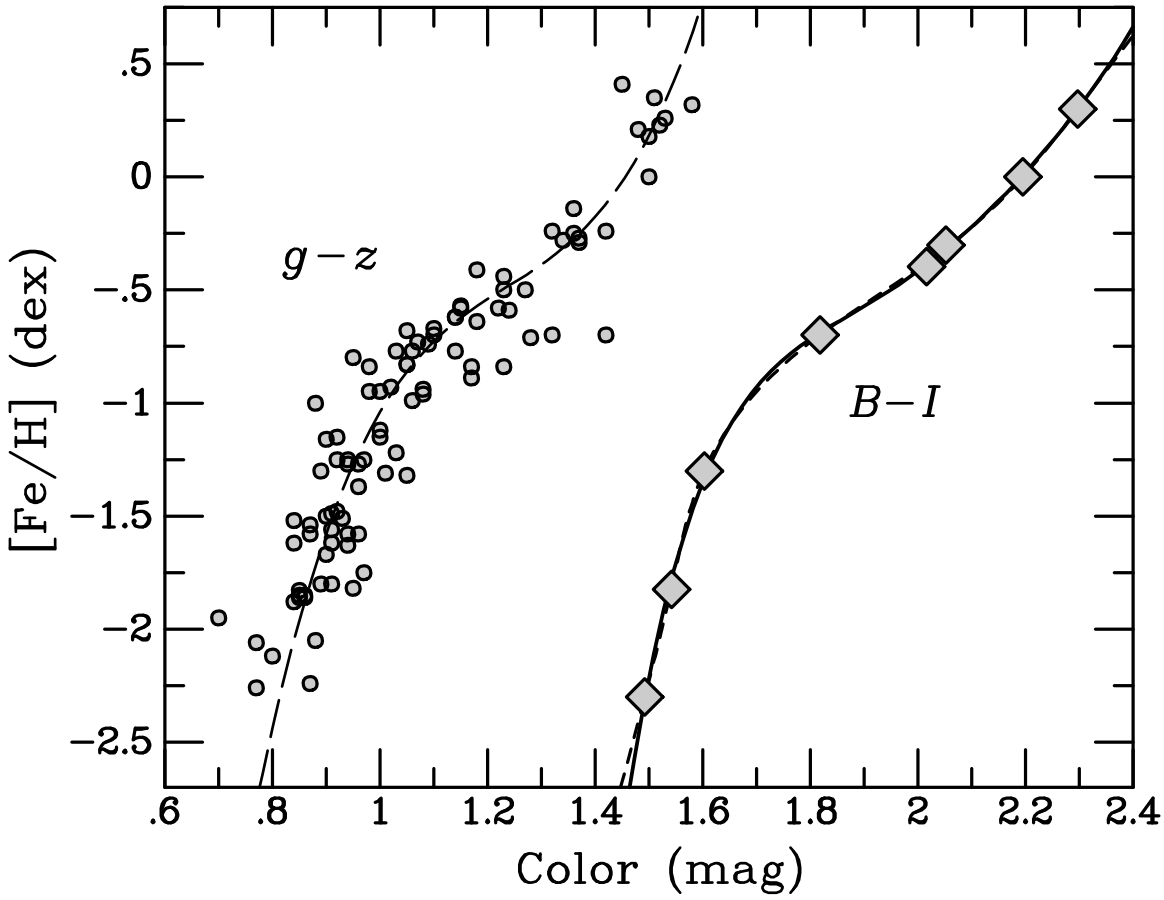

Figure 6.8 This plot shows the non-linear relationship between the colors, g - z and B - I, and metallicity, [Fe/H], courtesy of J. P. Blakeslee

differences due to the combination of photometric and spectroscopic observations indicating that GC systems are typically old, with little variation in age (Binney 1998; Chies Santos et al. 2011). High numbers of [Fe/H] correspond to metal rich values. Metallicity is directly obtained using spectroscopy. However, one major factor for the ubiquitous nature of bimodial color in massive ellipticals GCs, stated by Brodie & Strader (2006), may be a consequence of a unimodal metallicity distribution and a nonlinear color-metallicity relationship (Yoon et al. 2006). Figure 6.8 shows that the colors g - z and B - I have a non-linear relationship with metallicity,[Fe/H].

Recently stellar population models were used by Cantiello & Blakeslee (2007)

and Blakeslee et al. (2010) to see if they could reproduce color bimodality and the "blue tilt", mentioned in section 6.4, using a stellar population with a unimodal metallicity distribution. Cantiello & Blakeslee (2007) looked at the color distribution: B-V, V-R, V-I, B-I, U-R, V-K, J-H, J-K, and H-K and found that "a unimodal metallicity distribution can be projected into a bimodal color distribution in almost any of the colors considered here, depending on the properties of the metallicity distribution, on the particular color index, and on the photometric uncertainty of the sample." Figure 6.9 shows the bimodality created using different unimodal metallicity populations in the color g - z. Each colored curve represents varying metallicities. The redder curves are more metal rich and the bluer curves are more metal poor.

The metallicity to color relations were plotted and some are seen to have quite nonlinear form (see Figure 6.8), especially in the color V - I. The nonlinear curve that relates V - I to metallicity could explain the color bimodalty in V - I that is mentioned in many studies (Brodie & Strader 2006). A similar shape is mentioned in Blakeslee et al. (2010) for the [Fe/H] verses color plot (Figure 6.8). There is an inflection point in these plots that can explain the near equality of red and blue populations in the "blue tilt" situations because the inflection point is roughly equal to the peak metallicity of the GC population. The "blue tilt" could also be reproduced using a unimodal metallicity distribution (Blakeslee et al. 2010) and it is "when the peak metallicity begins to move through the inflection point that the 'blue tilt' becomes most pronounced" (Blakeslee et al. 2010).

The more linear the color-metallicity relation, the more likely a bimodal color distribution points to actual subpopulations in metallicity, examples being colors V-K and V-H. The Milky Way GC population has been found to truly be bimodal in metallicity and so the possibility is present that there are subpopulations of GCs based on one being metal-poor and one being metal-rich. However, the rule that all massive ellipiticals have bimodal color distributions may not be due to a bimodal metallicity distribution.

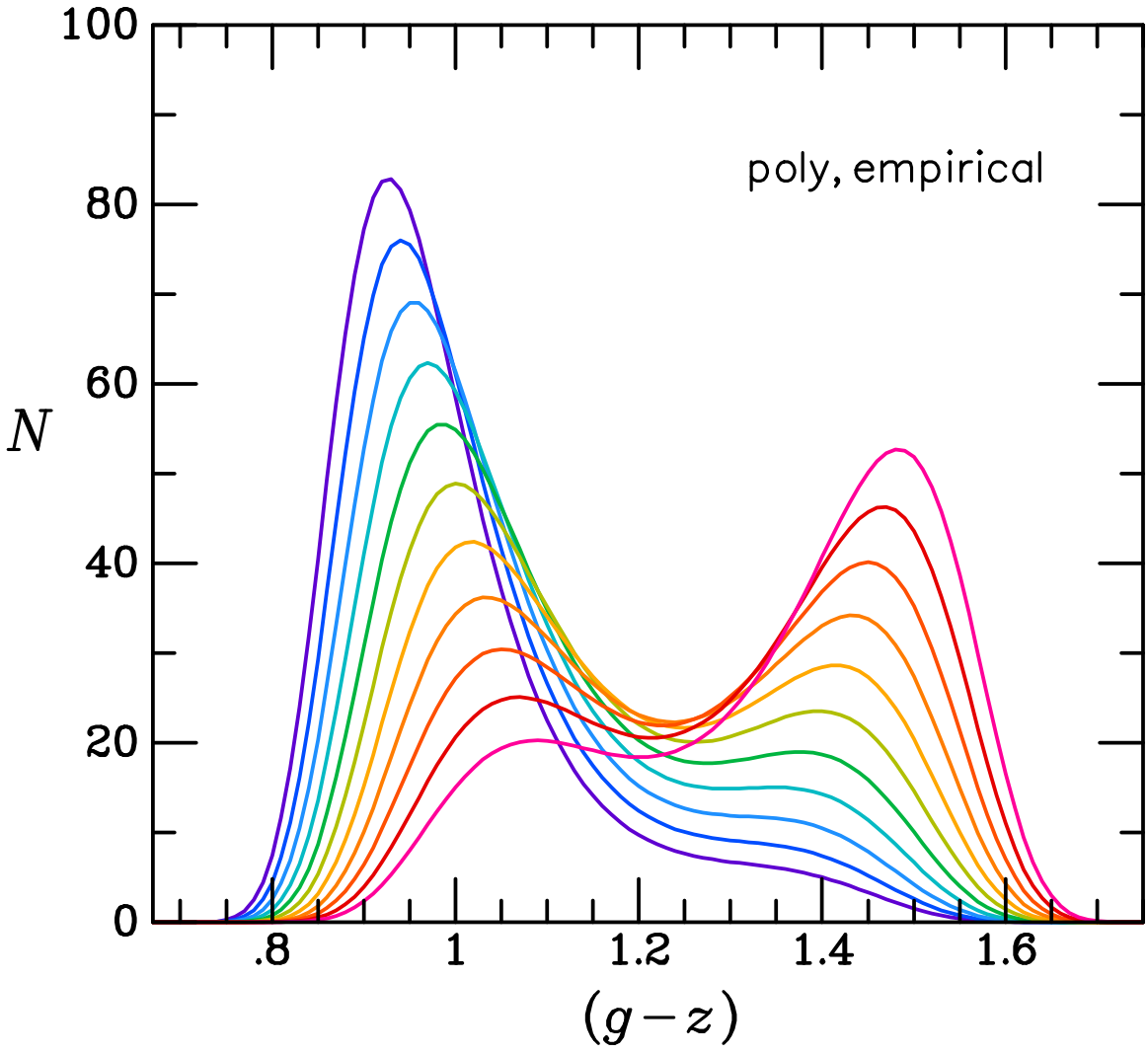

Figure 6.9 This plot shows the production of bimodal color, g - z, using unimodal metallicity GC populations, courtesy of J. P. Blakeslee. The varying colors for each curve go from red, metal rich, to blue, metal poor.

6.6 Conclusion

We analyzed the galaxy ESO325-G004 using images taken in filters, F475W, F625W and F814W. They were first run through the object detection program SExtractor and the F814W image was also studied using the object detection program DAOphot. The two catalogs were merged and then subjected to selection in I_{814} magnitude, g_{475}-I_{814} and r_{625}-I_{814} colors. This new catalog was then tested with KMM to detect bimodality in the color g_{475}-I_{814} . KMM indicated that the GC population was bimodal in the color g_{475}-I_{814} and gave a blue peak at the value 1.489 and a red peak at 1.785. The separation between blue and red GCs is g_{475}-$I_{814} = 1.70$ mag.

The distribution of the red and blue subpopulations showed the red GCs tended to be more concentrated at the galactic center. This may be due to settling of enriched gas toward the galaxy center during the process of formation. Like other ellipticals in recent studies, the blue population is greater (274) than the red population (131) and the red GCs are more concentrated at the center (Ashman & Zepf 1998; Peng et al. 2006).

The "blue tilt" cannot conclusively be detected in our study but is consistent with observations. In particular, there are no GCs brighter than $I_{814} = 24$ ($M_{I_{814}} \approx -11.8$) that have colors bluer than the blue peak of the color distribution. If the blue tilt is present, it is likely due to an overall mass-metallicity in the GC system. However, because the metallicity-color relations are not necessarily linear, it is difficult to interpret how the mean color is changing as a function of GC mass. In fact, nonlinear color-metallicity relations may also be the reason for the commonality of bimodal populations in massive ellipticals. Further spectroscopy is needed to verify if there exists true, distinct metal-poor and metal-rich subpopulations within GC systems.

A table of all GC candidates' RA, DEC, I_{814} magnitude (DAOphot), colors ($g_{475} - I_{814}$ and $r_{625} - I_{814}$) and galactic radius is included in Appendix A.

Bibliography

[1] Ashman, K. M., Bird, C. M., & Zepf, S. E. 1994, AJ, 108, 2348

[1] Ashman, K. M., & Zepf, S. E. 1998, Globular cluster systems, New York: Cambridge University Press

[3] Bailin, J., & Harris, W. E. 2009, ApJ, 695, 1082

[4] Bertin, E., & Arnouts, S. 1996, A&AS, 117, 393

[5] Blakeslee, J. P., Cantiello, M., & Peng, E. W. 2010, ApJ, 710, 51

[3] Blakeslee, J. P., & Barber DeGraaff, R. 2008, AJ, 136, 2295

[7] Binney, J., & Merrifield, M. 1998, Galactic astronomy / James Binney and Michael Merrifield. Princeton, NJ : Princeton University Press, 1998. (Princeton series in astrophysics) QB857 .B522 1998

[6] Brodie, J. P., & Strader, J. 2006, ARA&A, 44, 193

[7] Cantiello, M., & Blakeslee, J. P. 2007, ApJ, 669, 982

[10] Chies-Santos, A. L., Larsen, S. S., Kuntschner, H., Anders, P., Wehner, E. M., Strader, J., Brodie, J. P., & Santos, J. F. C. 2011, A&A, 525, A20

[11] Côté, P. 1999, AJ, 118, 406

[12] Harris, W. E., Whitmore, B. C., Karakla, D., Okoń, W., Baum, W. A., Hanes, D. A., & Kavelaars, J. J. 2006, ApJ, 636, 90

[13] Harris, W. E., Kavelaars, J. J., Hanes, D. A., Pritchet, C. J., & Baum, W. A. 2009, AJ, 137, 3314

[14] Mieske, S., et al. 2006, ApJ, 653, 193

[9] Peng, E. W., et al. 2006, ApJ, 639, 95

[16] Peng, E. W., et al. 2009, ApJ, 703, 42

[11] Yoon, S.-J., Yi, S. K., & Lee, Y.-W. 2006, Science, 311, 1129

[18] Zinn, R. 1985, ApJ, 293, 424

Chapter 7

Summary and Future Work

7.1 Summary and Results

The main study in this thesis is the survey investigating the globular cluster (GC) populations of 11 galaxies in the Shapley Supercluster. Due to the simplicity of globular clusters, the characteristics of these populations can contribute to observations that constrain galaxy, cluster or GC formation models. The characteristics discussed are total number, specific frequency, distribution and association with galaxy and cluster properties.

After an introduction to the history of globular clusters and various terminology in astronomy, we briefly cover galaxy formation and recent developments in globular cluster studies. We discuss bimodality in color of GCs surrounding giant ellipticals and the wide range of values for specific frequency, S_N, in this type of galaxy.

We then do a related study on the GC population of the S0 galaxy in the Dorado Group, NGC1533. NGC1533 was imaged by ACS through F814W and F606W. The galaxy was found to have a faint spiral structure after model subtraction. NGC1533 is known to have H II regions with possible star formation far from the galactic center. We found four H II regions along one of the faint spiral arms. This galaxy seems to

be in transition from an Sba to an S0 galaxy. These H II regions and the hint of transition may be due to interaction between neighboring galaxies. The interaction between NGC1533 and IC 2038/2039 is documented (Ryan-Weber et al. 2004).

We use the distance indicators described in Chapter 1 to find distance to NGC1533 three different ways. The SBF distance is 19.4 ± 1.1 Mpc. The distance obtained using the GCLF method was equal to 19.4 Mpc, within errors. Distance to NGC1533 calculated using the median half-light GC radius was 18.6 ± 2.0 Mpc. There seems to be a correlation between GC size (half-light radius) and distance from NGC1533 (galactocentric radius). We find S_N to be 1.3 ± 0.2, which is typical for a S0 galaxy.

The color F606W - F814W was converted to the color V - I to compare NGC1533's GC population to other studies. The KMM algorithm indicated that the GC population was bimodal in V - I with peaks at roughly 0.92 and 1.22 mag. There is no evidence for the "blue tilt" (blue GCs becoming redder at brighter magnitudes). However, the blue tilt has been more commonly seen in massive ellipticals.

The conclusion that NGC1533 is a galaxy in transition is further supported by the GC population having similarities in size, color and luminosity, with Virgo early-type galaxies but also showing a strong dependence of size of GCs with galactocentric radius like the GCs of the Milky Way (Barber DeGraaff 2007).

Ultra Compact Dwarfs (UCD) are a new classification of stellar system that is thought to be associated with globular clusters. Their physical size is greater than GCs (3-5 pcs) but smaller than dwarf galaxies. We searched for UCDs in the giant elliptical ESO325-G004, using three band imaging (F475W, F814W and F625W). This galaxy is a member of Abell S0740, a poor cluster in the Shapley Supercluster. We selected objects that were brighter than 99% of the expected GC population, the same GC color range at this redshift, shape similar to a GC and half light radii (size) in the 10-100pc range. Spectra need to be taken to confirm the UCD candidates found are associated with ESO325-G004. We also included a group of larger compact galaxies of 100-300pc in our study. When color data for all the UCD candidates was plotted, the population seemed to be weighted toward the red. There also seemed to be a bifurcation in UCD candidate size. There seemed to be a group with size similar to GCs and then another clump greater than 40pc. These two distinct groups

may point to two different mechanisms in creating UCDs. Some propose that UCDs are just tidally stripped dwarf galaxies. We found that most of the UCD candidates had visible surrounding halo light, which is consistent with galaxy threshing models. Other studies suggest that UCDs are just a high luminosity extension of the GC system. A combination of both views may be closer to reality (Blakeslee & Barber DeGraaff 2008).

The GC populations of the 11 galaxies in the Shapley Supercluster were then studied, using imaging from ACS in F814W. Data reduction was done using the detection software DAOphot and described in Chapter 4 along with a brief description of the Shapley Supercluster. We were interested in obtaining total number of GCs, distribution, and specific frequencies (S_Ns). To obtain the total number of the 11 GC systems, we needed to take into account many corrections. The number of GCs detected for each of the 11 galaxies was not a reflection of the actual GC population due to completeness in detection, background and foreground objects in the field, the magnitude range imposed in the selection and the radial limits imposed by our selection and HST/ACS. Another correction needed to be considered when counting the number of GCs associated with members of Abell 3558. Because the BCG, ESO444-G046, was massive and centrally located, we considered how much it's GC population "contaminated" the neighboring members.

Once all these corrections were obtained a total number of GCs, N_{tot} could be estimated for each of the 11 galaxies in the survey. The N_{tot} values ranged from $\sim$ 850 to 27,500. Plotting a log-log plot of N_{tot} verses L_V, luminosity of the galaxy in the V band, showed a relation of,

$$N_{tot} \propto L_V^{1.6} \tag{7.1}$$

where the power of 1.6 is contrary to the once believed value of 1.0. This result suggests that the formation of the GC population must be dependent on something other than simply the host galaxy's star formation history.

The S_N values ranged from values as low as 1.47 (similar to NGC1533) to values as high as 10.3. Note that these are the specific frequencies estimated within a radius of

100 kpc; the GC populations of the largest galaxies likely extend beyond this radius, so the actual S_N values for these largest galaxies could be significantly higher. We find a strong correlation of S_N with the dynamical mass of the galaxy.

The lowest specific frequency value of 1.47 and the two highest values of 10.3 and 8.1 seem to not only relate to the size of the galaxy but also to the location of the galaxy in the host cluster. Additionally the reason for two galaxies, with drastically different sizes, having the same S_N values may be due to the bigger galaxy's great distance from its cluster center. This result points toward GC populations being associated with the host cluster as well as the host galaxy.

Stronger evidence comes in the form of the concept of Intracluster Globular Clusters (IGCs), which are thought to be GCs associated with the cluster's potential well. Figure 5.27 strongly suggests that four of the five Abell clusters contain IGCs. The IGC population may increase the GC population of centrally located cluster members, which makes sense when thinking of ESO383-G076 and ESO444-G046. Their large numbers of GCs may just be the addition of IGCs because ESO383-G076 and ESO444-G046 are both within 1 arcmin of the cluster center.

The additional imaging of ESO325-G004, used to search for UCDs, was used to receive color data for the GC population. The GC population from Chapter 5 was combined with data obtained in the study done in Chapter 3. The GC candidates were further selected with g_{475}-I_{814} and r_{625}-I_{814} . The KMM algorithm confirmed that the GC population was bimodal in g_{475}-I_{814} with a red peak at 1.785 mag and a blue peak at 1.489 mag. The minimum at 1.70 was used as the dividing value to separate the data into two populations, a red and a blue. The red population was found to be more concentrated towards the center of ESO325-G004. The blue population was found to be more abundant (274 blue, 131 red). The GC color population of ESO325-G004 is typical of a massive elliptical (Ashman & Zepf 1998; Peng et al. 2006).

The "blue tilt" discussed earlier was present, if only slightly. However, this phenomenon was produced in models of star clusters with unimodal metallicities (Blakeslee et al. 2010), so the tilt is not proof that there are really two distinct metallicity subpopulations. The bimodality through this color also may be a consequence of color-metallicity conversions. This concept, of directly correlating bimodality in color

to bimodality in metallicity, is discussed in Chapter 6 and first mentioned in Yoon et al. (2006). Models have been run that create bimodal color distribution using stellar populations with unimodal metallicity (Cantiello & Blakeslee 2007; Blakeslee et al. 2010). However, the Milky Way does have two populations of GCs that are bimodal in color and metallicity. This has been verified with spectroscopy. Therefore, it is possible that some GC populations are bimodal in both color and metallicity but the common observation that GC populations in ellipticals are bimodal in color (Brodie & Strader 2006) may not point towards bimodality in metallicity.

7.2 Future Work

Spectra of the UCD candidates in Chapter 3 have been obtained to verify the candidate's location and need to be further reduced. I hope to do this work directly after papers are published with results from this thesis.

Color data would be very helpful in investigating if bimodality is present in the other 10 galaxies. Second band imaging in F475W (comparable to g) will be available for ESO444-G046 and ESO509-G008. HST Proposal 12238 has been submitted by William Harris and accepted for Cycle 18 of HST which ends August 2011. I am a co-investigator on said proposal (Harris 2009).

One band imaging in F814w using HST/ACS of Abell 1689 was recently completed (HST Proposal 11710, Blakeslee 2008). It is an extreme GC population. Estimates for a galaxy of this size is a GC population of $\sim$ 100,000. At a redshift of $z = 0.183$, it would be the biggest, farthest GC population studied to date (Blakeslee 2008). A total number of GCs would be helpful in testing formation hypotheses. Since I am a co-investigator on this proposal, I hope to help with this important project.

Bibliography

[1] Ashman, K. M., & Zepf, S. E. 1998, Globular cluster systems, New York: Cambridge University Press

[2] Barber DeGraaff, R., Blakeslee, J. P., Meurer, G. R., & Putman, M. E. 2007, arXiv:0710.0893

[3] Blakeslee, J. P., & Barber DeGraaff, R. 2008, AJ, 136, 2295

[4] Blakeslee, J. 2008, HST Proposal, 11710

[5] Blakeslee, J. P., Cantiello, M., & Peng, E. W. 2010, ApJ, 710, 51

[6] Brodie, J. P., & Strader, J. 2006, ARA&A, 44, 193

[7] Cantiello, M., & Blakeslee, J. P. 2007, ApJ, 669, 982

[8] Harris, W. 2009, HST Proposal, 12238

[9] Peng, E. W., et al. 2006, ApJ, 639, 95

[10] Ryan-Weber, E. V., et al. 2004, AJ, 127, 1431

[11] Yoon, S.-J., Yi, S. K., & Lee, Y.-W. 2006, Science, 311, 1129

Appendix A

ESO325-G004 GCs

This table contains the id, RA, Dec, I band apparent magnitude, colors in g - I and r - I and radius from center of host galaxy in pixels. This data list was created by combining detections from the software DAOphot and SExtractor.

Table A.1. ESO325-g004 GC Candidates

ID	RA	DEC	I_{814}	r - I	±	g - I	±	radius
28.0	205.860642	-38.176554	24.838	0.714	1.729	0.065	0.095	1573.5
60.0	205.866475	-38.166312	25.715	0.575	1.238	0.080	0.097	1421.0
143.0	205.864477	-38.174271	25.275	0.695	1.360	0.060	0.064	1360.7
194.0	205.862420	-38.179985	25.085	0.755	1.789	0.051	0.075	1501.5
217.0	205.863161	-38.179395	25.454	0.607	1.648	0.065	0.092	1452.4
220.0	205.868002	-38.169589	25.522	0.571	1.405	0.061	0.079	1241.9
238.0	205.871978	-38.162298	24.180	0.694	1.725	0.031	0.042	1350.6
262.0	205.863328	-38.180511	25.683	0.485	1.353	0.066	0.083	1459.2
268.0	205.868376	-38.170628	24.762	0.483	1.391	0.038	0.049	1196.5
269.0	205.861405	-38.184845	25.877	0.607	1.722	0.083	0.128	1659.9
282.0	205.869298	-38.169429	25.610	0.564	1.672	0.066	0.101	1178.5
288.0	205.875191	-38.157614	25.453	0.300	1.240	0.049	0.061	1513.9
384.0	205.865601	-38.179738	25.627	0.549	1.482	0.072	0.093	1321.7
434.0	205.867985	-38.176280	25.716	0.679	1.448	0.079	0.100	1157.5
470.0	205.869978	-38.173636	24.638	0.529	1.408	0.039	0.047	1056.9
486.0	205.869758	-38.174379	25.429	0.559	1.494	0.059	0.082	1062.4
491.0	205.862783	-38.188885	24.444	0.594	1.441	0.035	0.041	1727.2
500.0	205.862277	-38.190174	25.566	0.799	1.830	0.075	0.114	1802.6
502.0	205.867855	-38.178942	26.459	0.893	1.508	0.095	0.095	1185.4
515.0	205.864157	-38.187009	26.650	0.209	1.478	0.088	0.151	1590.2
520.0	205.882600	-38.149587	24.680	0.480	1.455	0.045	0.045	1922.0
526.0	205.871950	-38.171548	24.752	0.596	1.351	0.040	0.046	983.6
530.0	205.861828	-38.192174	26.458	0.501	1.222	0.095	0.107	1908.6
569.0	205.867647	-38.181295	26.300	0.538	1.643	0.117	0.182	1239.1
619.0	205.874621	-38.168299	25.609	0.623	1.478	0.069	0.090	953.5
654.0	205.882859	-38.152191	25.109	0.617	1.658	0.058	0.070	1734.8
671.0	205.864322	-38.190322	25.281	0.725	1.732	0.062	0.089	1715.3
681.0	205.875948	-38.166896	25.420	0.605	1.469	0.064	0.083	958.1
721.0	205.873723	-38.172410	25.516	0.754	1.810	0.073	0.109	869.2
738.0	205.874474	-38.171242	25.223	0.478	1.312	0.049	0.061	857.7
754.0	205.873976	-38.172564	24.976	0.657	1.756	0.048	0.070	852.3
761.0	205.873975	-38.172760	25.038	0.571	1.588	0.046	0.064	848.5
762.0	205.865012	-38.191081	24.442	0.571	1.455	0.035	0.044	1718.6
765.0	205.877726	-38.165169	25.152	0.634	1.528	0.052	0.067	981.0
766.0	205.877858	-38.164948	24.312	0.618	1.621	0.032	0.042	989.0

Table A.1 (cont'd)

ID	RA	DEC	I_{814}	r - I	±	g - I	±	radius
776.0	205.874810	-38.171311	25.454	0.797	1.872	0.074	0.112	838.3
778.0	205.863339	-38.194702	25.220	0.602	1.587	0.053	0.073	1962.7
788.0	205.868578	-38.186931	24.953	0.611	1.631	0.050	0.068	1376.6
810.0	205.868411	-38.185071	25.209	0.680	1.601	0.058	0.074	1312.1
835.0	205.867649	-38.187895	24.597	0.765	1.824	0.046	0.066	1459.9
837.0	205.867762	-38.187681	25.506	1.044	1.718	0.089	0.097	1445.7
850.0	205.886633	-38.148787	25.449	0.536	1.439	0.075	0.076	1953.7
874.0	205.872874	-38.177420	24.674	0.605	1.472	0.042	0.052	887.4
888.0	205.871105	-38.181362	25.159	0.485	1.417	0.050	0.062	1056.9
890.0	205.869245	-38.185189	25.830	0.549	1.413	0.069	0.088	1276.0
895.0	205.874678	-38.174252	25.131	0.633	1.471	0.053	0.065	787.2
899.0	205.875298	-38.173206	23.225	0.690	1.820	0.022	0.029	767.9
900.0	205.875419	-38.173210	25.485	0.589	1.464	0.060	0.074	761.2
938.0	205.865496	-38.194187	24.008	0.641	1.617	0.029	0.038	1849.7
965.0	205.885538	-38.153930	24.715	0.674	1.741	0.044	0.060	1589.1
973.0	205.872986	-38.179690	25.689	0.528	1.369	0.079	0.090	916.1
974.0	205.884595	-38.156084	26.578	0.684	1.478	0.113	0.142	1442.0
1020.0	205.885471	-38.155084	25.739	0.719	1.614	0.081	0.111	1507.0
1049.0	205.877138	-38.172656	24.801	0.501	1.395	0.041	0.050	680.1
1055.0	205.871939	-38.183268	25.102	0.555	1.547	0.050	0.067	1074.1
1079.0	205.876105	-38.175246	25.063	0.741	1.786	0.057	0.077	699.1
1093.0	205.869380	-38.189388	24.745	0.589	1.495	0.040	0.053	1451.9
1097.0	205.868514	-38.191156	25.524	0.520	1.464	0.062	0.084	1574.7
1101.0	205.872392	-38.183365	25.398	0.546	1.652	0.058	0.088	1055.5
1106.0	205.885299	-38.157121	25.291	0.521	1.484	0.052	0.070	1362.5
1109.0	205.877614	-38.172840	25.526	0.524	1.450	0.062	0.084	650.2
1118.0	205.869887	-38.189896	25.857	0.642	1.810	0.077	0.128	1455.6
1121.0	205.874963	-38.178758	24.265	0.596	1.550	0.032	0.040	789.9
1127.0	205.876625	-38.175445	25.677	0.696	1.746	0.079	0.118	669.2
1131.0	205.879665	-38.169320	23.443	0.595	1.512	0.022	0.026	685.2
1135.0	205.888019	-38.152373	24.549	0.721	1.855	0.051	0.058	1693.0
1140.0	205.874940	-38.179069	24.510	0.762	1.889	0.041	0.062	797.2
1142.0	205.875634	-38.177639	24.828	0.601	1.422	0.045	0.052	735.1
1152.0	205.874670	-38.179760	25.133	0.667	1.708	0.064	0.080	827.4
1154.0	205.870054	-38.189302	25.638	0.622	1.687	0.072	0.105	1419.5

Table A.1 (cont'd)

ID	RA	DEC	I_{814}	r - I	±	g - I	±	radius
1168.0	205.880585	-38.168193	24.595	0.488	1.399	0.038	0.047	709.7
1169.0	205.880898	-38.167352	25.373	0.484	1.401	0.057	0.071	747.7
1202.0	205.884740	-38.160045	24.899	0.630	1.673	0.044	0.063	1159.4
1211.0	205.871117	-38.188197	23.271	0.602	1.674	0.021	0.026	1321.5
1230.0	205.883558	-38.163223	25.330	0.473	1.407	0.053	0.070	952.4
1244.0	205.874585	-38.181593	25.687	0.551	1.410	0.080	0.090	884.8
1250.0	205.878824	-38.173071	25.446	0.616	1.939	0.067	0.117	580.1
1260.0	205.870901	-38.189530	24.471	0.520	1.425	0.034	0.042	1396.3
1262.0	205.871379	-38.188618	23.944	0.671	1.752	0.029	0.038	1331.2
1272.0	205.874445	-38.182516	25.553	0.665	1.900	0.070	0.119	924.4
1290.0	205.879516	-38.172453	24.451	0.502	1.392	0.034	0.041	561.8
1307.0	205.884431	-38.162813	24.935	0.757	1.883	0.049	0.077	967.9
1336.0	205.884454	-38.163379	25.601	0.703	1.871	0.072	0.120	928.0
1341.0	205.878136	-38.176398	24.677	0.672	1.744	0.042	0.059	583.8
1360.0	205.880472	-38.172092	25.353	0.536	1.451	0.059	0.073	526.6
1369.0	205.878073	-38.177114	25.632	0.533	1.458	0.069	0.088	592.8
1381.0	205.878530	-38.176650	25.079	0.752	1.881	0.059	0.088	563.1
1392.0	205.878519	-38.176908	25.151	0.715	1.869	0.060	0.094	565.7
1406.0	205.879198	-38.175896	24.964	0.727	1.860	0.053	0.078	522.5
1408.0	205.875311	-38.183856	24.826	0.745	1.860	0.048	0.070	938.5
1419.0	205.878146	-38.178253	25.344	0.474	1.392	0.058	0.071	606.5
1423.0	205.880592	-38.173308	25.523	0.698	1.733	0.073	0.107	480.8
1425.0	205.880902	-38.172718	25.657	0.489	1.618	0.069	0.104	483.1
1430.0	205.877879	-38.179017	24.846	0.647	1.631	0.048	0.061	638.5
1431.0	205.878875	-38.176978	25.146	0.636	1.617	0.058	0.075	546.6
1436.0	205.879446	-38.175922	25.061	0.592	1.588	0.054	0.071	508.5
1439.0	205.880350	-38.174126	25.162	0.532	1.351	0.054	0.063	474.5
1454.0	205.875859	-38.183540	24.633	0.496	1.480	0.039	0.051	899.8
1462.0	205.878033	-38.179299	25.578	0.612	1.457	0.074	0.090	637.7
1468.0	205.880818	-38.173701	24.556	0.780	1.787	0.045	0.059	458.6
1474.0	205.882297	-38.170771	25.250	0.688	1.634	0.062	0.081	505.9
1488.0	205.881464	-38.172738	25.480	0.699	1.539	0.072	0.087	454.6
1501.0	205.878516	-38.179115	25.056	0.682	1.545	0.056	0.067	607.4
1503.0	205.880189	-38.175799	24.584	0.578	1.441	0.041	0.048	466.5
1512.0	205.879948	-38.176494	25.726	0.540	1.604	0.081	0.112	482.1

Table A.1 (cont'd)

ID	RA	DEC	I_{814}	r - I	±	g - I	±	radius
1518.0	205.880748	-38.175037	25.153	0.770	1.906	0.066	0.098	439.0
1521.0	205.877692	-38.181316	25.083	0.589	1.460	0.056	0.062	722.8
1522.0	205.877771	-38.181370	25.318	0.634	1.631	0.066	0.084	721.1
1537.0	205.880583	-38.175754	24.992	0.648	1.817	0.052	0.078	444.3
1540.0	205.881337	-38.174266	24.741	0.641	1.649	0.046	0.060	418.0
1548.0	205.880318	-38.176435	24.607	0.553	1.502	0.040	0.049	460.8
1564.0	205.889992	-38.156971	25.472	0.516	1.440	0.059	0.077	1364.6
1567.0	205.874512	-38.188595	24.785	0.777	1.875	0.048	0.074	1207.5
1569.0	205.877210	-38.183156	24.562	0.556	1.478	0.037	0.046	823.1
1571.0	205.881514	-38.174459	25.043	0.745	1.704	0.059	0.075	404.6
1581.0	205.894087	-38.149067	25.106	0.597	1.317	0.065	0.056	1957.2
1601.0	205.877051	-38.184249	25.302	0.692	1.776	0.062	0.092	881.8
1606.0	205.884784	-38.168625	25.272	0.533	1.523	0.056	0.076	561.8
1607.0	205.885766	-38.167120	25.966	0.662	1.901	0.095	0.163	648.9
1613.0	205.880538	-38.177399	25.651	0.680	1.478	0.069	0.081	459.9
1634.0	205.882171	-38.174452	25.423	0.803	1.949	0.079	0.121	368.9
1638.0	205.888717	-38.161144	25.107	0.481	1.525	0.046	0.066	1061.4
1643.0	205.882121	-38.174694	24.921	0.598	1.658	0.051	0.070	367.2
1648.0	205.888230	-38.162357	25.839	0.704	1.369	0.074	0.079	974.0
1660.0	205.886279	-38.166494	25.423	0.729	1.623	0.068	0.086	686.9
1664.0	205.884342	-38.170505	25.390	0.646	1.614	0.067	0.089	451.2
1674.0	205.881537	-38.176497	24.685	0.712	1.794	0.049	0.067	392.6
1683.0	205.884799	-38.170031	23.431	0.552	1.511	0.023	0.028	468.8
1684.0	205.886196	-38.167121	25.045	0.642	1.598	0.050	0.066	643.5
1694.0	205.881633	-38.176599	24.401	0.592	1.582	0.038	0.048	388.1
1696.0	205.877732	-38.184567	24.500	0.731	1.761	0.040	0.054	870.4
1746.0	205.883153	-38.174474	25.494	0.582	1.947	0.077	0.132	315.5
1748.0	205.877034	-38.187045	24.165	0.574	1.433	0.030	0.036	1030.6
1786.0	205.878415	-38.185054	25.623	0.528	1.557	0.068	0.095	870.3
1803.0	205.883529	-38.175090	25.710	0.698	1.695	0.097	0.125	283.1
1815.0	205.882929	-38.176593	24.917	0.464	1.369	0.051	0.060	315.5
1821.0	205.874356	-38.194195	25.621	0.646	1.907	0.077	0.132	1540.5
1826.0	205.889276	-38.163971	24.271	0.506	1.343	0.031	0.036	859.0
1830.0	205.879954	-38.182930	25.694	0.583	1.498	0.083	0.099	698.3
1833.0	205.885606	-38.171483	24.755	0.635	1.751	0.045	0.066	354.9

Table A.1 (cont'd)

ID	RA	DEC	I_{814}	r - I	±	g - I	±	radius
1837.0	205.886972	-38.168687	25.716	0.550	1.333	0.074	0.085	524.6
1841.0	205.894397	-38.153642	25.648	0.551	1.649	0.086	0.100	1636.8
1850.0	205.883813	-38.175413	24.592	0.595	1.885	0.049	0.071	263.5
1851.0	205.880751	-38.181672	25.392	0.611	1.335	0.071	0.072	602.3
1871.0	205.884440	-38.174473	25.091	0.649	1.796	0.065	0.089	247.5
1881.0	205.879754	-38.184232	24.464	0.613	1.586	0.037	0.048	776.2
1896.0	205.885928	-38.171854	25.557	0.635	1.882	0.078	0.125	322.8
1899.0	205.881956	-38.180055	25.340	0.535	1.298	0.064	0.073	474.1
1914.0	205.885453	-38.173244	25.475	0.682	1.755	0.077	0.103	253.9
1938.0	205.876652	-38.191585	25.664	0.728	1.833	0.082	0.122	1312.4
1972.0	205.882998	-38.179149	24.031	0.643	1.763	0.032	0.043	387.1
1990.0	205.886311	-38.172621	24.223	0.567	1.654	0.032	0.041	263.8
1995.0	205.884312	-38.176739	25.479	0.653	1.674	0.098	0.119	241.1
2016.0	205.885690	-38.174296	24.368	0.694	1.714	0.047	0.058	192.5
2017.0	205.885816	-38.174262	24.959	0.565	1.395	0.060	0.065	188.4
2032.0	205.887516	-38.170791	25.123	0.512	1.442	0.052	0.064	370.3
2034.0	205.884097	-38.177795	25.465	0.631	1.624	0.086	0.108	281.3
2063.0	205.879652	-38.187188	25.962	0.675	1.831	0.086	0.139	953.4
2065.0	205.881038	-38.184352	25.516	0.597	1.438	0.067	0.086	739.6
2072.0	205.890812	-38.164549	25.636	0.563	1.640	0.072	0.107	827.1
2074.0	205.883454	-38.179552	25.106	0.737	1.868	0.063	0.094	386.1
2088.0	205.884535	-38.177648	25.622	0.744	1.873	0.103	0.142	254.4
2094.0	205.886089	-38.174908	25.116	0.802	1.845	0.075	0.091	150.0
2095.0	205.887187	-38.172367	25.666	0.600	1.676	0.086	0.115	262.7
2102.0	205.884455	-38.178205	24.843	0.603	1.494	0.057	0.066	280.2
2103.0	205.881487	-38.184118	24.884	0.593	1.455	0.050	0.057	711.3
2109.0	205.881829	-38.183545	25.799	0.729	1.960	0.091	0.143	666.3
2119.0	205.892006	-38.162979	25.493	0.532	1.343	0.059	0.074	950.9
2120.0	205.885379	-38.176497	25.156	0.375	1.384	0.076	0.088	178.1
2122.0	205.886619	-38.174018	24.647	0.717	1.732	0.057	0.070	168.9
2136.0	205.877507	-38.192758	25.663	0.765	1.940	0.080	0.141	1363.2
2140.0	205.886773	-38.173892	25.298	0.406	1.296	0.077	0.084	171.3
2151.0	205.890525	-38.166667	24.452	0.672	1.759	0.038	0.055	674.0
2156.0	205.880398	-38.187283	25.490	0.656	1.649	0.064	0.090	938.4
2162.0	205.891830	-38.164527	27.333	0.536	1.394	0.166	0.208	840.0

Table A.1 (cont'd)

ID	RA	DEC	I_{814}	r - I	±	g - I	±	radius
2163.0	205.885674	-38.176661	25.372	0.424	1.449	0.072	0.084	165.7
2169.0	205.879781	-38.188807	25.371	0.539	1.292	0.058	0.066	1051.5
2171.0	205.891437	-38.165052	25.621	0.585	1.262	0.070	0.080	798.3
2173.0	205.888472	-38.171118	25.775	0.650	1.413	0.090	0.101	342.9
2178.0	205.890835	-38.166371	25.392	0.477	1.365	0.057	0.071	698.3
2180.0	205.897424	-38.152976	25.412	0.574	1.388	0.083	0.072	1726.2
2206.0	205.887664	-38.173101	24.921	0.511	1.480	0.059	0.068	204.9
2214.0	205.880825	-38.187153	26.129	0.748	1.687	0.106	0.147	918.1
2220.0	205.894088	-38.160198	25.660	0.635	1.640	0.074	0.103	1173.9
2224.0	205.885504	-38.177752	24.990	0.486	1.592	0.060	0.076	213.4
2226.0	205.887077	-38.174513	25.974	0.441	1.340	0.140	0.149	124.5
2227.0	205.881728	-38.185491	24.693	0.543	1.438	0.042	0.048	789.0
2251.0	205.887418	-38.174198	25.118	0.678	1.675	0.085	0.100	134.0
2253.0	205.877457	-38.194695	24.819	0.522	1.440	0.025	0.032	1490.4
2253.0	205.877457	-38.194695	2872.743	0.522	1.440	0.025	0.032	1.8
2254.0	205.888221	-38.172691	24.705	0.659	1.670	0.053	0.066	229.9
2257.0	205.885542	-38.178233	24.359	0.676	1.685	0.045	0.055	235.3
2285.0	205.891226	-38.167040	25.212	0.617	1.609	0.054	0.073	656.0
2294.0	205.881130	-38.187766	24.658	0.587	1.554	0.039	0.052	950.2
2302.0	205.886567	-38.176811	24.492	0.622	1.890	0.073	0.101	124.8
2310.0	205.888872	-38.172283	23.713	0.686	1.665	0.030	0.036	260.4
2312.0	205.883834	-38.182550	25.418	0.730	1.914	0.076	0.114	546.1
2330.0	205.880772	-38.189202	25.333	0.642	1.552	0.062	0.082	1052.4
2338.0	205.889969	-38.170622	24.607	0.578	1.443	0.041	0.050	388.6
2346.0	205.888416	-38.173901	24.018	0.644	1.776	0.039	0.049	142.7
2353.0	205.889646	-38.171515	24.487	0.667	1.984	0.042	0.066	321.9
2356.0	205.888725	-38.173362	25.465	0.431	1.532	0.088	0.109	182.2
2363.0	205.891171	-38.168456	25.687	0.719	1.678	0.081	0.106	556.8
2374.0	205.890324	-38.170375	25.758	0.650	1.552	0.085	0.108	410.8
2388.0	205.881572	-38.188556	24.959	0.828	1.896	0.054	0.082	991.6
2408.0	205.892309	-38.167030	24.870	0.584	1.538	0.044	0.058	674.2
2409.0	205.884536	-38.182860	25.664	0.636	1.382	0.086	0.094	548.7
2414.0	205.888853	-38.174051	25.991	0.486	1.587	0.164	0.206	134.4
2416.0	205.887042	-38.177807	25.052	0.513	1.665	0.088	0.110	159.2
2486.0	205.884131	-38.184804	24.495	0.589	1.514	0.039	0.045	686.9

Table A.1 (cont'd)

ID	RA	DEC	I_{814}	r - I	±	g - I	±	radius
2499.0	205.886921	-38.179295	25.487	0.631	1.771	0.086	0.124	260.1
2505.0	205.894528	-38.163902	23.661	0.562	1.562	0.024	0.030	929.2
2535.0	205.890213	-38.173052	25.698	0.541	1.531	0.099	0.124	227.4
2559.0	205.887659	-38.178771	24.423	0.645	1.777	0.049	0.066	212.4
2571.0	205.879358	-38.193250	25.253	0.638	1.404	0.056	0.070	1351.8
2577.0	205.889886	-38.174476	25.395	0.560	1.694	0.126	0.157	130.3
2582.0	205.886254	-38.181998	25.457	0.756	1.914	0.078	0.118	457.2
2593.0	205.884845	-38.185022	24.834	0.667	1.885	0.049	0.071	688.6
2599.0	205.887877	-38.178902	24.400	0.634	1.767	0.046	0.062	219.6
2601.0	205.896529	-38.161294	25.177	0.739	1.889	0.055	0.093	1146.1
2610.0	205.886175	-38.182532	24.692	0.496	1.458	0.040	0.050	495.5
2622.0	205.884394	-38.186359	25.303	0.503	1.355	0.055	0.066	788.1
2640.0	205.883795	-38.187961	24.739	0.467	1.360	0.040	0.049	908.4
2654.0	205.900192	-38.154648	24.860	0.390	1.353	0.050	0.046	1667.6
2672.0	205.891263	-38.173026	25.508	0.732	1.808	0.093	0.129	260.8
2685.0	205.879747	-38.196722	25.623	0.497	1.288	0.067	0.080	1579.0
2692.0	205.891576	-38.172692	25.193	0.713	1.766	0.074	0.095	290.7
2710.0	205.894855	-38.166291	25.490	0.560	1.603	0.060	0.089	780.6
2715.0	205.886764	-38.182900	25.084	0.976	1.289	0.067	0.055	514.0
2730.0	205.890834	-38.174734	24.714	0.761	1.794	0.067	0.080	159.1
2731.0	205.895325	-38.165632	24.786	0.565	1.647	0.042	0.057	835.0
2741.0	205.891352	-38.173979	24.926	0.742	1.936	0.075	0.107	214.7
2749.0	205.893544	-38.168106	24.978	0.658	1.554	0.051	0.065	630.4
2796.0	205.893648	-38.169993	25.680	0.616	1.776	0.078	0.120	516.7
2797.0	205.887784	-38.181955	25.377	0.574	1.662	0.066	0.093	438.7
2799.0	205.886606	-38.184265	24.477	0.642	1.646	0.040	0.050	612.3
2806.0	205.891233	-38.175061	24.377	0.650	1.486	0.059	0.062	169.3
2808.0	205.891787	-38.173971	25.710	0.612	1.548	0.106	0.121	234.4
2810.0	205.894109	-38.169306	25.501	0.403	1.466	0.060	0.084	572.4
2812.0	205.887257	-38.183254	25.582	0.695	1.847	0.078	0.119	534.9
2813.0	205.894636	-38.168278	24.609	0.773	1.907	0.043	0.065	650.6
2818.0	205.879523	-38.199169	26.701	0.547	1.482	0.126	0.177	1750.7
2842.0	205.890764	-38.176583	25.525	0.562	1.517	0.111	0.118	141.4
2850.0	205.890994	-38.176336	23.751	0.617	1.640	0.042	0.049	148.8
2858.0	205.893517	-38.171274	25.768	0.471	1.519	0.078	0.110	439.4

Table A.1 (cont'd)

ID	RA	DEC	I_{814}	r - I	±	g - I	±	radius
2870.0	205.889972	-38.179520	25.249	0.625	1.772	0.069	0.101	276.1
2873.0	205.890713	-38.177481	25.843	0.596	1.448	0.090	0.105	173.1
2879.0	205.897528	-38.163354	25.235	0.503	1.464	0.050	0.070	1038.7
2891.0	205.891858	-38.175127	24.616	0.761	1.786	0.063	0.078	201.4
2895.0	205.890555	-38.177847	23.977	0.696	1.886	0.038	0.051	185.7
2907.0	205.900549	-38.158025	24.718	0.558	1.945	0.055	0.077	1457.4
2908.0	205.890343	-38.178478	24.866	0.654	1.771	0.059	0.078	216.0
2915.0	205.899609	-38.159741	25.574	0.704	1.932	0.072	0.126	1323.4
2923.0	205.890548	-38.178349	24.987	0.644	1.789	0.063	0.087	214.3
2924.0	205.892146	-38.175075	24.725	0.683	1.749	0.062	0.077	218.2
2930.0	205.890813	-38.177846	25.302	0.646	1.581	0.080	0.097	195.3
2932.0	205.897204	-38.164900	24.965	0.820	1.818	0.054	0.077	933.8
2946.0	205.886053	-38.187895	23.508	0.718	1.863	0.024	0.032	875.3
2948.0	205.890208	-38.179381	25.111	0.526	1.532	0.057	0.071	271.3
2953.0	205.891643	-38.176556	24.818	0.710	1.760	0.068	0.083	188.2
2954.0	205.892694	-38.174469	24.580	0.846	1.942	0.059	0.078	262.0
2962.0	205.891513	-38.177064	24.646	0.520	1.498	0.050	0.059	194.1
2963.0	205.892903	-38.174266	25.369	0.471	1.402	0.070	0.084	278.6
2967.0	205.901966	-38.155952	24.920	0.617	1.745	0.058	0.066	1626.8
2973.0	205.891664	-38.176988	25.709	0.540	1.526	0.102	0.122	199.6
2997.0	205.890222	-38.180289	25.342	0.685	1.834	0.069	0.102	333.1
3000.0	205.890637	-38.179596	24.345	0.595	1.564	0.035	0.044	294.8
3007.0	205.890496	-38.180059	25.590	0.629	1.424	0.068	0.079	323.2
3008.0	205.892241	-38.176495	25.086	0.482	1.451	0.057	0.068	220.4
3015.0	205.892943	-38.175199	25.249	0.657	1.638	0.074	0.095	260.2
3049.0	205.896038	-38.169465	24.824	0.630	1.725	0.046	0.066	631.8
3052.0	205.899274	-38.162875	25.031	0.745	1.822	0.052	0.078	1119.8
3053.0	205.889709	-38.182407	24.934	0.628	1.558	0.050	0.065	475.3
3059.0	205.889941	-38.182021	24.151	0.678	1.768	0.033	0.046	450.3
3063.0	205.899421	-38.162735	25.640	0.569	1.321	0.067	0.080	1132.9
3071.0	205.892573	-38.176798	25.060	0.630	1.664	0.066	0.084	243.6
3094.0	205.890121	-38.182202	24.561	0.574	1.541	0.038	0.050	465.0
3097.0	205.897118	-38.167961	25.349	0.789	1.980	0.070	0.113	753.1
3103.0	205.889636	-38.183364	25.537	0.390	1.511	0.061	0.087	543.0
3123.0	205.884680	-38.193769	23.926	0.580	1.539	0.027	0.035	1305.2

Table A.1 (cont'd)

ID	RA	DEC	I_{814}	r - I	±	g - I	±	radius
3124.0	205.892307	-38.178150	25.156	0.528	1.464	0.060	0.074	273.5
3127.0	205.880686	-38.201981	26.740	0.738	1.330	0.088	0.097	1929.7
3130.0	205.897171	-38.168385	24.280	0.570	1.601	0.033	0.043	732.3
3133.0	205.892979	-38.176921	25.485	0.719	1.865	0.086	0.124	268.2
3140.0	205.896046	-38.170920	23.888	0.688	1.819	0.029	0.041	559.9
3158.0	205.901722	-38.159752	25.518	0.757	1.541	0.077	0.091	1383.9
3171.0	205.893466	-38.176774	25.768	0.434	1.298	0.081	0.095	292.4
3179.0	205.887142	-38.189734	25.093	0.589	1.409	0.050	0.060	1000.0
3182.0	205.896523	-38.170646	24.877	0.593	1.547	0.048	0.061	593.4
3186.0	205.893648	-38.176567	25.477	0.425	1.293	0.066	0.081	299.5
3194.0	205.904190	-38.155235	25.058	0.544	1.695	0.065	0.072	1733.8
3198.0	205.896251	-38.171489	25.142	0.649	1.660	0.058	0.079	544.2
3203.0	205.893906	-38.176299	25.050	0.605	1.841	0.060	0.087	311.3
3204.0	205.895556	-38.172952	25.472	0.573	1.726	0.070	0.106	455.1
3213.0	205.902954	-38.158061	25.521	0.668	1.615	0.091	0.097	1524.0
3215.0	205.896038	-38.172201	24.140	0.539	1.563	0.031	0.042	505.7
3236.0	205.897960	-38.168763	25.678	0.757	1.823	0.081	0.122	744.1
3237.0	205.889176	-38.186692	25.065	0.570	1.498	0.053	0.065	779.4
3245.0	205.892957	-38.179142	25.573	0.497	1.726	0.071	0.109	347.4
3260.0	205.894080	-38.177059	25.329	0.771	1.776	0.077	0.100	330.8
3261.0	205.898023	-38.169047	25.227	0.666	1.856	0.059	0.099	732.9
3283.0	205.893179	-38.179370	25.641	0.640	1.733	0.083	0.127	367.9
3290.0	205.890106	-38.185717	25.349	0.600	1.533	0.065	0.078	714.4
3299.0	205.893516	-38.178908	25.733	0.475	1.626	0.072	0.103	360.7
3303.0	205.894071	-38.177806	25.269	0.580	1.301	0.061	0.067	348.0
3312.0	205.893400	-38.179393	25.101	0.812	1.877	0.064	0.096	378.1
3318.0	205.891416	-38.183509	25.699	0.507	1.491	0.077	0.113	574.5
3323.0	205.894169	-38.178080	24.186	0.531	1.409	0.033	0.038	361.3
3324.0	205.899904	-38.166378	24.686	0.705	1.817	0.042	0.063	943.5
3332.0	205.891332	-38.183910	25.247	0.578	1.480	0.058	0.073	601.0
3343.0	205.888653	-38.189500	25.383	0.615	1.812	0.060	0.103	980.6
3345.0	205.890994	-38.184737	24.754	0.669	1.621	0.046	0.058	653.8
3359.0	205.899417	-38.167897	24.868	0.685	1.787	0.047	0.073	846.9
3363.0	205.892012	-38.183120	25.499	0.630	1.452	0.073	0.089	559.1
3393.0	205.892563	-38.182550	25.667	0.803	1.854	0.089	0.128	534.0

Table A.1 (cont'd)

ID	RA	DEC	I_{814}	r - I	±	g - I	±	radius
3415.0	205.891007	-38.186152	25.559	0.627	1.389	0.077	0.085	753.6
3433.0	205.892303	-38.183704	24.811	0.698	1.764	0.047	0.070	604.3
3442.0	205.894794	-38.178788	25.522	0.826	1.806	0.083	0.111	416.5
3490.0	205.897028	-38.174675	24.256	0.634	1.620	0.034	0.044	494.4
3497.0	205.892485	-38.184400	25.271	0.581	1.488	0.056	0.072	654.8
3516.0	205.893558	-38.182562	24.668	0.643	1.651	0.041	0.056	561.8
3517.0	205.896334	-38.176922	25.647	0.637	1.456	0.081	0.095	453.7
3558.0	205.905161	-38.159786	25.375	0.708	1.623	0.076	0.088	1496.8
3573.0	205.901782	-38.166851	25.275	0.451	1.360	0.052	0.066	997.0
3594.0	205.897362	-38.176317	23.619	0.650	1.633	0.025	0.032	506.6
3601.0	205.897244	-38.176612	25.310	0.659	1.825	0.065	0.101	501.6
3604.0	205.893325	-38.184598	25.731	0.598	1.943	0.077	0.139	686.0
3613.0	205.889805	-38.191943	25.563	0.577	1.533	0.071	0.105	1159.0
3615.0	205.896153	-38.179051	25.147	0.526	1.496	0.052	0.071	493.1
3620.0	205.894794	-38.182217	25.588	0.603	1.410	0.069	0.084	581.3
3625.0	205.901451	-38.168428	25.144	0.509	1.443	0.048	0.063	911.7
3638.0	205.896039	-38.179332	25.420	0.616	1.442	0.066	0.079	497.2
3639.0	205.892433	-38.187290	25.288	0.624	1.688	0.067	0.095	852.1
3648.0	205.898316	-38.175632	25.208	0.572	1.482	0.059	0.072	559.9
3662.0	205.897490	-38.177869	25.509	0.607	1.322	0.074	0.086	532.5
3683.0	205.904073	-38.164884	25.304	0.570	1.455	0.054	0.073	1188.0
3695.0	205.899017	-38.175538	24.704	0.601	1.518	0.047	0.065	599.8
3719.0	205.900370	-38.173256	25.378	0.479	1.506	0.064	0.112	701.9
3721.0	205.905994	-38.161840	25.507	0.806	1.900	0.074	0.118	1418.0
3733.0	205.893727	-38.187074	25.108	0.544	1.500	0.063	0.090	859.9
3743.0	205.903360	-38.167685	24.796	0.527	1.682	0.046	0.080	1030.8
3754.0	205.895036	-38.184945	24.947	0.876	1.871	0.058	0.087	752.1
3764.0	205.902083	-38.170784	26.009	0.511	1.373	0.106	0.145	855.5
3775.0	205.897924	-38.178566	25.709	0.523	1.782	0.093	0.167	571.1
3780.0	205.894396	-38.186971	24.909	0.829	1.610	0.066	0.077	866.9
3790.0	205.894970	-38.186131	25.407	0.269	1.355	0.064	0.083	825.6
3825.0	205.896285	-38.184573	25.447	0.744	1.750	0.084	0.123	767.7
3836.0	205.901846	-38.173565	25.058	0.777	1.797	0.063	0.093	777.5
3846.0	205.907393	-38.162392	25.167	0.662	1.622	0.057	0.083	1447.7
3857.0	205.905435	-38.166525	25.082	0.481	1.421	0.050	0.072	1175.0

Table A.1 (cont'd)

ID	RA	DEC	I_{814}	r - I	±	g - I	±	radius
3864.0	205.908702	-38.160035	24.390	0.511	1.431	0.050	0.046	1618.4
3894.0	205.904947	-38.168450	25.610	0.869	1.839	0.091	0.137	1077.2
3916.0	205.896466	-38.186385	24.639	0.534	1.495	0.037	0.049	882.5
3937.0	205.911328	-38.156397	25.670	0.589	1.726	0.111	0.122	1910.3
3938.0	205.897354	-38.185021	24.673	0.700	1.825	0.042	0.063	829.6
3939.0	205.897764	-38.184128	25.631	0.631	1.645	0.071	0.103	794.8
3948.0	205.905385	-38.168795	25.353	0.619	1.518	0.066	0.089	1087.0
3956.0	205.902592	-38.174833	25.476	0.561	1.371	0.062	0.074	805.2
3968.0	205.904657	-38.170720	24.875	0.625	1.550	0.045	0.060	991.0
3969.0	205.905041	-38.169924	25.318	0.531	1.491	0.055	0.074	1033.5
3973.0	205.903711	-38.172667	24.518	0.567	1.566	0.036	0.048	895.5
3977.0	205.901394	-38.177493	25.153	0.596	1.642	0.053	0.076	743.0
3983.0	205.904689	-38.171029	25.071	0.475	1.206	0.046	0.055	984.4
3994.0	205.890627	-38.200050	24.987	0.655	1.569	0.049	0.063	1744.5
4014.0	205.909311	-38.162412	24.461	0.697	1.716	0.040	0.052	1529.0
4021.0	205.903189	-38.175078	25.000	0.548	1.506	0.046	0.061	837.5
4028.0	205.909549	-38.162288	25.099	0.490	1.507	0.051	0.066	1545.1
4049.0	205.909414	-38.163117	24.979	0.458	1.339	0.043	0.054	1501.9
4050.0	205.900868	-38.180548	25.702	0.588	1.725	0.077	0.120	780.1
4055.0	205.905000	-38.172223	25.528	0.480	1.379	0.058	0.074	974.1
4056.0	205.905097	-38.172217	24.398	0.576	1.444	0.034	0.044	979.6
4058.0	205.894541	-38.193605	25.398	0.678	1.795	0.063	0.102	1322.2
4092.0	205.894583	-38.194612	25.498	0.479	1.418	0.058	0.080	1392.9
4131.0	205.897396	-38.189355	25.443	0.633	1.550	0.068	0.085	1094.9
4134.0	205.911990	-38.160245	25.159	0.518	1.528	0.065	0.069	1745.4
4138.0	205.907869	-38.168687	25.470	0.560	1.487	0.062	0.085	1216.2
4142.0	205.909127	-38.166255	25.570	0.491	1.336	0.062	0.078	1361.3
4143.0	205.908599	-38.167386	24.916	0.671	1.786	0.047	0.073	1295.3
4153.0	205.902529	-38.180119	25.134	0.497	1.353	0.048	0.059	854.4
4163.0	205.910801	-38.163589	25.532	0.493	1.444	0.058	0.080	1545.0
4182.0	205.904486	-38.177130	24.990	0.773	1.885	0.051	0.082	913.6
4193.0	205.903935	-38.178570	25.402	0.472	1.353	0.051	0.066	898.8
4207.0	205.909626	-38.167452	25.332	0.608	1.442	0.057	0.073	1344.7
4213.0	205.896474	-38.194486	25.650	0.437	1.425	0.065	0.089	1414.8
4215.0	205.893880	-38.199875	25.405	0.599	1.621	0.058	0.086	1754.9

Table A.1 (cont'd)

ID	RA	DEC	I_{814}	r - I	±	g - I	±	radius
4270.0	205.910860	-38.167192	24.329	0.712	1.627	0.035	0.046	1415.5
4289.0	205.904995	-38.180004	24.163	0.627	1.639	0.030	0.041	983.5
4298.0	205.909380	-38.171108	25.675	0.584	1.493	0.073	0.097	1234.7
4307.0	205.914726	-38.160524	25.162	0.539	1.574	0.064	0.069	1854.4
4316.0	205.912062	-38.166399	25.130	0.521	1.405	0.048	0.062	1501.9
4332.0	205.906766	-38.179334	24.376	0.532	1.492	0.034	0.043	1067.3
4373.0	205.914860	-38.162595	25.277	0.554	1.331	0.072	0.063	1775.9
4377.0	205.907785	-38.177118	25.014	0.669	1.609	0.050	0.065	1099.2
4389.0	205.914811	-38.163276	25.458	0.451	1.380	0.065	0.075	1747.6
4433.0	205.910055	-38.174748	25.389	0.341	1.376	0.056	0.076	1226.8
4459.0	205.911713	-38.172504	25.840	0.579	1.645	0.074	0.110	1340.3
4472.0	205.910666	-38.175438	24.136	0.586	1.562	0.029	0.038	1259.0
4550.0	205.912292	-38.176423	25.121	0.697	1.861	0.056	0.091	1351.2
4551.0	205.903048	-38.195670	25.297	0.556	1.485	0.056	0.073	1647.6
4606.0	205.911259	-38.181504	25.085	0.637	1.855	0.051	0.084	1354.1
4643.0	205.903257	-38.200037	25.142	0.703	1.551	0.054	0.070	1931.1
4646.0	205.907500	-38.191457	24.046	0.615	1.417	0.031	0.034	1556.5
4650.0	205.905520	-38.195768	24.119	0.534	1.305	0.029	0.035	1728.0
4653.0	205.907229	-38.192318	24.266	0.579	1.609	0.034	0.044	1591.4
4654.0	205.912951	-38.180713	25.527	0.574	1.617	0.065	0.096	1430.8
4672.0	205.915315	-38.176792	25.245	0.655	1.875	0.058	0.097	1523.2
4673.0	205.913728	-38.178294	25.467	0.462	1.266	0.055	0.068	1442.6
4707.0	205.914877	-38.179244	24.557	0.588	1.445	0.036	0.046	1516.4
4715.0	205.916273	-38.176574	25.282	0.697	1.834	0.060	0.095	1576.8
4745.0	205.920258	-38.169613	25.697	0.499	1.500	0.067	0.096	1857.3
4762.0	205.911233	-38.189002	25.413	0.652	1.512	0.062	0.081	1599.4
4810.0	205.919688	-38.173797	25.145	0.620	1.659	0.048	0.071	1775.7
4831.0	205.920615	-38.172687	25.563	0.607	1.589	0.066	0.094	1836.2
4854.0	205.908150	-38.199458	25.045	0.510	1.270	0.042	0.050	2031.4
4876.0	205.920500	-38.174979	25.211	0.700	1.627	0.055	0.078	1816.4
4939.0	205.913245	-38.192442	25.656	0.621	1.837	0.079	0.124	1842.4
4946.0	205.920150	-38.178620	23.850	0.691	1.949	0.026	0.041	1806.2
5033.0	205.914998	-38.192941	25.562	0.533	1.394	0.065	0.084	1941.6
5048.0	205.921798	-38.179923	24.510	0.564	1.357	0.035	0.042	1911.0